Dissertation
submitted to the
Combined Faculties for the Natural Sciences and for Mathematics
of the Ruperto-Carola University of Heidelberg, Germany
for the degree of
Doctor of Natural Sciences

presented by

Diplomphysikerin: María Díaz Trigo

born in: Santiago de Compostela

Oral examination: 17 April 2002

Collecting heat during the day, observing the sky at night:

the use of a heliostat field near Almería

to search for cosmic gamma rays

Referees: **Prof. Dr. John Kirk**
Prof. Dr. Rainer Plaga

Sie sind so jung, so vor allem Anfang, und ich möchte Sie, so gut ich es kann, bitten, lieber Herr, Geduld zu haben gegen alles Ungelöste in Ihrem Herzen und zu versuchen, *die Fragen selbst* liebzuhaben wie verschlossene Stuben und wie Bücher, die in einer sehr fremden Sprache geschrieben sind. Forschen Sie jetzt nicht nach den Antworten, die Ihnen nicht gegeben werden können, weil Sie sie nicht leben könnten. Und es handelt sich darum, alles zu leben . *Leben* Sie jetzt die Fragen. Vielleicht leben Sie dann allmählich, onhe es zu merken, eines fernen Tages in die Antwort hinein.

Rainer Maria Rilke

Zusammenfassung

Das GRAAL-Experiment (Gamma Ray Astronomy at ALmería) benutzt ca. 2500 m^2 Spiegelfläche eines Solarkraftwerkes in Südspanien als Cherenkov-Teleskop für die Hochenergie-Gammaastronomie. Der Detektor wurde im Zentralturm der Anlage installiert und mißt mit einer Gamma-Energieschwelle von 250 GeV die Luftschauer kosmischer Strahlung innerhalb eines Gesichtsfeldes von 15000 m^2. Hauptaufgabe war die Suche nach neuen VHE-Gammaquellen.

Diese Arbeit beschreibt den Aufbau des Experimentes und die Meßergebnisse nach zweijähriger Betriebszeit. Die Methoden der Datenanalyse und die Monte Carlo Simulation werden diskutiert. Besondere Aufmerksamkeit wird den speziellen Problemen gewidmet, die bei der Verwendung von Solarspiegelanlagen für die Beobachtung von Luftschauern auftreten, z.B. eine Angleichung von Gamma- und Protonsignalen wegen des relativ kleinen Öffnungswinkels.

Während mehr als 250 Stunden wurden auswertbare Daten von 18 verschiedenen kosmischen Strahlungsquellen registriert. Dazu gehörten u.a. der Krebs-Nebel, der Blazar Mrk 421 und der Gamma Ray Burst GRB010222. Die prinzipielle Verwendbarkeit von Solaranlagen für die Messung von kosmischen Gammaquellen wurde durch die Beobachtung des Krebs-Nebels und Mrk 421 nachgewiesen.

Abstract

The GRAAL experiment (Gamma Ray Astronomy at ALmería) is the result of the conversion of a solar power plant near Almería into a Cherenkov telescope with a total mirror area of 2500 m^2 for very high energy gamma astronomy. The detector is located in a central solar tower and detects photon-induced showers with an energy threshold of 250 GeV and an effective detection area of about 15000 m^2. The aim of the experiment was the search for very high energy gamma sources.

This thesis describes the installation of the detector and the results of its operation during more than 2 years. The methods developed for the Monte Carlo simulation and the analysis of the data are discussed. A special emphasis is put on the general problems encountered on the application of this new technique to the observation of gamma-rays common to all heliostat arrays. In particular, the effect of a field of view restricted to the central part of a detected air shower on the lateral distribution and timing properties of Cherenkov light are discussed. Under angular restriction the differences between gamma and hadron induced showers obliterate, making an efficient gamma-hadron separation difficult.

More than 250 hours of usable data were taken with the GRAAL detector on 18 different sources, among them the Crab nebula, the blazar Markarian 421 and the gamma-ray burst GRB010222. Evidence for a gamma-ray flux from the direction of the Crab pulsar and Markarian 421 was found, proving the feasibility of solar arrays for the observation of gamma-ray sources.

Contents

List of acronyms and abbreviations

AC	Alternating Current
ADC	Analog to Digital Converter
ACT	Air Cherenkov Telescopes
AGN	Active Galactic Nucleus
a.s.l	above sea level
BH	Black Hole
CGRO	Compton Gamma Ray Observatory
CIEMAT	Centro de Investigaciones Energéticas, Medioambientales y Tecnológicas
CR	Cosmic Rays
DC	Direct Current
EAS	Extensive Air Shower
ECS	External Compton scattering
EGRET	Energetic Gamma Ray Experiment Telescope
FADC	Flash ADC
fov	Field Of View
FSRQ	Flat Spectrum Radio Quasar
FWHM	Full Width Half Maximum
GLAST	Gamma-ray Large Area Space Telescope
GRB	Gamma-Ray Burst
HE	High Energy
HV	High Voltage
IACT	Imaging Air Cherenkov Telescopes
IR	InfraRed
ISM	Interstellar Medium
LED	Light Emission Diode
LONS	Light Of Night Sky
MBR	Microwave Background Radiation
MC	Monte Carlo
MHD	Magnetohydrodynamic
Mrk	Markarian
NS	Neutron Star
NSB	Night-Sky Background
p.e.	photoelectron
PIC	Proton-Initiated Cascade
PMT	Photomultiplier Tube
PSA	Plataforma Solar de Almería
Q-trigger	Charge trigger
QE	Quantum Efficiency
quasar	quasi stellar radio source
Seq-trigger	Sequence trigger
SN	Supernova
SNR	Supernova Remnant
SSC	Synchrotron Self Compton
UV	UltraViolet
VHE	Very High Energy
UHE	Ultra High Energy

XRB X-ray Binary

Chapter 1

Introduction

Gamma radiation represents the most energetic part of the electromagnetic spectrum. Energetic protons and electrons in the vicinity of astrophysical objects produce high-energy quanta, which can escape if there is less than ≈1 radiation length of matter surrounding the acceleration region (the mechanisms involved in the production are explained in sections 1.2.1-1.2.5). Gamma-rays can be traced back to their production sites; thus, observations of very high energy gamma-rays provide unique insight into the nature of cosmic-particle accelerators. Extragalactic sources serve as beacons that allow us to probe the intervening intergalactic medium and consequently give us hints to the conditions in the early universe.

The energy range of gamma-ray astronomy extends over more than twelve orders of magnitude (from about 500 keV to ca. 300 PeV) and has been "mostly" explored, either from space with satellite-based telescopes (at the lowest energies of the spectrum) or from the ground with Cherenkov telescopes and particle arrays (at the highest energies)[1]. However, there is still a part of the gamma-energy band which remains completely unexplored, ≈ 30-300 GeV. This energy gap is particularly interesting due to the fact that up to now more than 270 sources have been detected at energies below 30 GeV and only 4 above 300 GeV. The absorption of gamma-rays in the infrared background of the universe or cutoffs in the gamma-ray production sites play very likely an important role in the intermediate unexplored energy band.

The history of gamma-ray astronomy started around 1930, when Millikan and Cameron [159] realized that the energy density of cosmic rays in space is about as high as that of integrated star-light. They considered already the gamma rays included in the category of cosmic rays. In the 1950s the diffuse gamma-ray emission following the decay of π^0 mesons from cosmic-ray interstellar matter interactions was predicted by Hayakawa [108] and Morrison [167], and the gamma-ray emission from cosmic-ray *bremsstrahlung* by Hutchinson [117]. Gamma-ray bursts were discovered in 1967 by the VELA satellites and point sources were found by SAS-II and COS-B satellites in the 1970s and early 1980s. The major breakthrough came with the launch of the Compton Gamma Ray Observatory in 1991: more than 270 sources were discovered during its 10 years of life!. From the ground, the first gamma-ray detection occurred in 1989 when the Whipple collaboration, by using the atmospheric Cherenkov imaging technique proposed by Hillas, detected the Crab nebula with high significance. Since then, the number of well-established TeV sources is constantly increasing. Up to now 4 TeV credible detections of gamma-ray sources have been reported, the criterium to consider a gamma-ray source as *really*

[1] It must be remarked that though telescopes and particle arrays sensitive to the highest energies of the spectrum (300 GeV to ≈ 300 PeV) exist, this energy region is still "mostly unexplored" in the sense that less than a percent of the sky has been scanned with such telescopes.

credible being a "5σ detection coupled with an equally significant verification by another experiment" [236]. Nine more sources have been detected marginally or need confirmation by other experiments [238] (see table 1.2).

Fig. 1.1 shows the major milestones in observational gamma-ray astronomy and the increase in the number of sources with time. The gamma-rays of highest energy were detected from the Crab nebula at $\approx$ 70 TeV by the CANGAROO collaboration [216]. From 70 TeV up to the highest energies, no gamma-rays have been detected so far[2].

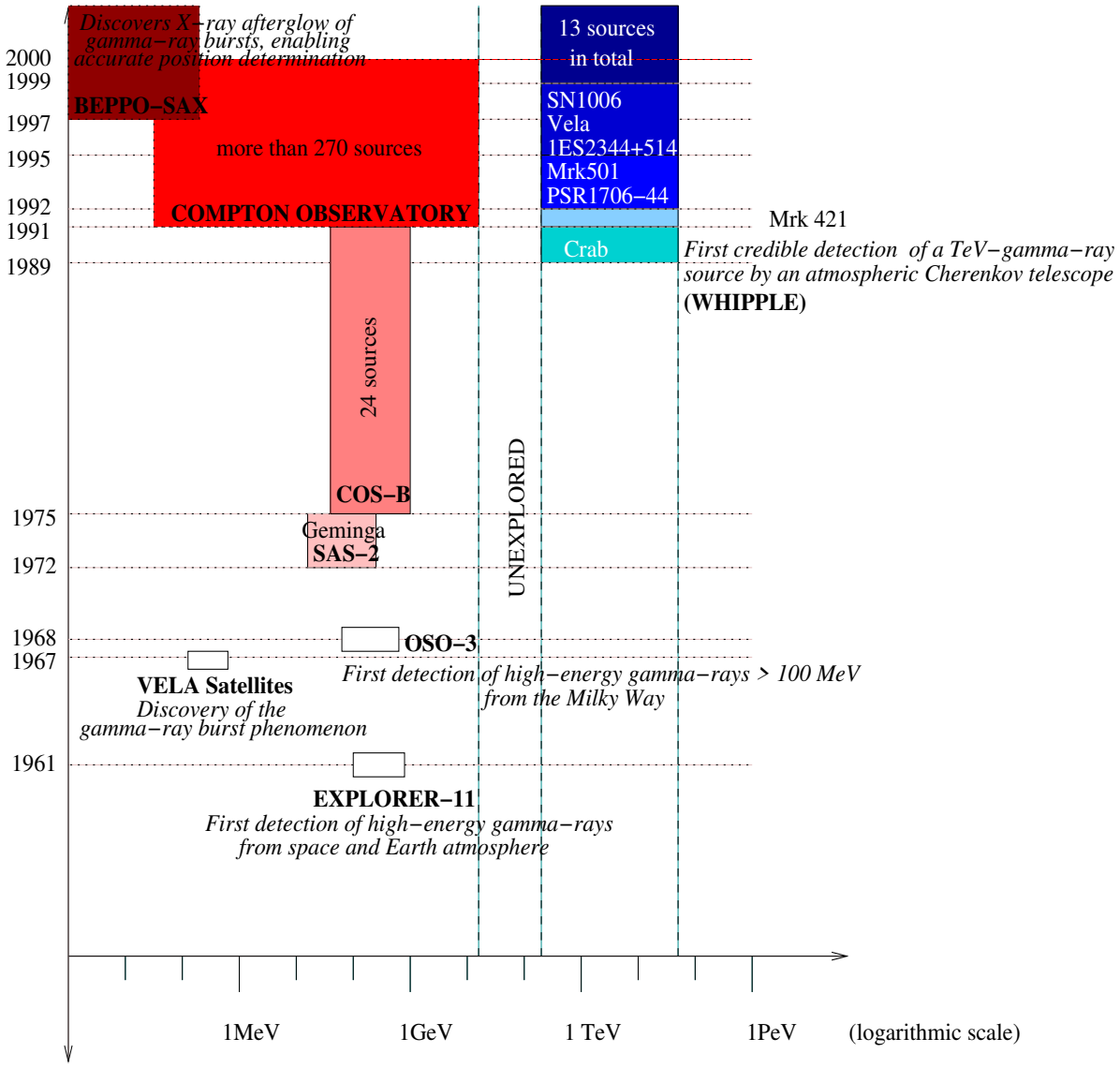

Figure 1.1: *Timeline of the development of gamma-ray astronomy. The energy region of 30-300 GeV remains presently unexplored. No gamma-rays have been detected at energies higher than 70 TeV.*

[2]For comparison, the highest energy cosmic ray detection was at about 10^{20} eV.

1.1 Mechanisms of gamma-ray emission

The most important processes for the production of high-energy gamma-radiation are:

- **Pion decay**: pions are created during strong interaction events such as collisions of cosmic ray protons with ambient-gas nuclei. Neutral pions decay rapidly (with a mean lifetime of $10^{-16}\gamma_\pi$ s, γ_π being the Lorentz factor of the pion) into two gamma-ray photons, with an energy distribution peaking at 70 MeV, half of the rest mass of the pion.

  Observation of a pion decay in a gamma-ray spectrum provides insight into collisions of energetic (>135 MeV) protons with nuclei. The pion decay gamma-ray bump is broadened as the momentum distribution of the high-energy collision adds a Doppler shift and broadening.

- **Inverse Compton Scattering (ICS)**: upscattering of photons of lower energy through collisions with energetic particles. If low-energy photons collide with relativistic electrons, these photons may gain energy in the collisions, thus being promoted in energy, e.g., from X-rays to gamma-rays.

  The ICS is important in regions of high photon densities. Considering that the typical energies of the high energy electrons which radiate in the radio waveband have Lorentz factors of $\gamma = 10^3$-10^4, the scattering of the photons of the cosmic microwave background generates X-rays ($\nu \approx \gamma^2\nu_0 \approx 10^{17}$ Hz) and the scattering of optical photons produces a flux of gamma-rays ($\nu \approx \gamma^2\nu_0 \approx 10^{21}$ Hz) [143]. Some examples of ICS happen in compact stars where an accretion disk is sufficiently hot to emit X-ray and the compact object generates beams of charged particles in its vicinity [206].

  If the differential spectrum of the electrons follows a power law $\mathrm{I}_e(\mathrm{E}_e) \propto \mathrm{E}_e^{-\Gamma}$; then, the resultant gamma-ray flux follows a power law as well: $\mathrm{I}_\gamma(\mathrm{E}_\gamma) \propto \mathrm{E}_\gamma^{-(\Gamma+1)/2}$ for $\gamma\epsilon \ll m_e c^2$ (Thomson limit) and $\mathrm{I}_\gamma(\mathrm{E}_\gamma) \propto \mathrm{E}_\gamma^{-\Gamma}$ for $\gamma\epsilon \gg m_e c^2$ (Klein-Nishina limit), where ϵ is the initial energy of the boosted photon [211].

- **Bremsstrahlung**: radiation produced by a charged particle in the Coulomb field of a nucleus or ion. The spectrum of *bremsstrahlung* radiation remains flat up to roughly the electron kinetic energy and it drops sharply towards zero above, as effectively all the kinetic energy of the electron has been transferred to the *bremsstrahlung* photon. If the *bremsstrahlung* is produced by high-energy electrons, the gamma-ray spectrum has the same shape, i.e., the same spectral index as the electron spectrum [211]. The contribution of *bremsstrahlung* to the Galactic diffuse emission is important in the energy range < 200 MeV.

- **Synchrotron emission**: radiation produced by high-energy charged particles when they are deflected by magnetic fields. Energetic electrons (1000 MeV) moving in the interstellar magnetic field radiate synchrotron photons, which can be observed in the radio regime. However, in order to produce gamma-rays by synchrotron emission large magnetic fields and/or energetic electrons are required. This can happen e.g. in the surface of neutron stars, where the magnetic fields are of $\mathcal{O}(10^{12})$G [206]. Alternatively, synchrotron radiation may provide the seed photon field for the inverse Compton process.

  If the electron spectrum follows a power law $\mathrm{I}_e(\mathrm{E}_e) \propto \mathrm{E}_e^{-\Gamma}$; then, the synchrotron photon spectrum will become $\mathrm{I}_\gamma(\mathrm{E}_\gamma) \propto \mathrm{E}_\gamma^{-(\Gamma+1)/2}$ similar to the case of the inverse Compton process [191].

Mechanism	$E_\gamma = 1$ MeV	$E_\gamma = 1$ GeV	$E_\gamma = 1$ TeV
Pion decay $\pi^0 \to 2\gamma$		$E_p >\sim 10^{10}$ eV	$E_p >\sim 10^{13}$ eV
ICS	Against microwave background		
	$\epsilon \sim 7 \times 10^{-4}$ eV $E_e \sim 1.7 \times 10^{10}$ eV	$\epsilon \sim 7 \times 10^{-4}$ eV $E_e \sim 5.3 \times 10^{11}$ eV	$\epsilon \sim 7 \times 10^{-4}$ eV $E_e \sim 1.7 \times 10^{13}$ eV
	Against starlight		
	$\epsilon \sim 1$ eV $E_e \sim 4.4 \times 10^{8}$ eV	$\epsilon \sim 1$ eV $E_e \sim 1.4 \times 10^{10}$ eV	$\epsilon \sim 1$ eV $E_e >\sim 1$ TeV
	Against X-rays		
	$\epsilon \sim 10$ keV $E_e \sim 4.4 \times 10^{6}$ eV	$\epsilon \sim 10$ keV $E_e >\sim 1$ GeV	$\epsilon \sim 10$ keV $E_e >\sim 1$ TeV
Bremsstrahlung	$E_e >\sim 2$ MeV	$E_e >\sim 2$ GeV	$E_e >\sim 2$ TeV
Synchrotron	$B = 10^{-4}$ G		
	$E_e \sim 7.7 \times 10^{14}$ eV		
	$B = 1$ G		
	$E_e \sim 7.2 \times 10^{12}$ eV	$E_e \sim 2.3 \times 10^{14}$ eV	$E_e \sim 7.2 \times 10^{15}$ eV
	$B = 10^4$ G		
	$E_e \sim 7.2 \times 10^{10}$ eV	$E_e \sim 2.3 \times 10^{12}$ eV	$E_e \sim 7.2 \times 10^{13}$ eV

Table 1.1: *Gamma-ray production parameters.* $\mathbf{E}_\gamma$ *= energy of the gamma-ray produced,* $\mathbf{E}_e$ *= energy of the relativistic electrons,* $\mathbf{E}_p$ *= energy of the relativistic protons,* $\mathbf{B}$ *= magnetic field,* ϵ *= energy of the initial photons for ICS. Taken from [191].*

Table 1.1 shows the parameters relevant to the production of gamma-rays by the various processes.

1.2 Sources of gamma-rays

The known celestial objects discussed in the next subsections are assumed or have been detected as gamma-ray emitters in the GeV and/or TeV energy range. Table 1.2 shows the gamma-ray sources detected up to now. The last column of the table indicates the "credibility" grade as given by Weekes [236].

1.2.1 Pulsars

The gamma-ray pulsars are sources in which the pulsar signals are generated by rotating, magnetised neutron stars (NS)[3], and the radiation luminosity derives ultimately from rotational energy[4]. Two classes of models have been developed to explain the gamma-ray emission in pulsars: polar cap and outer gap.

In *polar cap models* [213, 199, 102, 61, 10] the particles are accelerated by electric fields induced by rotation near the magnetic poles and close to the stellar surface. The gamma-

[3]The magnetic flux is conserved during the stellar core collapse which forms the NS. Then, the reduction of the star radius during collapse (from the initial 10^{11} cm to the 10^6 cm of the NS) implies an increase of the typical magnetic field of a normal star ($\approx 10^2$ Gauss) to values of the order of 10^{12} Gauss in a NS [206].

[4]The total rotational energy content of a young NS is of the order of 10^{51} erg [206].

Source	Type	Redshift	Discovery	EGRET	Grade
Galactic sources					
Crab Nebula	Plerion		1989([234])	yes	A
PSR 1706-44	Plerion?		1995([125])	no	A
Vela	Plerion?		1997([244])	no	B
SN1006	Shell		1997([217])	no	B-
RXJ1713.7-3946	Shell		1999([170])	no	B
Cassiopeia A	Shell		1999([8])	no	C
Centaurus X-3	Binary		1999([194])	yes	C
Extragalactic sources					
Markarian 421	XBL	0.031	1992([188])	yes	A
Markarian 501	XBL	0.034	1995([189])	yes	A
1ES2344+514	XBL	0.044	1997([41])	no	C
PKS2155-304	XBL	0.116	1999([46])	yes	B
1ES1959+650	XBL	0.048	1999([173])	no	B-
3C66A	RBL	0.44	1998([172])	yes	C

Table 1.2: *Source catalogue of detected TeV gamma-ray sources. XBL and RBL denote X-ray and radio selected BL Lac objects respectively. The last column shows the grade of "credibility" of the detection (A = really credible to C = least credible). Taken from [238].*

ray emission originates as curvature radiation[5] produced by the electrons as they follow the curvature of the open magnetic field lines [62] and/or inverse-Compton scattering of surface thermal emission and nonthermal optical, UV and soft X-ray emission [212]. The attenuation of gamma-rays near the neutron star surface caused by pair production (resulting from the interaction of gamma-rays with strong magnetic fields) predicts spectral cutoffs at high-energy which depend on the local field strength. Harding & de Jager [104] make a rough estimate of the spectral cutoff due to magnetic pair attenuation assuming emission along the polar cap outer rim at a certain height above the surface:

$$\mathrm{E_c} \approx 7.1\mathrm{MeV}\,\mathrm{P}^{1/2}\left(\frac{\mathrm{B_{cr}}}{\mathrm{B_0}}\right)\left(\frac{\mathrm{R}}{\mathrm{R_0}}\right)^{7/2} \tag{1.1}$$

where P, $\mathrm{R_0}$ and $\mathrm{B_0}$ are the NS period, radius and surface magnetic field and $\mathrm{B}_{cr} = 4.413 \times 10^{13}$ G is the critical field. They find cutoff energies consistent with the derived from experimental data for the known pulsars (4 MeV-75 GeV, see below). Moreover, they conclude that pulsed emission above 1 TeV can only be detected from pulsars having a combination of long period, low magnetic field or emission at a large height above the surface.

In *outer gap models* [49, 50, 51, 197] the primary particles are accelerated in vacuum gaps (free from the charged plasma which fills the magnetosphere) that form between the last open field line and the null charge surface ($\Omega \cdot B = 0$) in the outer magnetosphere. In contrast to the polar regions (which are very close to the star surface), in the outer magnetosphere relativistic effects from stellar gravity are of minor importance and magnetic fields are lower by many orders of magnitude. High energy emission results from curvature, synchrotron and inverse Compton scattering from the pair cascades, which are initiated by photon-photon pair

[5]The curvature radiation is emitted by relativistic particles moving in intense and bent magnetic fields.

Pulsar	Zhang & Harding	Rudak & Dyks	Romani	Cheng & Zhang
1932+1059	$< 580 \times 10^{-8}$	90×10^{-8}	$\approx 0 \times 10^{-8}$	$< 16 \times 10^{-8}$
2043+2740	50×10^{-8}	30×10^{-8}	$\approx 0 \times 10^{-8}$	50×10^{-8}
1803-2137	20×10^{-8}	20×10^{-8}	30×10^{-8}	$<16 \times 10^{-8}$
1801-2451	15×10^{-8}	10×10^{-8}	23×10^{-8}	$< 16 \times 10^{-8}$
1453-6151	10×10^{-8}	$< 2 \times 10^{-8}$	$\approx 0 \times 10^{-8}$	20×10^{-8}

Table 1.3: *Predicted gamma-ray fluxes (units of ph [E > 100 MeV] cm^{-2} s^{-1}) from four theoretical models for the gamma-ray emission of 5 pulsars. Taken from [221].*

production of gamma-rays with soft X-rays from the neutron star surface. Gamma-ray emission at TeV energies is predicted, for example, from inverse Compton scattering of synchrotron photons by primary particles [198].

Up to now, 7 pulsars have been detected by EGRET: Crab [174], Vela [122], Geminga [101, 24, 156], PSR B1509-58 [155, 137], PSR B1706-44 [219], PSR B1055-52 [83] and PSR B1951+32 [192]. They show extremely flat power spectra with maximum power often in the GeV energy range (see fig. 1.2). From these experimental results and from upper limits of ground-based observations, limits to pulsed gamma-ray emission are derived. For the known pulsars, such limits lie between 4 MeV and 75 GeV [171, 209]. Up to now no isolated pulsar has been detected at TeV energies (see below for detection of pulsars in a binary system), only upper limits have been reported, see e.g. [47, 209]. Therefore, strong constraints limit outer gap models. To prove the validity of polar cap models, the predicted cutoff in the energy spectrum (that lies in the unexplored range of energies 30-300 GeV) has to be observed. Table 1.3 shows the predicted gamma-ray fluxes from the above discussed models for gamma-ray pulsar candidates. The predictions differ by more than an order of magnitude for some pulsars. Therefore, a detection or non-detection of such pulsars would discriminate between the principal models.

A particular case in which TeV emission from a pulsar is predicted by different mechanisms from the above discussed is constituted by the pulsar B1259-63, the only known system in our galaxy with a radio pulsar orbiting a main sequence star (section 1.2.2 explains the main characteristics of binary systems). In general, pulsar winds that are confined by a companion star atmosphere produce shocks that may accelerate protons [103] and/or electrons[218]. The contribution of synchrotron radiation from the accelerated electrons to soft gamma-ray emission is calculated by Tavani & Arons [218], having values very close to the EGRET detected upper limits. In addition, Kirk et al. [129] calculate the gamma-ray emission at TeV energies from the inverse Compton scattering of the Be-star photons with relativistic electrons and positrons of the shocked pulsar wind. The obtained limits for gamma-ray fluxes at TeV energies are similar to the flux sensitivity of the current Cherenkov detectors. However, only a marginal detection (4.8σ) of the pulsar B1259-63 has been reported by the CANGAROO collaboration at energies larger than 3 TeV up to now [200].

1.2.2 Binary systems

X-ray binaries (XRBs) consist generally of a binary-star system with (at least) one component being a compact object at the end of its stellar evolution: a white dwarf, a neutron star or a black hole [206].

The accretion of matter of the companion star onto the compact object releases gravitational

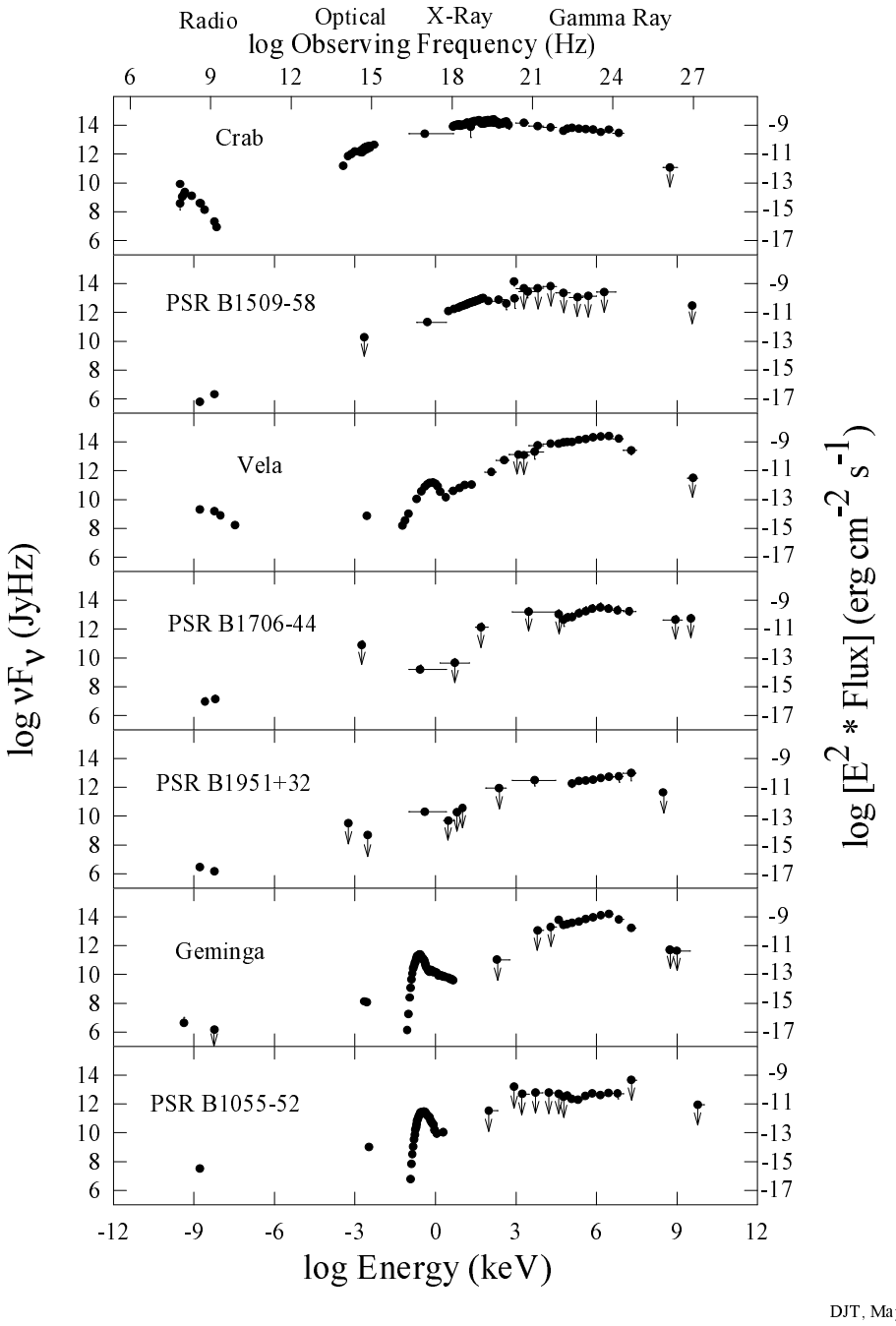

Figure 1.2: *Multiwavelength energy spectra for the known gamma-ray pulsars. These spectra emphasize that emission in the X- and gamma-ray region dominates the radiation budget of these pulsars. Taken from [220].*

energy which is converted into radiation and emitted as X-rays. The spectra of XRBs, resulting from the accretion process, typically cut off at a few tens of keV.

A particulary interesting class of XRBs is constituted by the microquasars. Stellar-mass black holes in binaries expel bipolar radio jets with relativistic speeds [160, 162], resembling the ones of the quasars (see section 1.2.4) and from which they receive their name. The microquasars can help to understand the nature of jets. Due to the proportionality between the characteristic times in the flow of matter onto a BH and its mass, variations with intervals of minutes in a microquasar (where the BH has masses of a few $M_\odot$) correspond to analogous phenomena with durations of thousand of years in a quasar of 10^9 $M_\odot$, not observable by humans. This is fundamental for the gamma-ray astronomy, since jets are observed not only in quasars (see next section) and microquasars but also there is evidence that the most common class of gamma-ray bursts (see section 1.2.5) can be conceived as extreme microquasars, since they are afterglows from ultra-relativistic jets associated to the formation of black holes at cosmological distances [60]. Fig. 1.3 shows the multiwavelength observations of the microquasar GRS 1915+105 with a scheme indicating the positions on the jet where the emission at the different wavelengths are originated.

Although in the 1970s and the 1980s about 10 XRBs had been reported to emit TeV gamma-rays (see e.g. [235] and references therein), none of them (except maybe CenX-3, see below) was confirmed by the posterior more sensitive detectors. Currently, the question of whether XRBs are high-energy gamma-ray emitters or not is still open. Only a detection of a XRB at TeV energies, Cen X-3 (which has also been detected by EGRET), has been reported (see table 1.2) but it has not been confirmed by other experiments operating on the ground.

Various mechanisms have been proposed for the emission of X-rays (see e.g. [13, 150, 91]). In particular, Atoyan & Aharonian [13] explain the production of gamma-rays by inverse Compton scattering of synchrotron photons by relativistic electrons in the jets.

Atoyan et al. [14] have proposed various emission mechanisms for Cen X-3 considering extended and compact source models, and the combination of both. A leptonic extended source model seems to explain the data observed up to now by EGRET and the imaging telescope Mark-6 (this one at TeV energies), but it cannot interpret modulations of the gamma-ray emission with the pulsar spin period (which are not yet confirmed). In contrast, there are two compact source models: hadronic, that assumes a powerful beam of relativistic protons accelerating in the vicinity of the pulsar that hits a dense plasma cloud in the jet propagation region [2], and leptonic, the microquasar model of Atoyan & Aharonian [13]. Both models can explain modulations of the gamma-ray emission but predict that this pulsed gamma-ray emission can be only episodic, with a typical duration of no more than a few hours.

1.2.3 Supernova Remnants

Supernova Remnants (SNR) are objects produced by the violent explosion (supernova) of massive stars at the end of their life.

The SNRs are thought to be one of the cosmic ray generators (mainly the shell-type SNRs, see below) and permit the dispersion of the products of explosive nucleosynthesis during the supernova. Generally, three basic types of SNRs are known [206]: shell-type SNRs, plerions and composite SNRs (this is a cross type between the first two types).

Plerions form when the relativistic wind from a pulsar is confined by a more slowly expanding ($v_{exp} \ll c$) shell of the surrounding supernova remnant [104]. The spin-down energy of the pulsar may then be dissipated in a shock which accelerates the particles [124]. These relativistic particles then radiate synchrotron emission in the magnetohydrodynamic (MHD)

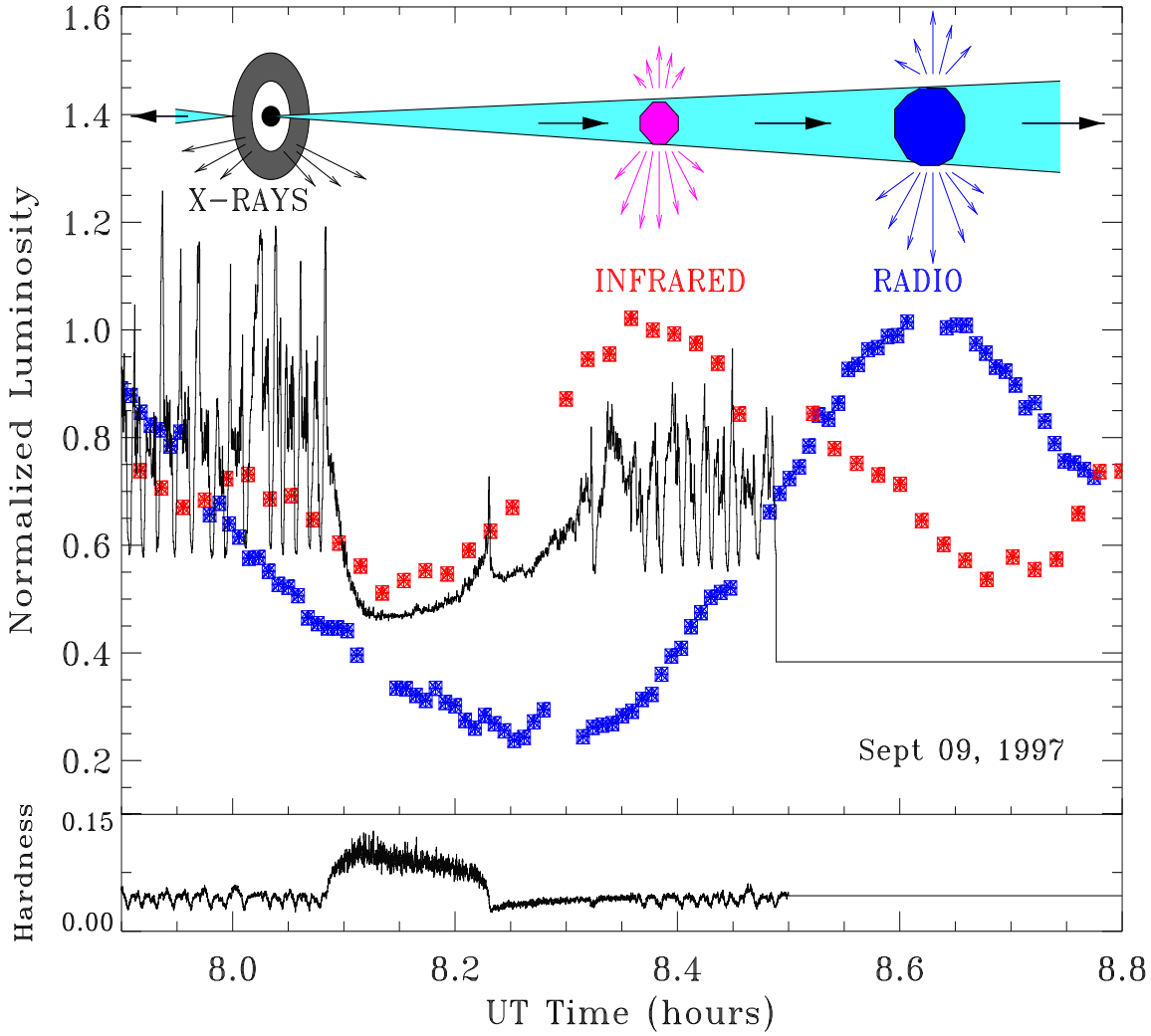

Figure 1.3: *Radio, infrared and X-ray light curves for GRS 1915+105 at the time of quasi-periodic oscillations on 1997 September 9 [161]. The infrared flare starts during the recovery from the X-ray dip, when a sharp, isolated X-ray spike is observed. These observations show the connection between the rapid disappearance and follow-up replenishment of the inner accretion disk seen in the X-rays [22], and the ejection of relativistic plasma clouds observed as synchrotron emission at infrared wavelengths first and later at radio wavelengths. A scheme of the relative positions where the different emissions originate is shown in the top part of the figure. The hardness ratio (13-60 keV)/(2-13 keV) is shown at the botton of the figure. Taken from [162].*

flow downstream of the shock. Gould predicted in 1965 [97] that the synchrotron emitting particles would also produce inverse Compton emission at TeV energies (see also [64]). This is the model known as SSC (Synchrotron Self Compton) and is present in young plerions with strong magnetic fields as in the Crab Nebula [65]. In the older plerions the inverse Compton emission will be due primarily to scattering of the relativistic electrons with sources of background photons (microwave cosmic background (MCB) radiation, galactic infrared background radiation or galactic starlight). Up to now, emission of two plerions has been detected from ground-based detectors at a high confidence level (see table 1.2)[6], but only the Crab Nebula seems to fit the classic model of a pulsar nebula [65, 4] while PSR1706-44 (and also Vela, if the detection is confirmed) has more complicated morphologies at lower energies and needs more complicated models to be explained [104].

In **shell-type SNRs** (around 80% of all SNRs) the shell (composed of hot material) is the result from the interaction of the shock wave of the SN explosion and the interstellar medium [206].

Shell-type SNRs are specially interesting, since they have a sufficiently large energy output to replenish the dominant nucleonic component of the cosmic rays (CR) in the galaxy, although a high efficiency, ∼10%-30%, for converting the kinetic energy of the SNR explosions is required (see e.g. [76, 140, 77, 232]). The acceleration of those CRs up to 1 PeV by diffusive acceleration at the remnants' forward shocks [18] is thought to be the main source of cosmic rays at energies up to the *knee* ($\approx 4 \cdot 10^{15}$ eV[7]). This is supported by the fact that the energy spectrum which results from diffusive shock acceleration follows a power-law $dN/dE \propto E^{-2.1}$, which is consistent with the observed local CR spectrum $dN/dE \propto E^{-2.7}$ after correcting for galactic diffusion [215].

Furthermore, those CRs can generate gamma-rays via interactions with the ambient interstellar medium, including nuclear interactions between relativistic and cold interstellar ions, by *bremsstrahlung* of energetic electrons colliding with the ambient gas and IC emission of cosmic background radiation (see e.g. [232, 17] for a review of recent models of gamma-ray emission from SNRs). Detailed modelling of SNR environments together with radio and X-ray observations predict TeV gamma-ray emission near the sensitivity of the present Cherenkov experiments [23, 18]. Therefore, a positive detection from a shell SNR is vital to establish SNRs as sites of CR production.

Up to now, gamma-ray emission at TeV energies might have been detected (the emission has not been confirmed yet by other experiments) from three shell-type SNRs (see table 1.2). However, the main source of gamma-rays for SN1006 seems to be the ICS of photons of the MCB and starlight [152, 187], which is supported by the fact that synchrotron emission in X-rays has been detected by ASCA (confirming the acceleration of electrons up to 100 TeV) [133]. Furthermore, the detected gamma-ray fluxes are too high in comparison with the predicted emission from π^0 disintegration [152, 78]. This indicates that even if the gamma-ray emission from π^0 disintegration exists, it constitutes only a fraction of the total gamma-ray output from the remnant. The same situation is observed for Cas-A [81]. In spite of these discouraging results, e.g. Aharonian & Atoyan [5] discuss different values of the magnetic field in the supernova remnant SN1006 as a possibility not to rule out yet the hadronic channel. In particular, they propose that a magnetic field of order 100 μG, 10 times larger than the one that results from the interpretation of gamma-ray emission from ICS, could explain the gamma-ray emission from shock accelerated protons in the rim through production and subsequent decay of π^0 mesons.

An adequate source to test the production of gamma-rays from the π^0 disintegration in

[6] A third plerion, Vela, might have also been detected (see grade of credibility in table 1.2).

[7] The energy of the *knee* has been taken from [11].

SNRs is the Tycho Supernova Remnant (see e.g. [37] and references therein). First, although Tycho is a young ($\sim$ 430 years) supernova remnant, proper motion studies indicate that the remnant has been decelerated and is near the Sedov phase of expansion where the maximum of gamma-ray luminosity is expected from diffuse shock acceleration models [78]. Second, the optical light curve is sufficiently well defined that it can be classified as a type Ia supernova. The well-known characteristics of type Ia supernovae allow the estimation of the distance of the SNR. It has been concluded that this SNR is relatively close, at a distance of $\sim$ 2.3 kpc and has an small angular size ($\sim$ 8'), suited for observations with Cherenkov telescopes. Third, it has been suggested [196] the presence of dense material along the eastern side of the remnant. Finally, Tycho presents X-radiation dominated by thermal processes (in contrast with the other detected SNRs) [183]. For all these reasons, a detection of gamma-rays at TeV energies from Tycho would imply a confirmation of the acceleration of Cosmic Rays in SNRs, however, only upper limits have been set up to now for a gamma-ray flux from this source [9].

Notwithstanding the contradiction of the experimental results with the acceleration of hadronic cosmic rays in SNRs (see above), the energy budget is still in favour of this theory . Therefore, Kirk & Dendy [130] have recently reviewed previous assumptions and simplifications done in the calculation of expected gamma-ray fluxes to fit the models within the constraints imposed by gamma-ray observation. In particular, they focus on three main "old" problems: the injection of particles from a thermal pool up to an energy where they can be assumed to diffuse, the maximum achievable energy and the resultant spectral index. Some progress has been achieved, which might throw some light on all these problems. For example, taking into account the importance of self-generated turbulence at the shock front, the maximum energy of the accelerated particles rises to 10^{16} eV [144]. Regarding the injection problem, there are two different approaches for ions and electrons. For ions, the injection process at a parallel shock is described given that some fraction of the thermal ions counter-stream [145]. For electrons, it has been shown that energisation can occur in the turbulence driven by a population of reflected ions [73].

Aharonian et al. have considered these new aspects of the "standard" theory of the acceleration of CRs in SNRs to explain the upper flux reported by the HEGRA collaboration for the Tycho SNR [9]. Although only rough calculations are performed, the value obtained for the expected flux is still acceptable in comparison with the observed flux upper limits.

1.2.4 Active Galactic Nuclei

Active galaxies consitute a type of galaxy with a bright nucleus. Thus, Active Galactic Nuclei (AGN) are the central regions of those galaxies where high-energetic processes take place which cannot be attributed to normal (thermal, nuclear) processes in stars.

The "standard model" for AGNs (see left panel of fig. 1.4, [227]) explains the different types of AGNs as symply being an orientational effect. The central object is thought to be a supermassive black hole (BH) with masses of the order of $10^6 - 10^{10}\,\mathrm{M}_\odot$. There is a thin accretion disk around the BH at several hundreds of Schwarschild radii[8] surrounded by a thick torus lying in the equatorial plane of the hole. In radio-loud AGNs a well-collimated jet of relativistic particles emanates perpendicular to the plane of the accretion disk.

In the AGN unified model, the central engine is powered by matter accretion (release of gravitational energy in a deep gravitational potential). This is a very effective process which can convert $\approx 10\%$ of the rest mass of the accreted matter into radiation. There is an upper limit on the mass accretion rate and therefore on the luminosity resulting from the accretion

[8]The Schwarzschild radius $\mathrm{R}_s = \frac{2GM_{BH}}{c^2}$ is about 10^{-5} pc for a $10^8\,\mathrm{M}_\odot$ black hole.

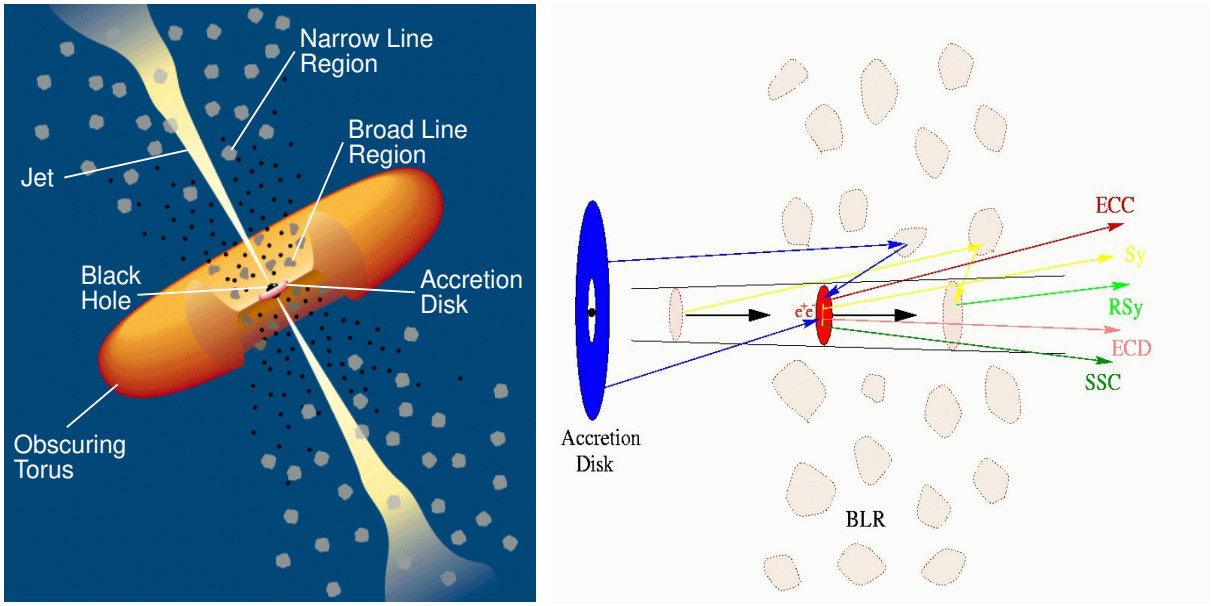

Figure 1.4: *The left panel shows the schematic diagram of the unified model for AGNs (see text). Taken from [227]. The right panel shows the various sources of soft-photons in the leptonic models that explain the emission of gamma-rays in AGNs (see text). Taken from [34].*

process. The so-called Eddington limit is given by the balance of the gravitational force and the radiation pressure on the accreting material. If the radiation pressure dominates, the accretion stops.

Regarding gamma-ray emission, blazars are the most important AGN subclass. About 60% of the identified EGRET AGN sources above 100 MeV seem to be blazars [169] and all of the presently known AGNs at TeV energies are BL Lac objects belonging to this class (see table 1.2).

The gamma-ray fluxes of blazars are observed to be highly variable, with variability time scales from less than an hour (e.g. for Mrk 421 [135]) to several months (e.g. for Mrk 501 [40, 6]). The multiwavelength campaigns of Mrk 421 and Mrk 501 reveal correlations of TeV gamma-ray flares with X-radiation on time-scales of hours or less (see e.g. references above and [201, 149]). In addition, the hardness ratios (2-5 TeV/1-2 TeV) do not show evidence for spectral variability during the flare [135]. In contrast, the variability of quasars, like 3C279, shows different features. In this case there is no clear pattern of time correlation, different bands do not always rise and fall together, even in the optical, X-ray and gamma-ray bands, and during a high state the gamma-ray luminosity dominates over that at all other frequencies by a factor of more than 10 [106]. In addition, a considerable spectral variability, particularly in the gamma-ray band, is found between different epochs for 3C279 and in general for all the flat spectrum radio quasars (FSRQ)[9] observed by EGRET [169].

There is a general agreement that the TeV photons are created in the jets of AGNs, but the mechanism responsible for the high-energy emission is still uncertain, although relativistic shocks are the favoured process (see e.g. [127]). There are basically two types of models: leptonic and hadronic.

[9] BL Lac objects and FSRQs comprise the blazar class of AGNs, radio-loud objects with weak or absent emission lines [227].

In the former (see e.g. [34]), electrons and positrons are assumed to be the primary accelerated particles in the jet which scatter soft photons to gamma-ray energies via inverse Compton process. Depending on where the photon source and the acceleration site are located in the jet, various models are distinguished (see fig. 1.4, right panel). In *Synchrotron Self Compton* (SSC) models the electrons are themselves the source of the photons by synchrotron radiation [148, 29]. In contrast, in the *External Compton Scattering* model (ECS), the source of photons is outside the jet. UV to soft X-ray photons from the accretion disk either entering the jet directly (*External Comptonization of Direct disk radiation* - ECD) [70, 71] or after reprocessing at the broad line regions (*External Comptonization of radiation from Clouds* - ECC) [207, 28] will be up-scattered in the jet. Finally, the *Reflected Synchrotron* (RSy) mechanism assumes that the source of photons is the jet synchrotron radiation reflected at the broad line regions [92, 21, 33]. Combinations of these models have been also proposed [72].

Conversely, in the hadronic models (see e.g. [190]) the high-energy gamma-rays are initiated by hot protons interacting with ambient gas or low-frequency radiation. Two models are distinguished: *Proton-Initiated Cascade* (PIC) models [146, 147, 20] assume that protons are shocked accelerated to ultrahigh energies (10^{10} GeV), interact with ambient photons and produce neutral pions that decay and initiate an electromagnetic cascade. The proton-initiated cascade models could be distinguished by the observation of high energy neutrinos produced as a result of photoproduction [147] or by the consequences of the escape of neutrons on the surroundings from the source as well as in the host galaxy [126]. In contrast, *Synchrotron Proton Blazar* (SPB) models [7, 168] assume that extremely high-energy protons ($E \geq 10^{19}$ eV) emit synchrotron radiation, this mechanism being responsible for the gamma-ray emission at TeV energies. In the leptonic and hadronic models the nature of the accelerated particles is different, but the gamma-ray production process is the same, ICS of soft photons by relativistic leptons.

Up to now, gamma-ray TeV emission has been detected from two blazars at a high confidence level and four more blazars need still confirmation of the detection by other experiments (see table 1.2). EGRET has detected about 90 AGNs at energies > 1 MeV. Multi-wavelength observations of Mrk 421 and Mrk 501 indicated a connection between TeV and X-ray bands (e.g. [135]) favouring the SSC models, that explain successfully the variability and give good overal fits to the spectra of Mrk421 and Mrk501 [128, 153, 154]. However, the flaring state of Mrk501 is also well explained by Aharonian [7] and Mücke & Protheroe [168] from X-ray to TeV energies in the context of SPB models.

In contrast, the explanation of the variability of 3C279 is controversial. Whereas the 1991 flare seen by EGRET [131] is well fitted with a RSy model according to [92], the 1996 flare [239] could rule out such model. The reason is that in the 1996 flare, a correlation of the declines of X-ray and optical fluxes with the EGRET gamma-ray fluxes were observed. However, the synchrotron component is not directly affected by the reflection process of RSy models [33]. Furthermore, Bednarek [21] finds that the shape of the gamma-ray light curve for the 1996 flare can be explained in terms of the RSy model if the density of relativistic electrons increases exponentially towards the end of the blob, but such a distribution is difficult to motivate in terms of the standard relativistic shock model moving along the jet. More likely distributions include a maximum of electrons on the front of the blob and the trail streaming away from the shock on its downstream side [128, 153]. Other models, like SSC and EC, were not initially considered to explain the 1996 flare of 3C279 [239] due to the non-consistency with the multiwavelength observations of such flare. However, Hartman et al. [106] use a combination of SSC, ECC and ECD models to fit successfully the 3C279 multiwavelength data (from radio to gamma-rays) including the high states of early 1999 and early 2000.

1.2.5 Gamma-Ray Bursts

Gamma-Ray Bursts (GRB) are short (from ms to 10^3 s) and intense (E $\approx 10^{53}$ ($\Omega/4\pi$) erg, Ω being the solid angle into which the energy is channelled) bursts of gamma-rays, which emit most of their energy in the MeV range.

The BATSE detector on board of the CGRO found that GRBs are distributed isotropically but not homogeneously [157]. This suggested a cosmological origin, since no known galactic objects had such a distribution and no disk models [179] produced the mentioned distribution. However, the possibility of galactic halo distributions, with a halo of at least 50 kpc in radius, without strong central condensation could still satisfy the isotropy observed by BATSE, though it seemed difficult to populate a halo with neutron stars (the favoured candidate for GRBs at that moment) [35]. The Beppo-Sax observations of X-rays afterglows of some GRBs [57] enabled accurate position determination and the discovery of optical [229] and radio [86] afterglows and host galaxies. The determination of red-shifted absorption lines in the optical counterparts of GRBs set definitely the origin of GRBs to cosmological distances, ruling out the galactic halo model.

BATSE registered 1 GRB per day between 30 and 300 KeV, with fluxes of 10^{-7} to 10^{-5} erg/cm^2 and durations from ms to 10^3 s (with several time structures like single-pulse or multi-peak smooth events). Allowing for the observational selection and coverage, GRBs are detectable at a mean rate of $\approx 10^3$ per year down to the limiting fluxes of 10^{-7} erg/cm^2 [75]. Lamb & Reichart [141] calculated the limiting redshifts detectable by BATSE [177], HETE 2 [112] and Swift [214] for the seven GRBs with well-established redshifts and found that BATSE and HETE 2 would be able to detect three of those GRBs out to redshifts of $20 \leq z \leq 30$. Swift would be able to detect the same three GRBs out to redshifts in excess of $z \approx 70$. Therefore, they concluded that if GRBs occur at very high redshifts, BATSE has probably detected them already. Then, an extrapolation from the observed rate and the detectable redshifts implies that GRBs occur roughly at a rate of a few per universe per day [75].

Many models have been developed to explain the origin of GRBs (which remains unknown up to date). Two types of progenitors of GRBs are preferred nowadays: explosions of very massive stars ("collapsar" [87] or "hypernova" [180] models) and mergers of compact stellar remnants [178, 80] (neutron stars, black holes, or even white dwarfs, but with at least one mergee being a NS or BH). In both cases the end product is a stellar mass scale BH, surrounded by a rapidly rotating torus, whose accretion can provide a sudden release of gravitational energy sufficient to power the GRB. There are several models to explain the dynamics of the GRB (for a review of GRB models see [158] and references therein). The most popular model is the fireball model [42, 95, 178], in which the initial accelerated blast wave produces the gamma-rays by interactions within outflowing material, the interstellar medium or the stellar wind, or outer shell of the companion in a binary system.

The question of jets and beaming in GRBs was really brought into focus by the combined observations of GRBs and their afterglows. In particular, the redshift measurements [138, 139] of GRB 971213 and GRB 990123 implied isotropic gamma-ray energy releases approaching $\approx 10^{54}$ erg. Such a kinetic energy is larger by orders of magnitude than the maximal plausible kinetic energy release in the merger of neutron stars and of neutron stars and black holes, or in the accretion-induced collapse of white dwarfs and neutron stars [60]. This *energy crisis* is solved if GRBs are collimated, since in that case, the total energy emitted by the source is smaller by a factor of $\Omega/4\pi$ than if the source were spherical (as initially suggested by the fireball model).

In addition, some of the observed GRBs present multipeak structure and short time variability (see e.g. [84]). It was suggested that collisions between narrow shells moving with different

bulk Lorentz factors can explain the light curves of multipeaked GRBs. However, a variable central engine must be fine-tuned in order to arrange for shells to collide only after a distance where the produced gamma-rays are not readsorbed, which is larger by many orders of magnitude than the size of the central engine, and even with this fine tuning, variability on timescales comparable to the total duration of the GRB are inferred [204, 60].

Independent of the specific model, the broken power-law spectral shapes and the rapid variability of gamma-ray bursts are almost certainly produced by nonthermal particles in a synchrotron process or to some extent in inverse Compton interactions [206]. It has been shown [90] that synchrotron emission from electrons or positrons accelerated in ultra-relativistic shocks accounts remarkably well for the observed power-law spectra of GRB afterglows. The synchrotron nature of the prompt emission is instead controversial and alternatives have been proposed (see [93] and references therein).

No high-energy cutoff above a few MeV has been observed and emission up to TeV energies is predicted by several models. EGRET has detected emission in the range 30 MeV-20 GeV for some GRBs (see e.g. [205, 208]) and Milagrito reported the a tentative detection of GRB970417a at TeV energies [12]. Other detectors, like HEGRA, have searched for gamma TeV emission from GRBs (see e.g. [181]) from the ground. However, no other GRBs have been detected from the ground. This might be dew to the combination of the narrow field of view of Cherenkov telescopes and to their delay in slewing to the correct position, although both assumptions are uncertain (e.g. EGRET saw GeV gamma-rays up to 90 min after burst).

1.3 Absorption of gamma-rays by the Interstellar Medium

On their journey from the source region to the earth, gamma-rays must traverse long paths of interstellar[10] space. Whereas low energy gamma-rays can travel through interstellar space practically without scattering or absorption, the universe presents a higher opacity for high energy gamma-rays (for low-energy gamma-rays the opacity is very small, see fig. 1.5). The source of opacity is the interaction of gamma-ray photons with ambient photons from the 2.7 K microwave background radiation field (a remnant from the Big Bang) and the extragalactic Infrared (IR, from dust emission) to Ultraviolet (UV) starlight photon field (produced in the phase of early galaxy formation) to produce e^-e^+ pairs. The e^-e^+ pair production from the interaction of two photons is only possible above a threshold energy given by the rest mass of the pair [206]:

$$E_{th-pp} = \frac{2m_e^2c^4}{(1-\cos\phi)(1+z)^2E_\gamma} \approx 1\left(\frac{1+z}{4}\right)^{-2} \cdot \frac{30\mathrm{GeV}}{E_\gamma}(\mathrm{eV}) \qquad (1.2)$$

(for head-on collisions, ϕ is the photon collision angle). From this equation, we can see that above 30 GeV the energy loss of gamma-rays in interstellar space from scattering with starlight becomes significant and limits the horizon to 500 Mpc at 1 TeV, while at higher energies scattering on cosmic background photons effectively cuts the visibility distance to the few nearest galaxies. Sources at distances above $z \approx 2$ cannot be seen directly above 30 GeV. Fig. 1.5 shows the opacity of the universe to gamma-rays of all energies[11].

[10] Interstellar space denotes the space among stars along the whole universe, also among stars of different galaxies.

[11] The optical depth τ is calculated as: $\tau = 0.061\Omega_b h_{100}\int_0^z (1+z)^{0.5}\frac{\sigma(z)}{\sigma_{Th}}dz$ where $\sigma(z) = \sigma[E_0(1+z)]$ is the combined cross section for all processes, E_0 is the photon energy as seen by the observer and σ_{Th} is the Thomson scattering cross section [15].

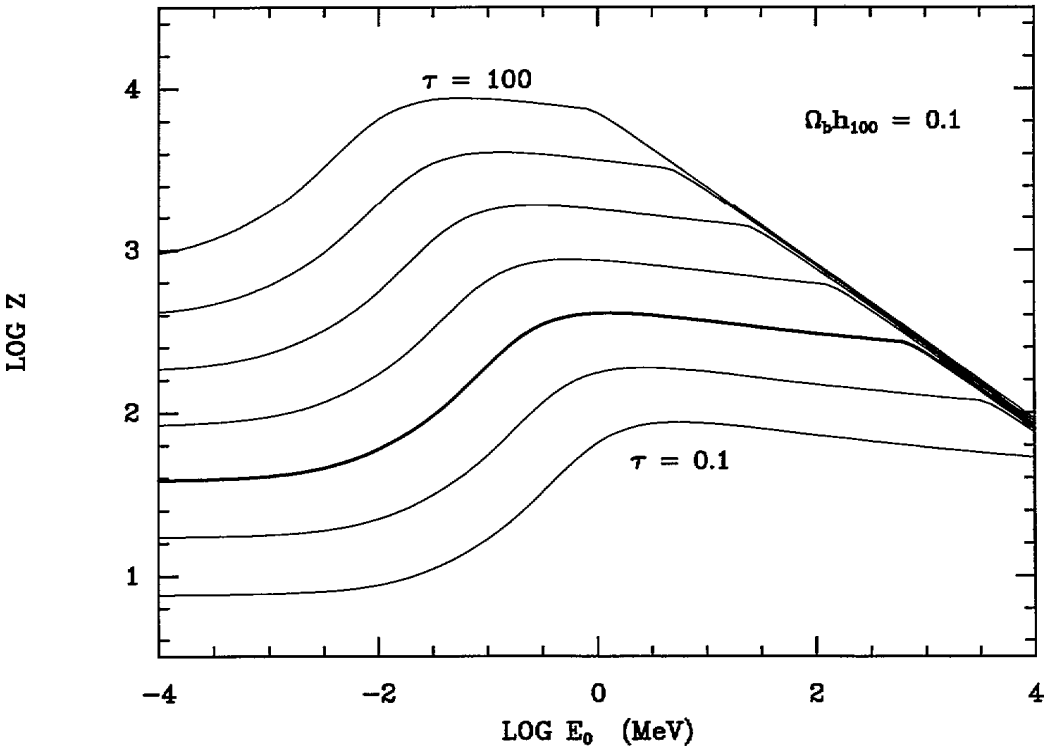

Figure 1.5: *The lines of constant optical depth from $\tau = 0.1$ to $\tau = 100$ are shown in the photon energy-redshift diagram for $\Omega = 1$. Thick line corresponds to $\tau = 1$. Taken from [15].*

Photon-photon pair production results in high-energy charged particles, these will inverse-Compton scatter the same photons and redistribute the high-energy gamma-ray energy to lower gamma-ray energies according to ([206])

$$E_{\gamma,IC} \approx 10 \cdot \left(\frac{1+z}{4}\right)\left(\frac{E_e}{30GeV}\right)(MeV) \tag{1.3}$$

thus producing a diffuse-cosmic continuum spectrum in the form of a power-law $I \propto E^{-\alpha}$ with index $\alpha \approx 2$.

There are two ways in which these results can be used. For a known intensity and spectral index of the intergalactic IR background, it can be used to predict the furthest distance from where TeV gamma-rays can be expected to be detected. However, the distribution of IR photons is presently not very well known, and one may use the fact that multi-TeV gamma-rays have been observed from two extragalactic sources (see table 1.2), Mrk 421 and Mrk 501, to limit the density of the IR photon field. Recently, the Whipple collaboration presented an energy spectrum for Mrk 421 consistent with a power-law with exponential cutoff derived from the flare of January-March 2001 [136]. This has important implications, since an exponential cutoff had been observed already for Mrk 501 at similar energies it might well be that the the cutoff is due to the IR background. One of the main difficulties of this kind of studies is to separate absorption in the source of gamma-rays from absorption along the interstellar medium.

1.4 Motivation for the gamma-ray observation at energies between 30 and 300 GeV

About 300 celestial gamma-ray sources (excluding the more than 2000 gamma-ray burst sources) are currently known, of which two thirds are still unidentified. Figs. 1.6 and 1.7 show the gamma-ray sky at two different gamma-ray energy ranges, the low energy range (with an upper energy threshold of 30 GeV) has been observed with satellites and the high energy range (with a lower energy threshold of about 300 GeV) has been covered by ground-based detectors. The difference in the number of observed GeV and TeV gamma-ray sources is obvious, it results from combined changes in the instrumental and source characteristics.

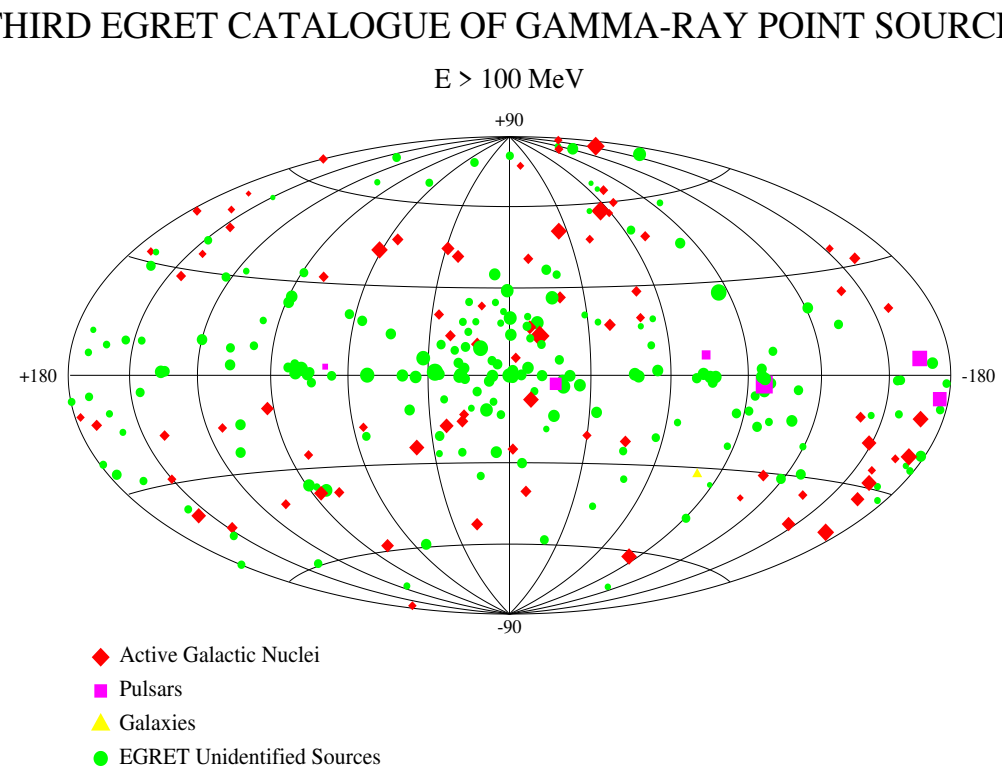

Figure 1.6: *Third EGRET source catalogue, shown in galactic coordinates. The size of the symbol represents the highest intensity seen for this source by EGRET. Source types: pulsars, pink squares; galaxy (LMC), yellow triangle; AGNs (blazars, with the exception of Cen A), red diamonds; unidentified sources, green circles.*

The sensitivity of EGRET was about 4-5 orders of magnitude lower than present imaging telescopes like Whipple or HEGRA. Extrapolating the power-law spectrum with average spectral index of about -2 of EGRET sources to TeV energies, it was logical to expect a large number of detections of gamma-ray sources at the energies of the ground-based telescopes (see e.g. [100]), not only of the sources detected by EGRET but also of new sources not detected in space due to the low sensitivity of the satellites.

The non-detection of EGRET sources at TeV energies can indicate two cutoff mechanisms: for pulsars and perhaps unidentified galactic EGRET sources an intrinsic cutoff at the gamma-ray production site is likely to occur [62, 100] whereas for extragalactic sources (e.g. EGRET blazars) the cutoff can be intrinsic to the gamma-ray production site or due to the increasing

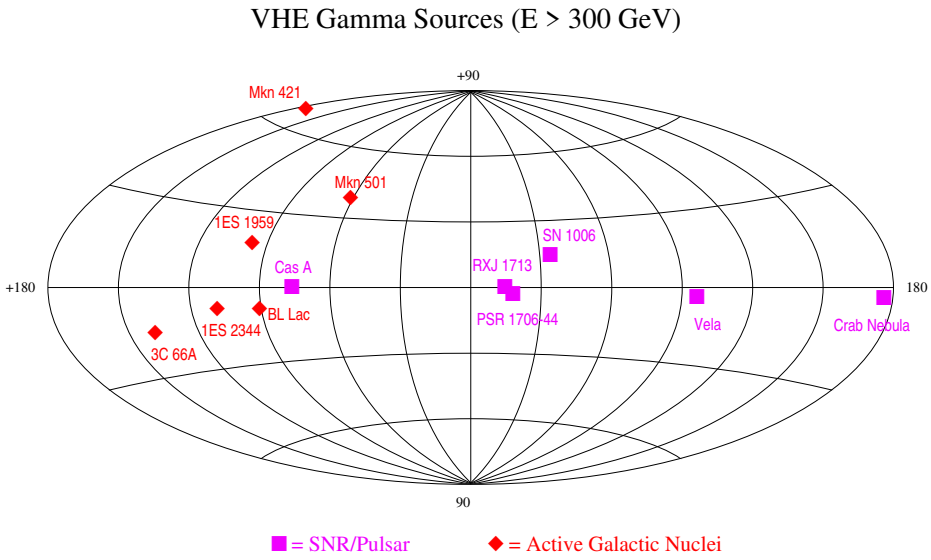

Figure 1.7: *Catalogue of TeV gamma-ray sources. See table 1.2 for a grade of "credibility" of the detection.*

opacity of the universe with extragalactic distance scales (see previous section). The non-detection of other galactic sources (apart from the mentioned ones) and blazars with redshifths $z \leq 1$ (where the universe is practically transparent for photon energies $E \leq 40$ GeV) implies that the energy threshold has to be lowered (ideally to the upper energy threshold of EGRET).

The new generation of gamma-ray detectors are designed to cover the energy gap existent on gamma-ray observations, on one hand GLAST [132] will increase the upper energy threshold achieved by satellites to 200 GeV and on the other hand large imaging telescopes like MAGIC [19] or arrays of imaging telescopes like HESS [115] and VERITAS [237] will lower the ground-based telescopes energy threshold to ≈ 30 GeV. While waiting for the construction of these detectors, three collaborations (CELESTE [45], STACEE [176] and GRAAL[12]) chose the risky path of converting existent solar power plants into huge Cherenkov detectors and developing a new technique for gamma-ray observation in order to achieve low energy thresholds in a short time. The risk was not only due to the new technique to be developed but also to the different requirements for the elements of a Cherenkov detector in comparison with a solar farm (e.g. the angular beam spread of the light reflected in the mirrors or the weather conditions). In spite of this, the challenge was accepted due to the low costs of the conversion of the solar farms in comparison with the execution of the above mentioned projected experiments.

The GRAAL experiment is the result of the conversion of the Plataforma Solar de Almería to a Cherenkov experiment for the detection of gamma-rays and has been reported extensively in two theses (see also [98] and the GRAAL web-site [99] where all the GRAAL contributions

[12]One more collaboration, Solar Two [246] has finished recently the construction of a fourth gamma-ray detector with similar characteristics to STACEE.

to international conferences are listed). Borque [32] was concerned mainly with the design and simulation of the experiment as well as with a pilot experiment 'Mini-GRAAL' [30], built before GRAAL to test the capacity of the solar power plants as Cherenkov detectors. This thesis complements the one of Borque [32] reporting of the execution of the project, the analysis of the data taken with GRAAL and the problems derived from a new, not yet established, technique for the observation of high-energy gamma-rays.

1.5 Outline of this thesis

This thesis has been structured to take into account that solar-arrays[13] constitute a new Cherenkov technique for the observation of gamma-rays and therefore special attention has been drawn to the "technical"aspects of the experiment. In particular, the first part (chapter 2) makes a detailed review of the ground-based Cherenkov wavefront sampling detectors, especially focusing on the novel features of the solar farms as gamma-ray detectors with respect to other Cherenkov detectors.

Concentrating already on GRAAL, the second part comprises the technical description (chapter 3) and the calibration (chapter 4) of the detector.

Following with technical aspects of the data, the third part explains how the Monte Carlo simulation of the detector was done and the fourth part explains the techniques which have been developed for the analysis of the data taken with GRAAL consisting of the reconstruction of the incoming direction of the Cherenkov showers (chapter 6) and the methods which attempt to discriminate gamma-ray from hadron generated showers (chapter 7).

The fifth part discusses the expected detector performance obtained from extensive Monte Carlo simulations (chapter 8) and compares such simulation results with the experimental values obtained from the data taken with GRAAL (chapter 9).

It has been mentioned that the heliostat-approach is a new technique of gamma-ray detection and therefore problems have been found which, with hindsight, were not treated with enough detail in the experiments' proposals. The sixth part deals with a two general problems of the heliostat arrays. First, the restricted field of view (chapter 10), that caused inconveniences which were only fully realized after the construction of the experiments and the analysis of the data. Second, the influence of Night-Sky-Background (chapter 11), a problem of all the Cherenkov detectors but especially critical for the heliostat arrays.

The seventh and last part presents the results of all the studies performed throughout this thesis, namely, the analysis of the data taken with the GRAAL detector since its construction, in August 1999 through to March 2001, aimed at the detection of gamma-ray signals from point sources. The data selection together with the properties of the observed sources is explained first (chapter 12) and the search for a gamma-ray signal from the observed sources with two different analysis methods and its results is discussed thereafter (chapter 13).

[13] The terms "solar arrays" and "solar fields" are equivalent and are used without any distinction throughout this thesis. The first term is mostly used by the "astrophysics" community whereas the second one is used by the "solar power-plants" community.

Chapter 2

Techniques of gamma-ray observation

Gamma rays have been observed over a wide energy range (from MeV to ≈ 50 TeV[1]). In addition, upper limits for the gamma-ray flux from point sources have been set up to energies of ≈ 300 PeV (see e.g. [1, 56]). This large range of energies requires the use of several types of detectors for the observation of gamma rays in the field of gamma-ray astronomy.

The detectors can be classified into two main groups, satellite instruments and ground-based experiments (see fig. 2.1). The first group covers the energy range between 20 MeV and 30 GeV whereas the second measures from about 300 GeV up to the highest energies. In this chapter a short description of the satellite detectors and a brief overview of the ground-based detectors are given (sections 2.1 and 2.2 respectively), followed by an extensive discussion of a particular class of the latter, the Cherenkov detectors (section 2.3).

In 1982 it was first proposed [59] to use solar power plants as Cherenkov detectors in order to cover the unexplored energy range between $\approx 10^9$ and 10^{11} eV. Section 2.3.3.1 describes the steps in the development of the solar approach which led to the construction of 3 gamma-ray detectors (based on this technique) in operation presently[2].

In section 2.3.3 the differences between all wavefront samplers have been stated. Some trends in the performance of the heliostat-arrays are already foreseen from the special characteristics of these detectors in comparison with other wavefront samplers. This is analysed in section 2.3.3.3. The physical mechanisms that determine the performance of the heliostat-arrays are studied throughout this thesis.

2.1 Satellite detectors

The satellite experiments detect gamma-rays via their conversion to electron-positron pairs in a layer of dense material within the detector.

The arrival direction of a gamma is determined by tracking the e^-e^+ pair with e.g. a spark chamber (used in the EGRET detector [121]) or silicon strip detectors (used in GLAST [132]). The energy of the photon is measured with calorimeters which completely absorb the energy of the particle. An anti-coincidence mechanism (e.g. plastic scintillators [121]) discriminates

[1] The highest energy gamma-rays were observed at about 50 TeV for the Crab nebula at large zenith angles by the CANGAROO collaboration [216].

[2] A fourth detector has been already built but is not fully in operation yet.

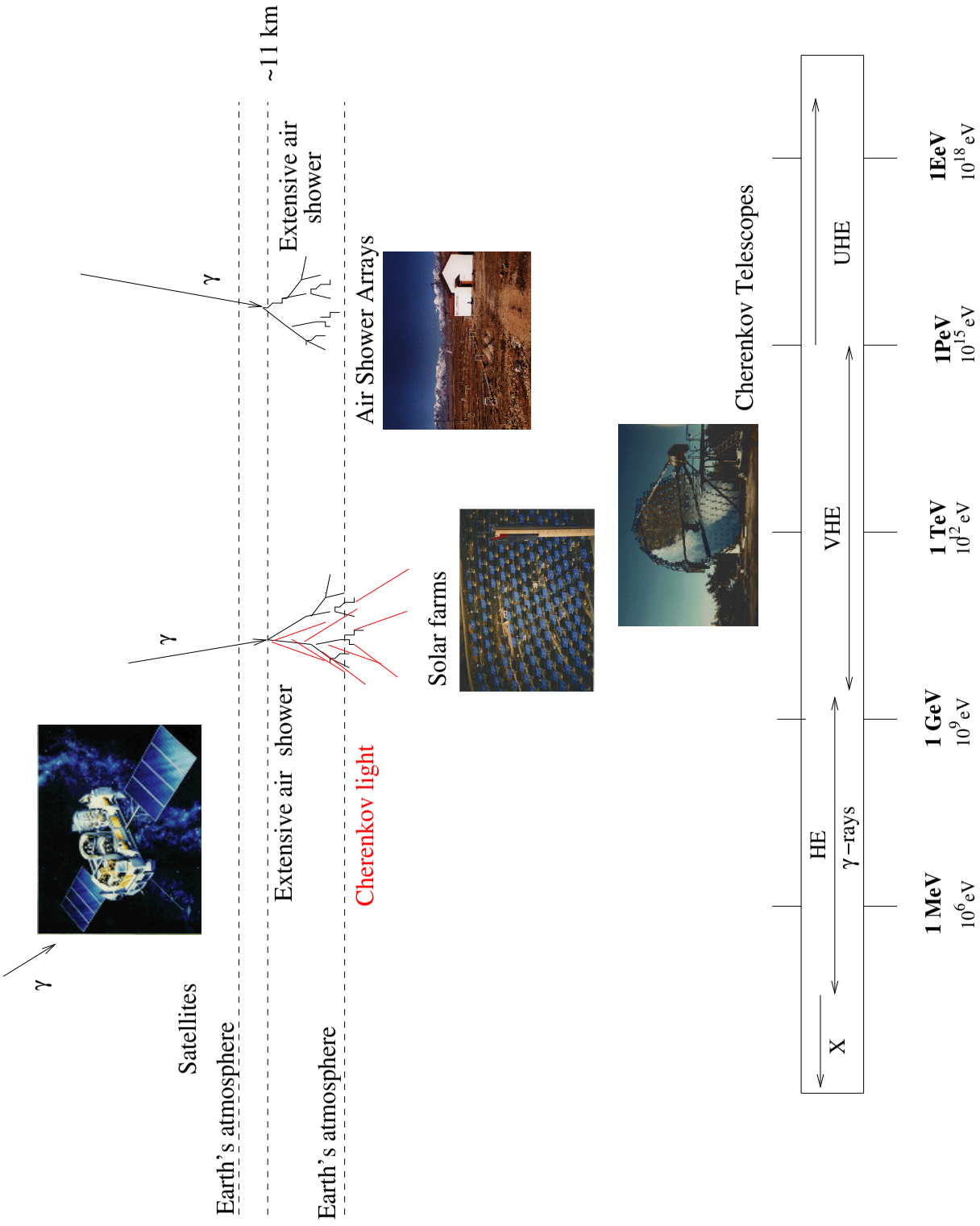

Figure 2.1: *Shown are the detectors that observe gamma-rays along almost 4 decades of energy. The technique used by each detector for the detection of the gamma-rays is also sketched.*

against charged particles arriving to the detector and the gammas produced by hadrons disintegration in its body.

The satellites SAS-2 and COS-B, launched in the 1970s, inaugurated the era of high energy gamma astronomy with the first detailed maps of the gamma-ray sky and the detection of 3 pulsars, Crab, Vela and the one now known as Geminga. COS-B published in 1981 its second catalogue of gamma-ray sources with 25 positive detections [110].

More than 15 years later, on April 1991, the EGRET (Energetic Gamma Ray Experiment Telescope) detector on board of the satellite CGRO (Compton Gamma Ray Observatory) was carried into orbit. EGRET covered the energy range from 20 MeV to 30 GeV with an angular resolution of 3.5° at 100 MeV and 0.35° at 10 GeV and an energy resolution of 9-12% (depending on the energy) until June 2000, when its destruction was decided after a technical problem. EGRET was very successful with its major achievements being a detailed map of the diffuse emission of the galaxy and the detection of numerous (271 published up to now [105]) point sources among which 7 pulsars and 66 blazars were identified with a high level of confidence. The likely detection of a radio galaxy and 27 sources which "may be" AGN were reported. About 170 sources remain unidentified (they have not been associated with any source at other wavelengths).

The project GLAST (Gamma-ray Large Area Space Telescope) [132], scheduled to be launched in 2005, will cover the energy range between 10 MeV and 200 GeV with a sensitivity greater by a factor 50 in comparison with EGRET thanks to its larger effective area (8000 cm^2) and field of view (2.4 sr).

2.2 Ground-based experiments

At very high energies the gamma-ray fluxes are too small (e.g. for the Crab nebula the gamma-rays differential flux decreases with the energy as a power law with index -2.4 [114]) to be detected by satellite experiments due to the small collection area of the detectors (see previous section). Therefore, gamma-ray astronomy is done by ground-based instruments. In contrast with satellites, the direct detection of gamma-rays is impossible for ground-based detectors due to the interaction of the gamma-rays with the earth's atmosphere. However, at very high energies, the earth's atmosphere can be used as a detection medium, i.e., the gamma rays can be detected indirectly through the cascades, or Extensive Air Showers (EAS), of particles (sect. 2.2.1) generated by the gamma-rays and which propagate through the atmosphere. The ground-level instruments can detect the secondary charged particles and photons produced by the EAS.

There exist several techniques of detection of the EAS. If the incident gamma-ray has energies of the order of TeV or higher, a large number of the charged particles arrive to the ground and are detectable by the so-called "air shower arrays" (see [175] for a review). In contrast, for lower energies, the particles of the generated EAS are less penetrating and the number of particles on the ground is too low for sufficient detection. Therefore, the Cherenkov light emitted by the ultrarelativistic particles of the EAS when they traverse the atmosphere is used to detect the gamma-ray indirectly (section 2.3). At the highest energies it is also possible to use the Cherenkov technique for detection of EAS.

An advantage of the ground-based detectors over the satellites is that even with a small *collection* area (e.g. a few square metres for the imaging telescopes) they can detect the photons emitted by a shower falling at various tenths of metres of the detector. The *effective* area (determined by the number of detected showers, section 8.3) is much larger -for example, about

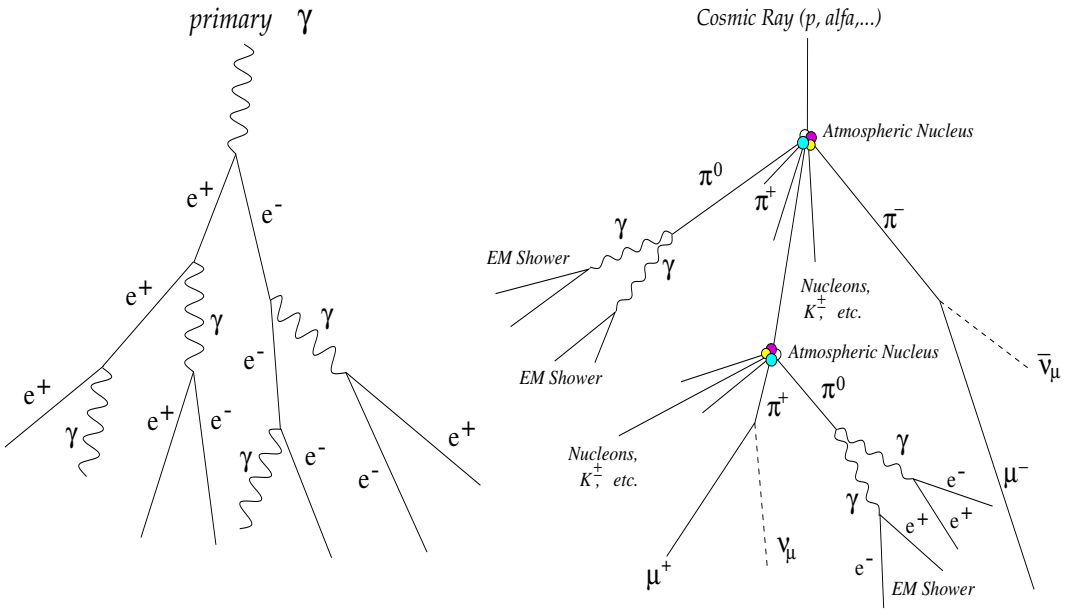

Figure 2.2: *Development of a pure electromagnetic (left) and a hadronic (right) atmospheric showers.*

5 times larger for GRAAL- than the collection area.

On the other hand, the EAS initiated by hadronic cosmic rays are similar in many aspects to those initiated by gamma rays. Therefore, and due to their large flux[3], the cosmic rays constitute a huge background for ground-based detectors.

2.2.1 Extensive Air Showers

An Extensive Air Shower (EAS) is a cascade of particles generated by the interaction of a single high energy primary cosmic ray nucleus or photon near the top of the atmosphere, at altitudes between 10 and 15 km (see e.g. [88, 143] for an extensive description of EAS mechanisms). The number of particles at first multiplies, then reaches a maximum and attenuates as more and more particles fall below the threshold for further particle production.

Depending on the primary particle which originates the EAS, we distinguish between *pure* electromagnetic air showers (generated by a gamma-ray) and hadronic air showers (generated by a proton or a nucleon of higher mass) which also have an electromagnetic component (see fig. 2.2).

2.2.1.1 Electromagnetic cascades

When a very high-energy gamma-ray interacts with an air molecule in the atmosphere, the e^-e^+ pair produced by the interaction initiates an electromagnetic cascade. Photons are generated via *bremsstrahlung* and subsequent pairs are created from the photons. Due to the multiple scattering of the $e^{\pm}$, the particles that make up the shower move away from the direction of the incident photon and form a disk of about 1 m thickness which travels towards the earth's surface with relativistic speed. The maximum development of the shower is reached when the

[3]For example, in a circular angular bin of radius 0.5° the cosmic ray rate above 1 TeV is about 400 times higher than the integral gamma-ray flux from the Crab Nebula above the same energy [175].

mean energy of the $e^{\pm}$ of the shower falls below the critical energy ($E_c \approx 80$ MeV [88]), at that point the energy loss by ionization dominates the energy loss by *bremsstrahlung* and the number of charged particles decreases exponentially.

2.2.1.2 Cosmic ray showers

A hadronic air shower is initiated when a high-energy hadron interacts with the earth's atmosphere, producing primarily hadronic particles (nuclei, pions, etc.). Interactions of high energy hadrons replenish the electromagnetic component via π^0 production as the showers develop. As a consequence, cosmic ray showers are similar in many respects to those initiated by gamma-rays and it is very difficult to distinguish between the two kinds of shower by looking at the electromagnetic component alone. This is one of the major problems of the ground-based detectors seeking to detect gamma rays (see footnote 3 of this chapter).

2.3 Atmospheric Cherenkov technique

For energies lower than 50 TeV, the number of particles of the EAS generated by a gamma-primary is only ≈ 1000 at 11 km altitude[4] (see fig. 2.3) and most of the particles do not reach the ground. As an alternative method to the direct detection of the shower particles, the Cherenkov light emitted by the ultrarelativistic particles in the optical and ultraviolet spectral range (see below) is used by the ground-based telescopes to detect the air showers. The atmospheric Cherenkov technique is well established in the field of gamma-ray astronomy to search for point sources of very high energy radiation from energies of 300 GeV up to the highest energies (section 2.3.2).

The minimum energy threshold is limited by the fact that a Cherenkov telescope triggers on the signal of Cherenkov photons produced in EAS amidst the noise of night sky photons.

The energy threshold of a Cherenkov detector is given by:

$$E_{th} \propto \sqrt{\frac{\Omega \tau \phi}{A_{eff}}} \tag{2.1}$$

where A_{eff} is the effective area of the detector (section 8.3), $\Omega \approx \pi(\frac{fov}{2})^2$ is the solid angle (where *fov* is the field of view of the detector), ϕ is the value of the night sky light (photons/m^2/s/sr) and τ is the time during which night sky light is integrated by the detector (this is only a rough estimate of the energy threshold, based on the assumption that the angular aperture is big enough to accept all Cherenkov photons). Therefore, the threshold of the detectors can be lowered by increasing the mirror area.

2.3.1 Cherenkov light

When a fast charged particle moves through a medium at a constant velocity $v = \beta \cdot c$ which is greater than the velocity of light in that medium ($\beta > 1/n$, n being the refraction index), it emits Cherenkov radiation (see e.g. [118, 143] for complete description of the Cherenkov emission). The process is the following: the charged particle loses energy due to Coulomb interaction with the electrons of the medium, this energy is absorbed in the vicinity of the particle track and part of it is emitted as radiation if the particle velocity is high enough. In the case of materials of high optical transmissivity the emitted energy can escape from the matter.

[4] 11 km correspond to an atmospheric depth of ca. 230 g/cm^2.

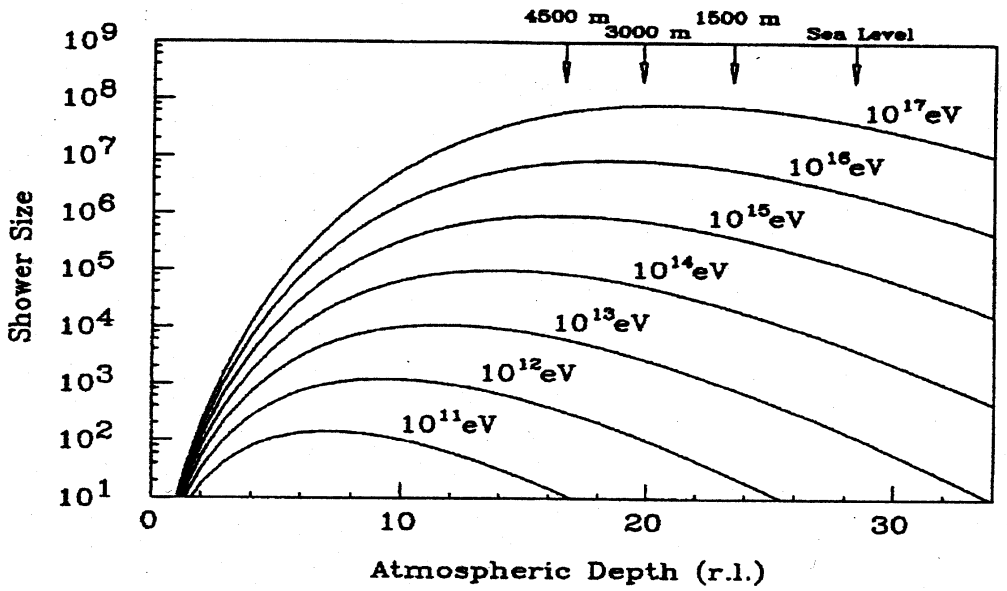

Figure 2.3: *Longitudinal development of air showers initiated by gamma-ray primaries. The average number of particles in the shower (shower size) is plotted as a function of depth in the atmosphere for various primary energies. The depth is defined by the number of radiation lengths (r.l.). The radiation length of air is* $\sim$ *37 g/cm*^{2}*. Taken from [175].*

The wavefront of the emitted radiation propagates at a fixed angle with respect to the particle direction since only in this direction do the wavefronts add coherently according to Huygens' principle (see fig. 2.4). The Cherenkov angle θ_c at which the light propagates is given by $\theta_c = 1/(\beta \cdot n)$. In the atmosphere, θ_c changes with the altitude due to the variation of the refractive index n with the atmospheric density, that depends on the altitude.

2.3.2 Imaging Atmospheric Cherenkov Telescopes

Up to now, the Imaging Atmospheric Cherenkov Telescopes (IACT) have discovered most of the VHE sources. This and the high-level of significance achieved on the detections convert the IACT into the most successful ground-based detectors (for a review of the imaging technique see e.g. [82]).

The Cherenkov telescopes make use of one or more mirrors to focus the Cherenkov light of an airshower to a camera composed of photomultiplier tubes (PMT), so that an *image* of the development of the EAS is obtained by focusing the light of different altitudes to different points in the focal plane. This is the well-known "Imaging Technique". The main success of this technique has been the hadronic rejection up to a 99% level. In 1989, the first detection of a gamma-ray source, the Crab nebula, with a high significance was achieved by the Whipple collaboration [234] thanks to the imaging technique (the rejection of the hadronic background was at that moment already higher than 98%).

The Cherenkov telescopes achieve an angular resolution of about 0.1°. Presently, the IACTs have a mirror area of a few square metres (the Whipple telescope has the largest mirror area, 75 m^2 [43]), limiting the lowest achievable energy threshold to $\approx$ 300 GeV. Some telescopes like CAT [63] have achieved similar energy thresholds with a lower mirror area (16 m^2) by means of faster optics and electronics as well as finer pixels. The upper energy threshold of the imaging

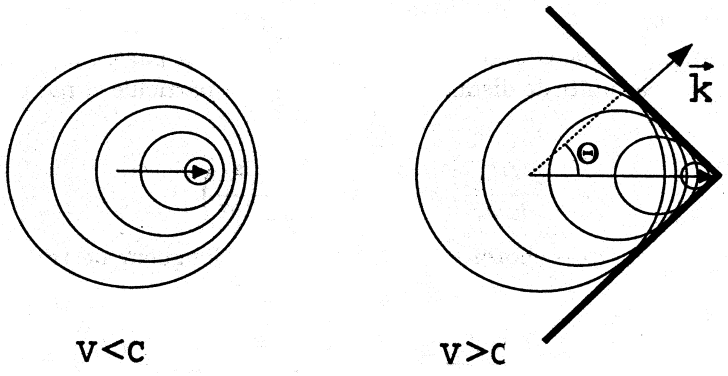

Figure 2.4: *Huygens construction showing the effect caused by a charged particle in a medium when such a particle travels faster than the light in that medium (see text).*

telescopes is around 100 TeV[5].

2.3.3 Wavefront samplers

Wavefront sampling is a technique that uses the variation of parameters like light density and arrival time over the light pool on the ground to infer shower parameters like the direction and energy of the primary particle. For the reconstruction of the direction only the arrival times of the showerfront are used. The reason is that they can be measured with much more accuracy than the light density, influenced by intrinsic fluctuations of the shower, the small number of photons and indeterminations in the conversion of charge registered by the detector and light density on the ground (section 4.4). Only the reconstruction of the shower core has been attempted by means of the light density information (see remarks in section 2.3.3.3 and section 6.2.3).

The wavefront samplers can not form an *image* of the shower development, in contrast to the imaging telescopes described in the previous section. If no imaging is done, a fixed field of view has to be chosen. The choice of the *fov* has important consequences for the detector performance which will be explained in chapter 10.

Table 2.1 summarises the main characteristics of some wavefrontsamplers.

The last column of table 2.1 shows the estimated energy threshold (multiplied by a proportionality constant C) according to eq. 2.1. In the estimation of the energy threshold the only values known with accuracy are the area A and the solid angle Ω of each experiment (see references in the table). The integration time τ has been assumed as 3 ns for all experiments (this is approximately the length of the Cherenkov pulse) except for GRAAL, where the integration over the Cherenkov pulses lasts 200 ns (in this case the trigger integrates various Cherenkov pulses). This introduces an uncertainty in the calculation in case that τ is longer than 3 ns for some experiment. We have estimated this uncertainty as $\approx$1 ns. The value of the night-sky-background ϕ has been taken from [94, 48, 186] for CELESTE, STACEE and GRAAL respectively. For THEMISTOCLE and ASGAT the same value for ϕ as for CELESTE was assumed since they are located at the same site. For PACT we ignore the value of ϕ and therefore we have assumed a value similar to the one of a dark mountain [163] and we have included an error of 50% for this value (this error is probably too large but since we do not have any reference, it is reasonable

[5]The technical limit depends on each individual experiment. However, gammas and hadrons tend to resemble each other more and more up to 100 TeV hindering the hadron rejection with the imaging technique.

	Number of detectors	Area of each detector (m^2)	FOV	Angular resolution	E_{th} (GeV)	$C \cdot \sqrt{\frac{\Omega\tau\phi}{A}}$[6]
THEMISTOCLE [16]	18	0.5	1.2°	0.15°	2000	0.9095
PACT [53]	25	4.5	1.5°	0.09°	900	0.3303
ASGAT [96]	7	38.5	2.5°	0.25°	600	0.3759
GRAAL	63	39.7	0.3°	0.70°	250	0.1093
STACEE [176]	48	37	0.35°	0.25°	140	0.0292
CELESTE [68]	40	54	0.3°	0.26°	50	0.0140

Table 2.1: *Main characteristics of wavefrontsamplers. The rows have been ordered according to decreasing energy threshold. The poor angular resolution of GRAAL in comparison with the other solar farms is probably due to the smaller area sampled on the ground (section 2.3.3.2). The last column shows the estimated energy threshold from eq. 2.1 (see text for details) multiplied by a constant of proportionality C. The constant of proportionality comprises the efficiency of the experiments (note that only the area A has been included in the calculation and not the effective area A_{eff} as in eq. 2.1), which is unknown (usually it has values of* $\approx$ *10%).*

to consider it). The values of ϕ are similar for all experiments (around $1.9 \cdot 10^{12}$ ph/m^2/sr/s) except for STACEE, which has a value ($4.3 \cdot 10^{12}$ ph/m^2/sr/s) higher by more than a factor of 2 with respect to the other experiments. The errors for ϕ are between 5 and 20% (the same as those quoted by the references) except for PACT (see above).

Fig. 2.5 shows the energy threshold given by each sampler with respect to the estimated energy threshold from eq. 2.1. The slope of the grade 1 polynomial which fits the data gives the conversion factor (constant term C in the last column of table 2.1) from $\sqrt{\frac{\Omega\phi\tau}{A}}$ to energy threshold. From this very rough calculation we obtain a good agreement for all the experiments considering the estimated uncertainties.

In this calculation the minimum amplitude required by the trigger above the NSB fluctuations has not been considered. In principle, an experiment that triggers far from the NSB, e.g. requiring a minimum amplitude for the single Cherenkov pulses of at least 5σ above the NSB, will have a real energy threshold above the estimated one. On the other hand the data is less influenced by the NSB (see chapter 11). This is probably the case for PACT, where the single pulse rate is only 5 kHz [231], indicating a trigger threshold at more than 4σ above the NSB if a Gaussian probability is considered[7]. In contrast, the other experiments are closer to the

[6] τ = 3 ns (assumed for all experiments except for GRAAL (see text))
τ = 200 ns GRAAL (sect. 3.3.2.2)
$\phi = 1.8 \cdot 10^{12}$ ph/m^2/sr/s THEMISTOCLE same site as CELESTE (see below)
$\phi = 1.9 \cdot 10^{12}$ ph/m^2/sr/s PACT assumed as [163] (see text)
$\phi = 1.8 \cdot 10^{12}$ ph/m^2/sr/s ASGAT same site as CELESTE (see below)
$\phi = 1.9 \cdot 10^{12}$ ph/m^2/sr/s GRAAL [186]
$\phi = 4.3 \cdot 10^{12}$ ph/m^2/sr/s STACEE [48]
$\phi = 1.8 \cdot 10^{12}$ ph/m^2/sr/s CELESTE [94]

[7] The calculation of the trigger level above NSB from the single rate is very rough and can only be considered for orientation due to the following reasons: first, a Poissonian probability should be considered at least for STACEE and CELESTE due to the small number of p.e.. Therefore, the consideration of a Gaussian probability introduces an uncertainty in this estimation. Second, we have considered a time coincidence window of 3 ns for single pulses. Then, if the time window is different for some experiment, the calculated probability will vary accordingly. Finally, the trigger setup can also change the calculated level above NSB if the single pulses are not discriminated, e.g. for the charge trigger of GRAAL.

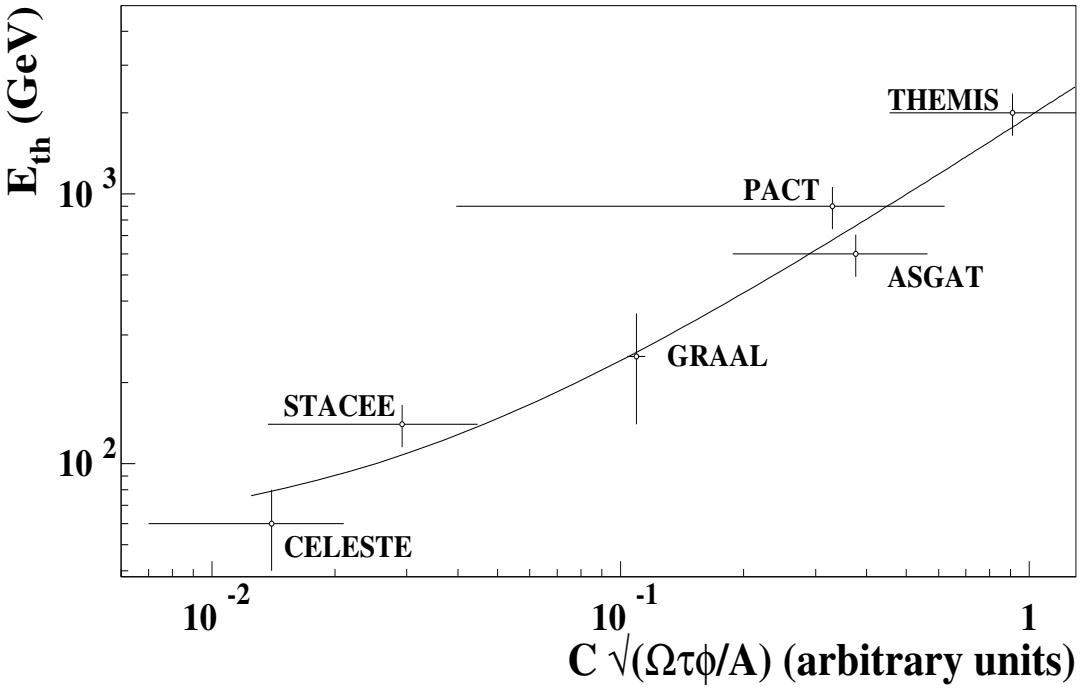

Figure 2.5: *Energy threshold of the wavefront samplers (from table 2.1) as a function of the expected energy threshold (calculated from eq. 2.1). C is a proportionality constant which includes the efficiency of the detectors (see text). The error of the estimated energy threshold comprises the uncertainty in the integration time τ and in the NSB ϕ (see text). The error of the real energy threshold is only known for the heliostat arrays. For the other three experiments, we have assumed an error of 18%, similar to the smallest error given by a heliostat-array (STACEE).*

NSB fluctuations, e.g. STACEE and GRAAL have single-pulse rates of 2Mhz [176](around 2-3σ above NSB) and 100-200 kHz (around 3-4σ above NSB) respectively. Themistocle reports a threshold of 4σ above NSB fluctuations [16]. For CELESTE, a threshold of ca. 2σ above NSB can be estimated from [69]. No information was found for ASGAT about this item.

Another factor which has not been taken into account in the estimation of the energy threshold is the trigger setup. Chantell et al. [48] describe and compare the two types of trigger used in Cherenkov telescopes, analogue and digital. Basically, the *analogue* trigger discriminates the sum of the analogue signals from each PMT and produces a trigger if the final sum exceeds a preset threshold, whereas the *digital* trigger discriminates each channel individually and generates a trigger if a minimum number of discriminated channels fire within a specified time interval. The former type is used e.g. in CELESTE and the latter type in STACEE. The analogue trigger provides the lowest possible energy threshold. In principle, the digital trigger takes advantage of the high multiplicity of a gamma shower and enhances the gamma-to-hadron showers ratio at the hardware level with respect to the analogue trigger. However, this is not completely true, since the intrinsic fluctuations of the gamma shower, although lower than for hadronic showers, still prevent a very high multiplicity. Therefore, the reason for the high energy threshold of

STACEE in comparison with CELESTE is very likely the different trigger setup.

In the case of GRAAL, we have implemented two types of trigger (section 3.3.2.1), the sequence trigger is "digital-like", whereas the charge trigger is "analogue-like". Both triggers are used in coincidence. The energy threshold of GRAAL is determined by the charge trigger, which provides the lowest energy threshold of the two triggers.

2.3.3.1 History of the heliostat approach

Systematic VHE gamma-ray observations were made in the 1960s by a number of groups [55, 142, 222]. Galbraith & Jelley were the first who observed the Cherenkov light produced by EAS initiated by cosmic rays in 1953 [89]. The first serious gamma-ray experiments were carried out by Chudakov et al. [55], who used a Cherenkov light telescope with a solid angle of $3{\cdot}10^{-3}$ sr and effective area of $5{\cdot}10^{4}$ m^2 to survey the most probable candidates for gamma-ray emission. They set the first upper limits to gamma-ray flux from some potential sources at an energy threshold of 5 TeV. Differential timing between separated detectors was used by Tornabene [222] in 1967. Jelley & Porter [119] remark already in their early review of 1963 the necessity of reducing the field of view of the experiments to reject part of the isotropic hadronic background and the problem of different night-sky-background levels in the observed positions.

More than two decades later, the THEMISTOCLE [16, 74] and ASGAT [96] experiments, located in the French Pyrenees, detected with a significance of 5.8σ and 5.7σ respectively gamma-ray emission from the Crab nebula with a similar technique, but increasing the number of detectors and reducing the field of view (see table 2.1), demonstrating the capability of wavefront samplers for the detection of gamma-rays. We have considered as wavefront samplers those detectors which make use of the sampling technique (see previous section) with a relatively small field of view (not large enough to do imaging).

In an attempt to lower the existing energy threshold for detection of gamma-rays on the ground (ca. 200 GeV in the early 1980s, see table 3 in [233]), Danaher et al. [59] proposed in 1982 the use of large solar mirrors (heliostats) as the primary collectors in an atmospheric Cherenkov telescope. The basic idea was to use the wavefront sampling technique but increasing by more than a factor of 10 the collection area of the experiment with respect to the Cherenkov telescopes. This was the first time the potential of the solar power plants as gamma-ray detectors was realized. The solar farms had been built in the 1970s to use the energy of the sun by focusing the solar light on a single furnace at the top of a high tower. Their large collection area was the key point which would allow to lower the energy threshold and enhance the sensitivity of ground-based Cherenkov detectors. However, many technical limitations had to be solved yet, all of them related to the detector in the central tower. For example, the long transit time spread (ca. 1 μs when integrating the light from all the heliostats) produced a loss of efficiency of factor 10 for EAS with duration of about 10 ns. The possibility of using an array of PMTs in the central tower to lower the energy threshold with respect to the single detector (since the night sky background can be integrated over a shorter time) was considered. However, there was a major "stumbling-block": the *efficient concentration of light* into the photomultipliers. This was not a trivial problem at that time for the following reason. The heliostats are spread over a large area, i.e., the angles from a point on the tower towards the heliostats differ by large amounts (20-30°). This implies that the mirrors can not be focused efficiently at one point (even if many PMTs are situated at that point). The focusing of the light to *different positions* in the focal plane of the detector would have been the solution to the problem, but this technique had not been proposed yet (the multi-pixel cameras had not been born). Danaher et al. concluded that "some radically different kind of detector must be used if the potential advantage of the

large collection area of the solar concentrator is to be realised". In addition to the technical problems, the use of an existing facility limited the election of a site for astronomical purposes (a study [59] presented at this stage showed that most of the solar farms were situated in bright and noisy locations).

One decade later much progress had been done and ideas to solve many of the technical problems had been given. Tümer et al. [223, 225] proposed the use of Fresnel lenses or Winston cones to concentrate the light into an array of PMTs (one per heliostat) in the central tower. This would solve the problem of a large NSB entering the PMTs by separating the images of the heliostats and *restricting the field of view* of each PMT to exclusively one heliostat. The capability of imaging with the PMTs array was considered since at that time the imaging technique had been proven successful by Cherenkov telescopes for gamma-hadron separation [234]. To operate a power plant like an imager, each of the 300 PMT would be one "pixel" of a huge camera, having the telescope mirrors an area of 40 m^2 each[8].

The timing spread would be reduced by adjusting the heliostat-to-PMT constant timing difference with cable delays. Taking into account these considerations and the high sampling density (which allowed to collect about 40% of all the photons reaching the detector level), an energy threshold of 10 GeV was estimated for the solar farms, lower by more than an order of magnitude in comparison with the Cherenkov telescopes at that time. A capability of hadron background rejection would be based in several factors: the more peaked structure on the ground of proton light pools in comparison with the smooth gamma-ray-originated showers, the circular ridges of the gamma-ray showers at about 120 m radius (where the photon densities are nearly 50% higher) and the fact that at low energies the proton primaries do not produce enough Cherenkov light to pass the detector threshold.

Finally, in 1996, the CELESTE collaboration made an experiment proposal [45] where the first detailed study of the technical details was made. A system of secondary optics in the detector of the central tower *restricted the field of view seen by each PMT to 0.6 degrees (full aperture)*. As explained in chapter 10, the restricted field of view would show up as the major drawback of the solar approach after beginning of operation of the three actual heliostat arrays (CELESTE, STACEE and GRAAL). A Monte Carlo (MC) simulation of the CELESTE detector was done in the proposal and the showerfront of the EAS were first reconstructed using the arrival times of the Cherenkov pulses at several mirrors of the heliostat field. The rejection of hadron-showers was based on the low light levels and the non-uniform shower illumination of such showers at the trigger level. A cut in the "goodness" of the fit of the measured showerfront to a spherical front could reject a factor of 5 to 10 of the recorded hadron showers in the simulation and the good angular resolution (see table 2.1) should further improve the flux sensitivity. However, the efficiency of the "goodness" cut was probably based upon a simulation that was not precise enough and was not used posteriorly due to the lack of agreement between the simulated protons and the real data [68].

2.3.3.2 Special features of GRAAL

Three collaborations, CELESTE [45], STACEE [210] and Solar-2 [246] followed the basic design proposed by Tümer of one PMT per heliostat [223]. The CELESTE collaboration was the first

[8]With hindsight, it would be possible to use a wavefront sampler like CELESTE as an imager by pointing with each heliostat to one part of the shower (each PMT being the pixel of a huge but coarse camera, of the order of the cameras of the first imaging telescopes on the 1980s). However, this would increase the energy threshold of the experiment. Besides having the mirrors of the telescope distributed over a large area would complicate the imaging analysis.

in presenting a full proposal of experiment solving the technical problems, followed by STACEE [210] one year later. Solar-2 [246] has recently finished the mounting of the experiment with practically the same features and common collaborators of STACEE. In contrast, GRAAL solved the technical problems of the "n heliostats to 1 large-area photomultiplier" approach of Tümer [223]. In particular, the use of time delays to discriminate the signals from the different heliostats makes GRAAL qualitatively equivalent to CELESTE.

The basic differences of the experiments in solar farms with respect to the traditional wave-front samplers (like Themistocle and ASGAT) is a collection area larger by more than an order of magnitude (which permits a lower energy threshold) and a field of view lower by more than a factor of 5 (see table 2.1).

The major differences between GRAAL and the other solar approaches are described in the following:

- The heliostat-arrays make use of their large collecting area (see table 2.1) to achieve low energy thresholds (below 300 GeV). The most important drawback of the non-imaging approach of GRAAL in comparison with the other heliostat arrays is that the night-sky background is higher roughly by the number of heliostats viewed by one cone (see section 11.1). This results in a typical expected background of 8-10 p.e./ns in GRAAL, compared to 0.7 p.e./ns in CELESTE. The hardware energy threshold for the detection of gamma rays, in principle achievable with the same mirror area used, is about 4 times higher in GRAAL due to the higher night-sky background. For pulses far above the threshold the performance of the two approaches is not expected to be very different because a similar amount of Cherenkov light is gathered by GRAAL and CELESTE.

- The advantage of the non-imaging approach is its greater simplicity, leading to savings by about a factor of 5-10 in hardware costs. The presence of only four data-acquisition channels makes automatization and remote control more feasible, leading to comparable savings in operational costs. In its present configuration GRAAL normally runs under remote control with only a PSA operator on-site, who is present for the maintenance of the facilities independently of GRAAL (section 3.17). The small number of channels allows the use of flash-ADCs with a time resolution of 0.5 ns/bin, higher than any other Cherenkov experiment (section 3.3.3).

- In CELESTE the angular field-of-view in the sky of each PMT is designed to be constant at 10 mrad (full angle). In GRAAL this is impossible because the distance of the contributing heliostats from the collecting cone varies. Therefore, the field of view has values between 6.5 and 12.1 mrad (chapter 10).

- Because the non-imaging approach of GRAAL requires that groups of directly adjacent heliostats in the field are chosen, its configuration is more compact. In GRAAL 63 heliostats that cover an area of about 160×80 m^2 are used, whereas CELESTE presently uses 40 heliostats spread over an area of 240×200 m^2, i.e. the sampling density is about a factor of 5 lower. From the Monte-Carlo simulations it seems that with a restricted field of view the irregular structure of the light pool in hadronic showers tends to be more pronounced at the large distance scales, so a more extended array tends to be advantageous for a possible gamma-hadron separation (see figs. 10.5 and 10.6).

- In the non-imaging approach it is impossible to avoid a temporal overlap of the signals from certain heliostats depending on the pointing direction (see section 9.3.1). This reduces

the number of times/amplitudes usable in the reconstruction by about 20%. When the incident direction lies northward (this is the case of the source 3EG 1835+35 at the location of GRAAL), the overlap becomes stronger leading to a substantial decrease in the quality of reconstruction (section 13.1.4.3). On the positive side, calibration is easier when signals from several heliostats are measured in the same PMT.

2.3.3.3 Comparison of the solar arrays with the other wavefront samplers

Looking at table 2.1, there are three striking features which differentiate the solar farms from the other wavefront samplers. First, the solar farms have huge collection mirror areas, of a few thousand square metres (e.g. GRAAL has 2500 m^2 of reflector area), in comparison with the modest values of the other wavefront samplers (from the 9 m^2 of THEMISTOCLE to the 269.5 m^2 of ASGAT). This lowers the energy threshold of the solar farms by more than an order of magnitude, in the most extreme case, with respect to the other wavefront samplers (from the 2000 GeV of THEMISTOCLE to the 60 GeV of CELESTE). Second, the solar farms have a very small field of view, about 0.3°, which is much lower than the field of view of the other samplers, from 1.2° of THEMISTOCLE to 2.5° of ASGAT. The field of view in the solar approach had to be chosen as small as 0.3 degrees (half opening angle) due to spatial restrictions in the central tower, where the detector is situated. Third, the solar arrays have a poorer angular resolution (except in the case of ASGAT) and what is more important, the angular resolution is comparable to the field of view. In contrast, the other wavefront samplers have angular resolution values which are much lower (ca. 10%) than the field of view.

The reason for the worse angular resolution of the solar arrays is very likely a combination of two factors:

- The showerfront is spherical for low energy showers (see below). Then, it is necessary to know the impact point of the shower to reconstruct the shower maximum. In contrast, for other wavefront samplers the conical timing structure of the showerfront gives automatically the impact point on the ground and therefore the shower maximum.

- The impact point of the shower can not be reconstructed. A reconstruction based on the light density distribution has been attempted without success by the solar arrays (see e.g. section 6.2.3 and [68]).

The showerfront of the EAS has a conical shape for high energy cascades, this shape is due to the most penetrating particles. In contrast, the wavefront of low energy showers is more spherical, since the low energy particles are less penetrating, i.e., most of the particles are emitted close to the maximum of the shower. Moreover, even if the showerfront of low energy cascades had a conical shape (which might be true to a certain extent), the heliostat approach will "transform" it to spherical. The reason is that the detector sees only the part of the shower which is emitted close to the shower maximum due to the restricted field of view and the conical shape is given by the light emitted far from the maximum.

Then, since the shower impact point can not be reconstructed, the angular resolution is limited to larger values than for the other samplers.

Moreover, the "real" angular resolution for hadronic showers is even worse than the one displayed. The reason is that, considering a hadronic shower as a collection of sub-showers, the solar arrays only "see" and therefore reconstruct a sub-shower which is emitted in the pointing direction due to the small field of view. The effect is a "pile up" of the proton reconstructed directions towards the pointing direction. Section 10.2.1 explains this effect in detail.

In summary, it seems that the solar-arrays can not enhance the significance of a gamma-ray signal by making a cut on the incident direction of the showers (see section 7.2.2). The better angular resolution of CELESTE and STACEE in comparison with GRAAL is of little importance since the reconstructed direction can not be used to reject hadron showers in any of the solar farms due to the above mentioned reasons.

2.3.4 A hybrid Cherenkov technique

Since the information contained in the lateral distribution is clearly correlated with that contained in the angular distribution, superior rejection would be expected by combining the imaging and the wavefront sampling techniques in a single telescope.

This has been studied in detail by Heß et al. [111] for the HEGRA-array of imaging telescopes. A relation between the arrival time of the photons and the position in the *image* in the camera was studied to search for a hadron rejection method in addition to the imaging technique. It was found that the use of various telescopes helped to reconstruct the shower direction, since the reconstruction of the shower impact point is improved with respect to one telescope. This increases the hadron rejection with angular resolution methods. For example, the HEGRA system of telescopes achieves a good accuracy in the reconstruction of the impact point of $\approx$10 m for showers with energies between 1-10 TeV. The accuracy in the impact point reconstruction increases rapidly for lower energies, with a mean of $\approx$20 m for energies between 0.6-0.8 TeV [226], which is better than the 20% resolution for showers between 0.8 and 30 TeV for the HEGRA single telescope CT1 [134]. However, a finer resolution of the camera of the telescope can increase the reconstruction accuracy of the impact point for single telescopes. For example, CAT reconstructs the impact point with 23 m accuracy for showers of energy 2 TeV and with 28 m accuracy for showers of 0.25 TeV [184] (at least at low energies, CAT seems to be as good as the HEGRA-array for reconstruction of the impact point). Therefore, a fine resolution camera for a single telescope could in principle have the same angular resolution as a telescope-array.

On the other hand, Heß et al. [111] find that the timing information contributes little to a further improvement in gamma-hadron separation due to the strong correlation of such information with the one contained in the images' shapes. The reason for the failure of the timing information to give an extra hadron rejection is that IACT systems select already with trigger conditions and "shape" cuts a "gamma-ray like" sample of hadronic showers, which also behave much like gamma-induced showers in their timing properties.

The results described above have direct implications for the future of the Cherenkov technique. The pure sampling technique can not compete for the moment with the imaging method, but it is used in most of the next generation of ground-based Cherenkov detectors, proposed or already under construction, like the imaging telescopes' arrays HESS [115] or VERITAS [237]. Nevertheless, single telescopes like MAGIC [19] can in principle achieve a similar performance in gamma-hadron separation if the camera resolution is fine enough.

Chapter 3

Technical description of the detector

3.1 The CESA-1 heliostat field

3.1.1 Location

CESA-1 is a heliostat field part of the "Plataforma Solar de Almería" (PSA), a solar thermal-energy research centre operated by the Spanish "Centro de Investigaciones Energéticas, Medioambientales y Tecnológicas" (CIEMAT). The PSA is located in the desert of Tabernas (37°.095 N, 2°.360 W) ca. 40 km from the city of Almería and the Mediterranean sea, at the foothills of the Sierra Nevada mountains (height a.s.l. of 505 m) (see fig. 3.1).

The PSA was originally conceived as a solar plant, where the heliostats of the field reflect the sunlight into a concentrator located on the top of a central tower and heat a substance like water, oil or sodium to produce electricity via thermal energy. The choice of the PSA site was made according to the requirements of a solar facility, namely, clear days and high temperatures. Wettermark [241] reports an average of 182 clear days/year and less than 10 rainy days/year. The main drawback of the application of a solar plant to a Cherenkov detector with respect to weather conditions has been the high humidity in clear winter nights. Fig. 3.2 shows the registered average humidity and temperature values for the year 2001. The humidity is ca. 20% higher during the night than during the day. In addition, there is a summer-winter effect. On winter nights, the humidity is around 10-15% lower than in summer nights. The humidity statistics are related to the temperature values to a certain extent. An increase of the

Figure 3.1: *Location of GRAAL.*

temperature indicates usually a decrease of humidity and viceversa. It was found that the low temperatures on winter nights produce water condensation on the mirrors for the given values of humidity. This effect is not observed during the day due to both higher temperatures and lower humidity. On nights with humidity surpassing 85% no data acquisition is done.

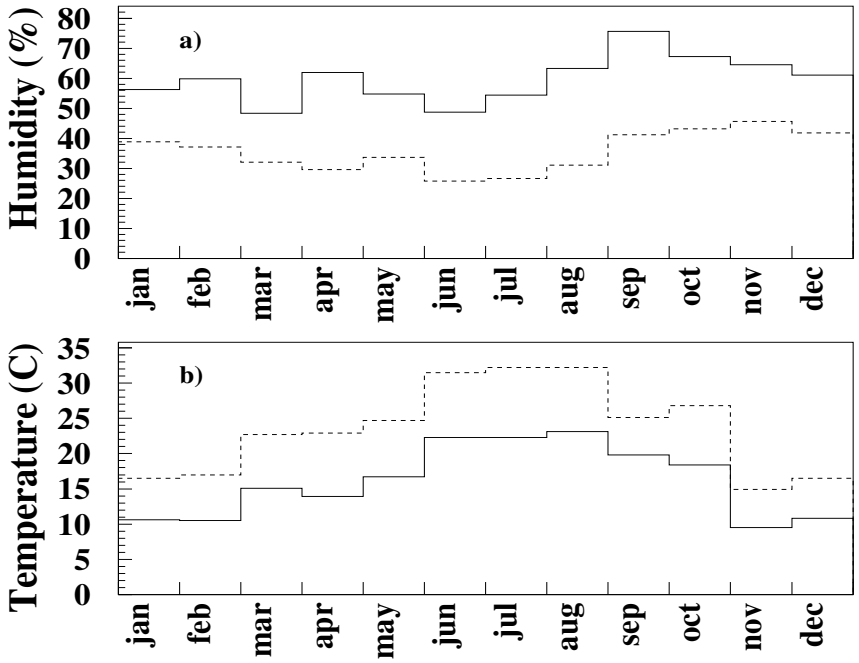

Figure 3.2: *Average humidity(panel a.) and temperature(panel b.) for year 2001 during day (dashed line) and night (full line). During the night the registered humidities are about 20% higher. This is only a problem during winter. At this time of the year the low temperatures registered during the night produce condensation of water on the mirrors at the given humidities.*

In general, the site is very dark (section 11.1), with the worst observing conditions to the Southwest, where the scattered light from the nearest village Tabernas and the nearest large city Almería brightens the night sky.

3.1.2 Description of the field

The CESA-1 heliostat field comprises 300 steerable mirrors to the north of a central tower. GRAAL uses 63 heliostats spread over an area of 200×70 m^2 and divided in four groups of 13, 14, 18 and 18 members respectively.

Fig. 3.3 shows the heliostat field seen from above. The tiled double squares symbolize the heliostats and the ellipses represent the four groups of heliostats used by GRAAL (see also fig. 3.4).

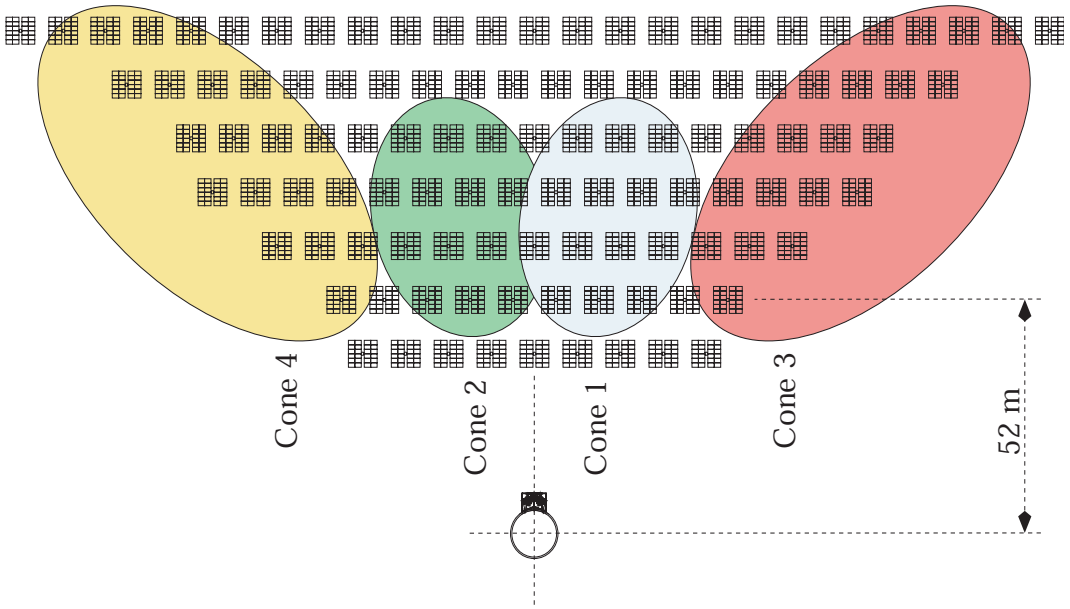

Figure 3.3: *Scheme of the detector geometry as seen from above. North is to the top of the page. The small circle is the tower, the tiled double squares symbolize the heliostats of CESA-1 in the 2nd and 7th row of the tower. The light from one of the group of heliostats used in GRAAL -indicated by ellipses- is concentrated into one of the four cones. The cone numbering indicated is used throughout the text.*

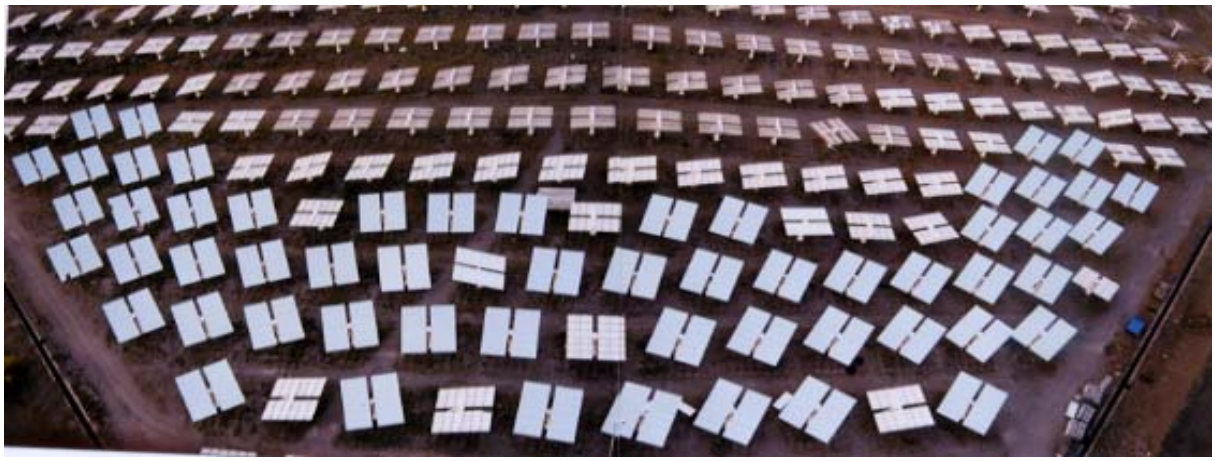

Figure 3.4: *GRAAL heliostat field seen from above. The heliostats used by GRAAL are pointing to the tower (compare with the sketch of fig. 3.3).*

Figure 3.5: *GRAAL heliostats.*

3.1.3 Heliostats

3.1.3.1 Description of the heliostats

The heliostats used for GRAAL have a total mirror area of 39.7 m^2 each and consist of 24 rectangular sub-mirrors which are screwed to metallic frames or *facets* (see fig. 3.5). Each facet supports 2 sub-mirrors.

Within a heliostat, the facets must be aligned (relative to the overall frame) in tangent planes to a sphere so that the overall focal distance of the mirror is one spot, which is chosen to lie on the central tower about 10 m below the GRAAL detector. The process of alignment is called "canting" and it is done regularly by the PSA staff. In the canting process the facets are adjusted manually with a wrench until the images of all the facets of one source of light (the sun or a laser) overlap on the mentioned spot (it is assumed that the heliostat is an optically centred system, i.e., perfectly focused at a point along its optical axis). In the standard or *off-axis* method, the image of sun near noon (usually on the spring equinox) is used for the canting. An alternative method developed in 1995 [166], the *on-axis* method, uses as a reference a laser beam attached to the top of the tower. The canting *off-axis* produces better images near noon than the *on-axis*. However, images at large incident angles are elongated when the canting *off-axis* has been done, which does not happen with the canting *on-axis*. In addition, the canting *on-axis* may be done at any time.

The mirrors are made of 4 mm glass plates and have a silver coating on the back side.

The beam spread function of the heliostats has an RMS of 0.21°, taking all errors into account [36]. This means that the heliostat array has a limited imaging capability for objects of 0.6 degrees diameter, which is the typical size of an extensive air shower (the maximum recorded size of the shower has been chosen as 0.6 degrees due to spatial restrictions in the central tower). This is one of the limitations of the heliostat approach to Cherenkov astronomy, the mirrors have not been designed for Cherenkov astronomy and therefore a light beam with smaller angular

spread[1] was not necessary.

3.1.3.2 Light-collection: efficiency of the heliostats

There are several effects which lead to a deterioration of light-collection efficiency with time: the dust accumulation on the mirrors, the "decanting" of the heliostat facets and the offsets of the shaft encoder positions. Besides, on certain nights the appearance of dew reduces the mirror reflectivity (this is explained in the next section).

The reflectivity of the mirrors is above 95%[2] in the wavelength range 400-550 nm and falls steeply towards lower wavelengths [32]. The mirror reflectivity is reduced mainly due to dust and under dew conditions. The accumulation of dust leads to a loss of light-collection efficiency of 30% in 4 weeks typically.

The process of "canting" has been described in the previous section. After some time more and more facets deviate from the original canting position. As a consequence the heliostat does not focus all the light in a single spot, but various spots can be seen on the focal plane at the central tower (each spot corresponds to the light reflected by a deviated facet). This effect produces light losses. Nevertheless, the process of "decanting" is slow and the deviations from the original position can be first noticed with the human eye after ca. 1 year time.

Many of the heliostats need to be periodically readjusted in their pointing due to mechanical disorders in the heliostat mountings. The effect of the mechanical disorders, that occur due to the constant wear out of the step motors and moving pieces, is that the image reflected by a heliostat is not at the desired spot in the tower. The PSA staff check regularly (usually every 3 days) this effect and corrects it by adding an "offset" to the step-motor calculation. However, some heliostats might present an offset in shorter times, and consequently their efficiency is reduced.

Finally, it can happen that a heliostat position fluctuates between 2 shaft encoder positions (each shaft encoder position corresponds to one step movement of the motor or 0.017°, see section 3.1.4) during the tracking of a source. This fluctuation reduces the efficiency of the heliostat but the effect is negligible. A serious mechanical problem with a heliostat which leaves it completely out of order for the data acquisition is registered on file. Typically 4-10 heliostats out of the 63 used for GRAAL were inoperational at any given time.

3.1.3.3 Dew formation on the heliostats

The difference of temperature between day and night in the PSA is large (typically 8°C, see fig. 3.2) due to its location in a desert. In clear winter nights this temperature change together with the proximity of the Mediterranean sea -that causes an average humidity over 60% (see fig. 3.2)- and the relatively thin glass used for the mirrors (4mm thickness) -which leads to a low overall heat capacity- produce dew formation on the mirrors surface. The formation of dew can reduce the mirror reflectivity from 95% to 10% in less than half an hour.

During the 1999-2000 winter period a large percentage of the nights (ca. 40% of the clear moonless nights) were lost due to this problem and a big effort was done to solve it. Several "anti-frost" solutions were tested, inspired by the usual application of solutions used in cars against window steaming. During the tests of the "anti-frost" solutions we found out that the solutions "pearled off" from the mirror glass. The reason was a silicon layer deposited on the

[1] For example, the imaging telescopes have a mirror (composed by many sub-mirrors) with a beam spread function of less than 0.1°.

[2] Average over all the sub-mirrors of one heliostat.

glass surface which is a common residue in glass manufacturing (section 3.1.3.1). We had to treat first the mirrors with CERESIT, a product by Henkel with an organic sulfur compound that removes the silicon. Only after that procedure could we test efficiently the anti-frost solutions. In the end the best method to prevent the micro-drop formation was to spray the mirrors in the evening with one of the solutions.

An alternative procedure to the "manual" spray had to be found due to the large area of the heliostats (39.7 m^2). A cart typically used to sulphurise trees was adapted to our necessities. Two 6.5 m long sticks with 13 valves each were attached at both sides of the cart and a key was installed to open/close the valves. The cart tank where the sulfates are usually contained is filled with the "anti-dew" solution, that flows through a hose to the valves and sprays the whole mirror area when the valves are opened. Every second day a PSA operator drove the cart along the heliostat lines spraying all the heliostats used by GRAAL.

In nights with very high humidity (above 80%) there was still some condensation on the mirrors but this was not a big problem because such nights were not good for data taking due to the absorption of Cherenkov light in the atmosphere.

3.1.4 Heliostat-tracking system

All the heliostats used in GRAAL are steerable via two step motors that control an alt-azimuthal mount. The motor movement is communicated to the heliostats in step values (*shaft encoder positions*) for axis, azimuth and elevation. The mirror plane can be tilted 180° with respect to the angle of elevation and 360° in an east-westerly direction, i.e., with respect to azimuth angle [241]. The maximum precision in the steering of the heliostats is 1 motor step, which is equivalent to 0.044 degrees. Every 3 seconds the heliostats receive an order to change their position ("refresh"). Thus, the maximum error introduced by the refreshing of the heliostats, just 0.017 degrees (change of the position of the source in the sky in 3 seconds), is well below the 0.044 degrees precision due to the motor steps [32].

The heliostats are connected via a serial line to the central control computer (a Windows PC) which is syncronised in time with the data acquisition Linux PC in the tower. Initially the control program of the heliostats was designed to track the sun. To adapt the heliostats' movement to Cherenkov astronomy purposes, a new tracking program has been developed. The new program offers various tracking possibilities as well as focusing strategies (see fig. 3.6 and operation manual in [99]).

Concerning the source of observation, the program allows two observation modes. The usual operating mode is the denominated **Star Tracking**. In this mode, the heliostats' positions are refreshed every 3 seconds so that they reflect the light of the observed object onto the defined focuses during the tracking time. An alternative mode to the tracking is the **Fixed Position** mode. In this case, the heliostats' position is fixed in time so that they continously reflect the light of a given fixed point onto the focus at the tower. The fixed point can be for example the position of a laser in the tower (used for calibration purposes in section 4.2) or a fixed point on the atmosphere (e.g. for comparison of real cosmic ray showers with Monte Carlo generated showers in the same position and detection of systematic errors).

With respect to the Winston cones, the program allows different focusing modes, that can be chosen with the option **Change of Focus**. The usual mode focuses the heliostats within the field of view of a certain cone to that cone (*OF 1*). In contrast, sometimes it is desirable to "defocus" the heliostats. For example, the *OF 2* mode focuses each group of heliostats to a position in the hut some metres away from the respective cone for calibration of the night sky background.

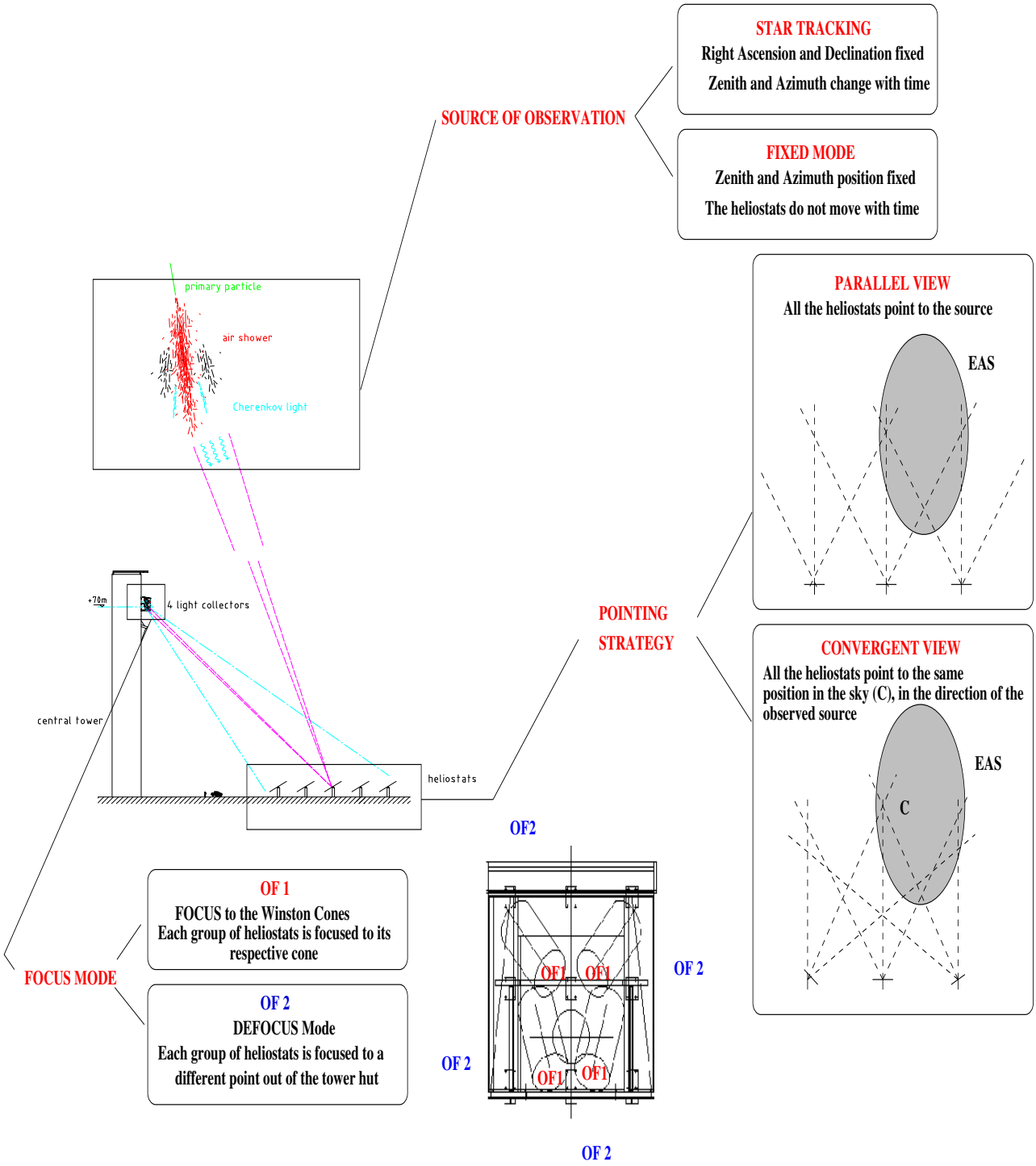

Figure 3.6: *GRAAL tracking system.*

Finally, there are various pointing strategies allowed in the Star Tracking mode to improve the light-collection efficiency. When all the heliostats track a given celestial source, their positions are parallel to each other (**"parallel view"**). Due to the restricted field of view of the collectors in the tower, the heliostats far away from the impact point of the shower on the ground will not see the shower and a lot of light will be lost. However, the collection of light can be improved (leading to a lower energy threshold) if the heliostats are pointed to the place in the atmosphere where the maximum development of the shower takes place (around 11 km a.s.l.) instead of to the source position at infinite. This is the so called **"convergent view"** strategy and was first proposed by the CELESTE collaboration [45]. All the 3 heliostat-field experiments taking data presently (CELESTE, STACEE and GRAAL) operate in "convergent view" mode. The major drawback of the "convergent view" is that showers generated far away from the pointing position will not be detected at all, lowering the effective area and therefore the sensitivity of the detector.

Two control modes are possible in the control program. In **Manual Control**, the physicist on shift introduces through the keyboard the orders for the program. For the **Computer Control**, a file containing the orders for the whole night and time of execution is written by a physicist and read by the program when it is started. The orders are executed sequentially until the stop order is given and the heliostats are sent to rest position. The Computer Control mode has been used regularly in the experiment after October 1999. It was the first step towards a complete automatization of the experiment (see section 3.4).

All the parameters of the tracking process (like positions of the heliostats after each step, position of the source at that time in elevation and azimuth and coordinates of the tracked source in right ascension and declination) are saved to a file. Any change in the tracking mode or the source being tracked is saved to a second file. All this information is processed during data analysis (see chapter 6).

3.2 Optics

3.2.1 Description of the hut

The Cherenkov light from four groups of heliostats (with 13, 14, 18 and 18 members respectively) is directed onto four single non-imaging "cone concentrators" (Winston cones) each containing a single large-area photomultiplier tube (PMT). The Winston cones are housed in a special enclosure, a hut of ca. 5 m height and 4×4 m^2 area, which is positioned as a "flange" to the central tower at the 70 m level (see fig. 3.7). The cones are attached to the ground of the hut (cones 1 and 2 to a lower level and cones 3 and 4 to a higher level) with a mounting that allows their movement.

The hut has a rolling door (like the typical garage doors) which remains closed during the day to protect the PMTs from sunlight. The door is opened at the beginning of data acquisition and closed automatically under any abnormal running condition (see section 3.4) with a motor situated in the hut. The motor is activated from a control switch that can be operated manually or via computer.

A part of the hut floor in front of the the lower cones (1 and 2) has been removed so that these cones can "see" the heliostats. For safety reasons this hole is closed with a highly transparent iron lattice that reduces by $\approx 15\%$ the light collected by the lower cones.

The trigger, read-out and control electronics is situated just behind the access hole inside the tower. Environmental sensors (humidity, temperature and wind speed) have been attached

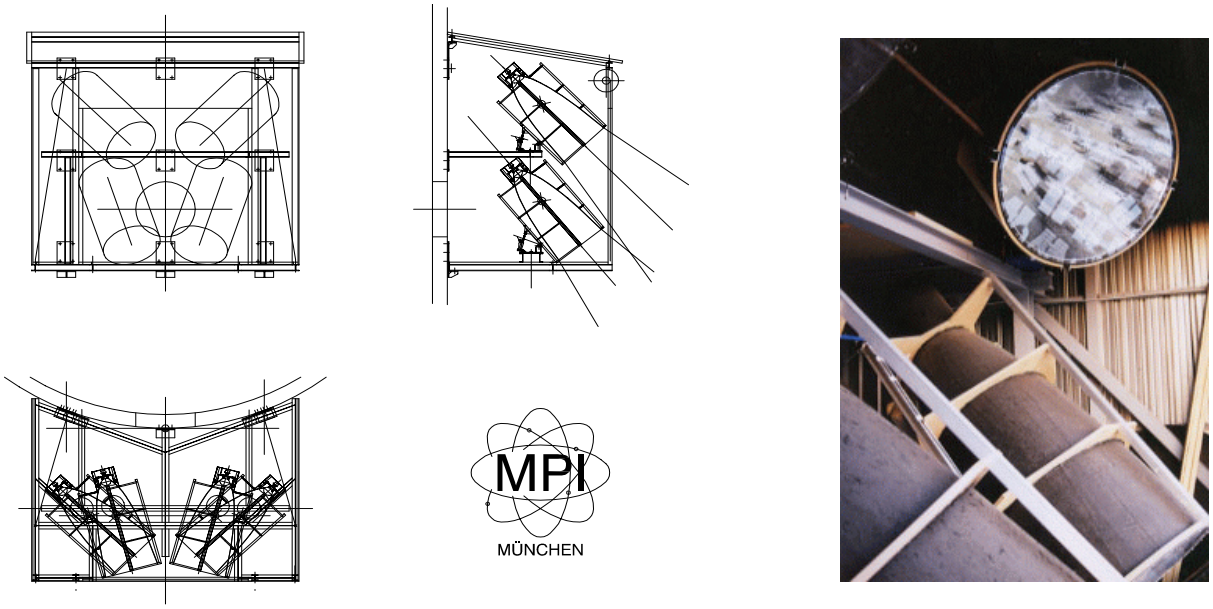

Figure 3.7: *The sketch shows the front (upper left panel) and side (upper right panel) views of the detector platform at the 70 m level of the central tower. On the side view only two of the four Winston cones pointing towards their respective heliostat subfields are sketched. The large-area PMTs are situated at the end of the cones. The wall of the central tower is at the left (in the side view) with a manhole to enter the platform. In the view from above (lower panel of the sketch), all four cones are shown, the half circle is the wall of the central tower. On the right side a picture of the side view of the hut is shown. The heliostats' images can be seen reflected on the window of the upper cone.*

to the outer wall of the hut.

3.2.2 Winston cones

The light collectors used by GRAAL have the shape of truncated Winston cones. A Winston cone is a reflector which transmits all of the light rays incident with a lower angle than the nominal angle characteristic of the cone and rejects all of the rest [240].

The Winston cones used in GRAAL were built in the workshops of the Max Planck Institut in Munich and have a window diameter of 1.08 m and a length of 2 m. A large-area PMT (with a cathode of 20 cm diameter) is attached at the end of each cone. The size of the Winston cones was limited by the available space. The window diameter of 1.08 m in connection with an average focal length of 100 m leads to an opening angle of 0.6°. This field of view does not cover completely an EAS (see section 10.1).

The Winston cones concentrate all the light arriving within 10° of their optical axis onto the PMT at the end of their body. Each Winston cone restricts the heliostats seen by its related PMT to a number which is determined by the chosen field of view (angle and direction). Heliostats outside of this field of view cannot contribute, neither to signal nor to noise due to night sky background light (NSB).

3.2.2.1 Efficiency of the Winston cones

The properties of the Winston cones have been calibrated before being installed in the PSA. The results are the following:

- **Fraction of light reaching the PMT**: only a fraction of the incident light on the cone reaches the PMT. To calculate this fraction, the pulse height P of generated pulses with a Light Emission Diode (LED) (see section 3.2.3.2 for a description of the LED) was measured with and without a diaphragm that stops all the light except the one that directly hits the PMT (not reflected on the walls of the Winston cone). The LED was situated far from the cone so that the light beam was almost parallel to the optical axis of the cone. The efficiency of light collection is given by:

$$\text{Efficiency of light collection} = \frac{\mathrm{P_{withoutdiaphragm}}}{\mathrm{P_{withdiaphragm}}} \cdot \frac{\mathrm{R_d^2}}{\mathrm{R_c^2}} = \epsilon^{\mathrm{n_r}} \tag{3.1}$$

  where R_c is the cone radius, R_d is the diaphragm radius, ϵ the reflectivity of the Mylar foil which covers the interior walls of the Winston cone at 440 nm (0.92) and n_r is the mean number of reflections which suffers a photon before reaching the PMT. If there would be no reflections in the Mylar foil, the law $P \approx R^2$ would be correct. n_r was determined as 1.36 from a Monte Carlo simulation. The measured value for the efficiency of light collection was 0.89±0.04, in perfect agreement with the expected value 0.89.

- **Efficiency with incident angle**: the efficiency of a Winston cone depends on the incident angle of the light with respect to the axis of the cone. Fig. 3.8 shows the acceptance of the cone with respect to the incident angle. For incident angles smaller than 10° the acceptance is nearly 100%. This value falls rapidly to zero for larger incident angles, in agreement with MC simulations.

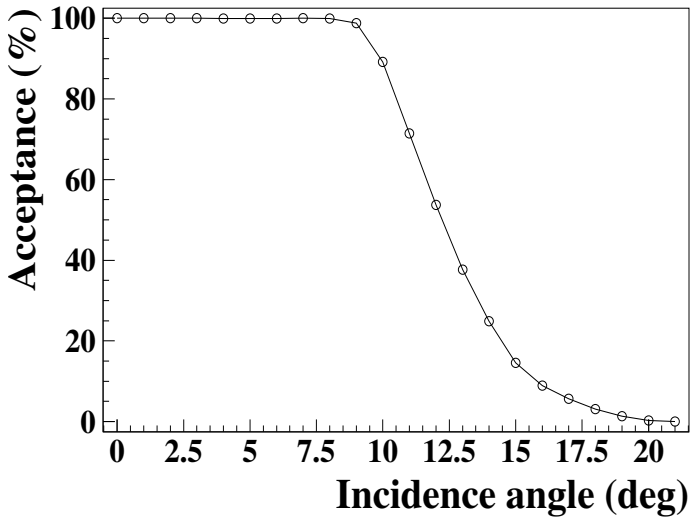

Figure 3.8: *Cone acceptance as a function of incident angle. The acceptance is close to 100% for angles smaller than 10° and falls rapidly to zero for larger incident angles. Taken from [32].*

3.2.3 Photomultiplier Tubes

A photomultiplier is a sensitive detector that converts light into an electrical signal by the photoelectric effect and amplifies that signal in various stages to a useful level by emission of secondary electrons. The primary electrons are electrostatically accelerated and focused onto the first dynode of an electron multiplier. On impact each electron liberates a number of secondary electrons which are, in turn, electrostatically accelerated and focused onto the next dynode. The process is repeated at each subsequent dynode (each amplification stage) and the secondary electrons from the last dynode are collected at the anode. The ratio of secondary to primary electrons emitted at each dynode depends on the energy of the incident electrons and is controlled by the high voltage (HV) between the dynodes.

We have chosen a six-stage 8 inch hemispherical PMT optimised for operation under high-background levels (model 9352KB manufactured by EMI). This has been done because the Night Sky Background (NSB) collected by a GRAAL PMT is higher than in other heliostat-array experiments due to the grouping of the light of various heliostats in one PMT and therefore the currents supported by a PMT are high, of the order of 10-25 μA. The chosen PMT model has a bialkali photocathode with a peak quantum efficency (QE) of 30% at 350 nm, falling down to 15% at 300 and 490 nm (see fig. 3.9).

The gain of a photomultiplier is derived by current amplification. Each dynode amplifies the incident electron current and the overall gain is given by the product of the individual dynode contributions, i.e. $I_a = G \cdot I_c$ where I_a and I_c are the anode and cathode currents respectively and G is the PMT gain. We can also express the gain as:

$$G = \frac{\text{Anode Sensitivity (A/lm)}}{\text{Cathode Sensitivity } (\mu\text{A/lm})} \times 10^6 \tag{3.2}$$

where

$$\text{Anode Sensitivity} = \alpha \cdot \text{HV(V)}^{\beta} \frac{\text{A}}{\text{lm}} \tag{3.3}$$

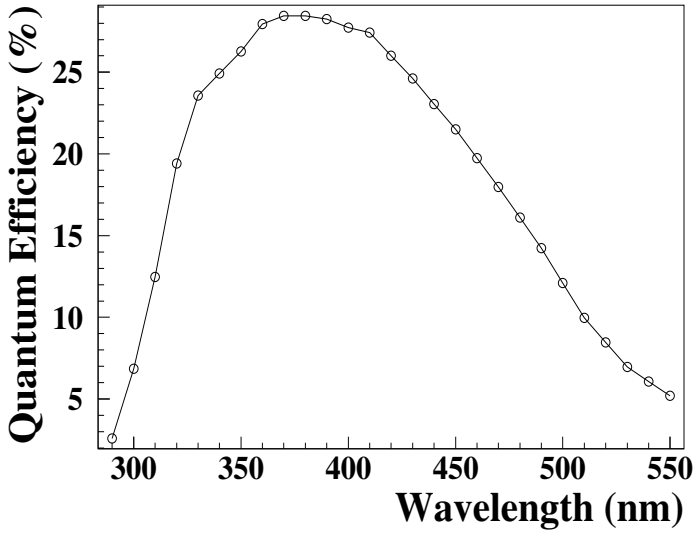

Figure 3.9: *Quantum efficiency of the GRAAL photomultipliers. The PMT efficiency is* $\approx$ *15% at the wavelength of the calibration LEDs (470 nm). Taken from [32].*

for our photomultipliers (α and β are constant terms and HV stands for High Voltage). The manufacturer provides the voltages required on each photomultiplier to achieve two fixed anode sensitivities (the nominal and the maximum). Then, we can infer the gain at a given voltage by constructing a gain-voltage curve using these two points. However, this calculation has large errors, since only two points of the curve are known. Moreover, we need to know the gain experimented by the amplitude of a light pulse, which is not necessarily equal to the gain experimented by the current (see next section) and this can introduce an additional error. In GRAAL, the PMTs were typically operated at 1300-1600 V, depending on their individual gain characteristics. The average gain was about 8000.

3.2.3.1 Non linearity of the PMTs

Normally one expects that the ratio of anode current and pulse height remains constant with changing high voltage. Therefore, knowing the current gain we have automatically the pulse amplitude gain. Conversely, we have observed that for our PMTs the pulse amplitude rises faster than the current with increasing HV.

To study this effect we fired the LED pulses (see next section for a LED description) at different voltages of the PMTs and measured current and amplitude of the output pulse for each voltage. To reduce statistical fluctuations we performed the measurement 30 times for each voltage. The amplitude of the pulses was measured right after the PMT, before the amplifiers. Fig. 3.10 shows the results of this study for the four PMTs. Each point of the curve corresponds to a different voltage and was obtained making an average over the 30 pulses corresponding to that voltage. It can be observed that the statistical fluctuation of the intensity is negligible whereas the fluctuation of the pulses amplitude is quite large (indicated by the error bars). Cone 1 has a "quasi-linear" behaviour whereas cones 2, 3 and 4 are fitted to power laws with indices between 1.8 and 2.7. Table 3.1 presents the results of the fit.

The reason for the non-linear behaviour of the PMTs could be the specific model of our

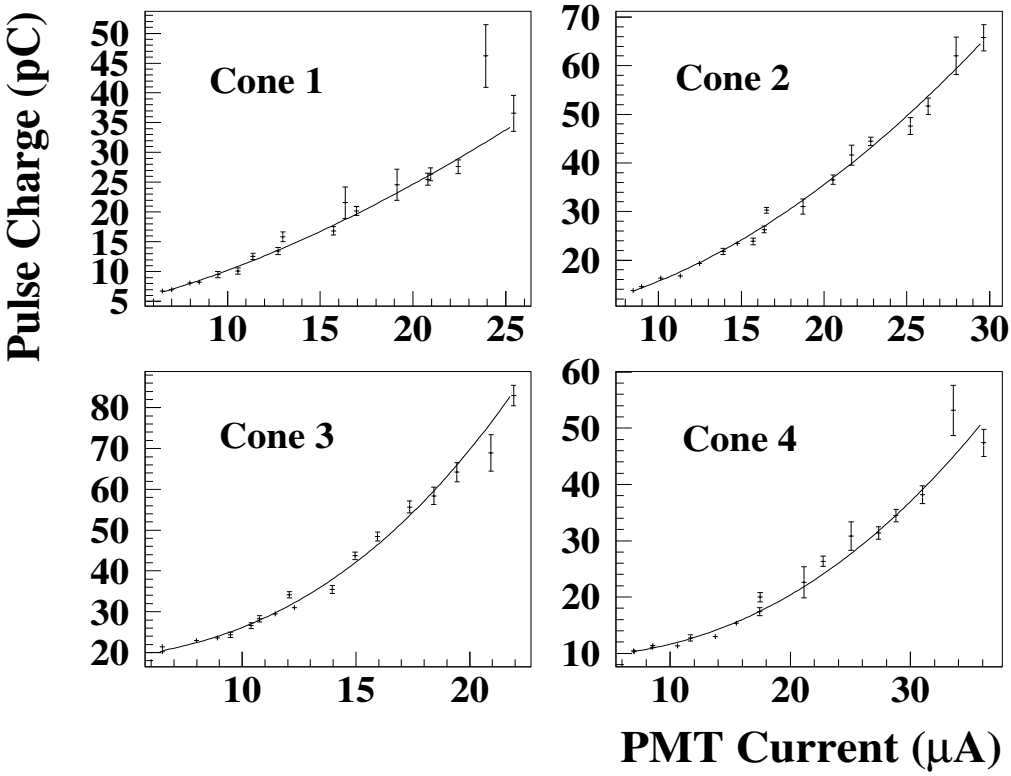

Figure 3.10: *Non-linear relation of the pulse amplitude with the current of the PMT.*

PMTs. The GRAAL photomultipliers have a large-area photocathode (see previous section). It might occur that some of the low energy electrons which leave the photocathode are not properly (in time) focused to the first dynode (this would happen mainly for the electrons on the edges of the photocathode) and therefore do not contribute to the short pulse. However, the measurement of the direct currents (DC) is not influenced. As the high voltage of the PMT is increased, the focusing of the photoelectrons (p.e.) improves. Hence, the increase in the pulse amplitude is not only given by the change of the gain but it is also due to a better focusing and therefore it is higher than the increase of the current.

3.2.3.2 Calibrator modules of the PMTs: the LEDs

The Light Emission Diode (LED) is a narrow-pulse (FWHM $\approx$ 4 ns) generator with a light output that peaks at a wavelength of about 470 nm. The fast-electronics generator is situated inside the calibration module to avoid the use of cables which would widen the pulse.

We use blue LEDs (model Nichia NSPB 500) for the time and amplitude calibration of our setup (see chapter 4). The light pulsers are fastened to the windows of the cones.

Initially, the light pulsers had the configuration shown in fig. 3.11. A large part of the LED light was emitted in the forward direction, towards the heliostat field, and only a small fraction (adjustable with a screw) was reflected back into the cone. This was thought to allow

Cone	a	b	c	χ^2/ndf	ndf
1	0.20±0.04	1.56 ±0.06	2.8±0.4	1.6	15
2	0.10±0.01	1.87 ±0.04	8.2±0.4	2.9	15
3	0.02±0.00	2.63 ±0.06	17.8±0.4	2.9	15
4	0.01±0.00	2.26 ±0.08	9.3±0.2	2.6	15

Table 3.1: *Values of the parameters obtained in the fit of the curves of fig. 3.10. The curves have been fitted to a power law function ampl* $= a \cdot I^b + c$*, where ampl is the amplitude of the pulses and I the DC current. The goodness of the fits is given by the* χ^2 *parameter and ndf (degrees of freedom of the fit). In a linear relation, the parameter b would be equal to 1.*

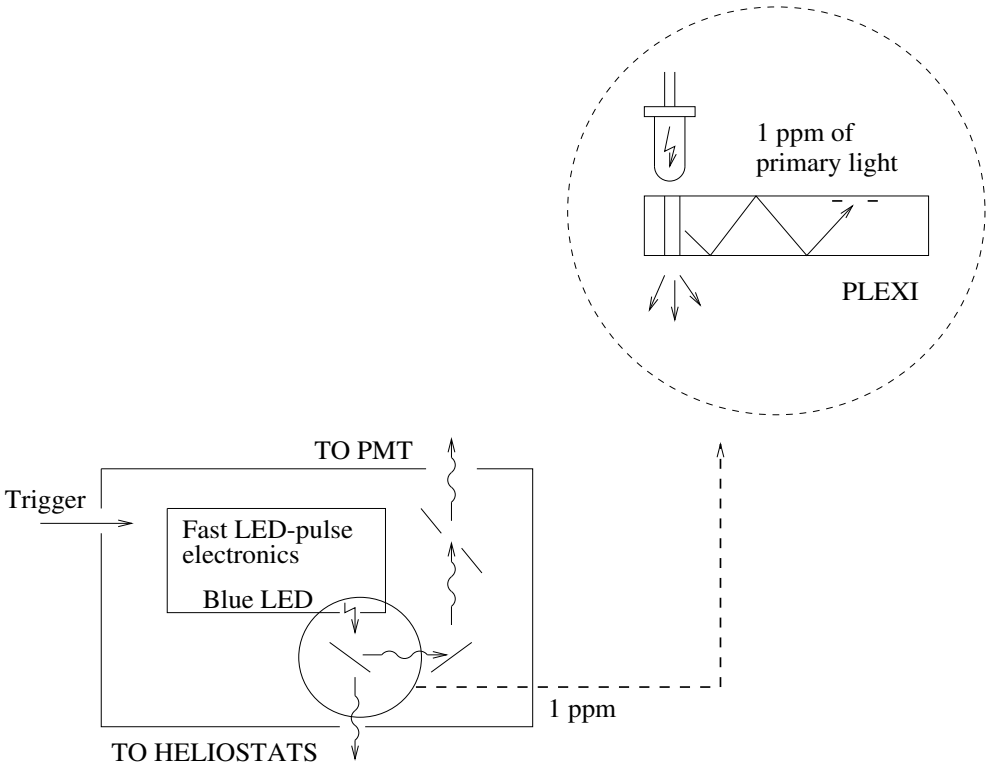

Figure 3.11: *Scheme of a LED calibrator module. The blue LED inside the box generates light pulses. The largest fraction of the light is transmitted in the forward direction.*

a permanent calibration of the heliostats positions (section 4.2).

These modules were replaced after 3 months of operation with ones which only emit light in one direction since the former mode produced an unstable output of light due to its complicated design. The amount of light emitted by the LED is determined with a Quantacon[3] RCA C31000 (low noise, high sensitivity photomultiplier[4]) that was previously calibrated by determining its single p.e. peak and fluctuation behaviour. The LED operating voltage is adjusted so that one LED pulse corresponds to about 100 p.e..

3.3 Electronics

3.3.1 Description of the electronics

Fig. 3.12 shows the scheme of GRAAL electronics. Four main branches, departing from the four PMTs, can be distinguished. All of them are completely equal but for the sequence trigger, which has not been implemented for the two lower branches (departing from photomultipliers 3 and 4).

The PMT signals are sent (with AC coupling) via two fast amplifiers, the first directly adjacent to the PMT and a second one after the transmitting cable to the trigger electronics and the data acquisition (this is the so-called "amplification stage" in fig. 3.12). The bandwidth of the amplifiers is $\approx$ 350 MHz and they have a gain of 15 to 25 each (depending on the input pulse height). The final width of the Cherenkov pulses is about 3.6 ns and mainly determined by path length differences within the PMT.

In a second stage, the trigger logic is configured with NIM coincidence and integrator modules. This is explained in detail in section 3.3.2.1.

Finally, the data is read out by a Digital Scope and recorded on a PC through a CAMAC interface. One Wiener CC16 crate controller is interfaced to a PC Pentium II using PC16-Turbo ISA cards. A new driver was developed for the CAMAC interface cards. The data readout is explained in section 3.3.3.

3.3.2 Trigger logic

3.3.2.1 Description of the trigger modes

The incoming light of an air shower is divided into a train of pulses or *trace*. The pulses are usually fully separated by pathlength differences. The pathlength is determined by the distance of the source to the heliostat (dependent on the position of the source) and the distance of the heliostat to the tower (fixed for each heliostat). Therefore, the time intervals among the pulses depend on the incoming direction of the shower and it can happen that for some direction several pulses of the trace overlap. In general, the overlap of the pulses has its maximum at the culmination of the source and it is larger for sources in the north (see section 13.1.4.3). Fig. 3.13 shows a typical shower event.

The trigger logic has been configured to take into account these special features of the shower events.

The "sequence trigger" has been implemented to filter Cherenkov events from noise attending to an expected time pattern. It is difficult to configure a trigger dependent on time intervals

[3]The name Quantacon means "able to measure single electrons or *quanta*".

[4]The Quantacon has an efficiency of ca. 20% in comparison with the ca. 15% efficiency of our PMTs (sect. 3.2.3).

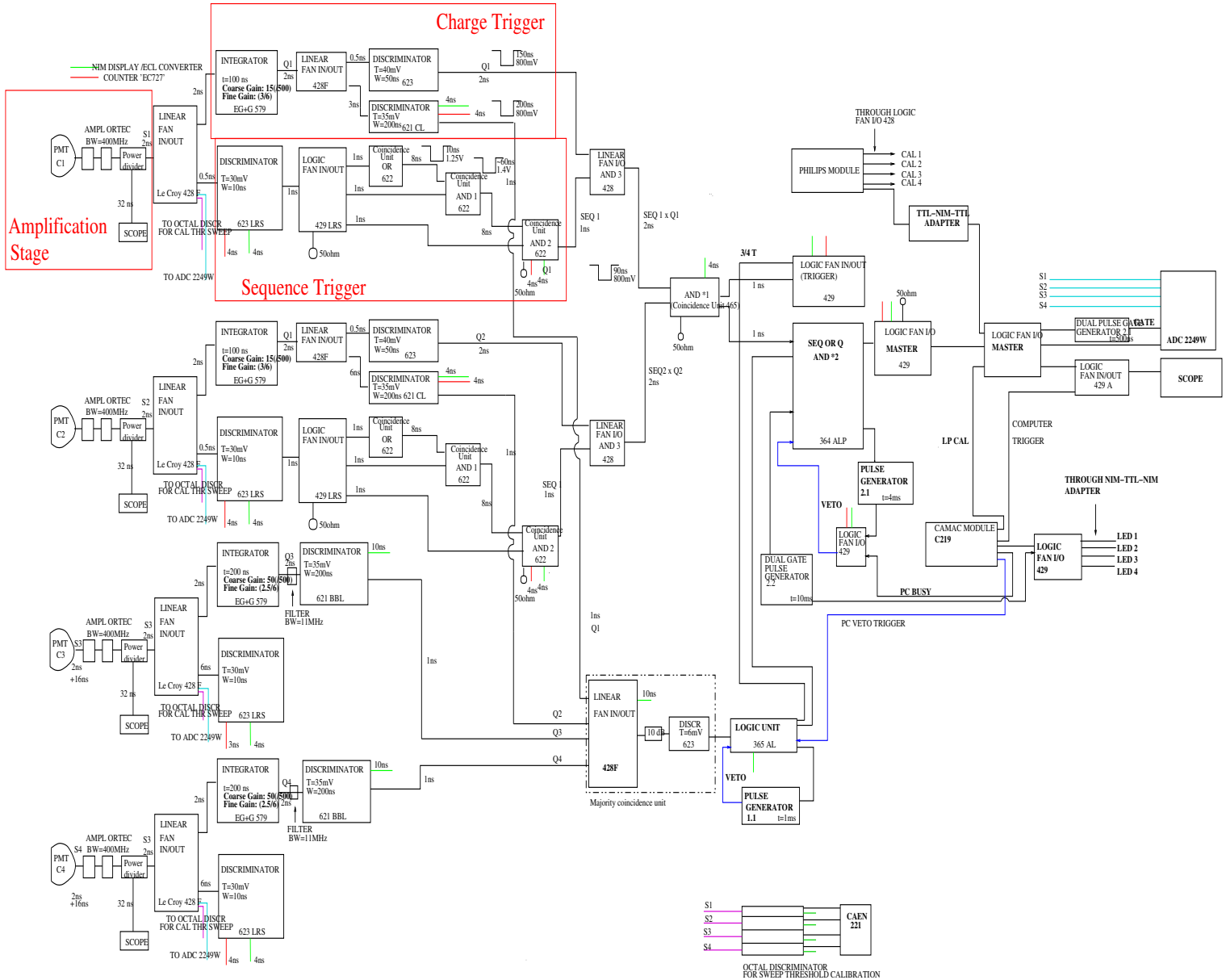

Figure 3.12: *Scheme of electronics for GRAAL (see text for description).*

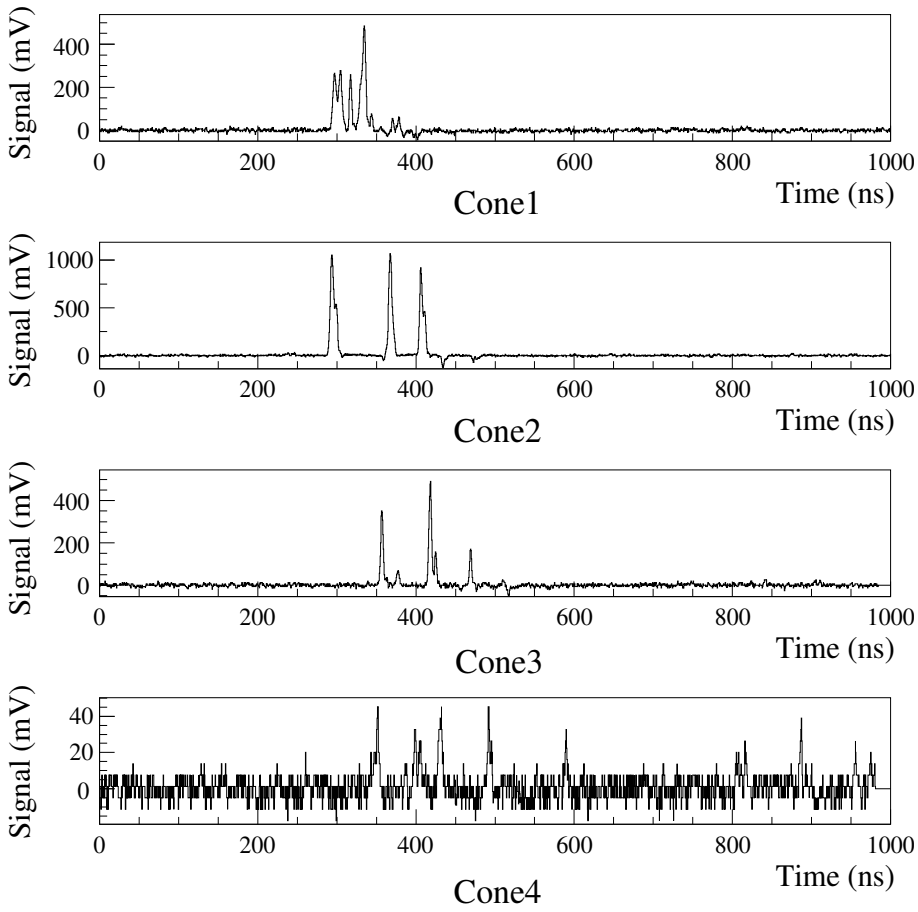

Figure 3.13: *The signal height in mV after amplification recorded in all four cones from one typical airshower is displayed as a function of time. The trigger occurs at 500 ns. The y-gain depends on amplitude, at 100 mV one mV corresponds to typically 0.25 photoelectrons. Each peak corresponds to the Cherenkov-light flash of the shower reflected by a different heliostat. The distribution of light intensity on the ground within the field of view of the cones is very uneven.*

among pulses for the reasons mentioned above. A change of the time intervals with the incoming direction of the shower means that not only a change of source has to be taken into account but also the change of the source position during the night.

The "charge trigger" is a more simple approach which filters events from noise by searching an increased charge on a small time interval.

If one of the trigger conditions (sequence *or* charge) is fulfilled, the total trigger is fired. This is represented in the electronics with an OR coincidence gate (NIM-module LC 364).

3.3.2.2 Trigger implementation

For the implementation of the "sequence (seq) trigger" (designed for the pilot project of GRAAL [30] where only 2 cones were used) we simply assumed a minimum of 4 well separated signals within 150 ns per event and field (13-14 heliostats). This behaviour was taken at first from observation and later confirmed by calculation. With respect to these conditions and for simplicity of electronics the following setup was chosen: after a discriminated signal above 30 mV

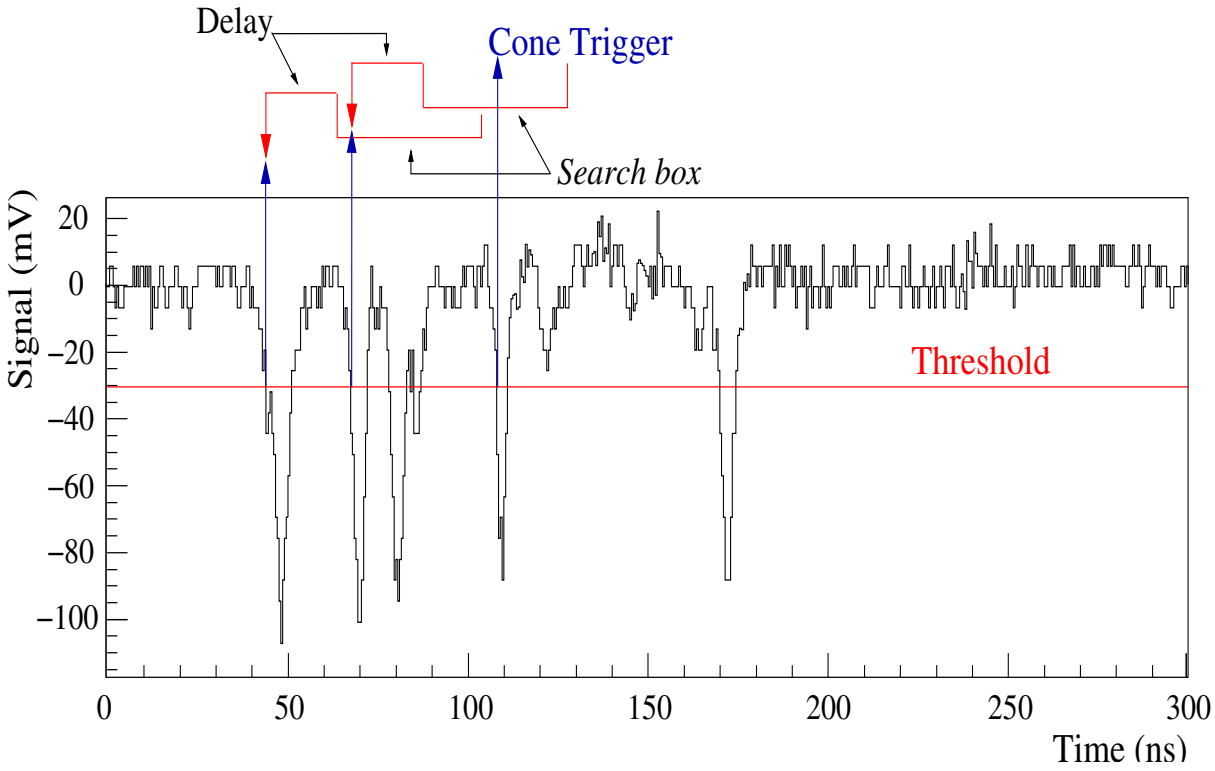

Figure 3.14: *MC simulation of the sequence trigger. Taken from [32].*

(NIM-module LRS 623) a gate of 40 ns length is opened (in a coincidence NIM-module LRS 622) after a delay of 20 ns. If a further signal is detected during gate duration (positive signal in the AND coincidence gate of NIM-module LRS 622), another gate of 40 ns (coincidence NIM-module LRS 622) is opened with a delay of 20 ns. If a third signal is detected in this second gate an event-trigger gate of 150 ns is opened to look for a coincidence with the second cone (in coincidence NIM-module LRS 465). If the cones 1 and 2 have a coincident event-trigger the final event trigger is formed. Fig. 3.14 shows the sequence trigger simulation.

For the "charge(q) trigger" a timing-amplifier (NIM-module EG&G579) integrates the signal with an exponential time scale of 100 (200) ns for cones 1+2 (3+4). The integrated signal is fed into a discriminator (NIM-module LRS 621) in all four cones and opens a coincidence gate of 200 ns duration if the 35 mV preset threshold is surpassed. The singles rate of this integrated signal is the "q-rate". A majority coincidence of "3 out of 4" cones is required for the final event trigger. Fig. 3.15 shows the charge trigger simulation.

3.3.2.3 Sensitivity of the trigger modes

The event rate of the "sequence trigger" depends on the incoming direction of the shower but is relatively insensitive to the level of night-sky induced background light (NSB). For sources lying in northern positions the probability of overlapping pulses is high and the experimental pattern differs from the expected one. Thus, the event rate will be usually dominated by the "charge trigger".

The "charge trigger" is more influenced by the NSB but it is almost independent of the arrival-time structure. The influence of the NSB leads in general to a lower energy threshold

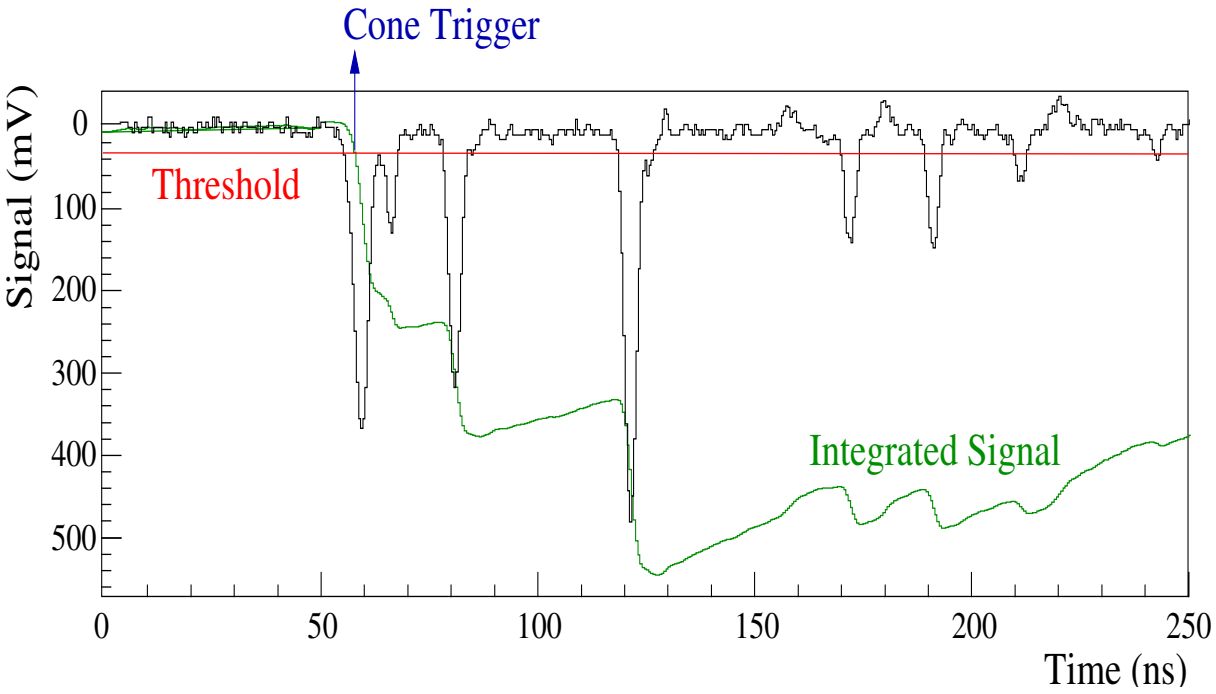

Figure 3.15: *MC simulation of the charge trigger. A trace with high time resolution is integrated in the electronic chain of the "charge(q)-trigger", resulting in the signal labelled "Integrated signal". Once this signal surpasses the threshold level a "cone trigger" is initiated. Taken from [32].*

for the charge trigger events, since an increase of NSB means more charge per time interval (independently of Cherenkov pulses).

3.3.3 Data readout

After the signal has been amplified in the first stage of the electronics (see fig. 3.12) the signal is distributed with a power divider and sent both to the trigger logic and to the analogue readout electronics.

In GRAAL a big effort has been made to keep the detector configuration as simple as possible in order to minimize systematic errors and increase the time resolution. Only four short cables ($\approx$ 6 m for cones 1-2 and $\approx$ 9 m for cones 3-4) connect the photomultipliers in the detector hut with the data acquisition electronics inside the tower.

The four pulse trains are then registered by one Digital Oscilloscope (Le Croy LC 564A) with a bandwidth of 1 GHz and a time bin of 500 psec. The time resolution of the oscilloscope ensures that the FWHM of individual pulses (typically $\approx$ 3.6 ns) is negligibly increased by electronic effects, and is due solely to shower properties, geometrical effects in the mirrors and basically PMT properties (section 5.2.1.3). The PMTs are responsible for the largest widening of the pulses, which have already a width of ca. 2 ns (see e.g. [52]) as they arrive to the heliostats due to shower properties. The oscilloscope is read out in sequence mode over a GPIB interface in a CAMAC crate to a Linux PC, with a speed of about 130 "waveforms"/s (i.e. 2000 time bins of 0.5 ns width with 1 byte/each per second). One byte per time bin is used, i.e. the amplitude resolution is 256 channels. In GRAAL we are interested in having a good resolution for small

showers. This means that, with the given amplitude resolution, the big showers will saturate the flash ADCs. Presently the maximum pulse amplitude measurable without saturation is 1.6 V.

3.3.3.1 Dead time

The transfer rate of 130 waveforms(traces)/s of our readout system means that the total dead time is about 15% for a trigger rate of 5 Hz and remains below 10% for our typical trigger rate of 2-3 Hz.

In general, dead-time losses in data acquisition systems are reduced by dumping data into a buffer [27]. In our oscilloscope up to 30 events (120 waveforms) can be recorded in a buffer. Once the buffer is full, they are saved to disk and the buffer is emptied.

We can compare the expected dead-time losses of the setup with the experimental ones in two different ways. The most direct way (method 1 in table 3.2) consists of dividing the "master rate" (total number of events which have triggered and have been saved to disk) by the "total rate" (total number of events which have triggered). Both rates are recorded during data acquisition.

The second method checks that the data acquisition system is working as expected, i.e., that the arrival of events follows a Poissonian distribution and that the dead time inferred from the distribution agrees with the expected value. Fig. 3.16 shows the distribution of the "lost events", i.e., the difference between the total and the master rate. We have not considered the events lost at the moment of emptying the buffer since they are not Poisson-distributed (the dead time is higher at that moment). The Poisson distribution of the incoming events is:

$$\mathrm{P(n)} = \exp^{\frac{-\delta \mathrm{n}}{<\mathrm{n}>}} \tag{3.4}$$

where n is the number of events. Then, we can infer the fraction of events lost due to dead time by dividing the number of lost events (integration of the distribution between 1 and ∞) by the total number of events (integration of the distribution between 0 and ∞):

$$\text{Fraction of lost events} = \frac{\int_1^\infty \exp^{\frac{-\delta \mathrm{n}}{<\mathrm{n}>}} \mathrm{dn}}{\int_0^\infty \exp^{\frac{-\delta \mathrm{n}}{<\mathrm{n}>}} \mathrm{dn}} = \exp^{\frac{-1}{<\mathrm{n}>}} \tag{3.5}$$

Hence, the slope of the fit of the distribution is a direct measure of the dead-time losses. Table 3.2 shows the comparison between expected and experimental dead time. We can see that the observed dead-time losses (5%) are slightly lower than the expected ones (6%). This can be due to the fact that the mean rate used to calculate the expected dead-time loss has been averaged over 150 min and the times with higher rates are not exactly compensated in dead time with the times with lower rates (the dependence of rate with dead-time losses is non-linear). On the other hand, from the fit of fig. 3.16 we infer a fraction of lost events much lower (2%) than the real one (5%). This is due to the fact that for this method the emptying of the buffer has not been taken into account and a big fraction of the dead-time losses appears at that moment. If the events arrived when the the buffer is being emptied are subtracted in method 1, the losses due to dead time fall from 5% to 2%, demonstrating that this is the reason for the increased dead time.

The dead-time losses of the readout system increase with the trigger rate. Therefore, it is important to operate the detector far away from random triggers which would increase the dead time losses and prevent the readout of real Cherenkov events.

	Rate (Hz)	Fraction of lost events	Dead time (ms)
Expected	2.1	**6** %	31
Measured (method 1)	2.1	5 %	**23**
Measured (method 2)	2.1	**2** %	**9**

Table 3.2: *Comparison of expected and measured dead-time losses for a run in January 2001 tracking the Crab during 150 min. The calculated values are bold faced on the table. The value of 31 ms for expected dead time has been estimated by the manufacturer of the Digital Oscilloscope. The rest of the values are directly measured during data acquisition.*

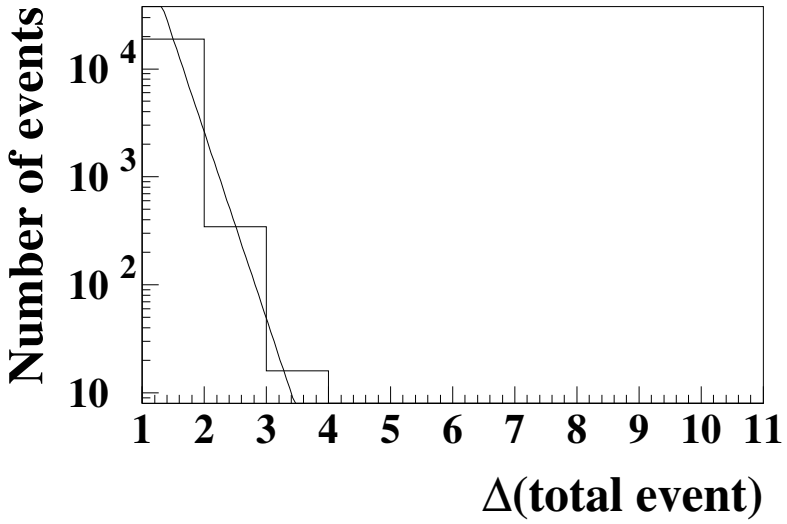

Figure 3.16: *Frequence of arrival of events to the data acquisition, following a Poissonian distribution. If Δ(total event) is bigger than 1, Δ(total event)-1 events are lost (see text).*

3.3.4 Environmental parameters

At the location of GRAAL, near the sea and only at a height of 550 m a.s.l., atmospheric conditions frequently affect the data acquisition.

The detector can not be operated at wind speeds > 35 km/h. Above this value, the oscillation of the heliostats would increase the timing fluctuations of the showerfront and the angular reconstruction would fail.

The data acquisition is not started if the humidity exceeds 85%. Dew is deposited on the heliostats under high humidity conditions and a big fraction of the Cherenkov light is absorbed in the atmosphere. The direct consequence is a fall of the rates.

3.4 Remote operation

The operation of GRAAL has been done since May 2000 by remote control. The main advantage of the remote operation is that travel and man-power costs are reduced. Occasional displacements to the PSA (approximately every 2 months) for the repair of damaged equipment or calibration work are unavoidable. The rest of the observation nights only the regular night-operator of the PSA is on-site. The automatization of the data acquisition leaves less "room" to human errors.

During remote field-control operation (section 3.1.4) the PSA operator starts the control program and the file with the night instructions is read. At the end of the night the last order of the file stops the program and sends the heliostats to rest position. The status of the field during the night can be checked at any moment by the remote physicist on shift, either reading the log files which are written every 3 seconds by the program or exporting the display of the PC to the physicist's local computer.

The data acquisition computer situated at the 70 m level of the central tower controls the electronics and the door of the hut (section 3.2.1). At the beginning of the night the door of the hut is opened and the electronics rack is switched on from a remote computer. Then, the data acquisition program is started (also from the remote computer) and switches on the photomultipliers and sets their high voltages. The program reads a file which has been written in coordination with the heliostats control file. Such a file indicates the setting for the PMTs, i.e. lowered HV during moon periods or during bright stars tracking (scheduled for calibration purposes), the off-time of the PMTs due to high light level and the normal HV settings. The stop of the data acquisition program is scheduled at the same time as the switch off of the PMTs and the closing of the hut door.

Various environmental parameters such as humidity, wind speed, ambient light and rates are checked regularly by the data acquisition computer.

In addition, several security systems have been installed to avoid the damage of the detector in abnormal conditions (see fig. 3.17). To protect the photomultipliers from high currents, we have activated two different mechanisms. A maximum value of the current through the PMTs of 35 μA has been imposed by hardware. If the current surpasses this value, the PMTs switch off automatically for 15 seconds. Besides, a light sensor has been installed in the hut. If the sensor detects excessive light, the PMTs are also switched off. The light sensor has been installed to prevent the continuous switch on/off of the PMTs in conditions of constant excessive light. If the excess of light has a duration larger than 10 minutes (e.g. at dawn) the data acquisition is stopped, the electronics and PMTs are switched off and the door of the hut is closed (all the operations are in this case software controlled). An infra-red camera has been installed in the hut so that the physicist on shift can check at any time the status of the door.

The data acquisition is also stopped and the door closed under extreme weather conditions (humidity over 85% and wind speed over 35 km/h) and high rates. The status of the electronic rack can be checked with a web-cam installed at the tower.

If for any of the mentioned reasons the data acquisition is stopped, the physicist on shift is called by the PC and can check all parameters and images of the cameras remotely. In addition, the physicist on shift is also called if the Internet connection between the PSA and the remote computer has been lost. In that case, the PSA operator starts a modem connection.

For emergencies the regular night-operator of the PSA is on-site on all observation nights.

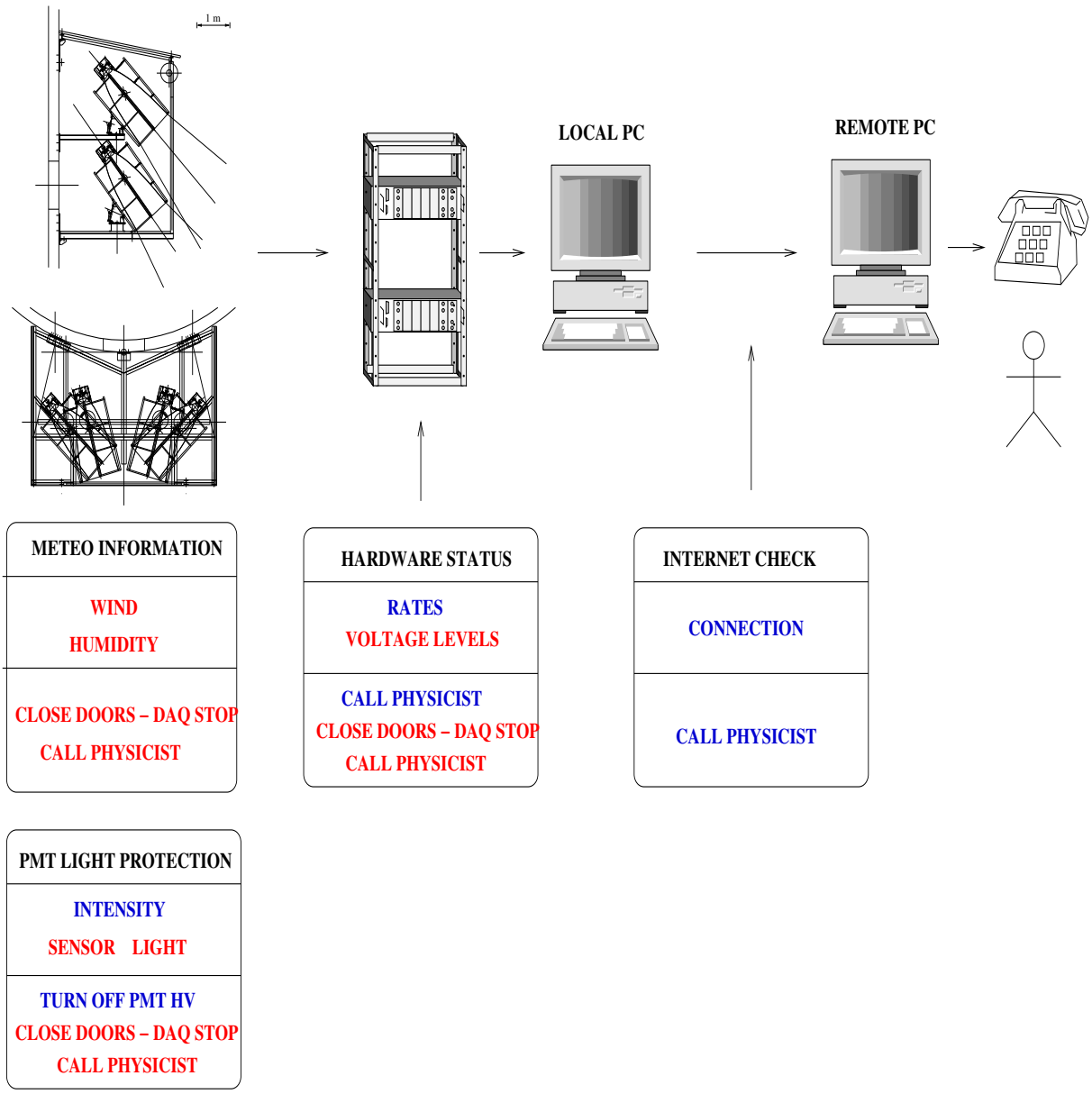

Figure 3.17: *Operational mode of the alarm system for remote control in GRAAL (see text). Under extreme conditions indicated by any of the parameters checked by the daq program the data acquisition is stopped and the door closed (red labels). The blue labels indicate conditions which can be temporary and do not immediately damage the hardware. If these conditions are registered the physicist on shift is called and has to check the parameters.*

Chapter 4

Calibration

This chapter explains the full calibration of the GRAAL detector. The calibration in the heliostat arrays is a difficult issue. The reason for this is that the detectors are spread out over hundreds of metres and consequently shower-front sampling and imaging properties are convoluted in a non-trivial way.

Next section gives an overview of all the calibrations performed. Following sections explain how each calibration was made and the corresponding results.

4.1 Overview

4.1.1 Field geometry

In comparison with the traditional Cherenkov telescopes, where all the mirrors are mounted in a single dish and fixed with respect to each other, the mirrors of a heliostat array are spread over a large area on the ground and are independently steerable. The overall movement of the heliostats must simulate the movement of a big dish with its focal point at the central tower. The field geometry is tested via comparing the signal delay from the different heliostats at their arrival at the tower with the expected delays (section 4.2).

4.1.2 Acceleration of the photoelectrons in the PMTs

We must correct the systematic errors involved in the measurement of the arrival times of the Cherenkov pulses to ensure a reliable time sampling of the shower front.

The operation of the GRAAL photomultipliers at slightly different voltages can introduce a delay in the pulses of one PMT with respect to the other PMTs, since the voltage of the PMT determines the acceleration of the p.e. through the tube. This is studied in section 4.3.

4.1.3 Conversion of p.e. to photons at cone entrance

The most important aim of GRAAL is the detection of new gamma-ray sources and of known gamma-ray sources at a low energy threshold on the ground. A flux determination is very difficult since there are many stages in the conversion of observed gamma rate to source flux where the values of the conversion factors have large error bars.

For the estimation of the energy of a shower the recorded total charge in ADC channels must

be converted to total number of photons of the Cherenkov shower[1] (the energy of a shower is proportional to its number of photons). This involves the conversion of p.e. at the PMT anode to photons at the entrance of the cone, which is one of the prime difficulties for experiments detecting atmospheric Cherenkov light (see e.g. [164]). This conversion is explained in section 4.4.

4.1.4 Reflection in the cables

In general, a reflection in a cable occurs if the impedance of the cable is not exactly the same as the impedance of the device connected at the end of such a cable.

In our setup, the cables which connect the fast amplifiers adjacent to the PMTs with the amplifiers situated right before the electronics chain (section 3.3.1) have an impedance of 50 Ω. The amplifiers used are not perfectly terminated. As a consequence, a fraction of the pulse is reflected back and forth at both ends of the cable and the resultant pulse is then recorded by the digital oscilloscope. The difference of impedance between the cable and the amplifiers determines the fraction of the original pulse which is reflected. For our setup, the reflected pulse has an amplitude which is less than 15% of the original amplitude. The arrival time of the reflected pulse is fixed with respect to the arrival of the first pulse, the time difference between both pulses being determined by the length of the cable (section 4.5.3).

The process of reflection is "recursive", i.e., a fraction of the pulse originated in the first reflection will undergo a second reflection and this process is repeated infinitely. We have considered only one recordable reflection per primary signal. The reason is that the pulse resultant of a second reflection is too small to be distinguished from the NSB fluctuations since the amplitude is strongly reduced in the reflections (see above).

The existence of spurious peaks is detrimental for the analysis, e.g. the timing reconstruction of the showerfront can fail if fake peaks are considered as real. Moreover, the energy resolution can worsen if an "extra" charge (due to the reflected peaks) is considered. For these reasons we are interested in subtracting all the pulses generated by reflection. Section 4.5 explains the calibration performed to quantify and correct the effect of reflection.

4.1.5 Influence of the LED calibrator modules in the calibrations

For the calibration of the PMTs we have used LED calibrator modules (section 3.2.3.2). For the consideration of errors induced by the calibration device, we have studied the dependence of the measurement on the position of the LED modules at the Winston cone. The LED modules are fastened to the windows of the Winston cones, the light emitted by the LED is reflected in the inner Mylar foil of the cones and finally hits the photocathode.

The position at the window can determine the photon distribution at the photocathode if e.g. the light pulse undergoes one reflection or hits the photocathode directly. With only one PMT and one LED module, measurements were made for three different positions, in the centre and close to the periphery of the window. The difference in recorded pulse amplitude within the three positions was always less than 5%, which is negligible within the statistical fluctuations.

[1] In satellite detectors, the energy of a gamma-ray can be obtained directly by measuring the energy deposited in a calorimeter by the pair $e^{\pm}$ created by the gamma (section 2.1).

4.2 Calibration of the field geometry

For the Monte Carlo simulation of the GRAAL detector the heliostats positions on the ground have been used. This simulation is not completely realistic since the reflection does not occur at a fixed position on the ground. Conversely, the centre of reflection of the overall mirror (equal to its geometrical centre) is at a height of about 3.4 m above the ground and changes with the heliostat movement, since the rotation centre of the heliostat is not situated at the mirror surface. Therefore, it must be calculated at all times.

In the CESA-1 field there are two different types of heliostats, CASA and Sener [202]. For each type a different method is used to calculate the mirror centre. With the calibration of the field geometry we want to verify that the mirror position calculated for both types of heliostats and used in the analysis is correct.

4.2.1 Calibration procedure

4.2.1.1 Position of the heliostats

Four groups of 6, 5, 11 and 11 heliostats contained in the field of view of the Winston cones 1, 2, 3 and 4 respectively were used for the calibration. The heliostats were selected so that the minimum time interval between 2 pulses were 30 ns. This was done to prevent an overlap of the pulses, which leads to a wrong identification of the heliostats and worsens the time resolution.

For the measurement, the heliostats were brought into a "back reflection" position, i.e., they were focused to a fixed point which was the corresponding Winston cone in the tower for each group.

The LED modules were fastened to the windows of the Winston cones, so that the forward total light output of the LED module shined onto the heliostat field (section 3.2.3.2).

4.2.1.2 Trigger mode

The standard trigger of the experiment was used for this calibration. In principle, the pulse reflected by the nearest heliostat to the detector fires the trigger and all the reflected pulses are contained in the 1000 ns trace (the first pulse comes typically at $\approx$ 200 ns and the largest time difference between heliostats of one group is $\approx$ 450 ns). The situation was different for the heliostats in groups 1 and 2. When the LED is placed on the window of cones 1 or 2, a part of the light is first reflected by the safety grid on the floor of the detector hut and triggers much earlier. Fortunately, the difference in time between the first and last heliostat for these groups was less than 200 ns and even if the first reflected pulse arrived 700 ns after the trigger, all the pulses were contained within the trace.

4.2.2 Analysis method

4.2.2.1 Search of the peaks

The standard method of data analysis was used for the determination of the amplitude and arrival times of the pulses (section 6.1.2). The arrival time of the pulses which saturated the flash-ADC was defined as the mean time of the saturated channels of the peak. Since no peak reconstruction is done, the error introduced in the arrival time determination is much higher for saturated than for non-saturated pulses (section 6.1.2). The saturated peaks are not taken into account in the usual data analysis to avoid a bias in the angular reconstruction of the showers.

Heliostat	$\delta t_{calc-meas}$ (ns)	$\sigma_t/\sqrt{N}$ (ns)	Amplitude (ADC units)	$\sigma_{ampl}/\sqrt{N}$ (ADC units)
202	-1.2	0.7	162.4	21.5
300	-0.5	0.8	29.8	8.1
306	+2.4	1.1	8.0	3.2
404	0.0	0.0	24.9	6.8
408	+1.4	1.0	6.0	1.7
504	+1.0	0.7	74.3	13.9

Table 4.1: **Heliostat**, $\delta t_{calc-meas}$ *Difference between expected time and mean experimental arrival time of the LED pulse in ns,* $\sigma_t/\sqrt{N}$ *Statistical fluctuation of the mean experimental arrival time,* **Amplitude** *Mean amplitude of the LED pulses,* $\sigma_{ampl}/\sqrt{N}$ *Statistical fluctuation of the mean pulse amplitude. All the heliostats of this table belong to the group 1.*

Heliostat	$\delta t_{calc-meas}$ (ns)	$\sigma_t/\sqrt{N}$ (ns)	Amplitude (ADC units)	$\sigma_{ampl}/\sqrt{N}$ (ADC units)
201	-2.2	0.5	254.7 (saturated)	2.3
301	-0.4	0.7	64.8	13.4
401	-1.1	1.2	5.4	1.4
407	0.0	0.0	37.2	10.1
503	+1.3	0.9	14.1	5.5

Table 4.2: *Entries as in table 4.1 but for heliostats of cone 2.*

Here, they have been included (see tables 4.2 and 4.3) but a higher systematic error in the time determination than for the other peaks must be considered.

4.2.2.2 Identification peak-heliostat

The expected arrival times of the peaks were calculated and compared with the measured ones. A reference pulse was chosen for each cone and the time differences of the other pulses with respect to the reference one within a trace were considered. The reference peak is recognized in tables 4.1-4.3 because the statistical deviation σ_t is zero (the difference of a peak with respect to itself is always zero). The only requirement to choose a peak as reference was an amplitude clearly above NSB but not saturated.

In the traces of cones 1 and 2 two clearly different groups of peaks are seen during analysis, the first group is due to the reflection of light at the safety grid (section 4.2.1.2) and the second one to the reflection in the heliostats. The signals arriving at the beginning of the trace (caused by the reflection at the grid) were not considered in the analysis.

4.2.3 Results: time response of the detector

The results of the calibration are shown in tables 4.1-4.3.

Column 2 of tables 4.1-4.3 shows the deviation of the expected arrival time of a peak with respect to the measured one ($\delta t_{calc-meas}$). The arrival times of the heliostats 306 (in cone 1) and 201 (in cone 2) present the largest systematic deviations from the expected value, more than

Heliostat	$\delta t_{calc-meas}$ (ns)	$\sigma_t/\sqrt{N}$ (ns)	Amplitude (ADC units)	$\sigma_{ampl}/\sqrt{N}$ (ADC units)
210	0.0	0.0	80.4	14.3
312	-1.3	0.4	254.9 (saturated)	1.8
414	-0.2	0.4	137.9	22.7
512	-0.9	0.4	47.3	7.7
514	+0.1	0.4	4.3	0.0
516	0.0	2.9	69.3	40.5
616	0.0	0.6	27.1	9.9
618	-0.9	0.5	111.3	20.6
620	-1.3	0.4	137.0	24.1
718	-1.6	0.8	8.1	3.5

Table 4.3: *Entries as in table 4.1 but for heliostats of cone 3.*

2 ns. Column 3 shows the statistical error of the experimental value ($\sigma_t/\sqrt{N}$), where N is the number of pulses used to calculate the mean. The statistical errors are always smaller than 1 ns except for the heliostat 516 of cone 3. Cone 2 shows the most significant ($> 2\sigma$ in some case) deviations from the mean.

We can observe that the two saturated peaks that have been considered have a significant deviation from the mean. This is an expected result, since the pulses are not reconstructed for the determination of the arrival time. In this way, a variable error is introduced for the saturated pulses. Such peaks are not considered in the standard analysis. In addition, the pulses near the NSB fluctuations, with amplitudes smaller than 10 ADC units, present the largest statistical fluctuations (except heliostat 516). This is also logical, since the pulses are more influenced by the background noise.

The systematic deviations are distributed around zero, this means that there is not a common source of error for a whole cone or for the whole array and rules out a possible error in the positions of the cones as well as in the calculation of the centre of the heliostat mirrors (which would show up for all heliostats of the same type).

In principle, a systematic error of 2 ns introduces an error of about 0.003° in the source position, which is negligible in comparison with other systematic errors in the directional reconstruction (section 10.2.1). Moreover, when all the heliostats are combined, the systematic errors in the arrival times increase the lsq_t^2 of the fit to the showerfront, but the reconstructed position is not affected unless many heliostats of a group present systematic deviations in the "same direction" (with the same sign). Fig. 4.1 shows the time deviation $\delta t_{calc-meas}$ for all the peaks of a sample of real showers for the final reconstructed directions. For each cone the distribution is centred around zero and has a width smaller than 0.7 ns. The peaks which fall out of the Gaussian are misreconstructed (section 6.2.2). The plot proves that the reconstruction of the shower direction is not being affected by the systematic errors of the individual peaks shown in tables 4.1-4.3. An overall systematic deviation for the peaks of a single cone is not observed.

4.3 Transmission time of the photomultipliers

Not only the gain but also the transmission time (time of flight) depend on the HV of the photomultipliers. A calibration of the dependence of the transmission time on the voltage is

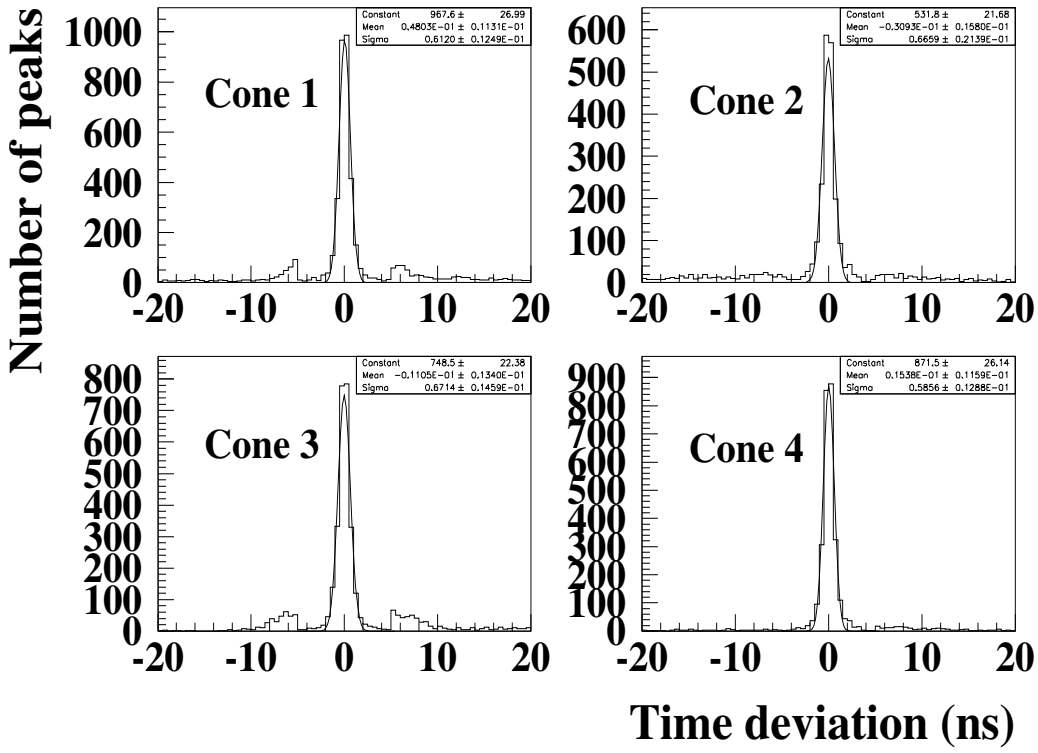

Figure 4.1: *Time deviation of the experimental peaks from the expected ones, for the final reconstructed direction of a number of real showers for all four cones. The central peak has been fitted to a Gaussian, the parameters of the fit are shown in the figure.*

necessary for each phototube, since such a dependence is different for each photomultiplier.

4.3.1 Calibration procedure

The calibration described below was made in December 1999. For the calibration of each PMT a pulse of light was emitted by the LED pulser into the cone at different voltages of the phototube and recorded by the data acquisition system.

A single LED module was used for the four calibrations. This was done in order to prevent falsification due to differences on the LED modules. The LED module was fastened at the window of the Winston cone in such a way that the light emitted by the LED was directed to the inside of the cone. Electronics and LED were triggered together.

The High Voltage of the PMTs was raised in 25 V steps over a total range of 475 V. The starting HV for each PMT was chosen so that the voltage sweep was centred in the nominal HV, which is $\approx$ 1292, 1255, 1367 and 1155 V for PMTs 1, 2, 3 and 4 respectively.

4.3.2 Analysis method

Thirty independent measurements of the arrival time and amplitude for each cone and voltage step were made in order to reduce statistical fluctuations. A mean arrival time was calculated making an average over all the recorded times for each voltage. The same was done for the amplitude. Sometimes it happened that less pulses were available to calculate the mean because the LED was not pulsed. In these cases the statistical fluctuations increased.

4.3.3 Results

The results of this calibration are shown in figure 4.2 for all four photomultipliers. The experimental points have been fitted to an exponential curve. The values of the parameters and χ^2 of the fits are given in the figures.

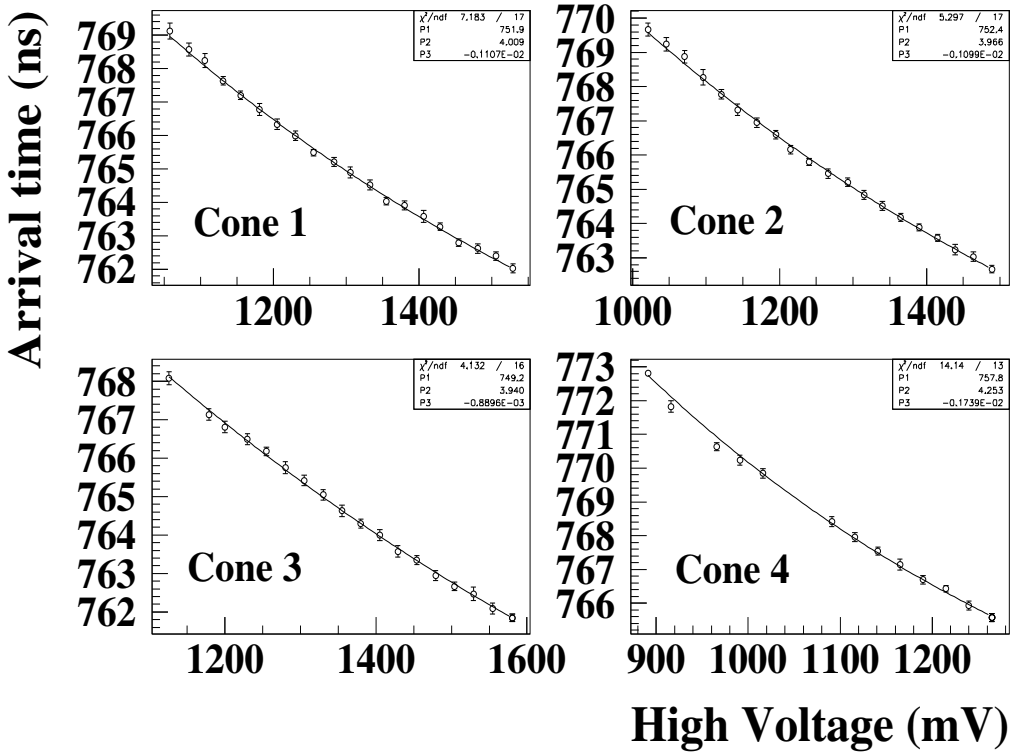

Figure 4.2: *Dependence of the arrival time of a LED pulse with the PMT high voltage. The experimental points have been fitted to the exponential curve P1+exp(P2+P3·x). The reduced χ^2 indicates a 99% confidence level for the fits of the cones 1-3. The fit of the cone 4 has a confidence level of ca. 40%.*

4.3.4 Application to standard analysis

During the analysis of a standard event the operational voltages of the 4 photomultipliers are read and the difference in the arrival time of one trace with respect to the others due to the PMT high voltage are calculated according to the functions of the previous section. The pulses of the traces 2-4 are then corrected for the delays with respect to the pulses of the first trace.

4.3.5 Regular cross check during data acquisition

It might happen that the aging of the PMTs affects this calibration. In order to have a routine cross check, four light pulsers (one for each cone) are fired every 5 minutes during data acquisition. Then, the time relations between the four traces are compared with the ones expected from the independent calibration discussed above in this section.

4.4 Conversion of p.e. to photons at cone entrance

The conversion of recorded charge (in ADC units) to number of photons of a shower comprises two stages. The first one consists of the calibration of the electronics chain. The non-linear gain of the amplifiers is calibrated so that a conversion factor from charge of the shower (in mV or ADC units[2]) to charge of the incoming pulses (in pC) can be obtained. The second stage includes the gain of the photomultipliers from which a conversion from charge of the PMT pulses to photons of a shower is inferred. For a detailed treatment of the calibration see [32].

4.4.1 Calibration procedure

A CAMAC module (model Phillips 7120) that produces charge pulses with characteristics similar to PMT pulses was used for the calibration. The module injected pulses into the preamplifiers, so that information was obtained about the electronic chain after the PMTs. The module was fired ten consecutive times, each time increasing the charge content of the pulse. The usual trigger mode of data acquisition was used. The four channels were fired simultaneously so that the response of the charge trigger was ensured.

4.4.2 Results

The search for the peaks was performed with the standard method (section 6.1.2).

The value of the non-linear gain of the amplifiers is obtained from the relation between the pulse amplitude (in mV) recorded by the digital oscilloscope and the charge (in pC) injected by the Phillips module (see fig. 4.3). Table 4.4 shows the parameters of the fit for the curves of fig. 4.3 (one per cone) to a second order polynomial $V=A \cdot C^2 + B \cdot C$, where V is the output voltage in mV and C is the input charge in pC.

For the conversion from injected charge to number of photons the calibrated LED pulsers (section 3.2.3.2) were used. Table 4.5 shows the relation between number of photons of the LED pulses (known from a previous calibration) and the signal amplitudes at the input of the oscilloscope.

We can calculate the charge injected by the LED pulses with the curves of fig. 4.3 and infer directly the conversion of p.e. to pC. Due to the relatively low gain of our PMTs, the conversion of p.e. to pC in the PMT is linear up to a saturation limit which is determined by

[2]One ADC unit is equivalent to 6.25 mV.

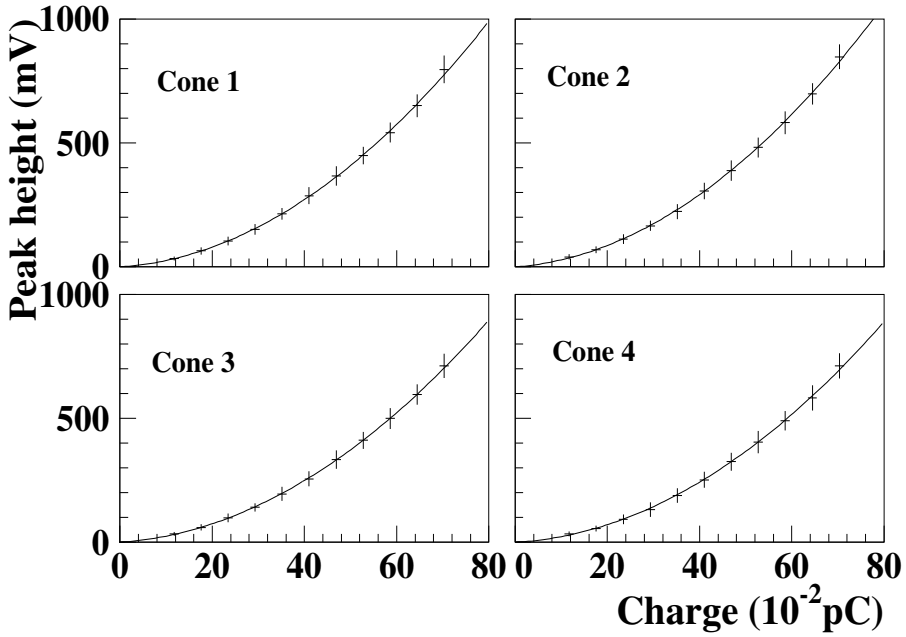

Figure 4.3: *Non-linear gain curve obtained from the calibration of the electronics (see text). Shown is the maximum amplitude in mV as a function of the initial injected charge. Taken from [32].*

the oscilloscope. Therefore, we can apply the conversion factor of p.e. to pC in all the range of the measurement.

4.4.3 Systematic errors

The largest error in the conversion of p.e. to mV arises from the first factor (photoelectrons to pC). Besides the statistical fluctuation of the measured amplitude of the peaks in mV, the linearity predicted for the conversion of p.e. to pC (see previous section) might be erroneous at some stage. This constitutes the first systematic error.

In addition, in the conversion factor from pC to mV, the errors in the fit parameters of table 4.4 are high ($\approx 15\%$ in the A parameter and $\approx 30\%$ in the B parameter).

	Cone 1	Cone 2	Cone 3	Cone 4
A	0.136 ± 0.022	0.137 ± 0.027	0.122 ± 0.022	0.128 ± 0.025
B	2.9 ± 0.9	3.5 ± 1.2	2.8 ± 1.0	2.5 ± 1.1

Table 4.4: *Results of the fit of the points of fig. 4.3 to a second order polynomial* $V=A \cdot C^2 + B \cdot C$.

	LED pulse (photons)	Maximum amplitude (mV)
Cone 1	829	146 ± 5
Cone 2	690	167 ± 5
Cone 3	624	179 ± 5
Cone 4	581	103 ± 4

Table 4.5: *Relation between number of photons of the LED pulses and maximum amplitude of the pulses in mV.*

The combination of the errors introduced in the calculation of both conversion factors makes a precise absolute calibration of the electronics chain difficult. This is translated into large error bars in the energy estimation of a shower and consequently in the flux estimation of a source (sect. 13.1.4.1).

4.5 Reflection in the cables

4.5.1 Calibration procedure

During the calibration performed with the Phillips pulser (see previous section) it was noticed that a small pulse, slightly higher than the NSB fluctuations, arrived always at a fixed time after the Phillips pulse, as a consequence of the reflection of the Phillips pulse in the cable. The time interval between both pulses indicated the point at which the reflection occurred, namely, the ends of the cable connecting the two amplifiers (section 4.1.4).

The Phillips module was used for the calibration.

4.5.2 Analysis method

In order to quantify the reflection effect, the arrival time and amplitude of the Phillips pulse and its reflection were recorded. The time interval between the original and the reflected pulse was measured first for those pulses with an amplitude larger than the NSB fluctuations. Then, the calibration curve was extended to the lowest amplitudes by searching the reflected pulses near the NSB fluctuations at a fixed time interval after the initial pulse (inferred from the first measurement).

4.5.3 Results

The pulse reflected in the cables was found to appear at a 67 (99) ns interval (for cones 1-2(3-4) respectively) from the initial pulse. The difference in the time interval between cones 1-2 and 3-4 (32 ns) is due to an extra cable of 16 ns length between the amplifiers for cones 3-4 (the 32 ns correspond to the way into and back into the cable for the reflected pulse).

Fig. 4.4 shows the ratio of original to reflected amplitude versus original amplitude. The points have been fitted to the polynomial function $\frac{Ampl_{original}}{Ampl_{reflected}} = a + b \cdot Ampl_{original}$. Table 4.6 shows the parameters of the fit for cones 1 and 2. Cones 3 and 4 could not be properly fitted due to the saturation of the original pulses. The fits of the curves for cones 1 and 2 agree within the errors.

A dependence of the fraction of the initial pulse which is reflected with the amplitude of such a pulse can be observed. This effect is due to the non-linearity of the amplifier situated

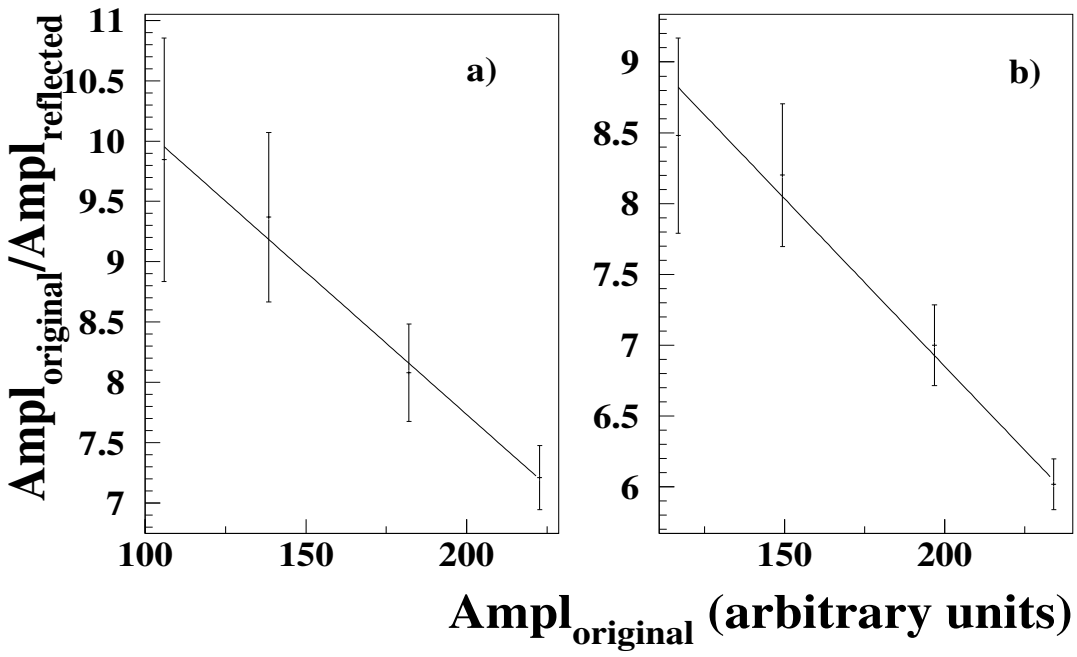

Figure 4.4: *Dependence of the ratio original-to-reflected amplitude in the cables on the incident pulse amplitude for cones 1 (panel a.) and 2 (panel b.). Both curves are fitted to a polynomial function of grade 1. The results of the fit are shown in table 4.6.*

Cone	a	b	χ^2/ndf	ndf
1	12.4±1.3	-0.024 ±0.006	0.058	2
2	11.6±0.9	-0.024 ±0.004	0.211	2

Table 4.6: *Parameters of the fit of the curves of fig. 4.4 to a polynomial function of grade 1.*

before the electronics. In reality, the fraction of the initial pulse which is reflected is constant (and has been inferred from the curves of fig. 4.4 as $\approx 5\%$). However, the gain of the amplifier increases with the amplitude of the pulse and therefore, reflected pulses from large pulses will be more amplified than those from small pulses. As a consequence the fraction of initial to reflected (measured, i.e. after the amplifier) amplitude increases for small pulses.

4.5.4 Application to standard analysis

The final aim of the reflection studies is to subtract the reflected peaks from the traces so that they do not interfere with the analysis process (see section 4.1.4 and chapter 6). Thus, if a peak is found above the imposed software threshold (section 6.1.2.1), a fraction of its amplitude -given by the curve of the previous section- is subtracted 67(99) ns later for pulses belonging to cones 1-2(3-4). The subtraction is performed channel by channel for all the time channels of the peak. All the subtractions are done in the initial trace, the recursiveness of the reflection process is not considered (section 4.1.4).

Chapter 5

Monte Carlo simulation of the detector

The GRAAL detector can be only fully understood with the aid of a simulation. The simulation of the detector is essential to predict the behaviour of the Cherenkov EAS of low energy at the detection level and permits the optimization of the detector before construction.

The simulation plays a fundamental role in the analysis of the data, where the interpretation of certain parameters, e.g. the integrated charge as primary estimator of the energy of a shower (section 8.2), and of differences between hadronic and gamma-ray showers, e.g. the time deviation of small pulses from the shower front (section 7.2.3), is exclusively derived from the comparison with the Monte Carlo (MC) simulated showers.

In contrast with the imaging Cherenkov telescopes (section 2.3.2), GRAAL and in general all the heliostat arrays can not reproduce the "image" of a Cherenkov shower in the sky and its development through the atmosphere, since the light reflected by one heliostat is focused to only one PMT and not to a matrix of PMTs[1]. Therefore, the heliostat arrays are more dependent on the MC simulation to "translate" the information about time and density of light on the ground to the shower development characteristics.

The simulation comprises of two parts. Section 5.1 explains the generation of an airshower by a cosmic ray and its development through the atmosphere. Section 5.2 explains the path of the Cherenkov shower photons through the optics and electronics of the detector until the data acquisition system, where they are recorded.

Further details about the simulation process are given in [32].

5.1 Generation of the MC showers

The process of generation of a Cherenkov atmospheric shower from a cosmic ray was simulated with the program CORSIKA (COsmic Ray SImulation for KAskade), version 5.20 [39], which includes the loss of energy of charged particles due to ionization and the modification of their trajectories due to the interaction with the earth's magnetic field (the value of the earth's magnetic field in central Europe was considered). For the transport of the particles in the atmosphere the absorption due to ozone, Rayleigh and Mie scattering was included (see e.g. [228] for a description of the absorption processes).

[1] It must be remarked that, in principle, a heliostat array could be operated as an imager with a low resolution camera (see section 2.3.3.1).

Azimuth (deg)	0	0	45	45	90	90
Zenith (deg)	10	30	10	30	10	30

Table 5.1: *Incoming directions of the gamma-ray generated MC showers. The proton showers were generated around the shown directions with a maximum angular deviation of 4 degrees.*

5.1.1 Characteristics of the MC generated showers

The generated Monte Carlo library includes showers originated by protons of primary energies between 250 and 4000 GeV and gamma-rays of primary energies between 50 and 1000 GeV in 6 different incident directions (see table 5.1). The core position of the showers was randomly generated up to a maximum distance from the centre of the array of 150 (300) m for gamma-ray (proton) primaries. While gamma-rays were generated as incident from a point-like source in the observed direction, the incoming directions of protons were randomly generated around the observed direction with a maximum angular deviation of 4 degrees.

8000 independent showers (with different energy and core position in the case of gamma primaries and in addition a different incoming direction around the point-like position of table 5.1 in the case of proton primaries) for the two species were simulated for each of the incident directions. As a procedure to maximize the usefulness of the CPU time, for every simulated shower the GRAAL response was calculated for 5 different core positions. A final library of 40000 (or 8000 completely independent) showers for each species and incident direction is available.

The generation of all the showers was performed by Borque [32] in various computers, the total time of processing being equivalent to one year of CPU in a Pentium III (500 MHz). This "short" processing time was only achieved by generating both primaries with core and energy distributions which minimize the CPU time. The differential energy spectrum of both primaries follows a power law with index -1 instead of the real one. This allows to achieve sufficient statistics at high energy without having to produce a non-affordable (in CPU time) number of events at low energies. The distance r from the centre of the array to the core position follows the law $P(r)dr = Cdr$ where $P(r)$ is the probability of generation of one event in the differential interval dr and C is a constant term. Finally, the angular distribution of proton showers is not isotropic, but follows a law $P(\theta)d\theta = Cd\theta$ where θ is the angular distance between the real incoming direction of a shower and the point-like position of table 5.1, $P(\theta)$ is the probability of generation of one event in the interval $d\theta$ and C is a constant term.

5.1.2 Weight of the MC showers

After the generation of the MC showers, a "weight" (multiplication factor) was assigned to each shower to convert the above described distributions into distributions of cosmic ray showers which reproduce the reality. Figs. 5.1 and 5.2 show the MC distributions before and after weighting.

The overall weighting factor of a gamma-ray shower is the product of "energy" and "core" weights whereas for proton showers an additional "angular" weight is applied. The "energy" weighting factor was such that the corrected spectral index was -2.7 for protons [242] and -2.4 for gamma-rays (taking as reference the energy spectrum of the Crab nebula from [114]) (see panels a. and b. of figs. 5.1 and 5.2). The "core" weight consisted of a factor proportional to r and was assigned to each shower to obtain a radial distribution (see panels c. and d. of figs. 5.1 and 5.2). Finally, an extra factor was assigned to the proton-originated showers in such a way that

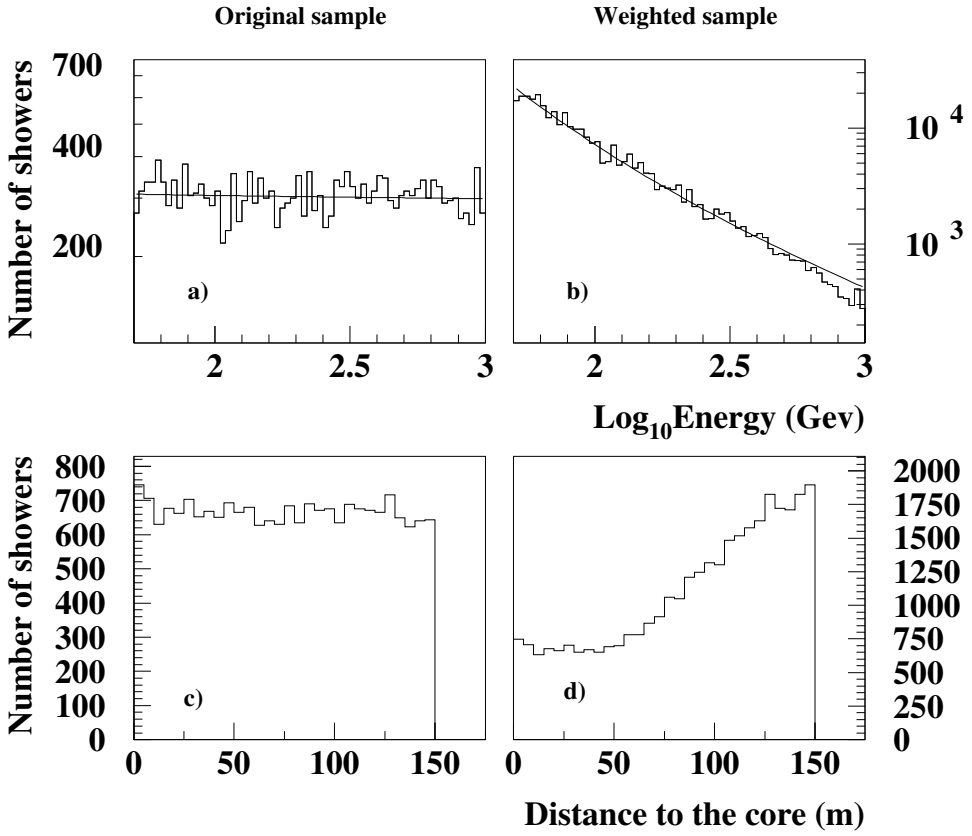

Figure 5.1: *Top (panels a. and b.): energy distribution for a MC gamma sample of 20000 showers (4000 independent). Bottom (panels c. and d.): number of gamma showers as a function of distance to the core. The plots on the left (a. and c.) show the original simulated sample. The plots on the right (b. and d.) show the MC sample after weighting.*

the incoming directions of protons around the observed direction follow a radial distribution, in other words, they are isotropically distributed around the observed direction after weighting, see panels e. and f. of fig. 5.2).

5.2 Simulation of the detector

5.2.1 Optics

5.2.1.1 Heliostats

Each heliostat has been simulated as one single spherical mirror divided in 2 sections of 6.75 m^2 each. The focal length of each heliostat (distance from the heliostat to the point where the image is formed) corresponds to the focal length of the sub-mirrors of the simulated heliostat.

For each Cherenkov photon hitting the heliostat the simulation program [32] determines first the position of the mirror where the photon is reflected and then the reflection in the normal plane to the incident direction in the point of reflection and in the heliostat system of reference.

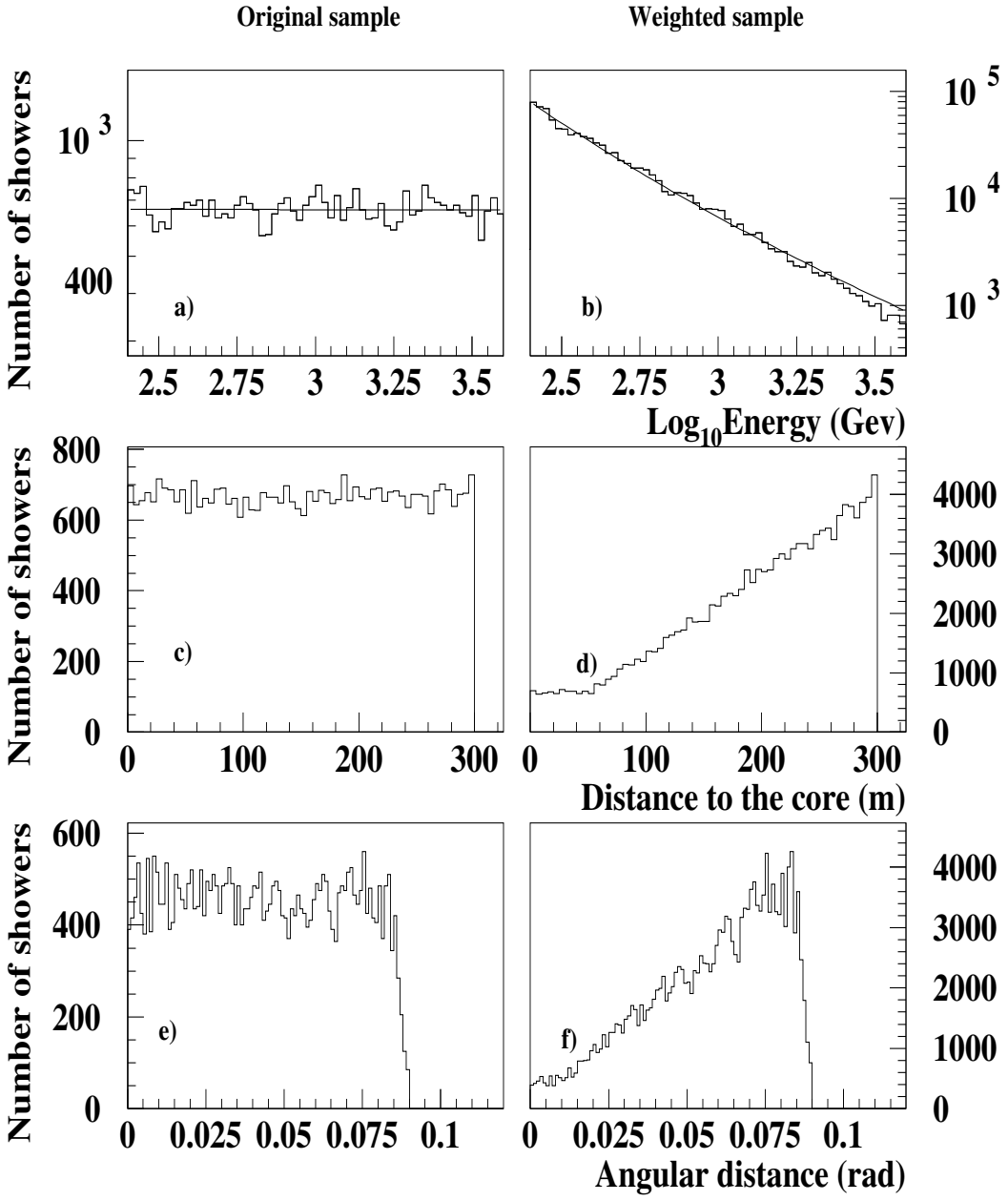

Figure 5.2: *Top (panels a. and b.): energy distribution for a MC proton sample of 40000 showers (8000 independent). Middle (panels c. and d.): number of proton showers as a function of distance to the core. Bottom (panels e. and f.): number of proton showers as a function of angular distance from the point source position. The plots on the left (a., c. and e.) show the original simulated sample. The plots on the right (b., d. and f.) show the MC sample after weighting.*

Mirror imperfections are simulated by generating random errors in the reflection point and its derivative.

5.2.1.2 Winston cones

A Cherenkov photon arriving at the outer window of a Winston cone will undergo some reflections in the inner walls of the cone on its way to the photocathode. For the simulation of the Winston cones it is not necessary to follow the photon path along the cone. There are two reasons for that: first, all of the light rays incident on the centre of the cone have the same probability of acceptance. The Winston cones have a constant acceptance of $\approx 100\%$ for incident angles up to 10° (see fig. 3.8), which is the maximum angle between a light ray reflected by a heliostat and the axis of the cone to which it is focused. Second, the mean number of reflections of a photon in the walls of the cone has been determined to be 1.36 (section 3.2.2) and this value has a small spread.

Therefore, the cone response has been simulated as a function of three parameters: the diameter of the outer window of the cone, the angular acceptance curve and the mean reflectivity of the Mylar foil for the mean number of reflections (all these parameters have been given in chapter 3).

5.2.1.3 Photomultiplier Tubes

After the arrival of a photon to the photocathode, the probability that the photon is converted to a photoelectron by the PMT is simulated. The quantum efficiency curve of the photocathode shows the probability of conversion of a photon to a p.e. as a function of the wavelength of the photon (see fig. 3.9 in section 3.2.3). Then, a photon will be converted to a p.e. by the PMT randomly depending on the acceptance probability corresponding to its wavelength.

In addition, the PMT produces a widening of the Cherenkov light pulses which is dominant over the widening of the pulses in the GRAAL fast electronics. The difference between the width of the Cherenkov detected pulses (after being corrected for the non-linear gain) and the width of the pulses that arrive at the photocathode according to our simulation gives the instrumental widening of the PMTs. The mean standard deviation is 2.10 ns for the real pulses and 1.28 ns for the simulated pulses. To consider this effect the simulated signals have been convoluted with a Gaussian of width σ_{instr}= 1.84 ns [32].

Finally, we have to simulate the gain of the PMTs. The manufacturer provides the gain value for DC current for each PMT but we need the value for fast current pulses which is not linearly proportional to the DC current for our PMTs (section 3.2.3.1). For this reason a different method, that consists of calibrating the conversion of number of p.e. to charge in pC for each channel with real data (section 4.4), is used to infer the gain of the PMT. The obtained gain is then included in the simulation.

5.2.2 Electronics

The simulation of the electronics comprises the non-linear gain of the amplifiers and the trigger logic.

5.2.2.1 Amplifiers

The simulation of the PMT gain was explained in the previous section. The gain introduced by the amplifiers situated after the PMTs is obtained from the experimental calibration of section

	Input				Output			
Cone	Max (mV)	t_{rise} (ns)	t_{fall} (ns)	FWHM (ns)	Max (mV)	t_{rise} (ns)	t_{fall} (ns)	FWHM (ns)
1	250	6	12	7	145	24	580	98
2	290	6	12	7	160	24	580	98
3	260	6	12	7	260	75	750	160
4	250	6	12	7	260	75	750	160

Table 5.2: *Characteristics of an experimental pulse before (input) and after (output) the integrator module.*

4.4, that provides the amplitude in mV of a pulse originated by a charge injection with the shape of the generator (CAMAC-module Phillips 7120) pulse. Thus, knowing the shape of the Phillips pulse the charge injected on each channel can be inferred. In particular, if an original Phillips pulse with a Gaussian shape is assumed, the relationship is the following:

$$\frac{\mathrm{C_i}}{\Delta \mathrm{t}} = \frac{\mathrm{C_P}}{\sqrt{2\pi}\sigma_\mathrm{P}} \tag{5.1}$$

where C_i is the charge contained in a channel of width Δt and C_P is the corresponding charge of the pulse of width σ_P. Since the Phillips pulse is not a Gaussian but an asymmetric function (semi Gaussian plus exponential) a relation has to be inferred between both functions. Borque [32] gives a value of $C_{asymmetric} = 1.32 \cdot C_P$, i.e., the charge injected by the asymmetric pulse ($C_{asymmetric}$) is 1.32 times the charge injected by a pulse with a Gaussian shape (C_P). Using the previous results the conversion of charge to mV for each time bin Δt can be applied.

5.2.2.2 Charge trigger

The logic of the charge trigger has been explained in section 3.3.2.1. The main component of the trigger is the EG&G579 module which will be the centre of the Q-trigger simulation.

Previous to the simulation the behaviour of the EG&G579 module was studied with fast single pulses in the four cones. The characteristics of the signal before and after the integrator module were used to simulate the module [32] and are listed in table 5.2. To simulate the asymmetry of the input signals two semi Gaussians were used. The semi Gaussian characteristics were chosen so that they reproduce the experimental characteristics, i.e., the FWHM of the pulse is the same as the experimental one and the fall time is double the rise time, as for the experimental pulses.

The integrator module was simulated as a convolution algorithm with an exponential function $V_{out} = A \cdot V_{in} \cdot e^{-t/B}$, where A and B were adjusted until the output function was similar to the experimental output. Table 5.3 shows the values chosen for the parameters A and B and the characteristics of the input and output signals of the simulated module. The comparison of this table with the previous one shows that there is a good agreement for most of the signal characteristics. The largest disagreement corresponds to the rise time of the pulses, which is not very important for the experiment, and at a lower scale the fall time, probably due to the difficulty of determining the end of the pulse due to the NSB fluctuations.

During data acquisition the integrator module is fed with the 1000 ns trace of Cherenkov pulses. The total integrated signal is the sum of the output pulses of the integrator during the integration time (100 (200) ns for cones 1-2 (3-4) respectively). If the total integrated signal

	Input				Output			
Cone	Max (mV)	t_{rise} (ns)	t_{fall} (ns)	FWHM (ns)	Max (mV)	t_{rise} (ns)	t_{fall} (ns)	FWHM (ns)
1	250	6	12.5	7	145	13.5	531.5	89.5
2	290	6	12.5	7	160	13.5	531.5	89.5
3	260	6	12.5	7	260	14.5	922.5	149.5
4	250	6	12.5	7	260	14.5	922.5	149.5

Table 5.3: *Characteristics of a simulated pulse before (input) and after (output) the integrator module.*

surpasses a discriminator threshold the trigger for the cone is fired (see fig. 3.15). It is required that 3 out of 4 cones trigger within 200 ns to fire the total Q-trigger.

5.2.2.3 Sequence trigger

The simulation of the sequence trigger is simpler than the one of the Q-trigger. The shape of a pulse and its variation as it passes through the NIM coincidence modules is not taken into account. The trigger logic described in section 3.3.2.1 is followed for the simulation. If a pulse surpasses the discriminator threshold imposed, a second peak is searched in a time window of 40 ns after a delay of 20 ns. If the second peak is found, the process is repeated for a third peak. If the third peak is also found a trigger is generated for that cone. Hence, the trigger for a single cone is fired with a maximum delay of 120 ns after the arrival of the first pulse over the threshold. The final electronic pulse for one cone has a length of about 90 ns (see fig. 3.14).

If cones 1 and 2 have a trigger within 150 ns the sequence trigger is fired.

5.2.3 Simulation of the NSB

After the optical simulation of the detector, i.e., once the p.e. have arrived at the photomultiplier anode, four histograms are generated, one per cone, where the number of p.e. per channel as a function of time is stored. Each time bin is 0.5 ns, the time resolution of the oscilloscope. The night sky background is added to the Cherenkov pulses at that moment, following a Poisson distribution of mean N. The value of N has been determined by calculating the contribution of each heliostat to the number of p.e. N which arrive at one PMT in the time interval Δt:

$$N = L \cdot S \cdot \Omega \cdot Q \cdot R \cdot \Delta t \tag{5.2}$$

where L is the absolute value of the Light of the Night Sky (measured in photons/m^2/s/sr), S is the heliostat area, Ω is the solid angle seen by the PMT through the heliostat, Q is the quantum efficiency of the photocathode and R is the mean reflectivity of the heliostat and of the interior of the cone in the considered wavelength range.

L has been measured at the PSA on a very clear night using the single photon counting method described in [163]. A value of $3 \cdot 10^{12}$ ph/m^2/s/sr was obtained between 300 and 600 nm [186] (see chapter 11). The values of S, Q and R have been already given in chapter 3. The solid angle has been estimated by Borque [32] to be $\approx 1.33 \cdot 10^{-3}$ sr ($\approx 0.87 \cdot 10^{-3}$ sr) for cones 1-2 (3-4). Substituting all the values in eq. 5.2 a value for N of $\approx$ 13(9) p.e./ns for cones 1-2(3-4) is obtained.

5.3 Fine tuning of the simulation

The process of simulation and the detector interact with each other. The comparison of real data with the MC simulation is a check of the "accuracy" of the simulation, corrections are applied to the simulation for the parameters known with less accuracy so that it fits better with the data. Fine tuning of the Light of Night Sky L and of the gain G has been performed so that the trigger rate of cosmic rays ($\approx$ 4 Hz in good nights) and the distribution of amplitudes of the NSB are reproduced.

The value of L has been set as 8 ph/m^2/s/sr, which is higher than the value measured in the PSA of 3 ph/m^2/s/sr, in a second MC version (the first version of the MC simulation used the value measured in the PSA). This is because the measured value was obtained on a night with exceptional weather conditions, so the value of L on a typical night in the PSA must be higher. Moreover, for the first version of the MC simulation (used throughout this thesis) it was found that the signal to NSB ratio was higher than for the experimental data. This is the reason to increase the software threshold for MC with respect to data analysis in order to obtain the observed experimental proton rate (section 8.3). In a second version of the MC (used by Borque [32]) the NSB level was increased to the given value of 8 ph/m^2/s/sr to solve this problem.

An effect which has not been simulated in any of the MC versions is the photomultipliers afterpulsing. The afterpulsing occurs when an electron from the photocathode of the PMT, while accelerating towards the 1st dynode, collides with and ionizes a molecule or an atom of a rest gas which is contained in the volume or is adsorbed on the surface of the dynode material. Such ions are accelerated towards the photocathode where they deposit their energy and release many electrons [165]. These electrons produce a "pulse" a few hundred ns "after" the arrival of the first pulse, the so-called "afterpulse". In our setup, the afterpulsing effect is detrimental for analysis, since the afterpulses can be confused with real Cherenkov pulses in the FADC trace. This is partially corrected by allowing the analysis program to reject some pulses which do not fit in the expected time pattern (section 6.2.2). However, it can happen that some afterpulses are considered in the analysis, either because they are confused with real peaks or because the maximum number allowed of peaks has already been rejected. Thus, these pulses are one reason of discrepancy between MC simulated and real showers (sections 9.2 and 9.4).

The final gains applied in the simulation are shown in fig. 5.3. The error boxes of the LED calibration show the indetermination existent in this part of the simulation.

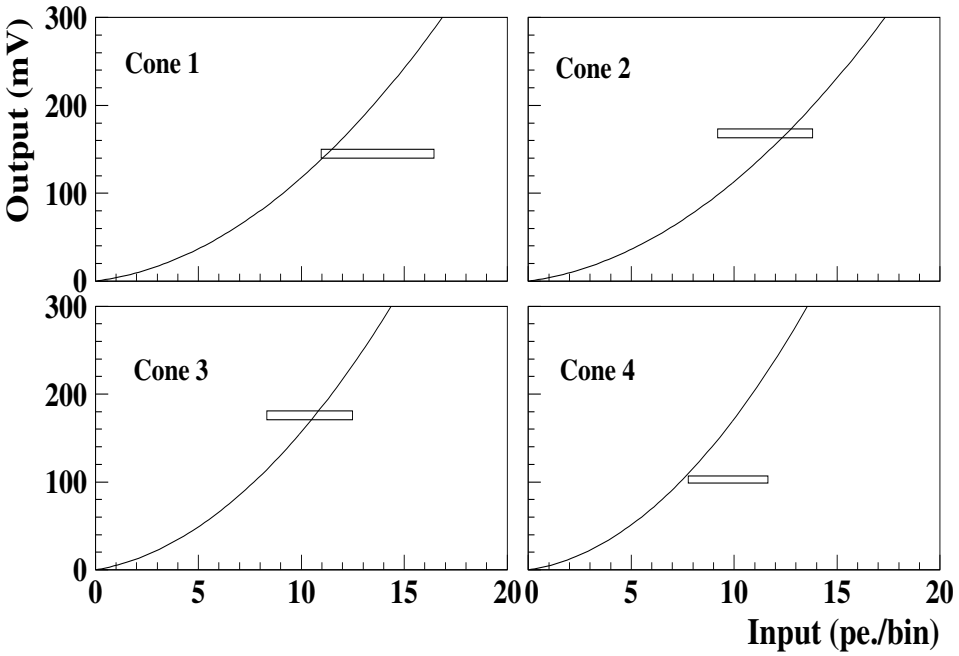

Figure 5.3: *Final gain curves of the electronic simulation. The rectangles represent the error boxes of the experimental values of the LED calibration.*

Chapter 6

Event reconstruction

The analysis of the GRAAL data is performed in a two-stage procedure.

The first step (section 6.1, see fig. 6.1) consists of searching for the Cherenkov peaks in the FADC recorded traces and determining their arrival time and amplitude. Pulses above a variable software threshold, dependent on the fluctuations of the NSB, are selected (section 6.1.2.1).

The second step (section 6.2, see fig. 6.2) consists of the reconstruction of the showerfront. The arrival times of the Cherenkov light are fitted to a spherical front which is assumed to be emitted from a point in the atmosphere at about 11 km distance in the pointing direction.

6.1 Software-trigger threshold

6.1.1 Selection of the events

The data sample must be "cleaned" before analysis. This includes the rejection of periods where malfunctions of the detector are found and to sort out of the Cherenkov events from the whole data sample, where also events with time calibration purposes (section 4.3.4) and periods of tracking in exploded view mode (see below) are included.

Firstly, we want to prove the correct operation of the heliostat field during data acquisition. The positions of the heliostats have to be refreshed every 3 s in the tracking mode (section 3.1.4). It can happen that the refreshing time is longer than 3 s due e.g. to some communication problem between the control computer and the heliostats (this occurs very seldom, ca. 6 times per year). During analysis a maximum refreshing time of 30 s is allowed once during one period ON-OFF. A period corresponds to 20 min of tracking: 10 min tracking the source (**ON**) and 10 min tracking a position which is 10 min away from the source (**OFF**). According to section 3.1.4, a refreshing time of 30 s introduces an error of 0.17°, which is still smaller than our angular resolution (section 6.2.2) and can be accepted if it occurs sporadically. If the refreshing time has been longer than 30 s during one period ON-OFF, such a period of observation is removed from the analysis.

Secondly, we only want to reconstruct the direction of the Cherenkov events. The regular calibration events have a different label in comparison with Cherenkov events and are rejected at the beginning of the analysis. Besides, there are Cherenkov events which arrived while the heliostats were moving to a new source (typically 30 s between ON and OFF positions of a same source and 30 min between two different sources) and are not considered for analysis. Finally, each night one period ON-OFF of each observed source is tracked with focusing mode OF 2 (section 3.1.4). These periods are not taken into account at this level of analysis, since they

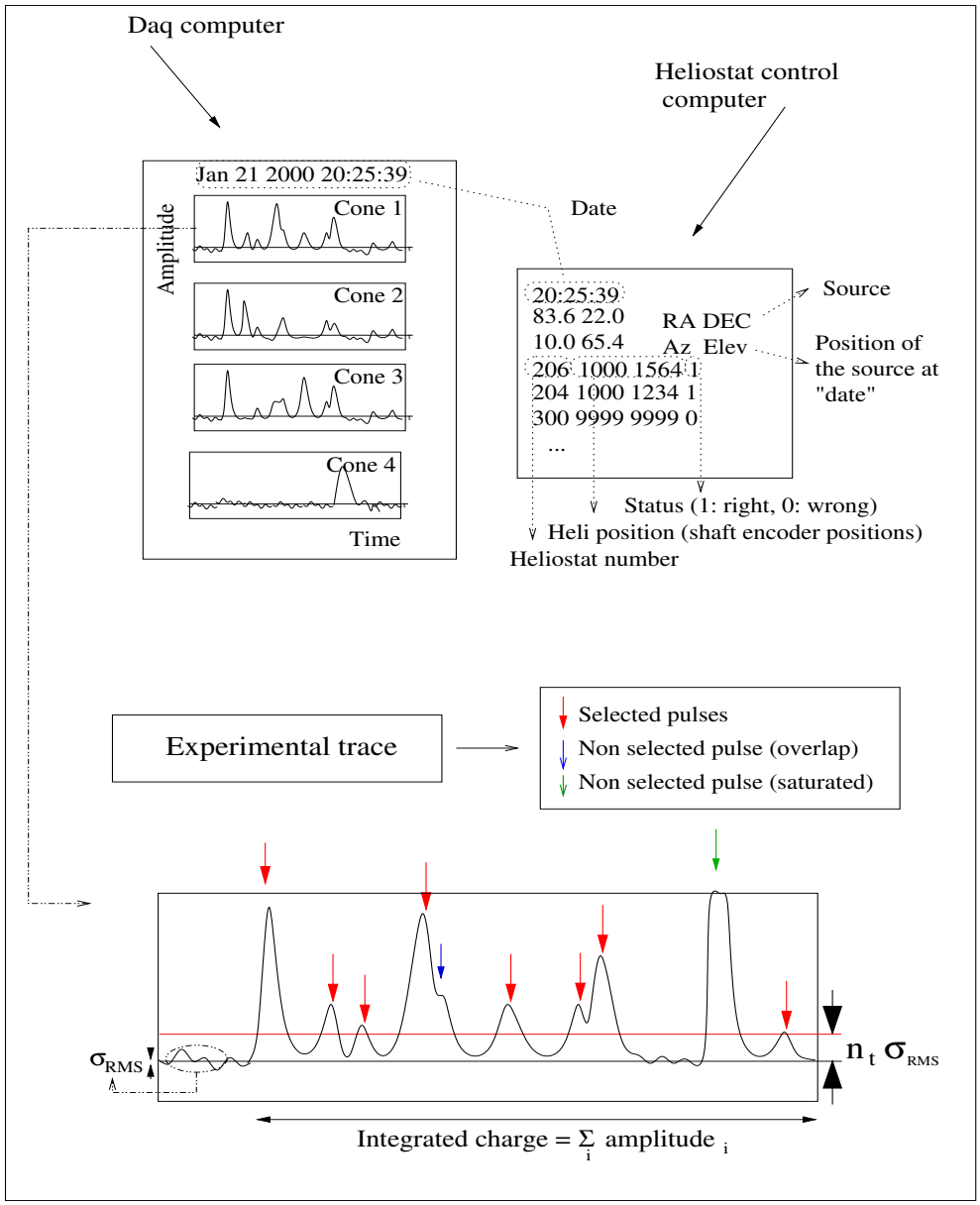

Figure 6.1: *Scheme of the first step of the GRAAL analysis (see section 6.1).*

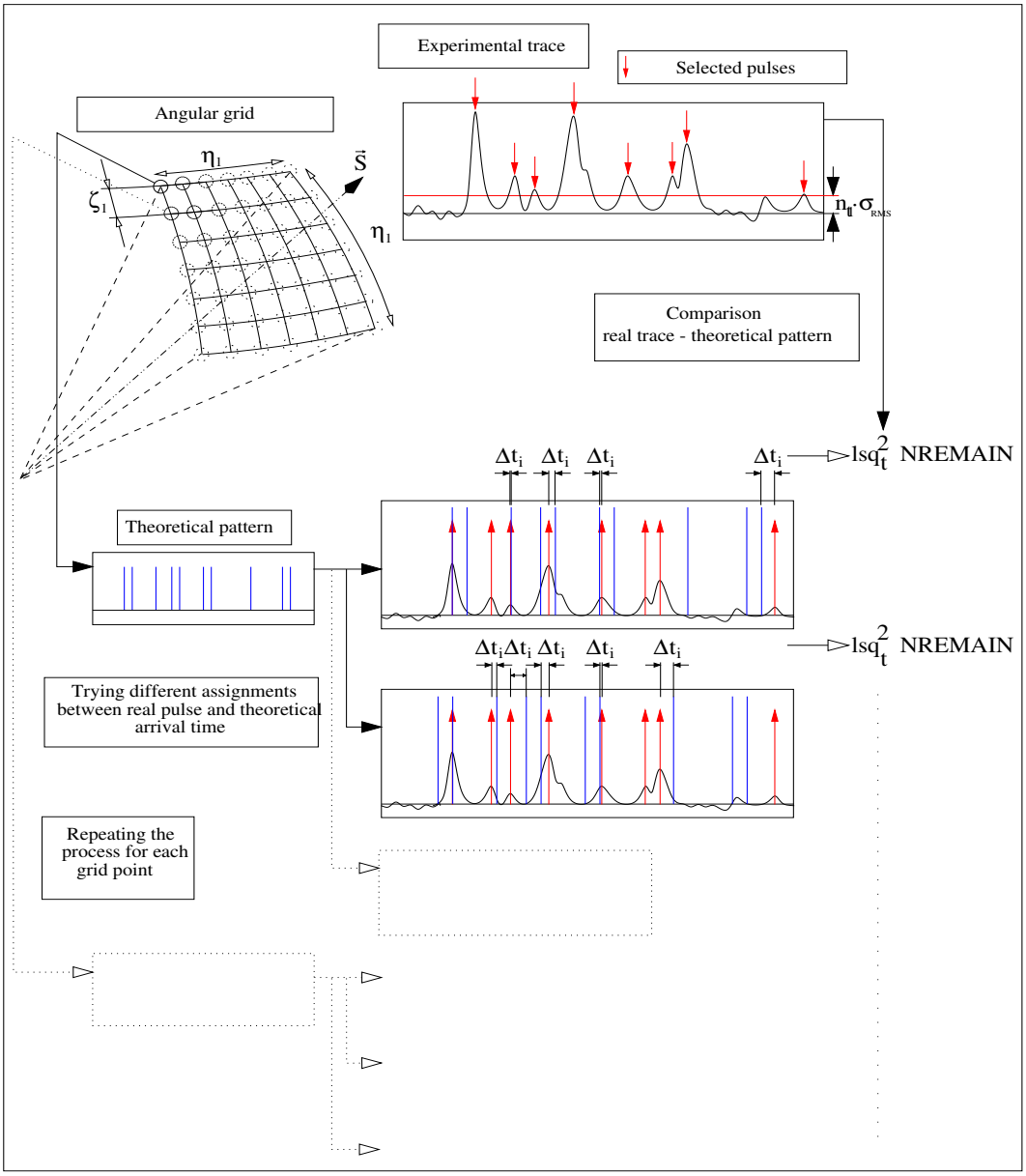

Figure 6.2: *Scheme of the second step of the GRAAL analysis (see section 6.2).*

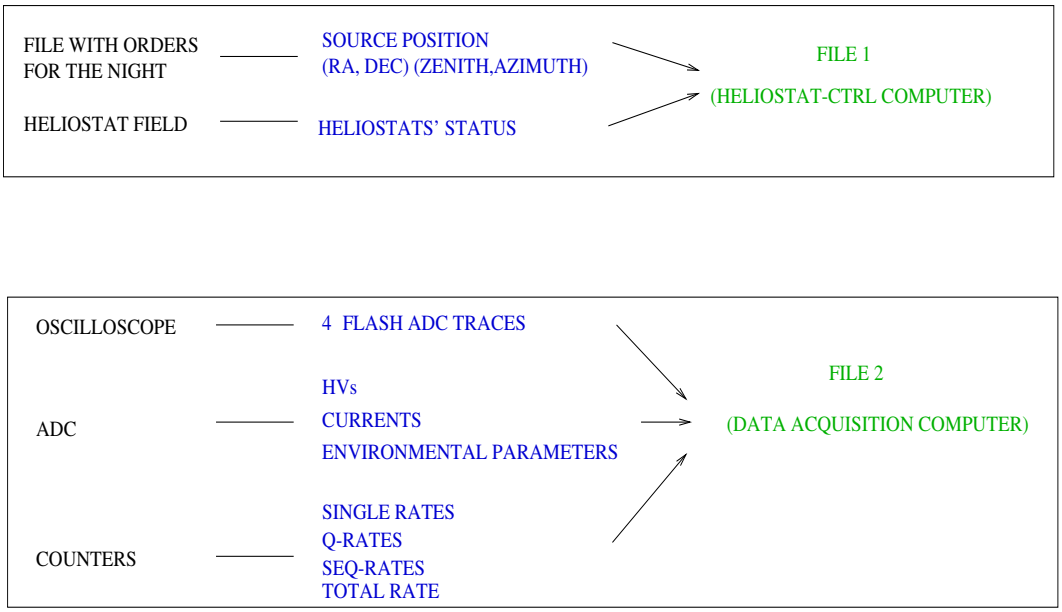

Figure 6.3: *Organization of the data into files. Shown are the devices or files which provide the information (in black, left side of the picture), the kind of information recorded (in blue, middle of the picture) and the computer in which the information is stored (in green, right side of the picture).*

have been recorded for NSB fluctuations and accidentals rate control (section 11.2.1.1).

Fig. 6.3 explains the organization of the recorded information into various files depending on the origin (heliostat control PC or data acquisition PC) and type of information. The arrival time of a Cherenkov event is searched in the heliostat control file to find the source observed at the arrival of the event (given by the right ascension and declination coordinates), the source position in the sky at that time (zenith and azimuth coordinates) and the status and positions of the heliostats. All the information about the event (observed source, position of the observed source, environmental parameters, currents and HVs of the photomultipliers, trigger rates and flash-ADC recorded traces) is read and all the necessary parameters for analysis are written to one single file.

6.1.2 Search for the peaks

We want to sort out the Cherenkov light pulses of the shower from the night-sky background fluctuations. This is not a trivial procedure for several reasons. Firstly, not only the temporal structure of the trace depends on the position of the observed source (section 3.3.2.1), but also the arrival times of the Cherenkov pulses can be shifted from their expected positions. Such a shift can occur due to either the intrinsic Cherenkov timing front fluctuations or to the NSB fluctuations. Secondly, it can happen that an expected Cherenkov pulse is not recorded due to a heliostat failure or that its amplitude is too small to be distinguished from the NSB fluctuations. It can also occur that a NSB fluctuation is intense enough to be mistaken for a Cherenkov pulse. Therefore, all the pulses above a certain threshold (see next section) are selected independently of their position. The pulse arrival time, absence of certain peaks and existence of "fake" peaks will be taken into account in the next step of analysis (section 6.2.2).

6.1.2.1 Software threshold

We are interested in minimizing the difference in energy threshold between the two observed regions of the sky ON (pointing to a source) and OFF (pointing to a test position) (sect. 13.1.3) caused by slightly different levels of night-sky background. Therefore, a variable threshold, dependent on the NSB fluctuations of each trace, was chosen (section 11.3.2). The software threshold for a Cherenkov pulse amplitude was set at $n_t \times \sigma_{NSB}$, where n_t is a fixed number for each sample of data and σ_{NSB} represents the RMS fluctuations of the NSB.

The σ_{NSB} was estimated from the portion of the trace where no Cherenkov signals are expected (in our case, the first 40 ns of the trace were chosen). The σ_{NSB} was calculated for each event and cone individually.

The value of n_t was typically between 5 and 7 (section 12.1) and it was chosen as a value as low as possible to avoid a large number of NSB induced "fake" signals in the sample. The lowest possible value of n_t was found to depend on the source position due to the varying temporal overlap of signals in the trace (see fig. 6.4).

With a variable threshold the events taken on a noisy region of the sky are analysed with a higher effective software threshold than the events taken on a region with smaller fluctuations of the night-sky background. A possible worsening of the reconstruction efficiency due to large time fluctuations in the Cherenkov peaks in a noisy region of the sky (the fluctuations increase with the level of NSB) is prevented by choosing peaks with larger amplitudes, which are less influenced by the NSB fluctuations.

Section 11.3.2 explains the effects of a variable threshold in the analysis.

6.1.2.2 Determination of the arrival time and amplitude of the Cherenkov pulses

Previous to the determination of the arrival time and amplitude of the Cherenkov peaks two corrections must be made on the traces. The first one consists of subtracting the amplitudes of the trace due to the reflection of pulses in the cables (section 4.5). The second one consists of shifting in time of the traces 2-4 with respect to the first to eliminate the time delay due to the different high voltages of the corresponding photomultipliers (section 4.3). In addition, a delay of 16 ns is applied to cones 1 and 2 to compensate for an extra cable of that length which communicates the PMTs of cones 3 and 4 to the electronics.

To determine the arrival time of a peak, the channel of maximum amplitude is searched in the flash-ADC recorded full pulse shape. Peaks arriving closer to each other than 6 ns are excluded to avoid a bias from overlapping pulses. The reconstruction of the full pulse shape of saturated peaks is necessary to determine their arrival time. This is a complicated procedure since for saturated amplitudes it is difficult to determine if two or more peaks overlap. Therefore saturated peaks have not been considered in the analysis.

6.1.3 Determination of the integrated charge

The integrated charge (IC) of a Cherenkov shower is related to the energy of the primary particle since the energy is proportional to the number of photons of the shower [88] and the number of photons can be obtained from the integrated charge according to the calibration of section 4.4.

The sum of the base-line corrected amplitudes of all the channel-contents in the trace between 100(200) ns before the arrival of the first peak above threshold and 100(200) ns after the arrival of the last peak above threshold gives the value for the integrated charge for cones 1-2(3-4) respectively.

6.2 Reconstruction of incoming shower direction

6.2.1 Calculation of the theoretical pattern

The expected arrival times for all heliostats in each of the four cones were calculated and stored in a "library" for a 5×5 degree grid. It can happen that the showers are reconstructed preferentially in the centre of the grid. Therefore, if the grid is centred on the pointing position there will be an "artificial" bias towards "correct pointing". This is prevented by placing the centre of the grid 1 degree away from the pointing direction of the heliostats. The position of the centre of all the heliostats was calculated for the pointing position, due to the dependence of the mirror centre on the pointing position and the type of heliostat (section 4.2), and used throughout the grid.

For the calculation of the expected arrival times of the Cherenkov pulses, a spherical shower front was assumed to propagate from the maximum of a point-like shower at a penetration depth of 230 g/cm^2 (the mean penetration of showers induced by a photon of 100 GeV, ca. 11 km over the ground) in the pointing direction. Tests with plane and parabolical timing fronts showed that while the former leads to worse fits to the timing data, the latter does not improve the quality of the fit significantly.

As an example, fig. 6.4 shows the calculated theoretical pattern for all 4 cones in three different positions.

6.2.2 Matching of the theoretical and the experimental patterns

The measured arrival times are compared to the calculated "library" (see previous section). The time difference TIMEDIFF is defined as

$$\text{TIMEDIFF} = (\text{measured arrival time}) - (\text{nearest expected time from the library}) \tag{6.1}$$

In each point of the angular grid, the total expected time pattern is shifted in time with respect to the experimental pattern. This is done due to the uncertainty about the time at which the event was triggered. For example, it might happen that the first expected peak is not detected and consequently the first experimental peak has to be identified with the second expected peak. The SHIFT parameter is defined as the difference in time between the arrival time of the first peak and the time at which the first peak is expected. For each value of SHIFT the TIMEDIFF for all peaks and a least squares sum "lsq_t^2" defined as

$$\text{lsq}_\text{t}^2 = \sum_\text{i} (\text{TIMEDIFF}_\text{i})^2 \tag{6.2}$$

are calculated. For each point of the angular grid the value of SHIFT which gives the minimum lsq_t^2 is chosen. The direction (or point of the grid) yielding the smallest "lsq_t^2" is chosen as the final reconstructed direction of the shower. The initial resolution of the grid is 0.5 degrees. For the final direction the resolution is inferred as the position of the minimum of a quadratic fit to lsq_t^2 values of the four grid points adjacent to the one with smallest lsq_t^2.

There is a possibility that spurious pulses induced by the night-sky background, afterpulsing in the PMTs or due to cross talk between the subfields manage to pass the software threshold (section 6.1.2.1). These pulses do not fit into the correct timing pattern and bias the fit. Therefore up to n peaks with TIMEDIFFs above 5 ns were allowed not to be taken into account in the calculation of the lsq_t^2. The value of n was chosen as 5 for all the analyses discussed in chapter 12.

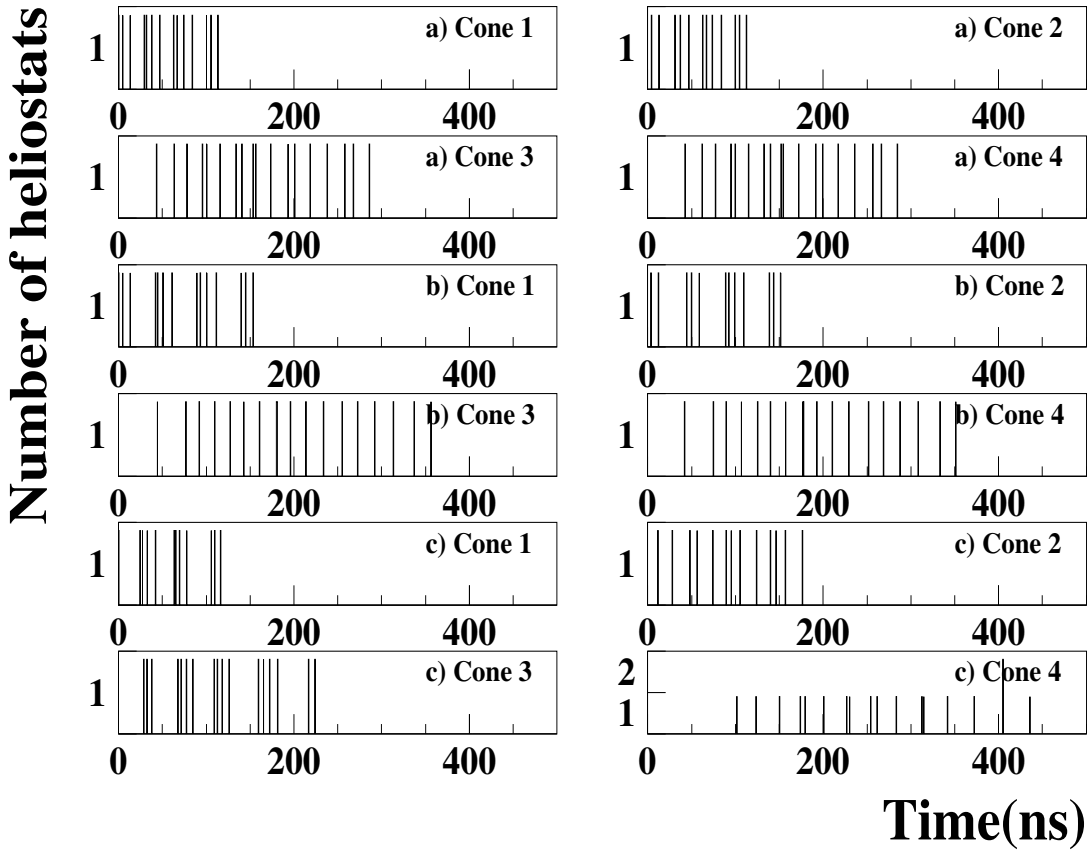

Figure 6.4: *Theoretical arrival times of the Cherenkov pulses for 3 different incoming directions: a) zenith = 10 degrees, azimuth = 0 degrees, b) zenith = 30 degrees, azimuth = 0 degrees and c) zenith = 30 degrees, azimuth = 45 degrees (see appendix B for azimuth convention). For the configurations a. and b. the pattern is quasi-symmetric with respect to the north-south direction (see very similar pattern for cones 1 and 2, and 3 and 4 respectively). In addition, there is a change in the pattern when going from zenith = 10 degrees (a.) to zenith = 30 degrees (b.). The situation is completely different for panels c., where all the cones have very different time patterns (having the same zenith angle as the direction of panels b.).*

Fig. 6.5 shows projections of the angular reconstructed directions both for ON and OFF source directions for a large data sample. The origin corresponds to the pointing direction determined by the heliostat tracking. A combined fit is performed with a Gaussian for the events reconstructed near the centre and a linear function for the "smooth background" extending to large off-axis angles.

The directions of events in this "smooth background" were found to be systematically misreconstructed. These events have a systematically lower number of reconstructed peaks (close to the imposed software cut of 5 peaks in section 13.1.2) and lower lsq_t^2 than the "central" events because the incorrect reconstructed direction allowed incorrect "heliostat-measured signal" assignments. A wrong assignment of the signals for showers with a large number of peaks leads to values of lsq_t^2 which do not pass the software lsq_t^2 cut ($lsq_t^2 \leq 100$ from section 13.1.2). Therefore, a stricter software cut in the number of peaks (e.g. number of reconstructed peaks $\geq$10) rejects all the showers with misreconstructed directions which lie on the tails of fig. 6.5 (see fig. 8.1 in section 8.1).

If the "misreconstructed directions" are excluded, the angular resolution σ_{63} (the opening angle within which 63% of the events are contained) is 0.7° (see sections 7.2.2 and 8.1 for a detailed treatment of the angular resolution).

6.2.3 Calculation of the shower core on the ground

The distribution of light of a gamma-ray shower on the ground follows a circular structure of regular intensity up to a radius of $\approx$ 120 m. At longer core distances, the light intensity begins to fall steeply with the distance from the core, independently of the gamma-ray energy (section 7.1.4). Then, using the amplitude information recorded by the flash-ADCs it should be possible to reconstruct the position of the shower-cores of individual showers on the ground.

To determine the centre-of-gravity of the light distribution, different light-gathering efficiencies of the heliostats due to different distances to the tower, mirror quality etc. were first corrected via normalizing the amplitudes over many showers. It was verified that the mean of the centre-of-gravity over all detected showers lies at the geometrical centre of the used field within 1 m so that the assumption of a "fixed core" (section 6.2.2) at this position introduces no bias. This is mainly due to the restricted field of view of our detector, which selects only a part of the ring (section 10.2.2).

From the Monte-Carlo data it was found that the mean deviation of the real shower core from the shower core reconstructed from the amplitude information for each individual shower was about 30 m. This deviation is larger than the deviation of the real shower core from the "fixed core" due to the rather compact size (section 2.3.3.2) of our field, the showers with a real core near the field boundaries will not be detected in general due to the "convergent view" configuration and the restricted field of view (section 10.2.2). Therefore we assumed that all shower cores lie at the "fixed core" in the reconstruction algorithm.

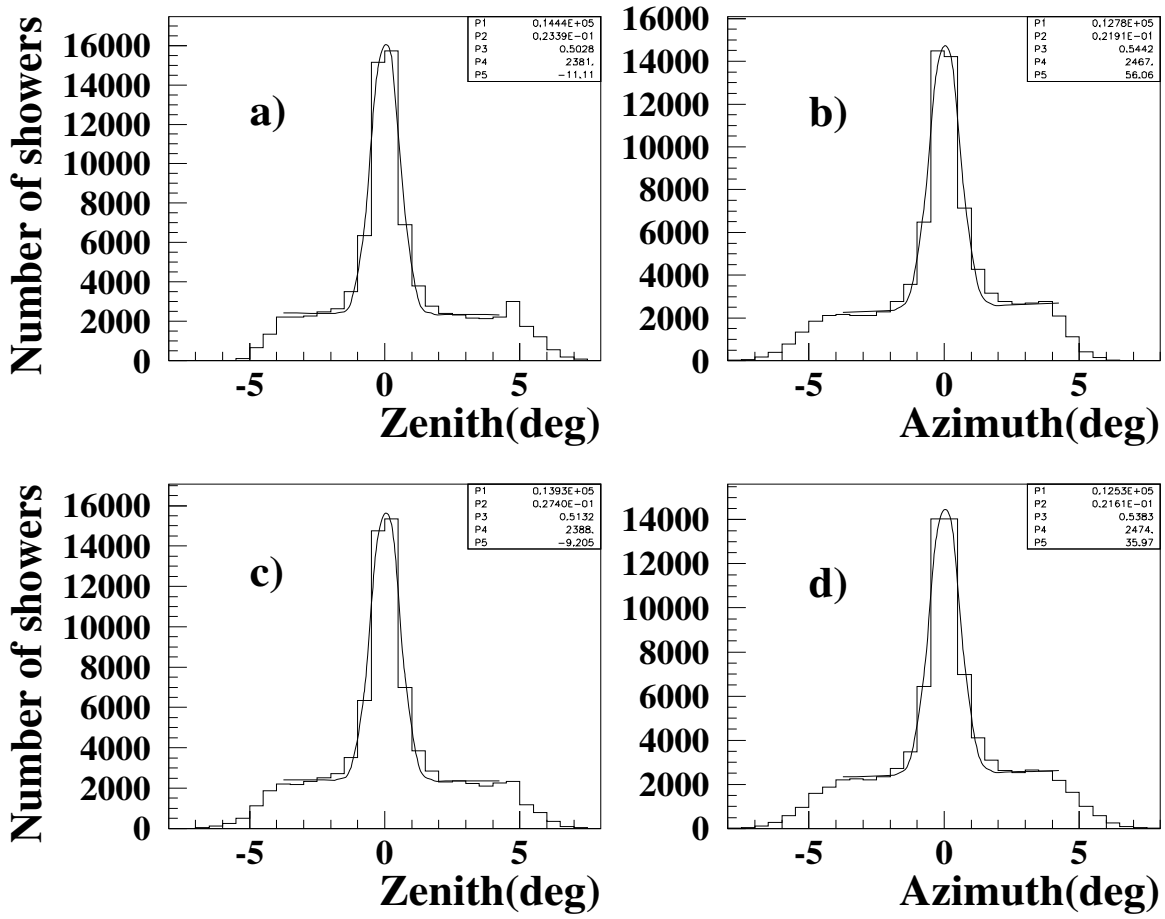

Figure 6.5: *Projections of the number of showers as a function of shower directions as reconstructed from the timing data. Shown is the deviation of the reconstructed direction from the pointing direction on the elevation-axis (left two panels a. and c.) and azimuth-axis (right two panels b. and d.). The origin then corresponds to the pointing direction as determined by the orientation of the heliostats. Two components are apparent: a peak near the origin, and a "flat background" corresponding to events misreconstructed in direction (see text). The data sample comprises of 32 hours of ON-source time on the Crab pulsar (upper panels a. and b.) and an equal amount of OFF-source time (lower panels c. and d.) taken under variable weather conditions in the season 1999/2000. The "Gaussian plus linear function" fit is performed to each subsample. The parameters of the fit are indicated in the figure:* **P1, P2, P3** *- height, mean and sigma of the Gaussian;* **P4, P5** *- constant term and slope of the linear function. It is seen that the Gaussian -corresponding to successfully direction reconstructed events - is always centred within* $< 0.05°$.

Chapter 7

Gamma-hadron separation

At the lowest energies of the Very High Energy (VHE) electromagnetic spectrum (between about 10 GeV and 30 GeV) the satellite detectors reach good sensitivities because they are able to reject very efficiently hadrons with anti-coincidence counters (section 2.1). However, the satellites are limited to the detection of relatively high gamma-ray fluxes due to their small collection area. Presently, the ground-based Cherenkov detectors, with effective areas of $\mathcal{O}(10^4)$ m, have proven to be the most efficient detectors at energies between 300 GeV and 10 TeV (section 2.3.2). One of the main difficulties in observing gamma-ray sources in ground-based Cherenkov experiments is the large hadronic background (see footnote 3 of chapter 2). Since all the cosmic ray particles produce extensive air showers, an effective gamma-hadron separation technique (that increases the signal-to-noise ratio) is crucial to improve the detector sensitivity.

Up to now, the most successful method to reject the hadronic background is the "Imaging Technique" for Air Cherenkov Telescopes (ACT), first proposed by M. Hillas [113], developed to technical perfection by the Whipple collaboration and used since 1989 when the first detection of gamma-rays from the Crab nebula at a high significance level was presented by the former collaboration [234]. The Imaging technique consists of parametrizing the "image" (2-dimensional light distribution) of a Cherenkov event (recorded by an ACT camera consisting of a square matrix of fast PMTs) into the so-called "Hillas parameters" - mainly classified in *image shape* parameters (called "Length" and "Width") and *image orientation* parameters (called Azwidth and Alpha) [113]. The image that results from a typical gamma-ray shower is elliptical and compact (smaller Length and Width) with an orientation that points towards the centre of the field of view (smaller Azwidth and Alpha) in comparison with the hadronic cosmic ray showers, which are much less regular, extended and randomly oriented in the focal plane. Current imaging cameras are capable of rejecting more than 99.7% background while keeping 50% of the gamma-ray signal (for a review of the imaging technique, see e.g. [82] and [175]).

The wavefront sampling technique has been developed as an alternative to the Imaging technique (see section 2.3.3). The "sampling" of the Cherenkov light is done by multiple detectors using fast timing techniques. The background rejection is accomplished by improving the angular resolution through fast and accurate timing of the wavefront arrival time at several independent reflectors, located within the Cherenkov light pool of individual showers. In addition, time and amplitude parameters may be used to obtain a partial discrimination of the hadron showers at the hardware level. Experiments using the wavefront sampling technique usually have a "camera" made up of one photomultiplier for each reflector, and therefore they can not apply the Imaging technique.

Other hadron rejection techniques like spectral separation, or methods based on fractal

parameters of the Cherenkov images are used or studied by different experiments [195, 107, 203].

In GRAAL the imaging technique can not be reasonably applied and therefore we have studied the possible exploitable differences between gamma- and hadron-originated showers for wavefront samplers (section 7.1 and subsections) and the methods to profit from such differences and obtain an efficient hadron rejection (section 7.2 and corresponding subsections).

7.1 Characteristics of the cosmic ray showers

7.1.1 Time showerfront

The most promising hadron rejection method for the heliostat arrays is the one based on the temporal characteristics of the showerfront. The reason is that the arrays can profit from the measurement of the arrival times of the Cherenkov signals in various points distributed over a large area ($\approx 200\times70$ m^2 for GRAAL) with an excellent time resolution (for example, 1 ns in CELESTE [68] or 0.5 ns in GRAAL (section 3.3.3)) which is larger by more than an order of magnitude compared with the one of the imaging telescopes (e.g. 8.3 ns in the stereoscopic HEGRA system [111]).

The wavefront of an electromagnetic shower has a clear spherical shape when all the Cherenkov emitted light is recorded by the detector (section 10.2.3 explains the problems of recording only a part of the emitted light, e.g. for experiments with a restricted field of view). The more irregular development of a hadronic shower, composed by many sub-showers, compared to a gamma-ray shower (see following sections) produces a large scatter in the arrival times of the Cherenkov light on the ground [52] (see also panels b. of figs. 10.5 and 10.6 in chapter 10). Therefore, the difference between the spherical narrow showerfront of a gamma shower and the more fluctuating front of a proton shower can provide a method for the discrimination of proton showers. Section 7.2.1 describes the study made with MC simulated showers and real data to find out the efficiency of such a method.

7.1.2 Incoming direction

An important method to discriminate gamma-ray and proton induced showers is given by the incoming direction of the Cherenkov shower. The uncharged gamma-rays emitted by the sources follow straight lines on their way to earth (we observe only point-like sources). In addition, because of the large energies of the primaries (gamma-rays and hadrons) involved in the production of Cherenkov airshowers, the secondary particles are strongly beamed in the forward direction and, on average, retain the directionality of the primary [233]. Therefore, it is possible to track back the path followed by the gamma-rays and infer the source position. In contrast, the charged cosmic rays (e.g. protons) are deflected by the galactic magnetic fields on their way to earth and the final distribution of hadronic primaries is isotropic (this is reflected in the distribution of the airshowers generated by them).

Hence, all the showers which do not arrive from the direction of the observed source within the angular resolution can be rejected. The increase of the angular resolution of the experiment permits a stricter cut in the acceptance of showers according to their incoming direction and therefore a higher reduction of hadronic background can be achieved. Section 7.2.2 explains the application of this hadron rejection technique in the case of GRAAL.

7.1.3 Shape of the Cherenkov pulses

The shape of the Cherenkov pulses can carry information about the primary species. The rise time reflects the longitudinal growth of the cascade in the atmosphere while the decay time exhibits the cascade attenuation past the shower maximum and the FWHM is a measure of the Cherenkov photon production profile [52, 79, 85]. Monte Carlo simulations indicate that the pulses from proton showers have longer rise and decay times than those from gamma showers. In addition, the former can present a superimposed microstructure due to Cherenkov light produced by single muons moving close to the detector system [3, 195].

Besides all the MC simulations, there is also an experimental work where the detection of the Crab nebula at a 4.35 significance level at TeV energies is reported after an analysis of extensive air showers which utilizes the temporal profiles of the Cherenkov pulses for gamma-hadron separation [224].

If the predicted differences in the pulse shape parameters are measurable for GRAAL, the signal-to-noise ratio can be improved. Section 7.2.3 studies this possibility.

7.1.4 Density of light on the ground

The distribution of Cherenkov light from gamma-ray showers at ground level is determined mainly by the Cherenkov emission angle θ_c and by multiple Coulomb scattering of the charged shower component over some hundreds of metres from the impact point [82]. The focusing of Cherenkov photons from a large range of heights, over which the product of height and Cherenkov angle ($h\theta_c$) is approximately constant produces a characteristic hump at a distance of about 120 m from the core at the altitude of GRAAL, 505 m a.s.l. (the position of the hump is independent of the gamma-ray energy over a large range of energies). In the case of proton primaries, the larger particle transverse momentum spread and a higher penetration into the atmosphere (the interaction length of protons and mesons in the air is 80 g/cm^2, compared to about 38 g/cm^2 for photons [82]) produce lateral distributions which show an irregular structure on the ground without any noticeable hump [193]. In addition, since the number of charged particles which emit Cherenkov light is about 3 times smaller for proton showers in comparison with gamma showers at the shower maximum, the former must have a greater initial energy so that they produce the same amount of light than the latter.

Fig. 7.1 shows the circular structure of the light distribution on the ground for gamma showers in comparison with proton showers. Three detection configurations are shown:

- **Without restrictions** (upper panels (a. and b.) of figure 7.1): all the Cherenkov light generated by the airshowers is detected, i.e., the effect of the detector is not simulated.
- **Restricted field of view and parallel view** (middle panels (c. and d.) of figure 7.1): only Cherenkov photons arriving within a field of view of 0.6 deg (full opening angle) are detected. The heliostats point to the source position (parallel view, see fig. 3.6).
- **Restricted field of view and convergent view (GRAAL configuration)** (lower panels (e. and f.) of figure 7.1): this configuration is similar to the previous one but the heliostats point to the origin of the airshowers in the atmosphere, around 11 km above the ground (convergent view, see fig. 3.6). The convergent point is the position in the sky from which the projection on the ground lies on the centre of gravity of the heliostats used.

For the gamma-ray shower the mentioned circular structure is clearly seen in the first configuration, when all the Cherenkov photons are detected (see panel a. of fig. 7.1). Three components are apparent, a circle extending from the impact point to a distance of about 120 m

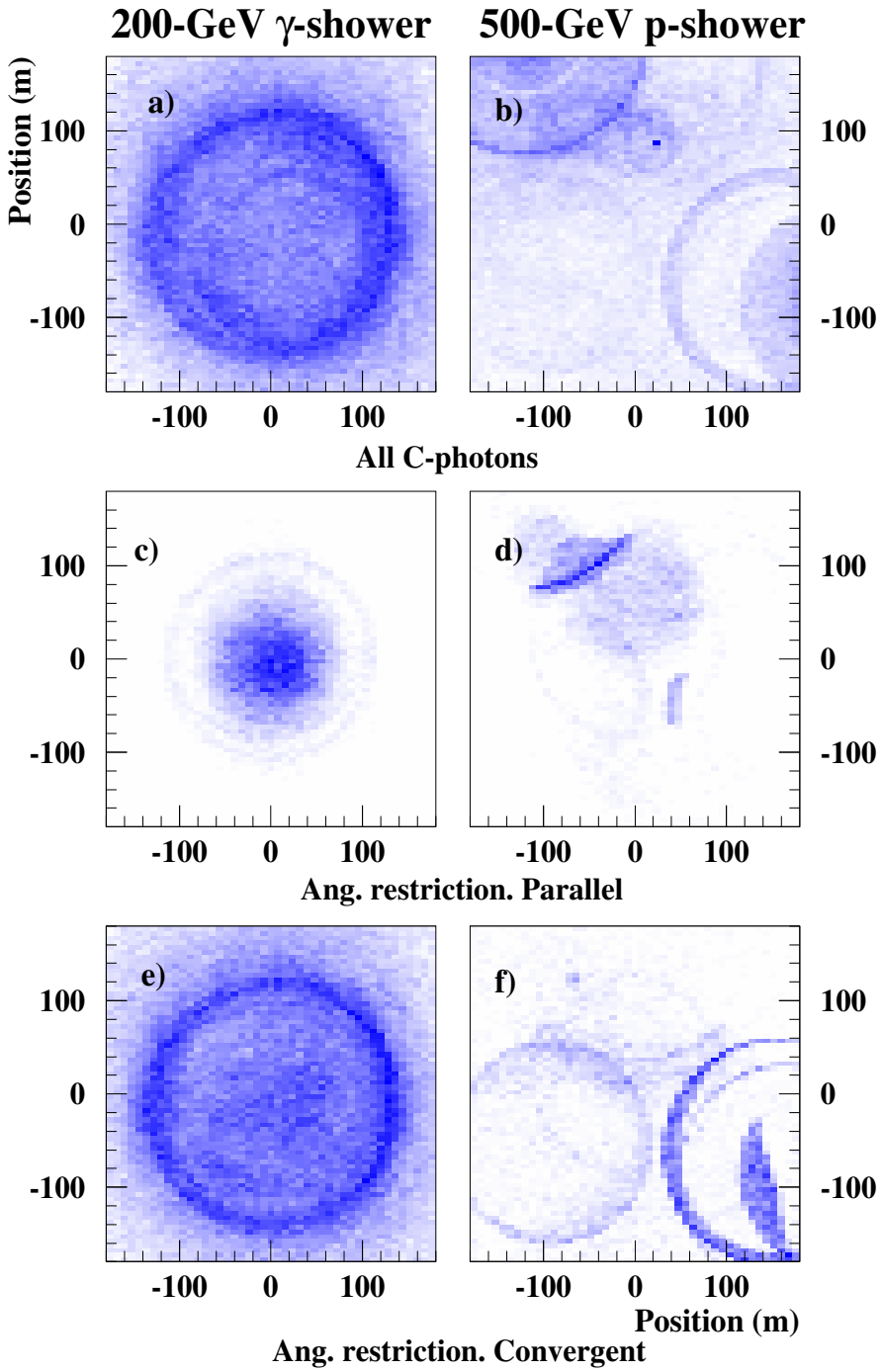

Figure 7.1: *Typical distributions of Cherenkov light detected at ground observation level (505 m a.s.l. for GRAAL). The showers were MC generated by a gamma-ray (panels a., c. and e.) and a proton (panels b., d. and f.) vertically incident with the core situated on the centre of the array. The grey scale is linear in number of collected photons, the maximum intensity being the maximum number of collected photons (the same scale is used in all of the panels). See text for explanation of the different configurations. Taken from [32].*

Configuration	gamma 200 GeV	p 500 GeV	gamma 1000 GeV	p 2000 GeV
All light	0.09	0.34	0.07	0.20
GRAAL	0.42	0.63	0.47	0.51

Table 7.1: *Expected fluctuations in the collected Cherenkov light when ALL the light is collected (first row) and for GRAAL detector (second row).*

with relatively constant luminosity, a disk which is about twice as luminous as the internal circle extending from 120 m to 130 m and a faint distribution of light which extends from the hump to some hundreds of metres but becomes rapidly undetectable due to the decreasing luminosity with distance. In contrast, the proton shower exhibits an irregular structure (see panel b. of fig. 7.1).

The prominence of the hump reduces as the energy of the gamma-ray increases since higher energy electrons penetrate deeper into the atmosphere, increasing the contribution to Cherenkov radiation from electrons at lower altitudes where $h\theta_c$ starts decreasing [32].

Borque [32] studied the possibility of using the differences of the light distribution on the ground to discriminate gamma-ray and proton originated showers in the GRAAL detector. For showers with an impact point in the centre of the array the circular structure of the gamma showers is still seen in the GRAAL configuration (see panel e. of fig. 7.1). However, the fluctuations in the Cherenkov light among gamma showers increase significantly under the conditions of GRAAL approaching the fluctuations of hadronic showers (see table 7.1). This is mainly due to the restricted field of view of the detector, that converts in "irregular" the light distribution of showers far from the core (section 10.2.2). In short, the restricted field of view together with the convergent view maximize the detection efficiency near the aiming point of the heliostats, but for low altitudes the efficiency decreases rapidly since the heliostats far away from the core do not see the light (see section 10.2.2). Therefore, large shower cores produce an irregular distribution on the ground also for gamma showers and hamper any efficient hadron rejection for the GRAAL detector (see fig. 10.4 in chapter 10).

The hadronic rejection making use of the light distribution has not been tried with real showers due to the hopeless results from the Monte Carlo simulation.

7.1.5 Muon component

A cosmic ray induced air shower has three components, hadronic, leptonic and electromagnetic one. During the development of the hadronic component lower energy charged pions and kaons decay to feed the muonic component. Cabot et al. [38] proposed to exploit the Cherenkov light produced by muons to identify showers induced by hadrons of energies above several TeV. The idea is that the light from muons observed at a distance of a few tens of metres from the EAS core arrives several ns before the main signal produced by electrons and positrons and therefore it can be identified.

GRAAL faces two problems when trying to identify hadronic showers from their muonic component. The first one is the low probability of detecting a muon due to both the small number of muons per shower for low energy showers (calculated as less than 10 muons for a 500 GeV shower and less than 2 muons for a 100 GeV shower [68]) and the small detected fraction (5-10%) of the light emitted by a muon due to the restricted field of view of the heliostat arrays [68].

	Mean	Sigma
Gammas	0.07E-2 ± 0.46E-2	0.935 ± 0.005
Protons	-0.37E-2 ± 0.42E-2	0.886 ± 0.004
Experimental data	3.55E-2 ± 0.59E-2	1.185 ± 0.007

Table 7.2: *Mean and sigma of a Gaussian function fitted to the TIMEDIFF distribution for MC simulated gamma-ray and proton induced showers and for experimental showers for the data sample shown in fig. 7.2 (see text for discussion).*

De Naurois [68] estimates the probability of detection of a muon falling on the heliostats array in less than 10% for CELESTE. In GRAAL this probability is somewhat higher than for CELESTE due to the compactness of the field (sect. 2.3.3.2) but still too low (less than 20%) to provide an efficient hadron rejection mechanism (the probability of muon detection would have to increase to ca. 90% for an acceptable quality factor).

The second problem is that GRAAL records all the light pulses from the heliostats "seen" by a cone in one trace (see fig. 3.13) and therefore it is difficult to distinguish the hypothetical muon pulse from a certain heliostat from a real Cherenkov light pulse of a different heliostat. These two drawbacks prevent an efficient gamma-hadron discrimination based on the muonic component of the hadronic showers.

7.2 Hadron rejection techniques

7.2.1 Time showerfront

GRAAL measures with great accuracy the arrival times of the Cherenkov signals to the PMTs due to both the fast electronics and the high resolution of the digital oscilloscope (500 ps). This fact together with the mentioned properties of the temporal showerfront of Cherenkov EAS (section 7.1.1) should allow an efficient gamma-hadron separation method. We studied in detail two parameters related to the time properties of the showers, namely, the value of lsq_t^2 (which gives a measure of the "goodness" of the fit to a spherical showerfront, section 6.2.2) and the distribution of lsq_t^2 in the angular region around the reconstructed direction.

7.2.1.1 Deviation of the experimental shower front from an ideal sphere

According to section 7.1.1 and panels b. of figs. 10.5 and 10.6 the fluctuations of the showerfront with respect to an ideal sphere are much larger for proton- than for gamma-ray induced showers. Then, the deviation of the measured arrival times from the ideal spherical showerfront for the optimal fitted direction (given by the parameter TIMEDIFF of section 6.2.2) can be used to discriminate gamma-ray from proton induced showers. The distribution of the time deviations must be broader for protons and thus, a cut in the width of the distribution rejects a fraction of the hadronic showers. Fig. 7.2 shows the mentioned distribution for MC simulated gamma-ray and hadron induced showers.

The fit of the central peak to a Gaussian function gives the "width" of the showerfront (see table 7.2). The time deviation peak is well centred for MC showers and also for experimental data. The width of the peak (given by the sigma of the Gaussian) is slightly higher (0.05 ns) for gammas than for protons, this difference being completely negligible for our time resolution. For experimental showers, the peak is 0.3 ns broader, which is again negligible considering the

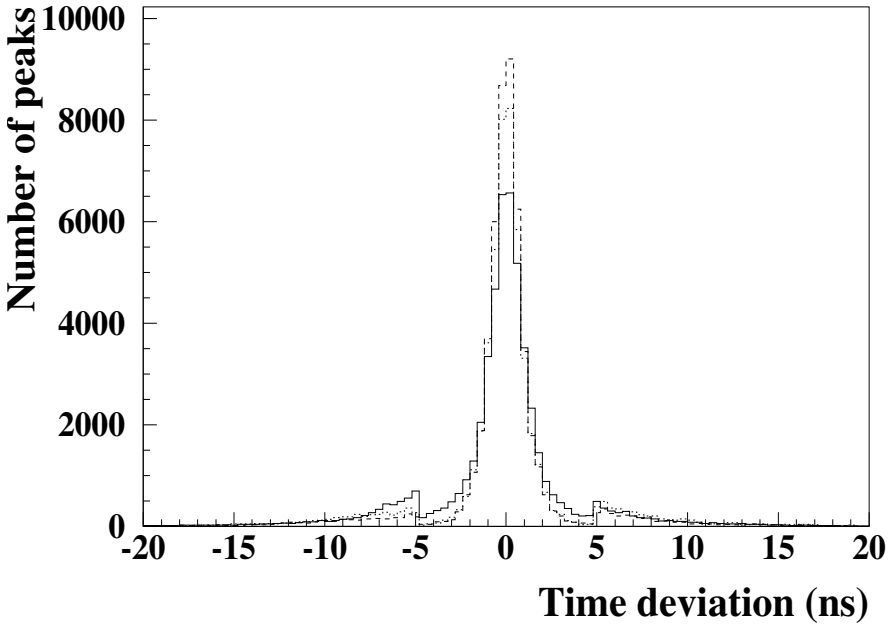

Figure 7.2: *The deviation of measured arrival times from the final fitted spherical shower front for MC gammas (full line), protons (dashed line) and experimental data (dotted line). The visible sharp reduction of events with a time deviation somewhat smaller than 5 ns is due to the fact that the reconstruction program allows the exclusion of 3-5 peaks with a deviation from the shower front larger than 5 ns (see section 6.2.2) from the final fit. The distributions have been normalized to the number of peaks of the experimental data.*

differences of the simulation with the real detector (chapter 5). The narrowness of the peak means that the times are very close to the theoretical sphere, not only for gamma-induced showers (as expected) but also for proton-induced showers. The same effect, narrowness of the shower front, is observed in the lsq_t^2 distribution (see fig. 7.3).

We find that the predicted smooth spherical showerfront for the arrival times of gamma-ray showers [52] is well reproduced by the MC data. However, the expected showerfront for protons, irregular and with large fluctuations far from the core, is not found in our MC sample. In contrast, the protons have a surprisingly smooth and narrow showerfront, caused by the restricted field of view of the detector (section 10.2.3). Hence, a hadron rejection by means of large fluctuations in the arrival times of the Cherenkov pulses with respect to a spherical front is not efficient.

7.2.1.2 Lsq_t^2 sampling

Although the method explored in the previous section fails for gamma-hadron separation (gammas and protons have both narrow spherical showerfronts), there can be still a difference between both primaries in the "lsq_t^2 map", i.e., in the distribution of lsq_t^2 values around the final fitted shower direction. The hadron rejection method explored in this section is closely related to the

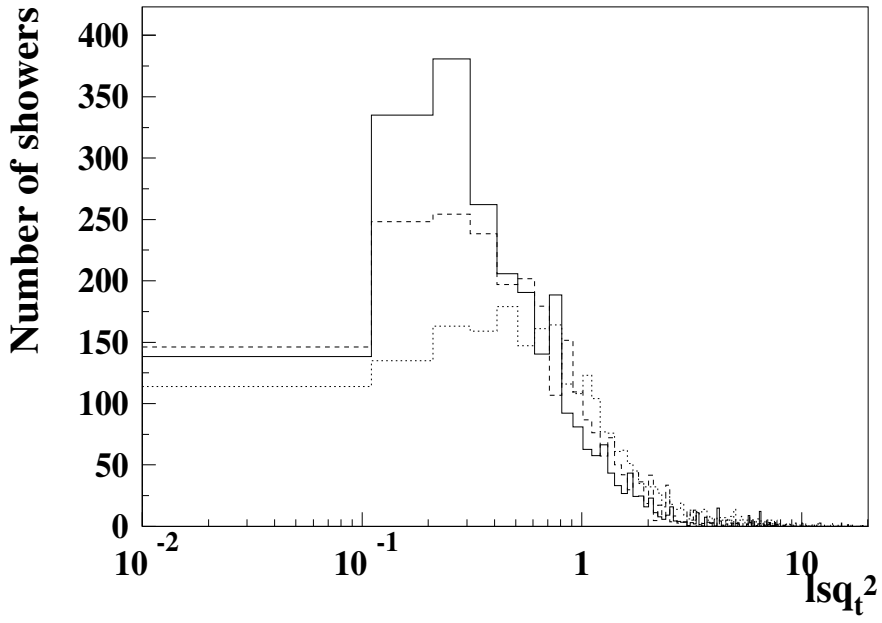

Figure 7.3: *Distribution of lsq_t^2 for MC simulated proton (dashed line), gamma (full line) and experimental showers (dotted line). The total number of showers was normalized to the experimental data for comparison.*

procedure used for shower reconstruction in GRAAL (sections 6.2.1 and 6.2.2) (see below). The idea is the following: gamma-ray induced showers have a narrow, spherical shower front. Then, as we move away from the real direction of the shower, we expect a progressive increase of the lsq_t^2 values due to the shift of the experimental time pattern with respect to the theoretical pattern. On the other hand, the time front of proton showers (initially wide) becomes narrow with the restricted field of view (see previous section and section 10.2.3). In this case, since the hadron shower is composed of many sub-showers, it can happen that for some directions (apart from the real one) a sub-shower is fitted and consequently the lsq_t^2 of the fit is a local minimum in the lsq_t^2 map. In short, we expect a lsq_t^2 map with one single minimum for gamma-ray induced showers but some local minima for proton-showers.

During the reconstruction of the incoming direction of a shower, the lsq_t^2 of the fit of the time front to a spherical front is calculated in all the positions of a $5\times5^\circ$ grid centred 1° away from the pointing position with 0.5° resolution (section 6.2.2). The incoming direction of the shower is chosen as the position of the grid with minimum lsq_t^2. We studied the distribution of lsq_t^2 values around this minimum to find differences between gamma-ray and hadron originated showers (see fig. 7.4).

In a qualitative way, by looking at many proton and gamma showers, we observed that the smoothness[1] of the lsq_t^2 map is independent of the shower primary and depends only on the number of peaks which have been reconstructed. For showers with a large number of

[1]We define the lsq_t^2 map as smooth if there is a gradient of lsq_t^2 towards the minimum, whereas a "non-smooth" map will present a "bumpy" structure, with local minima.

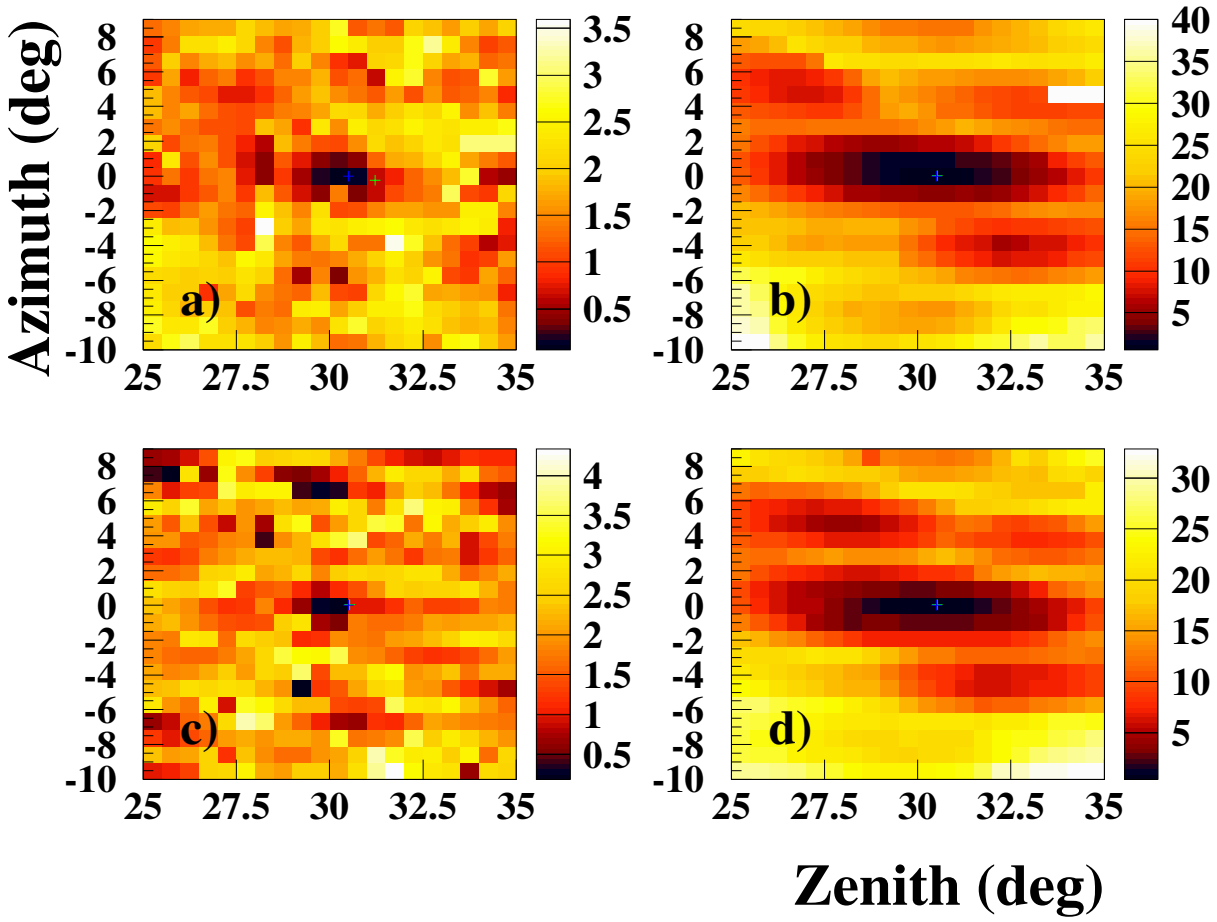

Figure 7.4: *Map of lsq_t^2 for hadronic (upper panels a. and b.) and gamma-ray (lower panels c. and d.) showers. Left panels (a. and c.) show two showers with 10 reconstructed peaks and right panels (b. and d.) show two showers with 50 reconstructed peaks. The blue cross indicates the reconstructed incoming direction and the green cross the real incoming direction. In panels b. and d. a smooth ellipse with a centre in the minimum lsq_t^2 and a gradient of increasing lsq_t^2 values towards the grid outer limits can be seen. Notice that the colour scale indicates maximum values of lsq_t^2 of 40 for the points of the grid lying far from the centre. In panels a. and c. no regular structure can be observed. The colour scale reaches only values of 4, since with few peaks it is possible to find a wrong identification "heliostat-peak" so that the lsq_t^2 is low.*

reconstructed peaks the lsq_t^2 increases rapidly as we move out from the minimum, however for showers with a low number of identified signals, it is relatively easy to find a wrong identification in various positions of the grid with a low lsq_t^2.

The "smoothness" of the lsq_t^2 map is independent of the energy and the shower core. In a sense, it is more likely that showers with high energy and cores close to the centre of the array have more peaks reconstructed and therefore the lsq_t^2 distribution is smoother in general in such cases. However, showers with low energies and cores far from the centre of the array can also have the same behaviour if they have many peaks reconstructed.

7.2.2 Incoming direction

In order to apply the well known hadron discrimination method based on the incoming direction of the showers (section 7.1.2) we have made a detailed study of the angular resolution for gamma and hadron showers. Fig. 7.5 compares the reconstruction of the incoming direction for gammas and hadrons. The two components discussed in fig. 6.5 of section 6.2.2 are clearly visible, a peak at small angular distances ($< 0.9^\circ$) and a background composed by the "misreconstructed showers".

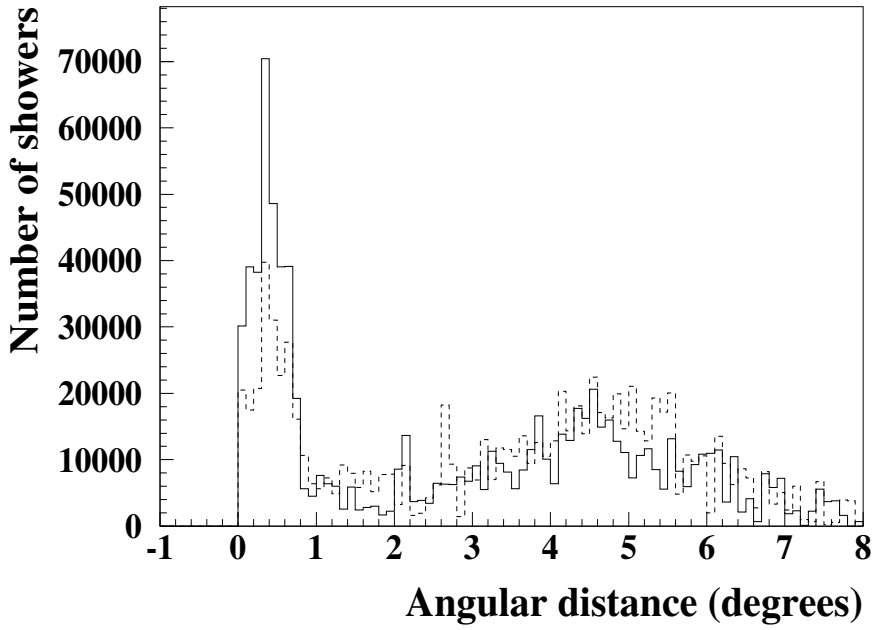

Figure 7.5: *Monte Carlo simulation of the angular reconstruction of events from a gamma-ray point source (full line, zenith angle 10°,azimuth angle 45°) and diffuse source of protons (dashed line). Shown is the number of showers as a function of angular distance from the pointing direction in degrees. It is seen that the relative fraction of showers with misreconstructed directions of the total data sample (flat background in fig. 6.5) is much larger for protons (see text). The ratio r_{io}=(events with angular deviation < 0.7 degree / all events) is 0.35 and 0.21 for gammas and protons respectively. The distributions of protons and gammas are normalized to the same number of showers.*

	Z10 A0		Z10 A45	
	gamma	proton	gamma	proton
	$n_t = 5$			
σ_{63}	0.6	0.7	0.5	0.7
r_{io}	0.26(0.63)	0.18(0.40)	0.35(0.72)	0.21(0.44)
	$n_t = 6$			
σ_{63}	0.5	0.6	0.5	0.6
r_{io}	0.43(0.71)	0.42(0.56)	0.61(0.83)	0.46(0.59)

Table 7.3: *Angular resolution (σ_{63}) and ratio r_{io} for weighted Monte Carlo samples in two different directions for gamma and proton primaries. The value given in brackets corresponds to the ratio r_{io} for the unweighted sample. The analysis has been performed at two software-threshold levels (n_t=5, 6).*

The angular resolution (σ_{63} in table 7.3) is defined as the opening angle (in a distribution of the number of showers as a function of the angular distance) within which 63% of the events are contained[2] (this definition will be used throughout this thesis).

To calculate the angular resolution the "misreconstructed" events are not taken into account, i.e., we consider the angular resolution as the opening angle within which 63% of the "well reconstructed" events are contained. The reason is that the misreconstructed events which populate the tails are caused by a wrong peak-heliostat assignment in showers with a low number of peaks (section 6.2.2) and can be eliminated from the distribution just by raising the actual software cut from 5 reconstructed peaks (NREMAIN in appendix A) to 10 reconstructed peaks (see section 8.1). We decided to set the threshold at 5 reconstructed peaks to maintain the tails of misreconstructed events and use them for normalization (section 13.1.3).

The most striking feature of table 7.3 is that the values of σ_{63} are similar for gamma and proton showers, with a mean value of 0.52° and 0.65° respectively (the σ_{63} is slightly better for gamma-ray showers but the difference is practically the same as the change of angular resolution for different incoming directions). Taking all incoming directions into account a mean value of 0.7° is obtained. The reason for the similar angular resolution of gammas and protons is the restricted field of view of the experiment and it is explained in detail in section 10.2.1. For the moment, the important conclusion of table 7.3 is that, since protons and gammas are reconstructed in the same angular region around the pointing position, it is not possible to discriminate between both primaries by means of their incoming direction.

The worsening of the angular resolution for solar arrays in comparison with the other wave-front samplers, explained in section 2.3.3.3, is obvious in table 7.3: the angular resolution is

[2]The definition of angular resolution is not always the same in airshower astronomy [123]. The angular distribution is often described with a 2-dimensional Gaussian distribution: $g(x,y)= \frac{1}{2\pi\sigma^2} e^{-(x^2+y^2)/\sigma^2}$. The variance of this distribution is given by $<(x^2+y^2)> = 2\sigma^2$. The σ of the distribution is sometimes used as angular resolution.

In contrast, we use the variance of the distribution $\sigma_{63} = \sqrt{<(x^2+y^2)>} = \sqrt{2}\sigma$ as the value for the angular resolution. This definition has the advantage that it is independent of the shape of the distribution. Instead of fitting the 2-dimensional distribution in zenith and azimuth to the Gaussian described above, we decided to calculate the "1-dimensional" angular distance from the zenith and azimuth values and infer the angular resolution from that distribution. The result is the same as if a 2-dimensional distribution were taken (for us the σ of the 1-dimensional Gaussian is $\approx$0.5°, which gives $\sigma_{63} \approx$ 0.7° (compare with the values obtained in this section with the other method)).

bad for both gamma- and proton-showers due to the sphericity of the showerfront and core reconstruction failure.

Improving the angular resolution is a difficult task for GRAAL. In addition to the above mentioned factors and the afterpulsing (section 5.3), common to all heliostat arrays, the angular resolution is worsened by the overlapping of Cherenkov pulses (section 9.3.1). However, the crucial point is not to reduce the angular resolution of the experiment to e.g. 0.1° but to avoid the bias of the reconstructed proton directions towards the pointing position (section 10.2.1). In principle, the mentioned bias can only be prevented by increasing the field of view of the detector (so that the complete shower is seen), but this is impossible for all heliostat arrays due to technical reasons (section 10.1). Therefore, an effective gamma-hadron separation making use of the spatial position of the sources (point gamma sources against diffuse proton background) is ruled out in the absence of new ideas.

7.2.2.1 Number of misreconstructed events

In fig. 7.5, it can be seen that the proton induced showers are more prone to the misreconstruction than gamma-ray showers and therefore populate the background preferentially. This can be due to the systematic higher fluctuation in arrival times of the proton showers and will be used in the analysis (section 13.1.3) to normalize ON and OFF rates. Another hypothesis to explain the higher misreconstruction for protons is that for these showers we might be detecting the light of a sub-shower (see sect. 10.2.1). In that case, the light will be distributed over a smaller area than for gamma showers, increasing the probability of misreconstruction.

The parameter r_{io}=(events with angular deviation < 0.7 degree / all events) quantifies the probability of misreconstruction for gamma- and proton-showers which is qualitatively seen in fig. 7.5. Table 7.3 shows the value of r_{io} for weighted MC samples (see section 5.1 for weighting procedure) of gamma- and proton-showers in 2 different directions. The analysis has been performed at two different software-trigger levels (n_t of section 6.1.2.1 has values of 5 and 6).

Three important features are visible in table 7.3, first, the value of r_{io} depends on the incoming direction of the showers (this is a direct consequence of the dependence of the efficiency of the showers reconstruction on the incoming direction of the shower, see section 9.3.1). Second, the value of r_{io} increases when the threshold is raised (from $n_t = 5$ to $n_t = 6$) due to the rejection of the peaks between 5 and 6 σ fluctuations of the NSB, which can be still noise peaks. Third, and most important for us at the moment, the ratio r_{io} is in general higher for gamma than for proton showers. Then, since the tails of fig. 7.5 (constituted by misreconstructed events) are preferentially populated by protons, we can use them to normalize the ON and OFF regions (section 13.1.3). These results might be affected by the weighting procedure of the MC showers, this possibility is explored in section 9.3.2.

7.2.3 Shape of the Cherenkov pulses and afterpulsing

In GRAAL there are four flash-ADCs which record the shape of the Cherenkov pulses. The widening of the pulses is mainly due to the PMTs (section 3.3.3). The dependence of the shape parameters of the pulses (rise time, fall time and width (FWHM)) with the primary of the shower was studied to search for a hadron discrimination method (sect. 7.1.3). The results of a study with the complete GRAAL detector simulation are shown below. Similar studies were made for MC showers without the effect of night-sky-noise [32].

Based on the results of several simulations (section 7.1.3), it was thought that the more irregular structure of the pulses from proton showers in comparison to those from gamma showers

could show up in an excess of tails or small pulses (close to the NSB fluctuations) for the proton-originated showers. Moreover, an excess of small pulses for proton showers could be also present due to an increased afterpulsing. Thus, we studied the rise and fall time of the Cherenkov pulses and the number of "small" peaks (between 3 σ deviation of the NSB and the imposed software threshold (section 6.1.2.1)).

We found that the rise time is smaller than the fall time for the Cherenkov pulses, but there is no difference between MC gamma and hadron showers. Likewise, there is no difference between the pulse width of both primaries.

Searching for tails or afterpulses (see above) we found that there is no difference between the number of small peaks per shower between the two primaries (see fig. 7.6, panel a.). However, the nature of the small peaks does not seem to be the same for both primaries. Whereas the time deviation from the shower front of the small peaks follows the same distribution than the "big" peaks (above threshold) for gamma-ray showers, i.e., a narrow peak centred in zero plus tails, the small peaks of proton showers have large deviations with respect to the spherical shower front. The distribution of the time deviations of the small peaks for protons is broader than for gammas and does not have a clear peak in the centre (see fig. 7.6, panel b.). This feature was studied in order to get a rejection factor of proton showers. Asking for a time deviation smaller than 2 ns from the centre for a 50% of the small peaks, a 30% of the gamma showers are accepted and a 91% of the proton showers are rejected. The discrimination parameter is not efficient enough to consider it and in addition there remains a doubt of whether the weighting procedure (section 5.1) is responsible for the difference.

7.3 Conclusion

The Monte Carlo simulations of the GRAAL detector indicate that the characteristics which differentiate gamma-ray from hadron induced showers obliterate due to the restricted field of view. This prevents a hadron rejection based on shower parameters like temporal showerfront, distribution of light on the ground and shape of the Cherenkov pulses. Furthermore, the reconstructed direction of the hadronic showers is biased towards the pointing direction invalidating a hadron rejection based on the isotropic incoming direction.

As a consequence of the lack of gamma-hadron discrimination methods, a comparison of absolute rates remains necessary for the heliostat arrays in order to detect a source. Under these circumstances, the sensitivity of the detectors is strongly reduced (section 8.6), since the NSB fluctuations introduce systematic effects which can not be corrected at a high precision level (chapter 11).

The direction misreconstruction of events with a small number of peaks is in GRAAL more likely for protons than for gamma showers. Although this can not be used as an efficient hadron discrimination parameter, it can be used to minimize the systematic effects introduced by the NSB and therefore to increase the sensitivity of the detector by using normalization methods (section 13.1).

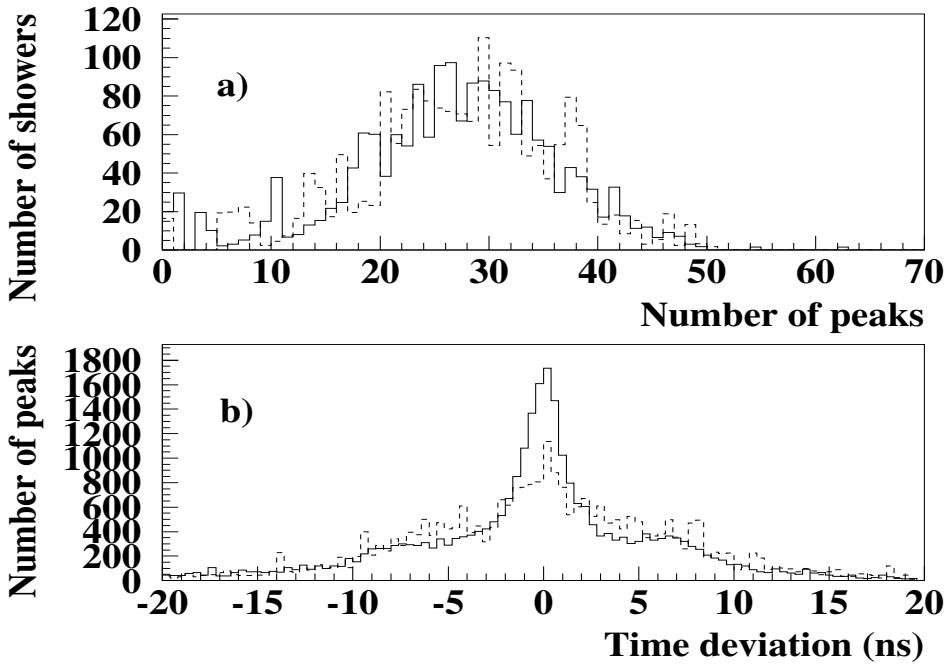

Figure 7.6: *Panel a. shows the number of peaks with an amplitude between 3·σ_{RMS} and 6·σ_{RMS} for MC simulated gamma-ray showers (full line) and proton showers (dashed line). Panel b. shows the time deviation of the measured arrival times from the fit to an spherical showerfront for the pulses plotted in panel a..*

Chapter 8

Detector performance

In all the sections throughout this chapter a weighted MC sample at a zenith angle of 30° and azimuth angle of 0° (section 5.1) was used to infer the capability of GRAAL for the detection and analysis of gamma-ray showers. The detection rate of gamma-ray showers is determined by the effective area and the energy threshold of the detector, which are described in sections 8.3 and 8.4 respectively. The analysis of the showers provides the angular and energy resolution that determine the flux sensitivity, these factors are examined in sections 8.1, 8.2 and 8.6 respectively.

All the showers surpassing the "software-trigger threshold" in the real data as defined in section 13.1.2 were counted as detected in this simulation. A value of $n_t = 9$ was chosen to obtain a proton induced rate of 4 Hz in agreement with the typical experimentally observed value in GRAAL. The chosen value of n_t is higher than the one used for the experimental data. This is due to the fact that the experimental signals seem to be smaller than the ones predicted by the MC simulation relative to the level of the NSB for the first MC version, used throughout this thesis (section 5.3). The effect was corrected by increasing the level of NSB with respect to the Cherenkov signal in a second version of MC.

8.1 Angular resolution

The concept of angular resolution has been defined with detail in section 7.2.2 and is the same throughout this thesis. In that section an average angular resolution of 0.7° is inferred, without taking into account the misreconstructed events. For these events the reconstructed direction is completely uncorrelated with the true direction of the shower due to a wrong assignment heliostat-pulse (see section 6.2.2). Therefore a derivation of angular resolution taking into account such events does not make sense. This is shown clearly in fig. 8.1, where the same reconstructed events are plotted with a software cut of 5 (panel a.) and 15 (panel b.) reconstructed peaks, called NREMAIN in section 9.2. The misreconstructed events disappear with a strict software cut, i.e., when a large number (e.g. 15) of reconstructed peaks is required to accept an event.

The number of peaks used in the reconstruction of the showerfront is the major determinant of the angular resolution (see fig. 8.2). If more than 30 peaks are used in the reconstruction, the angular resolution drops below 0.5°.

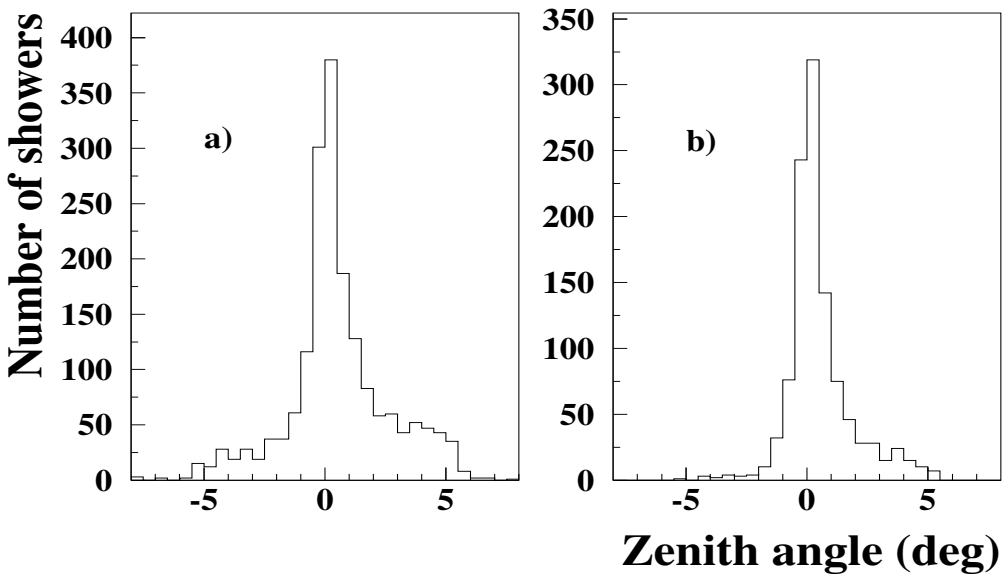

Figure 8.1: *Deviation of the reconstructed direction from the pointing direction on the elevation-axis for a MC sample of gamma-ray showers, generated with an incoming direction of 30° zenith angle and 0° azimuth angle, when 5 (panel a.) and 15 (panel b.) reconstructed peaks are required to accept an event.*

8.2 Energy resolution

The energy resolution of a detector can be inferred from the MC simulation. The quality of the energy estimation for an individual MC shower is defined as:

$$\Delta E = \frac{E_{mc} - E_r}{E_{mc}} \tag{8.1}$$

where E_{mc} is the energy of the primary particle (known only for MC simulated showers) and E_r is the reconstructed energy.

The overall energy resolution of the detector is given by the RMS of the ΔE distribution and the bias of the energy parameter estimation (or deviation of the reconstructed energy with respect to the real energy) is given by the mean of the ΔE distribution.

Using the integrated charge (IC, section 6.1.3) as a primary estimator of the energy of a shower, an overall energy resolution of 71.4% and a bias of 0.006 for MC gamma-ray originated showers are found (see fig. 8.3, panel c.). The conversion factor between the integrated charge and the energy has been inferred from the fit of fig. 8.3 (panel a.) to a first grade order polynomial $IC = a + b \cdot E_{mc}$. Hence,

$$E_r = \frac{(IC - a)}{b} \tag{8.2}$$

where $a = 26523$ and $b = 210.04$.

The great scatter of the IC values at high energies (>100% at 1000 GeV, see panel a. of fig. 8.3) could be in principle attributed to a saturation effect, i.e. the energy of high energy

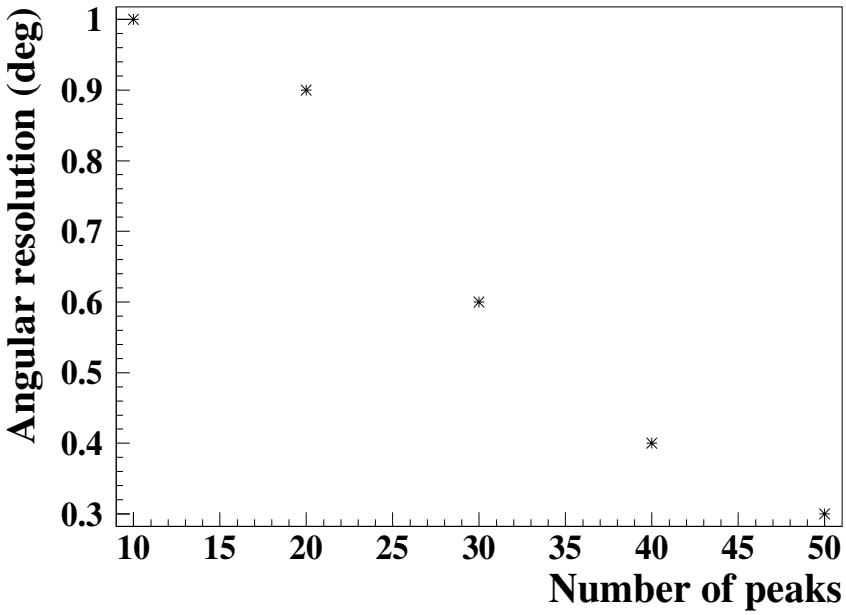

Figure 8.2: *Dependence of the angular resolution (σ_{63}) with the number of peaks used in the reconstruction of the shower front for a MC sample of gamma-ray showers generated with an incoming direction of 30° zenith angle and 0° azimuth angle.*

showers is underestimated due to the saturation of the pulse amplitudes in the oscilloscope. However, the scatter of the integrated charge for low energy showers is already large (>50%) compared to the mean IC value. The middle panel (b.) of fig. 8.3 shows the energy resolution as a function of energy. It is observed that the scatter of all the reconstructed values around the true energy for a certain energy (which gives the energy resolution) is constant. However, the bias with respect to the true value is worse for high energies than for the low ones. This is due to the fact that, in the calculation of the conversion factor from IC to energy, the number of showers decreases as a power law with energy. Therefore the low energy showers have a bigger weight and the conversion factor is more "adequate" for such showers.

Fig. 8.4 shows the real cause for the poor energy resolution. Due to the observation of the sources in convergent view configuration (section 3.1.4) and to the restricted field of view (see chapter 10), a large fraction of the total light of a shower is not "seen" by the detector for showers with impact point far from the centre of the array (the fraction $\frac{IC}{E_{mc}}$ decreases with the distance from the impact point to the centre of the array).

Therefore, if the factors a and b from eq. 8.2 are calculated for all the "distance from the impact point to the array centre" intervals (with 10 m distance bins), an energy resolution of 16% and a bias of -0.07 is obtained for all showers with distances up to 60 m (see fig. 8.5, panel a.). A 13% of the total number of detected showers has shower cores between 60 and 90 m from the centre of the array. The angular resolution for those showers is 47% and the bias 0.36 (see fig. 8.5, panel b.). No showers are detected at distances beyond 90 m. Hence, we can conclude that the dominating factor in the energy resolution is the distance from the showers impact

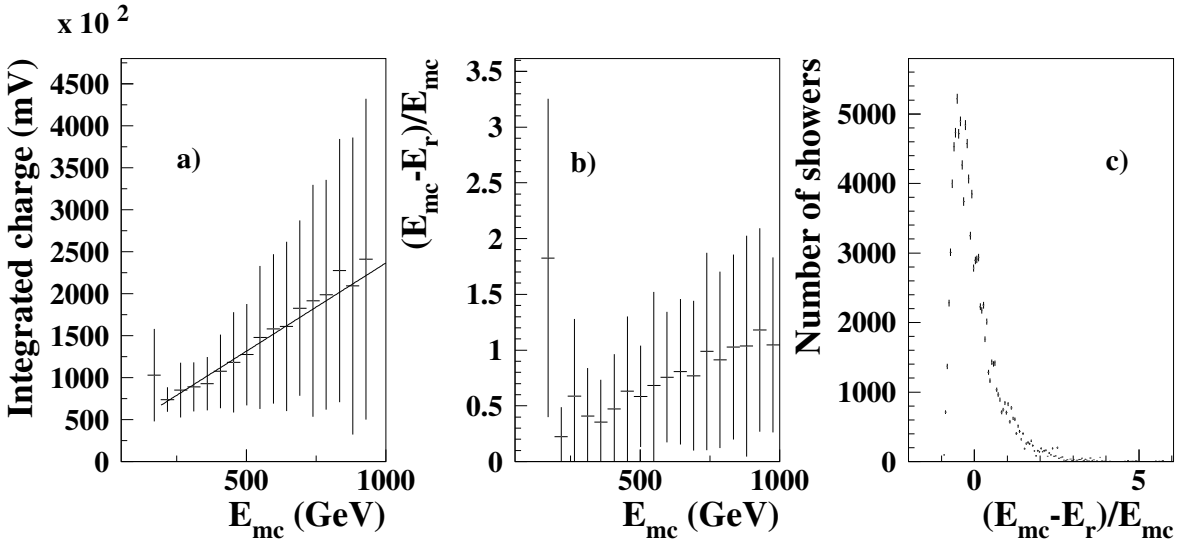

Figure 8.3: *Shown is the relationship between integrated charge (IC) and energy of a shower (panel a.) and the energy resolution for GRAAL (panel c.) using the conversion factor inferred from panel a. to reconstruct the energy from the IC (see text). The middle panel (b.) shows the energy resolution as a function of the energy of the shower (see text).*

point (or core) to the centre of the array. Fig. 8.4 (panel b.) shows the dependence of the energy resolution with the distance to the shower core. We can observe that the energy resolution is approximately constant up to 60 m from the core. The increase of the energy resolution at 60 m is due to low statistics. The conversion factor from IC to energy has been calculated for all showers between 60 and 90 m from the centre of the array in one single bin, since the number of detected showers at such distances is too low to make 10 m bins. By increasing the size of the bins, the energy resolution is worsened.

8.3 Effective area

The effective area of a Cherenkov telescope for the detection of a primary Z of incident energy E is defined as

$$\text{Effective area(Z, E)} = 2 \cdot \pi \int_0^\infty \text{P(Z, E, r)} \cdot \text{r} \cdot \text{dr} \tag{8.3}$$

where P(Z,E,r) is the probability of detection of a shower with an impact point on the ground within the radial interval *(r,r+dr)*.

The weighted MC sample (section 5.1) was used to estimate the effective detection area for protons and gamma-rays at a zenith angle of 30° and azimuth angle of 0° as a function of primary energy (for azimuth convention see appendix B).

The probability P(Z,E,r) for a primary Z was calculated as the fraction of showers surpassing the "software-trigger threshold" (number of reconstructed peaks ≥ 5) with respect to the total number of generated showers for each energy interval (see fig. 8.6). The effective area for gamma-initiated showers increases as a function of energy and has a quasi-asymptotic value of 10^4 m^2 for energies higher than $\approx$ 400 GeV.

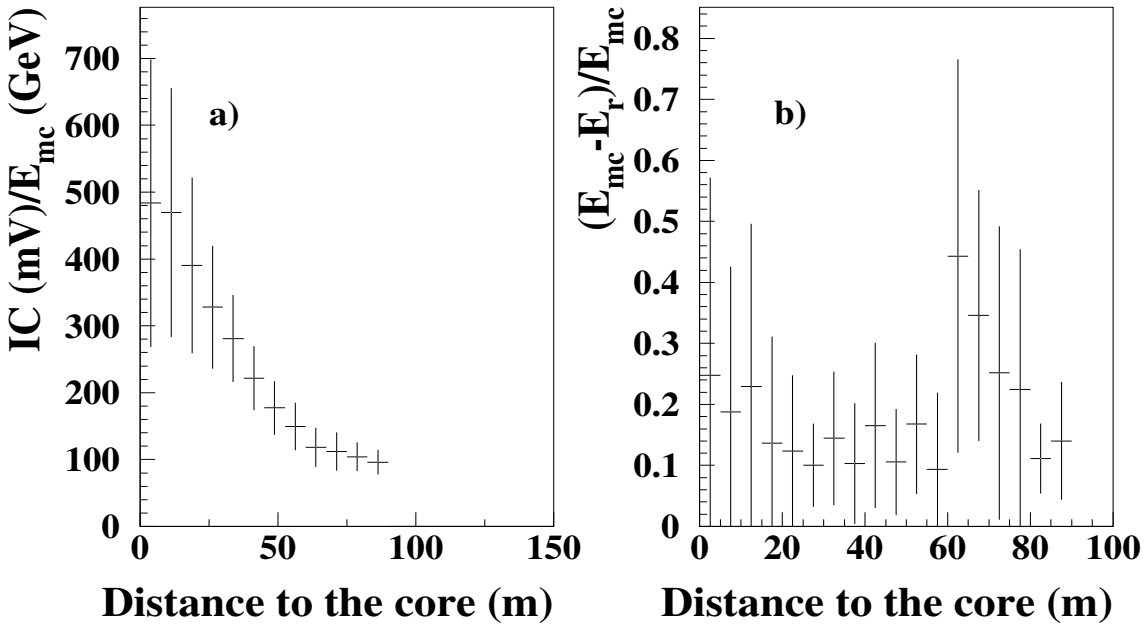

Figure 8.4: *Dependence of the factor IC/Energy (panel a.) and energy resolution (panel b.) as a function of distance from the shower core to the centre of the array. The energy resolution is constant for all energies if the impact point of the shower is known with an accuracy of 10 m (see text).*

Fig. 8.7 shows the dependence of the detection efficiency on the impact point of the showers. For energies above 600 GeV the detection efficiency is of a 100% for showers with impact points near the centre of the array (< 60 m) and it decreases rapidly for larger impact points. As the energy of the shower decreases, the impact point must be closer to the centre of the array in order to detect a shower.

Based on figure 8.6 and assuming the differential energy spectrum as a power law with index -2.7 (-2.4) for cosmic rays [242] (gamma-rays from the Crab nebula [114]) respectively, an event rate of 4 (0.011) Hz was estimated for proton (gamma) primaries. The proton event rate of 4 Hz is obtained experimentally in nights with exceptional conditions of observation, although the mean value is lower (typically between 1.5 and 2.5 Hz, section 13.2).

8.4 Energy threshold

The energy threshold for detection of gamma-rays is defined as the maximum in a plot of differential flux as a function of the primary energy (see fig. 8.8). The curves of this figure have been obtained taking into account the effective area of the detector (previous section) and the energy spectrum of the incident source (in this case, we have assumed the Crab nebula energy spectrum given by the Whipple collaboration [114]).

The energy threshold for GRAAL is derived from fig. 8.8 as 250 $\pm$ 110 GeV at 10° zenith angle and 300 $\pm$ 130 GeV at 30° zenith angle.

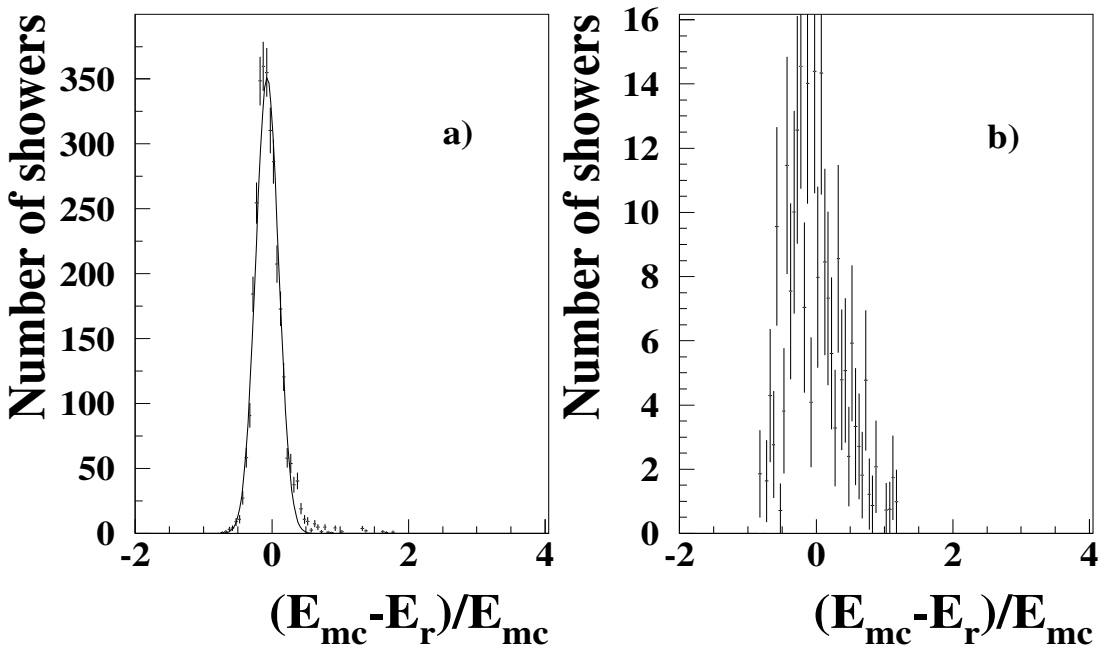

Figure 8.5: *Energy resolution as defined in eq. 8.1 for showers with distance to the core < 60 m (panel a.) and ≥ 60 m (panel b.). Compare with right panel of fig. 8.3 (see also text).*

The estimation of the GRAAL energy threshold with the second version of MC -which reproduces correctly the signal-to-noise ratio (section 5.3)- gives similar results [32].

8.5 Hadronic acceptance

We have seen that once that a limit for the detection of gamma showers is set, all the gamma showers within this limit are detected. The limit is given mainly by the energy of the showers and in second order by the distance to the core of the shower (see fig. 8.7).

For proton showers, this limit can not be set, in contrast the detector acceptance increases with the energy of the primary. Fig. 8.9 shows the acceptance of proton showers with the energy of the primary. It is observed that for low energies the spectrum of the detected protons is flat, indicating that the low collection efficiency is compensated by a high flux of protons at that energies.

Fig. 8.10 shows the acceptance of protons depending on the distance from the shower core to the centre of the array. It can be seen that the fraction of detected showers decreases with the distance to the core without a visible threshold effect (compare with fig. 8.7).

8.6 Flux sensitivity

In GRAAL, the detection of a gamma-ray signal can only be done by statistical comparison between the observed region of the sky where the source is expected (ON) and a test region

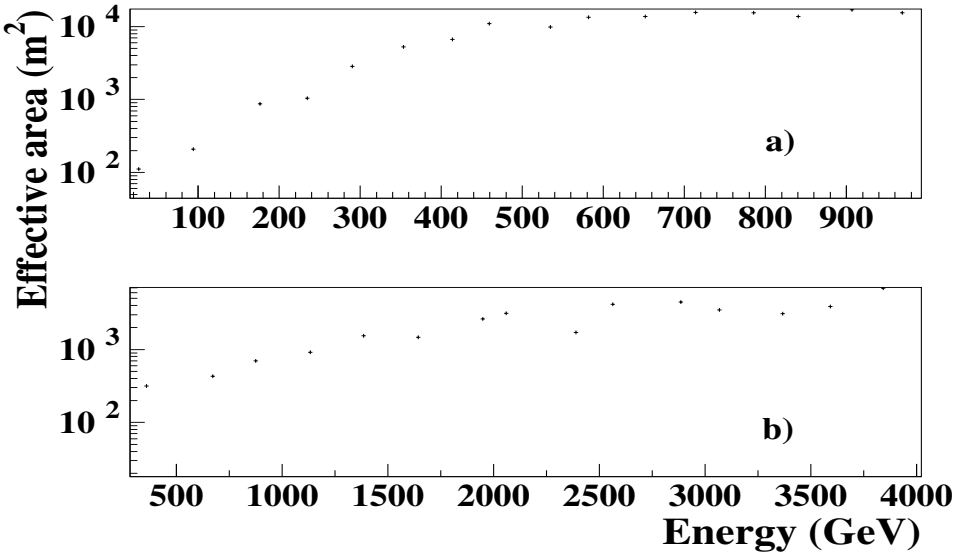

Figure 8.6: *Effective detection area for gammas (panel a.) and protons (panel b.) incoming from an zenith angle of 30 degrees and azimuth angle of 0 degrees.*

(OFF). Both regions are observed equal periods of time (10 min) under the same detector conditions.

The significance of the gamma-ray signal is given by

$$\sigma = \frac{\mathrm{ON} - \mathrm{OFF}}{\sqrt{\mathrm{ON} + \mathrm{OFF}}} \tag{8.4}$$

where ON (OFF) is the number of events recorded during an ON (OFF) period.

The sensitivity of the experiment can be estimated from eq. 8.4, taking into account the effective area for gamma and proton showers (section 8.3). About 459 hours of observation ON the source are necessary to detect e.g. the Crab nebula (assuming the energy spectrum given by the Whipple collaboration [114]) with a 5 σ significance without any kind of analysis. This is a much longer time than the initially calculated for the experiment, ca. 38 hours for the same level of significance[1]. This overestimation of the sensitivity was due to the original MC used in the proposal and for which the signal-to-noise ratio was much higher than for real data (section 5.3). Unfortunately, the error of the MC simulation was realized after the start of operation of the experiment and only then could be corrected.

The sensitivity calculated above refers to raw data. However, the real sensitivity of a detector is calculated for data after analysis, since in general the analysis favours the acceptance of gamma showers to the acceptance of proton showers increasing the sensitivity of the experiment.

[1]Initially (with the first version of Monte Carlo), a total rate of 0.068 Hz and 12.739 Hz had been predicted for gamma-rays and protons respectively [31].

At that time it was assumed that all the showers off-source (with deviation from the observation position larger than 0.2 degrees) could be rejected. This meant an acceptance of 63% of the gammas against 1% of the protons, decreasing the time needed for a detection of the Crab nebula at a 5σ significance to only 26 minutes ON source.

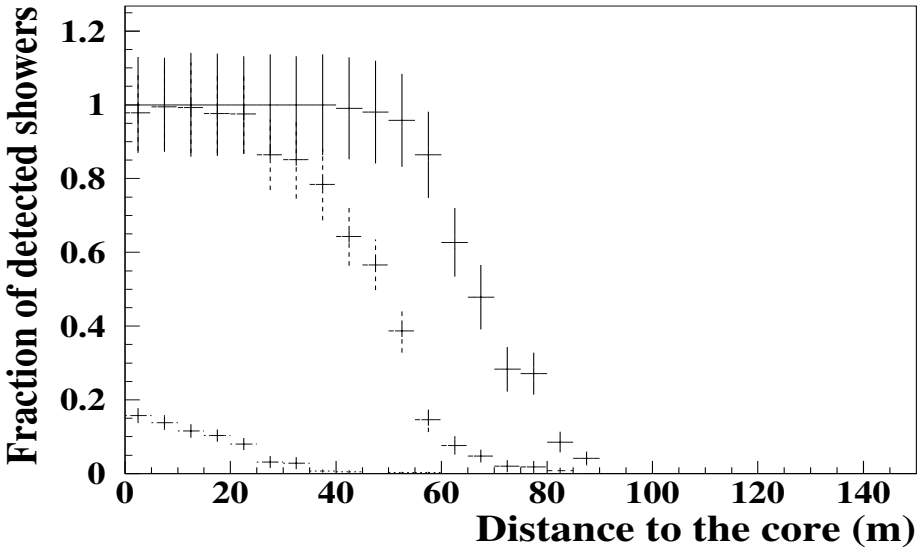

Figure 8.7: *Detection probability of gamma-ray originated showers (P(gamma,r)) as a function of distance of the impact point to the centre of the array. The showers have been divided in three energy intervals: 50-300 GeV (dotted marks), 300-600 GeV (dashed marks) and 600-1000 GeV (full marks).*

For Cherenkov detectors with an efficient gamma-hadron separation technique[2], the sensitivity increases significantly during analysis (e.g. the HEGRA CT1 telescope detects the Crab nebula at a 5σ level in about 3 hours). In contrast, detectors that lack an efficient hadron discrimination method, like the heliostat arrays, can only increase their sensitivity by means of angular cuts, requiring high multiplicity and working as close as possible to the energy threshold of the experiment (the ratio of gamma to proton showers increases with decreasing energy).

In GRAAL the flux sensitivity is increased during the data analysis that favours the rejection of hadrons to the rejection of gamma-ray originated showers. For example, taking into account fig. 7.5 in section 7.2.2, where proton showers are more misreconstruction prone than gamma showers, a cut that eliminates misreconstructed showers will favour gamma-ray over proton induced showers. As we will see in section 13.1.4.1, a signal of the Crab nebula at a 4.5σ significance is obtained in GRAAL after analysis in less than 8 hours, indicating an important increase of the sensitivity compared to raw data.

[2]An efficient gamma-hadron discrimination rejects more than 99% of the hadronic showers and accepts more than 50% of the gamma showers (see chapter 7).

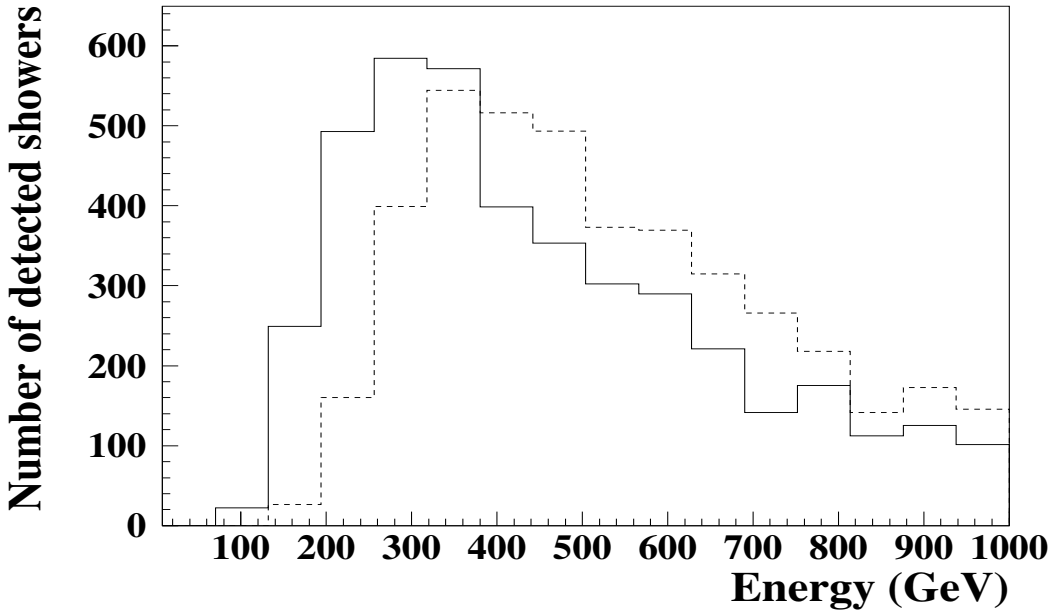

Figure 8.8: *Number of showers detected by GRAAL as a function of energy. The maxima of the curves indicate the energy threshold of GRAAL for showers incident from a zenith angle of 10° (250 GeV, full line) and for showers incident from 30° zenith angle (300 GeV, dashed line).*

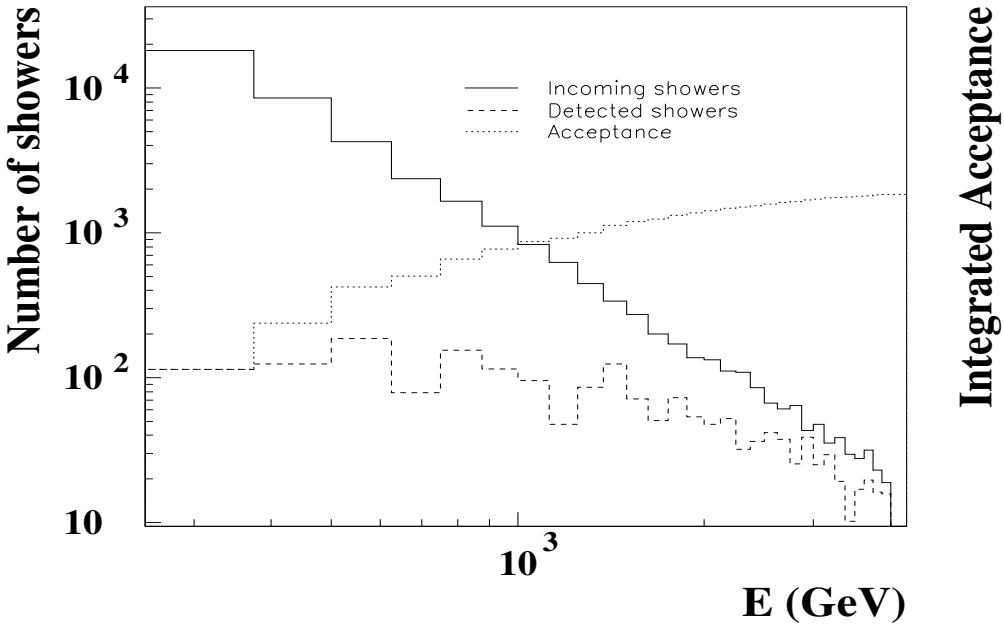

Figure 8.9: *Shown are the spectrum of the weighted MC sample of proton showers at zenith = 30 degrees and azimuth = 0 degrees (full line), the number of detected showers by GRAAL for the same sample (dashed line) and the integrated acceptance of the detector (dotted line). For low energies, the number of detected showers is quite flat (compare with full line). This means that the real spectrum (full line) is compensated with a low acceptance of the detector for low energy showers.*

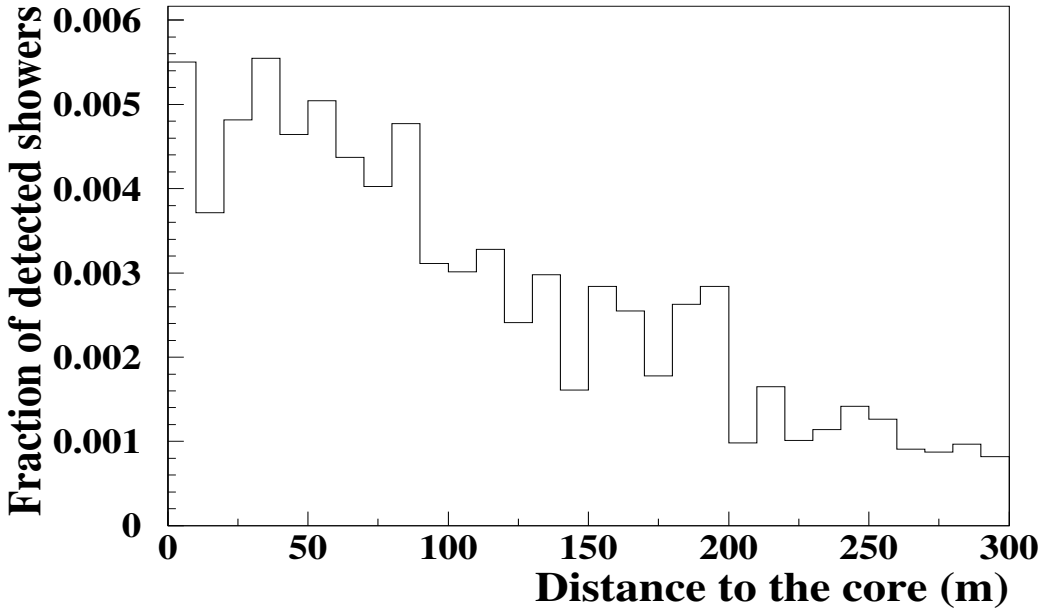

Figure 8.10: *Fraction of proton detected showers as a function of the distance to the core of the shower. The acceptance of the detector decreases with the distance to the core. No threshold effect is observed (compare with fig. 8.7).*

Chapter 9

Comparison MC-real data

We expect from the Monte-Carlo simulation (chapter 5) that it reproduces as accurately as possible the detection of the Cherenkov airshowers with GRAAL. This chapter describes the comparison of some basic parameters between experimental detected showers and simulated gamma-ray and proton induced showers. For the comparison we have chosen the MC sample with incident zenith angle 30 degrees and azimuth angle 0 degrees and a sample of the data taken on the source 3C 454.3 with zenith angle range 25-35 degrees and azimuth angle between 310 and 322 degrees.

The threshold parameter n_t (section 6.1.2.1) was set to 6 for the MC data and to 7 for the compared experimental data (section 12.1). The motivation for the slightly lower value of n_t for MC analysis is that experimental signals seem to be somewhat smaller than expected from the MC simulation (section 5.3). Some parameters of the reconstruction procedure were found to depend quite sensitively on the signal-to-noise ratio. We chose n_t=6 in order to reproduce correctly the experimentally observed ratio r_{io} as defined in section 7.2.2.

In all the sections which follow the comparison between MC simulated and experimental showers has been done with those showers which pass the software cuts (see table A.1 in appendix A).

Section 9.1 compares the charge spectrum of cosmic ray showers for the real events and the MC simulation which must reproduce the power law distribution of the cosmic rays.

According to section 8.1 the angular resolution of GRAAL is directly related to the number of peaks used in the reconstruction procedure (see fig. 8.2). Section 9.2 compares the number of detected and reconstructed Cherenkov pulses and section 9.3 and subsections compare then the angular resolution for the simulated and the real showers and explain the discrepancies attending to the dependence of the angular resolution on the incoming direction and the weighting procedure of MC showers.

Finally, section 9.4 compares the parameter lsq_t^2 of the timing fit to the showerfront (section 6.2.2) for simulated and real showers.

9.1 Total-charge spectrum

The total charge of a shower (section 6.1.3) is a direct measurement of the number of photons of the shower (section 4.4) and consequently of the energy of the primary particle (see fig. 2.3). Thus, the total charge spectrum for all showers must reproduce the well known power law energy distribution of the cosmic rays [242]. Fig. 9.1 displays the total charge spectrum for the showers which have passed the software cuts (see table A.1) both for MC-simulated proton

and experimental showers. Far above the threshold the experimental spectrum follows a power law with a differential index of about -1.6, which is much larger than the one of the primary spectrum of -2.7 [242].

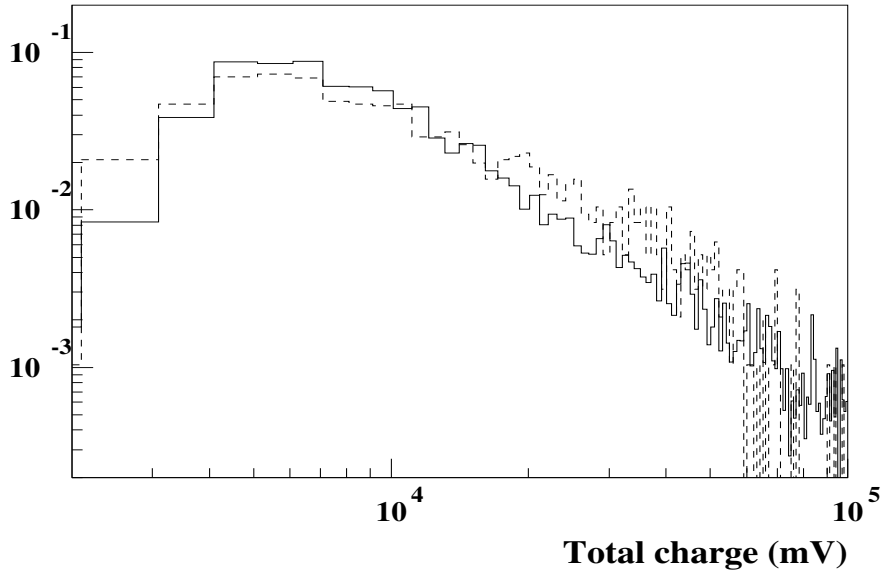

Figure 9.1: *The number of showers as a function of "total integrated charge" per shower. The dashed line corresponds to experimental data, the full line is from the MC simulation. The curves were normalized for the same number of showers. The x-axis is in units of summed flash-ADC amplitudes in mV.*

There are several reasons for this discrepancy. The first and most important one is that non-linear amplifiers are used in our setup (section 3.3.1), i.e. during the amplification stage, the large pulses are more amplified than the small pulses. Then, in order to compare the charge spectrum with the real energy spectrum, the signals have to be convoluted first with the non-linear gain. The second reason is the large scatter between energy and integrated charge (section 8.2). The energy of a shower is underestimated for showers far from the core, since only a fraction of the total light is collected for those showers (see fig. 8.4, left panel). Then, the fraction of showers far from the core will steepen the slope of the total charge spectrum (they move to lower energies in a plot of number of detected showers as a function of energy).

The Monte Carlo simulated spectrum looks qualitatively similar to the experimental data but follows a slightly steeper index of about -1.9. One reason for this is that far above the threshold the cutoff in simulated proton energy at 10 TeV is already expected to have a steepening effect on the MC spectrum.

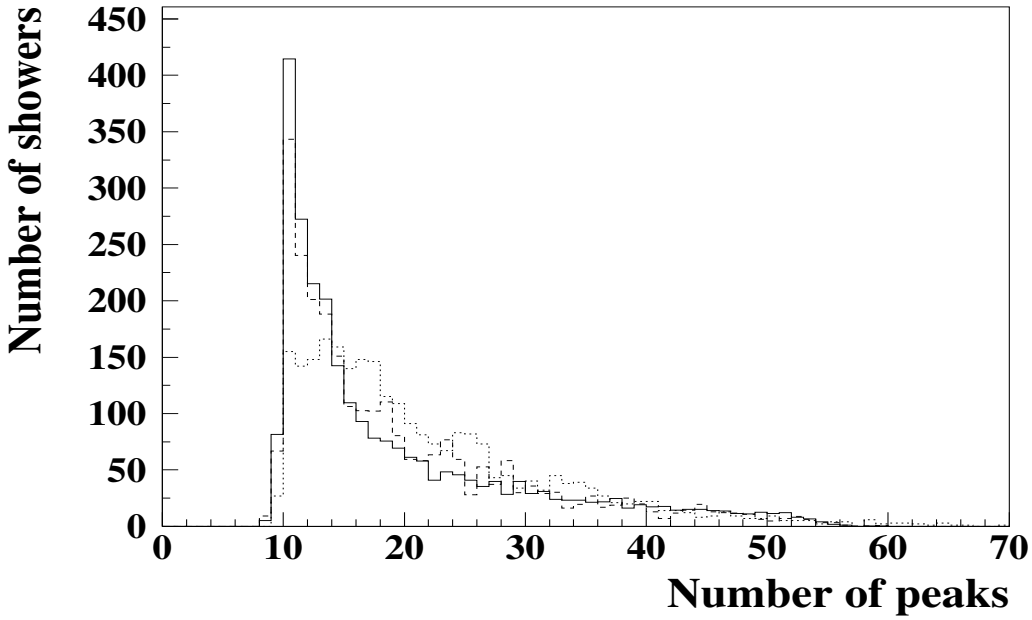

Figure 9.2: *Number of showers with a given number of peaks registered in all four recorded timing traces. The dashed line is for MC simulated protons, the full line for gammas, and the dotted line for experimental data taken under similar incident angles. The total number of showers was normalized to the experimental data for comparison.*

9.2 Number of heliostats with detected signal

A basic parameter in the showerfront reconstruction is the number of Cherenkov flashes from individual heliostats that have been recorded (section 6.2.2). Fig. 9.2 shows the distribution of the detected number of pulses over the threshold ($n_t \cdot \sigma_{NSB}$). The mean (RMS) of the distribution for proton MC is 19.6 (10.0) and for the experimental data 21.7 (10.3). Some peaks can not be identified as being due to a reflection from a certain heliostat and are not used for the reconstruction of the shower timing front (section 6.2.2). Fig. 9.3 shows the distribution of the "remaining" identified peaks that could be attached to individual heliostats (called NREMAIN). The mean (RMS) of the distribution for proton MC is 16.3 (10.9) and for the experimental data 16.0 (7.5). From this, the fraction of identified peaks is 83% for protons in the Monte Carlo and 73% in the experimental data.

Table 9.1 shows the results of a χ^2 compatibility test between simulated proton and gamma-ray induced showers and between proton-induced and experimental showers. The χ^2 values for the number of peaks show a compatibility with identity of the parent distribution for the number of degrees of freedom between gamma-ray and proton simulated showers. However, the proton and data distribution differ significantly. The difference is due in both cases to a disagreement near threshold and for very large showers, whereas for the majority of intermediate showers -with a number of peaks between about 15 and 40- the agreement is satisfactory.

The reason for the discrepancy for very small showers is probably that the discrepancy

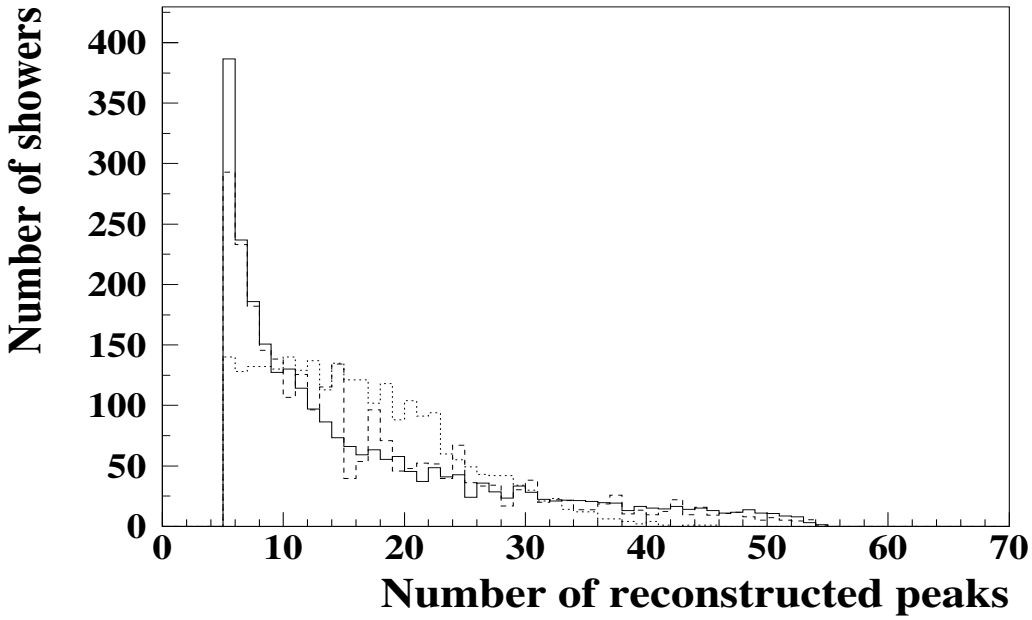

Figure 9.3: *Number of showers with a given number of peaks that were attached to individual heliostats and were used in the final determination of the shower direction. The dashed (full) lines are for MC simulated proton (gamma-ray) induced showers. The dotted line is from experimental data taken under similar incidence angles. The total number of MC showers was normalized to the experimental data for comparison.*

between data and MC in the ratio of shower sizes and size of the NSB discussed in section 5.3 is not completely resolved by the choice of slightly higher n_t discussed in the previous section.

For very large showers the reason for the discrepancy has a different nature. From figure 9.2 it is obvious that there is a tail of showers with large number of peaks (> 55) which is not present in the MC proton showers. This is due to the effect of afterpulsing in the PMTs which has not been MC simulated (section 5.3). An argument in favour of this possibility is that there are some showers with more peaks than the existent heliostats (63) meaning that some of such peaks are clearly fake. In figure 9.3 the tail at large number of peaks has disappeared, indicating that the analysis procedure which permits the rejection of some peaks for the showerfront reconstruction (section 6.2.2) is correct at least at some stage (see section 9.4). In fact, it can be observed that the "real" number of peaks for the largest showers is somewhat lower for the experimental data. This is an expected behaviour since during data acquisition it was noticed that typically 4-10 heliostats were inoperational at any given time.

Small discrepancies in the intermediate showers (with 15-40 peaks) can be due to the slightly different position in the sky (in the azimuth angle range mainly) of the MC-simulated and the experimental showers. The MC weighting procedure (section 5.1) can also introduce some additional fluctuation in the simulated showers (section 9.3.2).

	χ^2_{red}(gamma/p)	χ^2_{red}(data/p)	n_{dof}
Total number of peaks (fig. 9.2)	**1.05**	3.09	70
Selected number of peaks (fig. 9.3)	**1.2**	4.67	70

Table 9.1: *Results of a comparison of the distributions in fig. 9.2 and 9.3.* χ^2_{red}*(gamma/p) lists the values from a comparison of gamma versus proton induced showers, and* χ^2_{red}*(data/p) a comparison of proton induced showers and data.* χ^2_{red} *values that are acceptable on the 90% confidence level for the given number of degrees of freedom* n_{dof} *are bold faced.*

9.3 Angular resolution

Fig. 9.4 shows the angular reconstruction for MC simulated proton showers and experimental showers. The angular resolution is 0.8±0.5° for proton MC showers and 0.9±0.5° for experimental showers in this position.

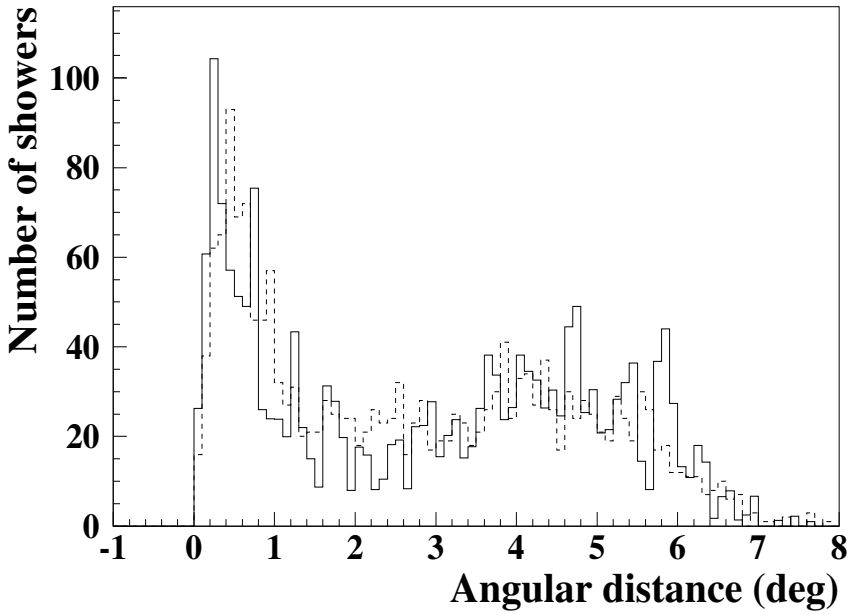

Figure 9.4: *Angular reconstruction of events from MC simulated proton showers (full line) and experimental showers taken in a similar direction (dashed line). The fraction of events with angular deviation <0.7 deg with respect to all events (*r_{io}*) is 0.27 and 0.26 for real and MC proton showers respectively.*

The slight difference between the angular resolution for MC proton and experimental showers can be explained taking into account the different incoming directions of both samples (section 9.3.1) and the fluctuations of the weighting procedure for MC showers (section 9.3.2). The given values for the angular resolution are slightly higher than the ones of sections 8.1 and 7.2.2, since in such sections an average angular resolution was inferred from the angular resolution at several

incoming directions.

9.3.1 Dependence of the angular resolution on the incoming direction of the showers

The angular resolution depends strongly on the number of peaks used for the reconstruction of the shower front (section 8.1). In addition, the number of detected peaks depends on the position of the source which is being tracked, since a change in the time pattern of the peaks (see fig. 6.4) entails a difference in the overlap and consequently in the total number of peaks. This dependence of the angular resolution on the position is seen in table 7.3 (section 7.2.2), where the parameter r_{io} (fraction of events with angular deviation <0.7 deg with respect to all events) differs for the two shown positions.

Nevertheless, the number of peaks is not the only factor which determines the angular resolution. The position of the peaks in the theoretical pattern (section 6.2.1) can produce a bias in the reconstructed direction if the pattern is regular, i.e. if the time interval between pulses is very similar. The reason is that a wrong identification heliostat-pulse may be easily found by shifting in time the whole pattern. Fig. 6.4 shows the theoretical patterns for three different incoming directions. For example, in the b. configuration it can happen that the identification heliostat-pulse is not correctly done if some peak is not recorded, since the pattern for cones 3 and 4 is very regular. In contrast, for the c. configuration, a failure in the assignment heliostat-pulse is very unlikely, since a wrong assignment increases the lsq_t^2 of the fit to the sphere significantly.

Fig. 9.5 shows the deviation of the reconstructed from the pointing zenith angle as a function of the pointing azimuth angle for a sample of real data taken on the source 3C454.3. The quality of the zenith angle reconstruction is strongly influenced by the pointing azimuth angle. For azimuth angles close to zero (360) degrees the theoretical pattern is very regular (see fig. 6.4, panels a. and b.). This worsens the angular reconstruction with respect to other pointing positions.

9.3.2 Influence of the weighting of the MC sample on the ratio r_{io}

The MC simulated sample has been weighted (section 5.1) for all the studies done throughout this thesis. It might occur that the weighting procedure affects some results. If the weighting introduces an additional fluctuation to the statistical errors of the distribution, the effect is more likely to be observed for showers with very low statistics (namely, at low energies and small shower cores).

In table 7.3 of section 7.2.2 the ratio r_{io} is shown for MC samples in two different directions. The unweighted value (in brackets) is shown to study the effect of the weighting in the showers. We have estimated the error introduced by the weighting procedure in the value of r_{io}. For gamma-ray showers, the error is about 5-15% of the r_{io} value. As the threshold from table 7.3 is increased from n_t=5 to n_t=6 the error decreases. For proton showers there is an additional weight with respect to gamma showers, the angular one. This weight is the one which introduces the largest error. Showers from a direction far from the pointing direction ($> 2^\circ$) have a very low probability of being detected (see fig. 10.1). However, if one of them is detected, it will be strongly weighted due to its incoming position. The error introduced by the weighting in the value of r_{io} for proton showers has been estimated in about 35-50% (again, the error decreases when the analysis threshold is increased).

This estimation indicates that we have to be careful when considering "differences" between gamma and hadron showers, which might have been induced just by the weighting procedure.

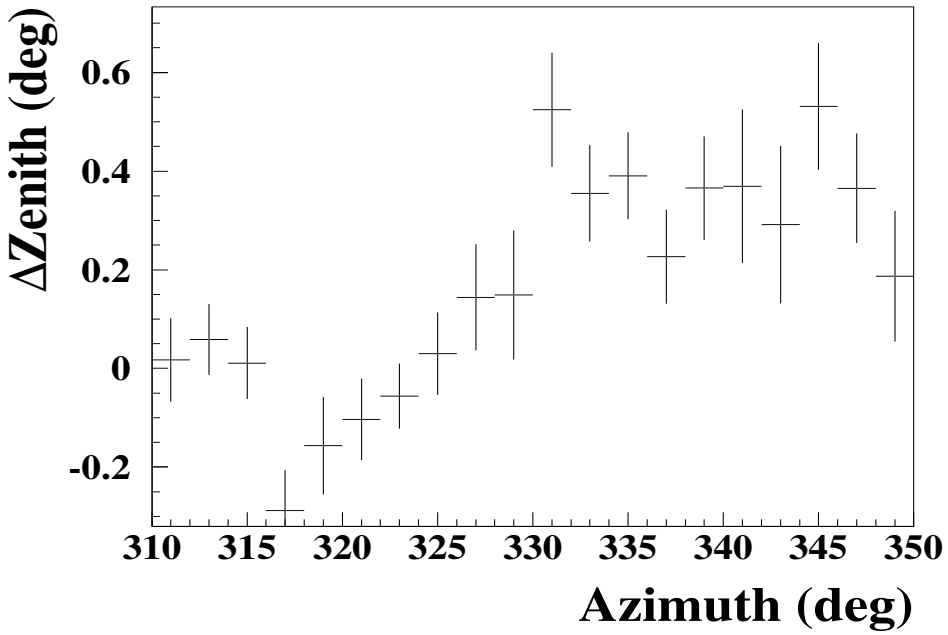

Figure 9.5: *Deviation of the reconstructed from the pointing zenith angle as a function of the pointing azimuth angle for a sample of real data taken on the source 3C454.3.*

9.4 Timing properties

The distribution of the lsq_t^2 (eq. 6.2) of the timing fit for MC simulated and experimental showers has been shown in fig. 7.3 (chapter 7).

The distributions for MC simulated gammas and protons are remarkably similar (section 7.2.1.1). The mean (RMS) values of the distribution are 1.46(1.93) and 0.99(1.37) for experimental data and MC proton-induced showers respectively. The χ^2 compatibility study of section 9.2 has been also made for the lsq_t^2 distribution. In this case, all χ^2 values are incompatible with identical parent distributions (χ^2_{red}(gamma/p) = 1.54 and χ^2_{red}(data/p) = 1.72 with n_{dof} = 200). While a difference between gamma-rays and protons is expected (the former have slightly smaller deviations from a spherical front), the larger deviation of experimental showers from a spherical front with respect to MC showers is very likely due to the effects of afterpulsing (section 5.3). Even if the analysis program has the possibility of rejecting a given number of pulses for the showerfront reconstruction (section 6.2.2), it can happen that -due to a higher number of "fake" peaks than expected or to the rejection of some real peak- after pulses contribute to the showerfront reconstruction and therefore to the lsq_t^2 distribution. Since such peaks have larger deviations from the showerfront than the real peaks, the mean of the lsq_t^2 distribution will be increased.

Fig. 7.2 shows that the time deviation from the shower front for the real pulses is very similar for MC proton and experimental showers, indicating that the "fake peaks" (with deviations larger than 5 ns from the showerfront) are the responsible for the increase of the lsq_t^2 for experimental showers with respect to MC proton showers. An alternative source of "fake peaks" to afterpulsing

(e.g. muons) has not been proven.

Chapter 10

Restricted field of view

In GRAAL, the field of view (*fov*) seen by one single heliostat has values between 0.42° and 0.84° for the heliostats furthest (146 m) and closest (52 m) to the central tower respectively (see fig. 3.3). We infer an average field of view for all the GRAAL heliostats of approximately 0.6° full opening angle. This value is small in comparison with the field of view of the traditional Cherenkov telescopes (e.g. 2.4° in Themistocle [16], 4.8° for CAT [185] and 4.3° for the HEGRA array [111]). Section 10.1 explains the reasons which force the election of such a small value in GRAAL.

The restricted field of view has proven to be one of the main drawbacks of the heliostat array approach for its capability to "erase" any existing difference between gamma- and hadron-induced showers. Section 10.2 and corresponding subsections explain the effects of the restricted *fov* on the Cherenkov airshowers.

10.1 Reasons to choose a small field of view

The gamma-ray energy threshold scales with the field of view as

$$\mathrm{E_{th}} \propto \sqrt{\frac{\Omega\tau}{\mathrm{A_{eff}}}} \tag{10.1}$$

where the solid angle Ω is well approximated by $\Omega = \pi(fov/2)^2$, τ is the time during which the night sky light is integrated by the detector and A_{eff} is the effective area. This assumes an angular aperture big enough to accept all the Cherenkov photons [45]. The angular size of an air shower as seen from the edge of the light pool is several milliradians. Therefore it is advantageous initially to increase the field of view in order to increase the source signal relative to the trigger threshold. Patterson & Hillas [182] obtain an optimum field of view of about 2.5° from their simulations without sky noise for an energy threshold of 200 GeV for gamma showers. The Cherenkov telescopes have values for the *fov* close to this optimum. For the heliostat arrays, the situation is very different.

To gain advantage of using many large mirrors with only one central detector the heliostats need to have a focal length longer than 80 m, about a factor 20-30 larger than those of the telescopes used for the imaging of VHE gamma-ray showers. For space reasons in the central tower (section 3.2.1) the light detector at the focus cannot be scaled up by such enormous factors. Moreover the construction of an imaging camera for each heliostat would be prohibitely expensive. These two factors force a crucial compromise in Cherenkov detectors using heliostat

fields: the field of view has to be chosen about one to two orders of magnitude smaller in solid angle than in traditional Cherenkov telescopes.

Nevertheless, at the low energies of the heliostat arrays a small field of view is somewhat acceptable since the showers are less extended spatially (the particles are less penetrating due to their smaller energy). Our MC simulations show that about 60% of the Cherenkov light of showers induced by gamma rays with small energies (100 GeV) is collected in the GRAAL setup, which means that ca. a factor 2 of the light is lost due to the restricted field of view. In contrast, GRAAL has a mirror area (2500 m^2) which is larger ca. a factor 30 in comparison with the traditional telescopes (e.g. Whipple has a mirror area of 75 m^2 [43]). Besides, the fraction of light lost due to the small field of view is larger for hadron than for gamma showers, favouring the hadronic rejection [45]. In spite of all the considered factors, the disadvantages caused by the restricted *fov* turned out to be numerous (see next sections).

10.2 Effects of a small field of view

10.2.1 Reconstructed direction of proton induced showers

Sections 7.1.2 and 7.2.2 explained the possibility of discriminating gamma- and proton-induced showers by excluding all showers that do not arrive from the source direction within the angular resolution. In our setup the combination of two factors, namely, poor angular resolution (0.7°, section 7.2.2) and restricted field of view ($\approx 0.6°$, see beginning of this chapter), prevents the use of this technique for hadron rejection.

According to our MC simulations, GRAAL can detect proton showers with incident directions till 2° angular distance from the observation point (see fig. 10.1). Fig. 10.2 (red line) shows the distribution of the difference between true and reconstructed shower direction. From that figure $\approx 90\%$ of the hadronic showers could be rejected attending to the reconstructed direction against a 65% of the gamma-ray showers (according to the ratio r_{io} of section 7.2.2) by accepting only the events which fall within our angular resolution (0.7°). Unfortunately, the angular restriction of GRAAL produces a bias of the reconstructed shower direction towards the source direction (see fig. 10.2, black line) and reduces the fraction of rejected protons to less than 80%.

Increasing the software cut NREMAIN of table A.1 from 5 to 15 reconstructed peaks, so that misreconstructed showers are not considered (section 8.1), we obtain a 85% of accepted gamma showers vs. a 27% of rejected proton showers within the angular resolution of the detector for the same MC sample as in figs. 10.1 and 10.2 (this does not allow an effective gamma-hadron separation). In contrast, if the bias towards the source direction caused by the restricted *fov* is not considered, the fraction of rejected proton showers increases to 70%. Thus, the angular resolution of our detector is not the main problem for an effective hadron discrimination, although a better angular resolution would still increase the calculated fraction of rejected proton showers (70%) with respect to rejected gamma showers (15%). In contrast, the bias of the reconstructed proton directions towards the source direction caused by the small *fov* is the responsible for the reduction of the fraction of rejected showers to a 27% and the failure of the method.

The reason for the above mentioned bias is sketched in figure 10.3. The field of view "selects" a part of the shower which lies towards the shower maximum of a shower arriving from the source direction. The timing-fit then finds the direction of this subpart of the shower, which is biased towards the source direction.

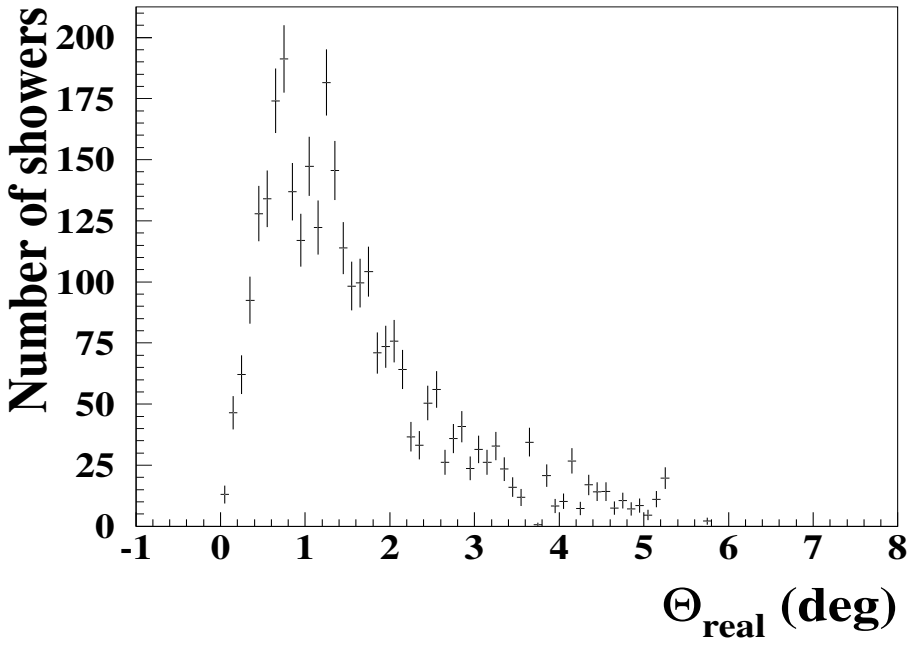

Figure 10.1: *Incoming direction of the proton showers detected by GRAAL with respect to the pointing direction. For the distribution, a weighted MC sample of protons with incoming directions from a sphere of 5° radius with centre in zenith angle of 10 degrees and azimuth angle of 45 degrees was used. At distances larger than 2° from the pointing position the number of detected showers is negligible.*

10.2.2 Density of light on the ground

The distribution of light on the ground of a Cherenkov airshower is determined by the development of the shower through the atmosphere (section 7.1.4). When all the Cherenkov photons emitted by the airshower are detected, a clear difference shows up between the distributions originated by gamma and proton primaries. Whereas a gamma-ray shower presents an homogeneous distribution of light on the ground, with a characteristic hump at a distance ≈ 120 m away from the shower core (at GRAAL altitude), the hadronic showers present a much more irregular structure, caused by the larger interaction length of protons with respect to photons in the air and the large transverse momenta of secondary particles produced in hadronic interactions.

Borque [32] studied the effect of a restricted field of view in the distribution of light from airshowers at ground level. A brief summary is exposed below.

Fig. 10.4 shows the distribution of light on the ground for showers originated by a 200 GeV gamma-ray and a 500 GeV proton. The same three configurations of fig. 7.1 (section 7.1.4) are shown, but for a shower falling at 40 m from the centre of the array. The imposition of a restricted field of view modifies remarkably the distribution of light on the ground, particularly for gamma-ray showers falling far from the centre of the heliostats array. When all the Cherenkov photons are detected (panel a. of fig. 10.4), the characteristic light distribution of gamma-ray showers (constant density of light in a circle of around 120 m radius and a *hump* more intense at

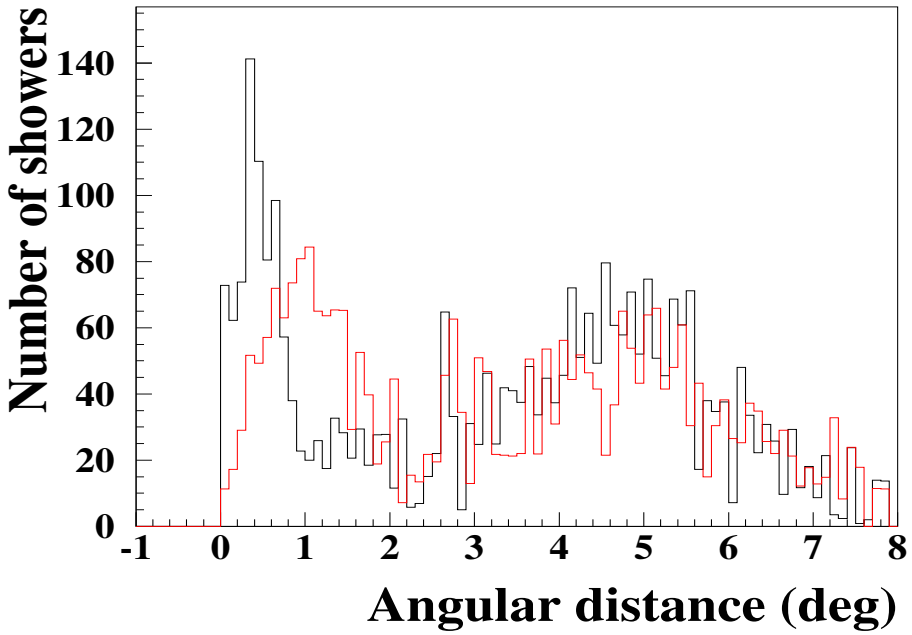

Figure 10.2: *Reconstructed direction of the MC proton showers with respect to the real (red line) and pointing (black line) position. The same MC sample from fig. 10.1 has been used. The reconstructed directions are artificially biased towards the pointing position due to the restricted field of view of the array (see text).*

the edge of the circle) is observed. Under restricted *fov*, if the heliostats are pointing in "parallel view" (panel c. of fig. 10.4), only those situated close to the core position detect a significant fraction of the incident light, i.e. the fraction of light detected decreases with the distance of the heliostat to the core. This is clearly seen in fig. 3.6. The heliostats far from the core of a shower are looking at a region in the sky far from the maximum of that shower. In addition, those heliostats can only see the light which is generated near the axis formed by the pointing position and the heliostat due to their restricted field of view. Thus, they can not see the light of the shower.

In the "convergent view" configuration the situation is somewhat different, if the shower falls in the centre of the array the restricted *fov* does not alter significantly the light distribution on the ground (see panel e. of fig. 7.1), since the heliostats point to the maximum of the shower and all the light generated at that point and above is detected, even at large distances from the core. However, if the shower core is far from the centre of the array, the radial structure of the light density on the ground is lost (see panel e. of fig. 10.4). In this case, the efficiency of each mirror to detect photons depends on the orientation of its optical axis with respect to the shower axis and on the distance to the core. Therefore, the angular restriction favours the detection of only one part of the ring, the one which lies closer to the centre of the array[1].

In the case of hadronic showers, the structure of the light distribution on the ground when

[1]The efficiency will be higher at the position above the centre of the array at which all the heliostats are pointing.

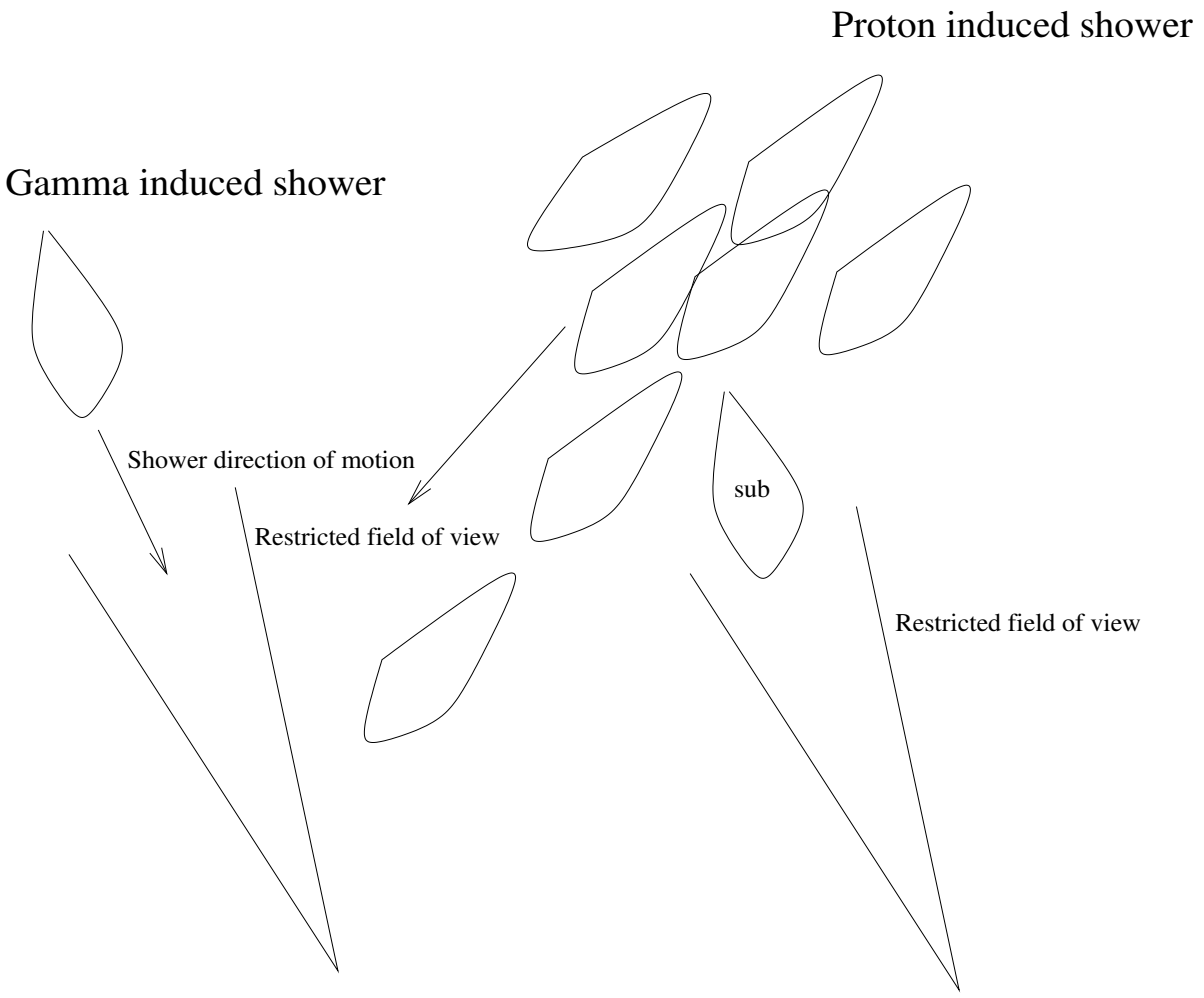

Figure 10.3: *Sketch to illustrate the effect of a small-field of view -necessitated by the heliostat-field approach (section 10.1)- on the determination of the timing structure. A gamma-ray induced shower is symbolized in the left part of the figure and a proton induced one with a slightly different incident direction on the right. The proton shower is spatially more extended and symbolized as a collection of small sub-showers. The restricted field of view " projects" out sub-showers in the central part of the shower out of the more extended proton shower. Other more penetrating and laterally extended sub-showers -that increase the fluctuation in the timing front- do not contribute to the light detected within the restricted field of view. One sub shower with an incident direction biased towards the pointing direction (symbolized by the label "sub") is preferentially detected and thus biases reconstructed directions towards the pointing direction.*

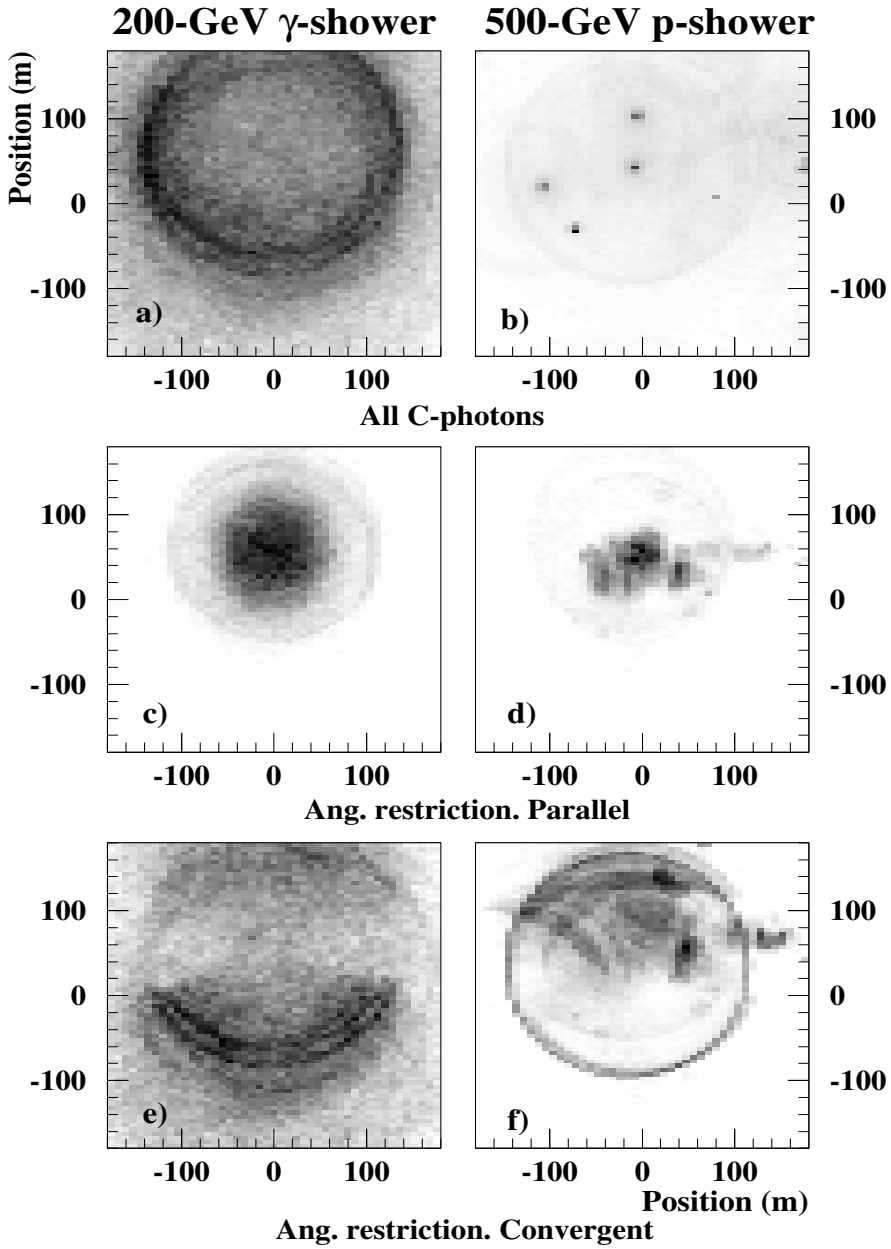

Figure 10.4: *Typical distributions of Cherenkov light detected at ground observation level (505 m a.s.l. for GRAAL). The showers were MC generated by a gamma-ray (panels a., c. and e.) and a proton (panels b., d. and f.) vertically incident with the core situated 40 m away from the centre of the array. The grey scale is linear in number of collected photons, the maximum intensity being the maximum number of collected photons. See text for explanation of the different configurations (compare also with fig. 7.1). Taken from [32].*

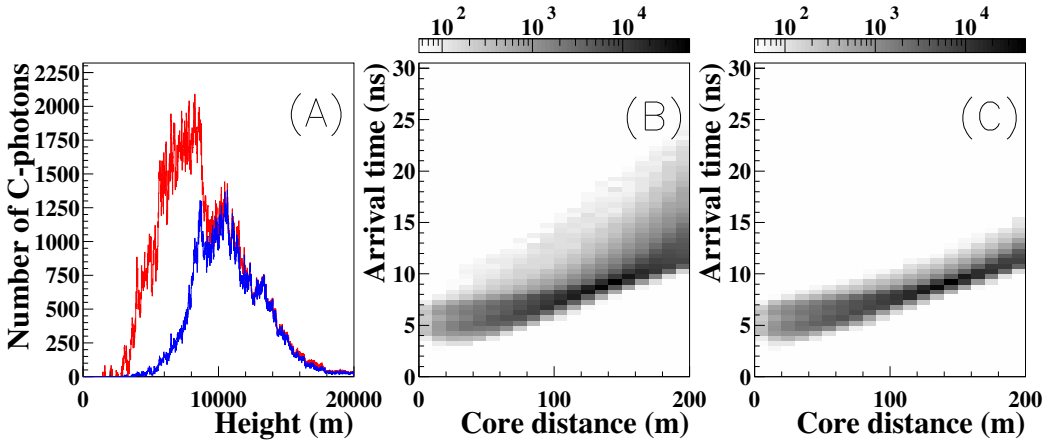

Figure 10.5: *Time structure of a typical gamma-ray initiated shower. b. The arrival time as a function of distance from the core in metres for a typical gamma shower. The shading is proportional to the Cherenkov-photon density. c. Same as b. but only those photons with an arrival direction within 0.3° from the direction towards the shower maximum from a position on the ground are displayed for the same shower. a. Number of Cherenkov-photon emitting electrons in the shower as a function of height a.s.l. when all the light is collected (red line) and when the restricted field of view is considered (blue line).*

all the Cherenkov photons are detected changes as well under restricted *fov* but still maintaining an irregular shape (see panels b. , d. and f. of fig. 10.4). This is an expected result, since we have said that the efficiency of the detectors depends on the orientation of the mirrors with respect to the shower axis and on the distance to the core in the configuration with restricted *fov* and convergent view. Consequently, the structure of the light on the ground is given in this case by a combination of the efficiency of the mirrors for each position and the total light generated at that position.

In summary, the differences which characterize the distribution of light on the ground of gamma and hadron originated showers when all the Cherenkov light is detected disappear under restricted field of view, turning in completely inefficient any hadron rejection technique based on such differences.

10.2.3 Temporal structure of the showerfront

The arrival times of proton-induced showers have a much wider scatter around the mean arrival time than the ones of gamma-induced showers due to the more irregular development in the atmosphere of the former (section 7.1.1).

Figs. 10.5 and 10.6 (b. (central) panels) show the structure of the shower front for a typical gamma and proton Cherenkov shower from the MC simulation without simulation of the detector. The large scatter of the proton shower in comparison with the gamma shower is evident. In panels c. of the same figures, the shower front is shown with a restriction on the incident angle of the photon similar to the GRAAL *fov*. The scatter at all distances from the core is smaller for both primaries (the showerfront narrows) but the effect is stronger for the protons.

Panels a. of figs. 10.5 and 10.6 demonstrate the reasons for this behaviour. The scatter of the arrival times of proton showers with respect to an ideal spherical timing-front is mainly due to the deeply penetrating part of the shower. Gamma-ray showers are less penetrating than

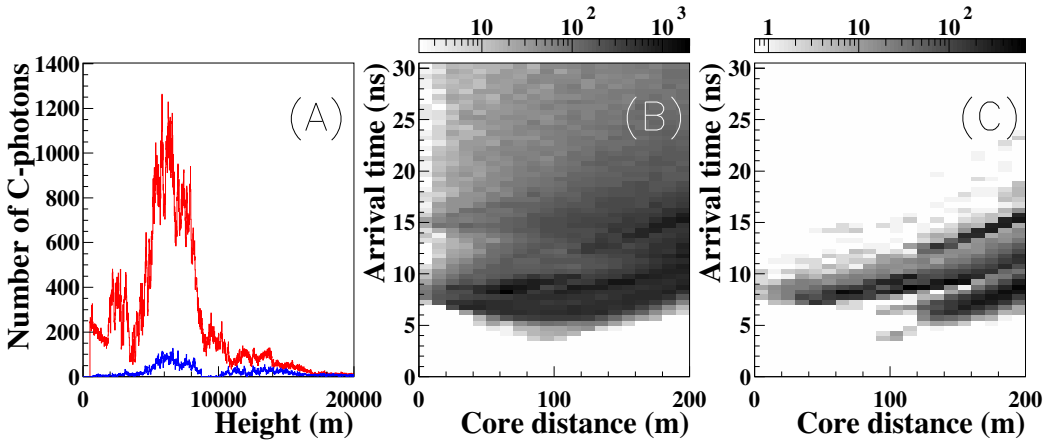

Figure 10.6: *Time structure of a typical proton initiated shower. The panels show the same quantities as in the previous fig. 10.5. Note that the proton emits a much smaller fraction of light within the restricted field of view because of its larger angular extension.*

protons and do not produce a significant fraction of light at lower altitudes in comparison with proton showers (see panel a. (red line) of figs. 10.5 and 10.6 respectively). Therefore the arrival times of the Cherenkov photons present small deviations from an spherical shower front (see panel b. of fig. 10.5). In contrast, the deviations from an spherical shower front are large for proton showers (see panel b. of fig. 10.6). Under restricted *fov* the photons emitted far from the shower axis are not detected due to the angular restriction (see panels a. of the same figures, blue line), but the convergent view maximizes the detection efficiency at the maximum of the shower and above it. Thus, the total effect is an almost identical, narrow and spherical shower front for gammas and protons. The experimental data reproduce this narrowness (see fig. 7.2).

As in the previous section, the restricted *fov* destroys the differences inherent to gamma-ray and proton showers. Any gamma-hadron separation technique based on the temporal structure of the showerfront is inefficient under angular restriction.

10.3 Conclusions

After the implementation of the solar-experiments, it has been shown that all the methods proposed for gamma-hadron separation based on different shower properties (chapter 7) are not effective. This is due to the restricted *fov*, that makes proton induced showers look like gamma-ray induced showers.

In addition, the rejection of hadronic showers attending at their arrival direction has a very low efficiency for the heliostat-arrays. This is again a consequence mainly of the restricted field of view (see sections 2.3.3.3, 7.2.2 and 10.2.1).

The software discrimination of the hadronic background, that fails for the solar-arrays due to the restricted *fov*, is very likely to work for wavefront samplers with a large field of view like the Pachmarhi array (PACT). We have seen throughout this chapter that the failure of gamma-hadron separation techniques based on timing and lateral distributions of the Cherenkov showers for the heliostat-arrays is indicated already by the Monte Carlo simulations. In contrast, the MC results are very encouraging for PACT. For example, Bhat & Chitnis [25, 54] report rejection factors of more than 95% of the protons retaining about 60% and 27% of the gammas with

two different methods. These methods have not been applied yet to real data. In addition, Vishwanath [230] describes another method for hadron discrimination that has been tested with success on PACT real data (no quality factor is given in this case). Finally, the hadronic rejection of showers by means of their arrival direction can be also applied in PACT. Vishwanath et al. [231] report a detection of the Crab nebula at a 12σ level significance using this method (no quality factor is given).

Chapter 11

Night Sky Background

The effect of the night sky background is a fundamental problem for all Cherenkov experiments, especially for those with an energy threshold very near the Poissonian fluctuations of the NSB, i.e. with a hardware trigger that requires a threshold for the Cherenkov pulse "slightly" above the NSB fluctuations.

This effect becomes crucial for experiments which lack an effective gamma-hadron separation method (see chapter 7). Those experiments can only detect gamma-ray emission from a source by statistical comparison of the events recorded in two regions of the sky, a region where the source is expected (*ON*) and a test region (*OFF*) (section 13.1.3). Differences in the NSB between the two observed regions can destroy a source excess of gamma-rays or indicate the presence of an excess where none exists (section 13.2).

GRAAL operates very near the background level (section 2.3.3) to achieve a low energy threshold. The situation is similar for the other solar arrays and some wavefront samplers like THEMISTOCLE. In contrast, other experiments like the HEGRA array of telescopes chose much higher discriminator levels (near 5σ above the NSB fluctuations [116]) to "stay away" from Night-Sky effects.

Section 11.1 gives the mean value of the NSB for GRAAL explaining all the sources which contribute to such value. Section 11.2 explains the systematic effects introduced by the NSB in the recorded data and section 11.3 and corresponding subsections (one for each systematic effect) describe the techniques which were applied in GRAAL during data analysis to correct for such effects. Finally, section 11.4 gives a conclusion about the NSB effects that can not be properly corrected.

11.1 Night Sky Background value for GRAAL

The Night Sky Background (NSB) is the sum of starlight, scattered man-made light, atmospheric fluorescence and backscattered light from artificial sources on the ground.

At the location of GRAAL the brightness on small angular scale of the night sky (inferred from the wide-angle[1] value measured at the zenith by Plaga et al. [186]) is:

$$\phi = 3.0 \times 10^{12} \text{ photons m}^{-2} \text{ s}^{-1} \text{ sr}^{-1} \tag{11.1}$$

between 300 and 600 nm wavelength, which is a value comparable to the very good Roque de los Muchachos site at La Palma [163] .

[1] The full angular acceptance of the phototube was ≈23 deg.

The main contributions to the NSB value of scattered man-made light at the site of GRAAL are the lights of the village of Tabernas (at 5 km from the GRAAL site) and the glow of the city Almería (40 km away from GRAAL), both in the Southwest direction.

Another source of background is the light reflected on the ground that surrounds the heliostats. This factor is minimized by adjusting the aperture of the Winston cones to the size of the heliostats image on the focal plane so that one PMT "sees" only the ground between the heliostats (but not around) and the heliostats assigned to the corresponding Winston cone. We can estimate the contribution of the light reflected on the ground, with an albedo of ca. 20%, to be about 10%.

The differences of NSB over the sky are of the order of a few per thousand to a few percent. Massey & Foltz [151] measured the NSB for different directions (with zenith angles from 1 deg to 60 deg and different azimuth angles) in two astronomical sites (Mt. Hopkins and Kitt Peak) and found differences in the NSB ranging from 0.9% to 2.5%. For GRAAL, the differences in NSB can be inferred from the RMS of the night-sky fluctuations once that the electronic noise has been subtracted (shown for the positions of all observed sources in column 3 (number in brackets) of tables 12.4-12.5 (section 12.4)). The largest NSB difference between 2 observed positions ON and OFF is $\approx 4\%$ for the case of Mrk421, this is due to the presence of a magnitude 6 star in the field of view of the detector for the ON position and therefore can not be compared with the values observed in [151], where the influence of stars in the field of view of the detector has been removed. Excluding the extreme value of Mrk421, we find differences in the NSB which range from 0.2% for the sources Crab and 3C273 to 2% for the source 3C454.3, being in general around 1%, which fits quite well with the values given in [151].

The intensity of NSB falls rapidly to zero at wavelengths below 300 nm due to ozone absorption and increases rapidly above 550 nm. However, above this value the quantum efficiency of the PMT is already very small (see fig. 3.9) and the noise is not detected. We have observed that there is a "reddening" of the NSB, i.e. a shift to larger wavelengths, at large zenith angles or in nights with high humidity. Both conditions entail more light being absorbed in the atmosphere due to more atmospheric depth to be traversed or low atmospheric transmission respectively. The ratio singles-rate to current is lower under such conditions. The low atmospheric transmission produces also a decrease in the difference of NSB between two positions of the sky with respect to clear nights, we found a 70% change in the difference between the two positions in the most extreme case. The value of NSB can also change from night to night due to e.g. the presence of clouds which scatter light. Nights reported as "bright" (air glow of the nearest city visible and general brightness on the sky) by the operator on the GRAAL site have typically NSB values $\approx$5% higher with respect to dark nights, the difference in two positions of the sky being usually lower in the brighter night.

The NSB reflected by all the heliostats seen by a certain cone adds in the GRAAL configuration, the total background being ≈ 10 times higher than for the other experiments on solar farms and producing an increase in the energy threshold (section 2.3.3.2). The total number of photoelectrons collected by a GRAAL PMT only due to the NSB contribution is 13(9) p.e./ns for cones 1-2(3-4) respectively[2], compared to 0.7 p.e./ns in CELESTE [45].

[2]The PMTs of cones 3-4 see 18 heliostats each vs. the 13 seen by the PMTs of cones 1-2, but the field of view seen by the former is much lower, from 0.2 deg of the last row of heliostats (seen by cones 3-4) to 0.4 deg in the first row of heliostats (seen by cones 1-2).

11.2 Effects of the NSB

11.2.1 Influence of the NSB on the trigger rate

An increase of the night-sky fluctuations over the normal level can produce an increase in the trigger rate, either by causing accidental events or by lowering the energy threshold of the detector. These effects are explained in the following sections.

11.2.1.1 Random events

Ideally, the trigger rate in a Cherenkov detector has only two components: the gamma-ray source events and the hadronic background events. The rate of these components is proportional to $E_{th}^{-\delta}$ where E_{th} is the energy threshold of the detector for each component and the index δ is equal to the source primary energy spectrum index, i.e., for the hadronic background $\delta = 1.7$ and for the gamma source δ is dependent on the source (e.g. $\delta = 1.4$ for the Crab nebula [114]). This is however only approximate for a real detector, where the various non-linearities in the shower development and the detector (amplifiers and instrumental effects) affect the weight of both components on the trigger rate.

Moreover, for real detectors a third component might appear, namely, additional background events originated due to random sky-noise pulses. The accidental trigger rate is determined by the NSB level. In general, the threshold of the discriminators used in the trigger configuration of the detector (section 3.3.2.2) is set so that the rate of accidental events is zero. However, it can happen that under abnormal conditions of light the NSB level increases and accidental events are recorded.

In GRAAL, the rate of accidental events caused by the charge trigger (section 3.3.2.1) is given by the probability of 3 cones out of 4 triggering simultaneously due to the individual q-rates at each cone:

$$R_{\mathrm{acc}}^{\mathrm{q}} = 4\tau^2(R_1^{\mathrm{q}} \cdot R_2^{\mathrm{q}} \cdot R_3^{\mathrm{q}} + R_1^{\mathrm{q}} \cdot R_2^{\mathrm{q}} \cdot R_4^{\mathrm{q}} + R_1^{\mathrm{q}} \cdot R_3^{\mathrm{q}} \cdot R_4^{\mathrm{q}} + R_2^{\mathrm{q}} \cdot R_3^{\mathrm{q}} \cdot R_4^{\mathrm{q}}) \tag{11.2}$$

where R_{acc}^{q} is the total rate of "charge" accidental events, R_n^q is the q-rate recorded at cone n and τ is the coincidence window time of the charge trigger (200 ns, section 3.3.2.2).

The rate of accidental events caused by the sequence trigger is given by the probability that cones 1 and 2 trigger at the same time accidentally and is calculated from the individual sequence trigger rates of each cone:

$$R_{\mathrm{acc}}^{\mathrm{seq}} = 2\tau^2(R_1^{\mathrm{seq}} \cdot R_2^{\mathrm{seq}}) \tag{11.3}$$

where R_{acc}^{seq} is the total rate of "sequence" accidental events, R_n^{seq} is the sequence rate recorded at cone n and τ is the coincidence window time of the sequence trigger (150 ns, section 3.3.2.2). Hence, the rate of accidental events rises with the individual sequence and q-rates. An increase of the NSB level affects mainly the individual q-rates. The high rejection of the very selective sequence trigger produces very small individual sequence-rates. Therefore, the q-trigger is the most affected by the NSB.

The probability of accidental events is calculated every 2 seconds, so that peaks of high intensity (e.g. due to the light of a car) can be detected.

The first data taken by GRAAL (during season 1999/2000) were contaminated by accidental events. This was due to a setting of the discriminators threshold (at the hardware level) very close to the fluctuations of the night sky -to achieve the lowest possible energy threshold- and which turned out to be very sensitive to NSB variations. With the new settings of season

2000/2001 the individual rates were lowered so that the total rate of real events was still the same as for season 1999/2000 but there were no more accidental events[3].

11.2.1.2 Influence of the NSB in the energy threshold

The night sky background fluctuations introduce a modulation of the base line and "push" over the threshold events which would have been rejected in the absence of NSB. The opposite effect, events over the threshold which do not trigger due to a negative fluctuation of the night sky, happens more seldom due to the negative power law dependence (with an index of -2.7 [242]) of the cosmic rays rate on energy.

Therefore, a difference in the fluctuations of the NSB between two regions of the sky (ON and OFF) produces a slightly higher trigger rate in the noisier region due to an excess of very low energy events (the overall effect is a lower energy threshold for this region).

For the GRAAL setup this effect was Monte Carlo simulated by raising the amount of random noise by 5% over its usual value. The detector Monte Carlo models the electronic pulse shaping and the response of the discriminator in detail (section 5.2) and so the effective change in threshold, due to the increased noise level could be deduced to be about 6±2%.

For the study of sources with low statistics and differences in the NSB of a few per thousand, as most of the sources studied throughout this thesis (see 4th column of tables 12.4-12.5 in section 12.4), the effect is within the statistical error. Nevertheless, as the statistics grow or if the difference in NSB increases to a few percent (for example a 2% in the case of Mrk421), a correction must be made.

11.2.2 Effect of NSB differences on reconstruction

A difference in NSB leads to slightly different noise levels in ON and OFF data and can introduce systematic effects in the reconstruction of the events.

Noise peaks can surpass the software-threshold ($n_t \cdot \sigma_{NSB}$, section 6.1.2.1) and be confused with real Cherenkov peaks by the analysis program under high levels of NSB. Besides, the real peaks can be "masked" by fluctuations of the night sky. In general, the timing fluctuations of the shower front increase due to the "deformation" of the Cherenkov peaks. The overall effect is a less effective angular reconstruction of the showers (section 11.3.3).

11.3 Correction procedures of NSB effects

11.3.1 Rejection of accidental events at the software level

Accidental events can be generated by our detector in conditions of high NSB (section 11.2.1.1). We are interested in rejecting all the accidental events during analysis, since they can create or destroy a gamma-ray signal.

In an analysis of raw events (without reconstruction of the direction of the showers), the number of random events can be calculated for a certain set of data (section 11.2.1.1) and subtracted from the total number of events (section 13.2) so that a proper evaluation of the excess events in the ON position with respect to the OFF position can be made.

An alternative analysis of the data involves the reconstruction of the shower front (section 6.2). In this case, the random events can not be subtracted from the sample since we know the

[3] This has been cross-checked with the events recorded in OF2 mode (section 3.1.4). Since in that mode all the heliostats are defocused, the recorded events will be only accidentals.

σ_{NSB}	n_t	Raw events	Rec evs	Central evs
1.014	5	5129	31	2
1.014	7	5129	0	0

Table 11.1: σ_{NSB}*: RMS fluctuation of the measured NSB (in flash-ADC units) of all events in sample,* $\mathbf{n}_t$*: level of software-threshold in analysis (defined in section 6.2.2),* **Raw events***: all hardware-triggered events which traces were recorded,* **Rec. events***: number of events after angular reconstruction and software trigger,* **Centr. events***: number of events in central angular region (within 0.7 degrees of pointing direction). The number of random reconstructed events is 0.6% for* n_t*=5 and 0% for* n_t*=7.*

number of events contained by the sample (see above) but not "which ones" are the random events. However, it is expected that the random events are rejected after the reconstruction of the showerfront by imposing software cuts (section 13.1.2) to the reconstruction parameters (see below).

To prove the validity of this hypothesis, random events were artificially generated. A tungsten lamp was adjusted to give a light intensity similar to the produced by the NSB (compare tables 11.1 and 12.4) and the generated accidental events were recorded by the data acquisition program. The door of the hut was kept closed during the whole measurement to prevent any influence of changing light conditions in the outside.

The data file was analysed with various threshold values (see table 11.1) similar to the ones used for the real data analysis. It was found that less than 0.6% of the accidental events pass the analysis cuts (see table 11.1) and only a 6% of these events are reconstructed in the centre (less than a 0.04% of the total number of events) for a value of $n_t = 5$, equal to the chosen for the analysis of Crab data. With a higher value of n_t no events are reconstructed.

The random events are rejected by the analysis program due to the incorrect timing pattern of the noise peaks. There are two possible reasons for the rejection:

- The number of peaks used for the reconstruction is lower than the limit value (set as 5 in section 13.1.2): this happens when the maximum possible number of peaks is rejected (since they do not fit in the expected time pattern) and only few peaks (less than 5) remain.

- The values of lsq_t^2 are higher than the imposed limit (set as 100 in section 13.1.2): this happens if the number of peaks used in the reconstruction (NREMAIN in section 9.2) is still high (above 5).

The reconstructed events for $n_t = 5$ are very noisy events. These events have exactly 5 reconstructed peaks and the value of lsq_t^2 is lower than the imposed limit due to the fact that 5 peaks can be fitted to a wrong direction with a low lsq_t^2. They can be rejected just by raising the usual software cut of "minimum number of reconstructed peaks" from 5 to 7.

In our analysis, the fraction of rejected events increases with the noise (section 11.3.3). Then, the increase of the number of accidental events during data taking does not affect the total number of events after analysis but it is still detrimental since it increases the dead time of the setup (section 3.3.3.1). Therefore, the GRAAL discriminators were set in the season 2000/2001 so that no accidental events are recorded.

11.3.2 Dynamical threshold

For all the experiments trying to detect a gamma-ray excess by statistical comparison of two regions of the sky ON and OFF, it is very important to prove that the difference in energy threshold between both regions is negligible within the statistical errors (section 11.2.1.2). In GRAAL, in order to eliminate this difference, the selection of the peaks which are used to reconstruct the temporal shower front is done with a "dynamical (variable) threshold". This means that the minimum amplitude necessary to consider a peak as a real Cherenkov pulse is not a fixed number of p.e. (or ADC channels) but a fixed number (n_t) of deviations from the fluctuations of the NSB (σ_{NSB}), σ_{NSB} being calculated for each of the four traces of a shower and for all the showers independently (section 6.1.2.1).

This section demonstrates that the analysis with dynamical threshold reduces the difference of energy threshold between two regions of the sky -caused *exclusively* by different levels of NSB fluctuations- to a non-significant value within the statistical errors.

To test the efficiency of the dynamical threshold technique we have chosen a set of data taken on the unidentified EGRET source 3C454.3 (1.5 hours pointing to the source and an equal amount of time pointing to an OFF position). The reason is that one of the largest difference of NSB fluctuations between ON and OFF regions (2%) has been observed for the data taken on this source (see section 12.4). In principle, an ON position where no gamma-ray source is expected is more suitable for the test. However, it seems likely that the results of this section are not influenced by the fact that a source was expected in the ON region when the data was taken, since no significant excess was found after 9 h 10 min of ON source observation (section 13.1.4.5) and we are using only 1.5 hours.

The data file has been analysed with two different thresholds:

- **Dynamical threshold**: the amplitude threshold for the Cherenkov peaks is calculated independently for each event.

- **Fixed threshold**: the amplitude threshold for the Cherenkov peaks is the same for all the events.

The results of the analysis with the two proposed thresholds are shown in table 11.2. The difference in energy threshold between ON and OFF periods (given by the integrated charge IC, section 9.1) is 0.6% for the analysis with a fixed threshold at a 2.1σ level of significance. After the analysis with dynamical threshold the energy threshold is equal for ON and OFF periods within the statistical error. The difference in energy threshold between ON and OFF periods with the former analysis translates in an excess of events in the OFF region (where the energy threshold is slightly lower), whereas the difference of number of events between ON and OFF periods with the second analysis is non-significant as expected.

A final check has been done to prove that the difference of energy threshold between ON and OFF regions after a fixed threshold analysis is the same independently of the absolute energy threshold. The same data file has been analysed again, this time with a fixed threshold (called "Fix th 1") which is a 2% lower than the fixed threshold used up to now (called "Fix th 2"). Table 11.3 shows the results of this study. As expected, the difference between ON and OFF regions is the same for both analyses, but the absolute energy threshold is higher for the "Fixed th 2" and therefore a smaller number of events is reconstructed.

	IC		Reconstructed events	
	Fix th	Dynamical th	Fix th	Dynamical th
ON	3.812±0.007	3.813±0.007	4420	4447
OFF	3.791±0.007	3.804±0.007	4621	4551
EXCESS	0.021±0.010	0.009±0.010	-201± 95	-104±95

Table 11.2: *Difference (EXCESS) in integrated charge (IC) and number of reconstructed events between the ON and OFF regions for two analyses performed with two different thresholds, fixed and variable (see text).*

	IC		Reconstructed events	
	Fix th 1	Fix th 2	Fix th 1	Fix th 2
ON	3.803±0.007	3.812±0.007	4488	4420
OFF	3.780±0.007	3.791±0.007	4697	4621
EXCESS	0.023±0.010	0.021±0.010	-209±96	-201± 95

Table 11.3: *Difference (EXCESS) in integrated charge (IC) and number of reconstructed events between the ON and OFF regions for two analyses performed with different fixed thresholds (see text).*

11.3.3 Software padding

The systematic effects introduced by the NSB in the event reconstruction (section 11.2.2) can be studied by adding noise artificially to the recorded traces at the software level. This method is known as "software padding" and was first used by the Whipple collaboration [44].

There are different methods of adding the noise (see e.g. [44] and [68]). In GRAAL, the first 40 ns (80 channels) of the FADC trace are considered as a "noise pattern" and this pattern is added sequentially along the trace considering the non-linear gain of the amplifiers (section 3.3.1). The conversion of the amplitude A_i of channel i to A'_i (with the additional noise) is given by:

$$A'_i = (A_i^{1/1.4} + a \cdot A_j^{1/1.4})^{1.4} \tag{11.4}$$

where $j = i - n \cdot 80$ and $n = integer(i/j)$ (the index j indicates the channel of the "noise pattern" which has to be added to each index i; n indicates the number of "80 channels" intervals that we have to go back in the trace to find the noise pattern). The factor a denotes the fraction of initial noise which is added and 1.4 is the non-linear gain of the amplifiers.

Fig. 11.1 demonstrates that the fraction of events near the source direction (well reconstructed events) decreases with increasing NSB, but the effect is only significant at relatively large increases on the order of a few percent.

Table 11.4 shows the decrease of the overall reconstruction efficiency with the increase of the RMS noise. An increase of RMS noise by 1% decreases the overall reconstruction efficiency by about 0.6% whereas the peak to tail ratio PT (section 12.2.2.2) remains invariable within the statistical errors. It is expected that the reconstruction efficiency worsens as the NSB increases. With an increased level of NSB, the Cherenkov peaks will be deformed by the NSB and noise peaks will pass the threshold being taken as real ones. The overall effect is an increased value of lsq_t^2, either because the identification heliostat-signal is wrong or due to the noise peaks which do not fit in the time pattern of the shower front. In both cases the events will be rejected by

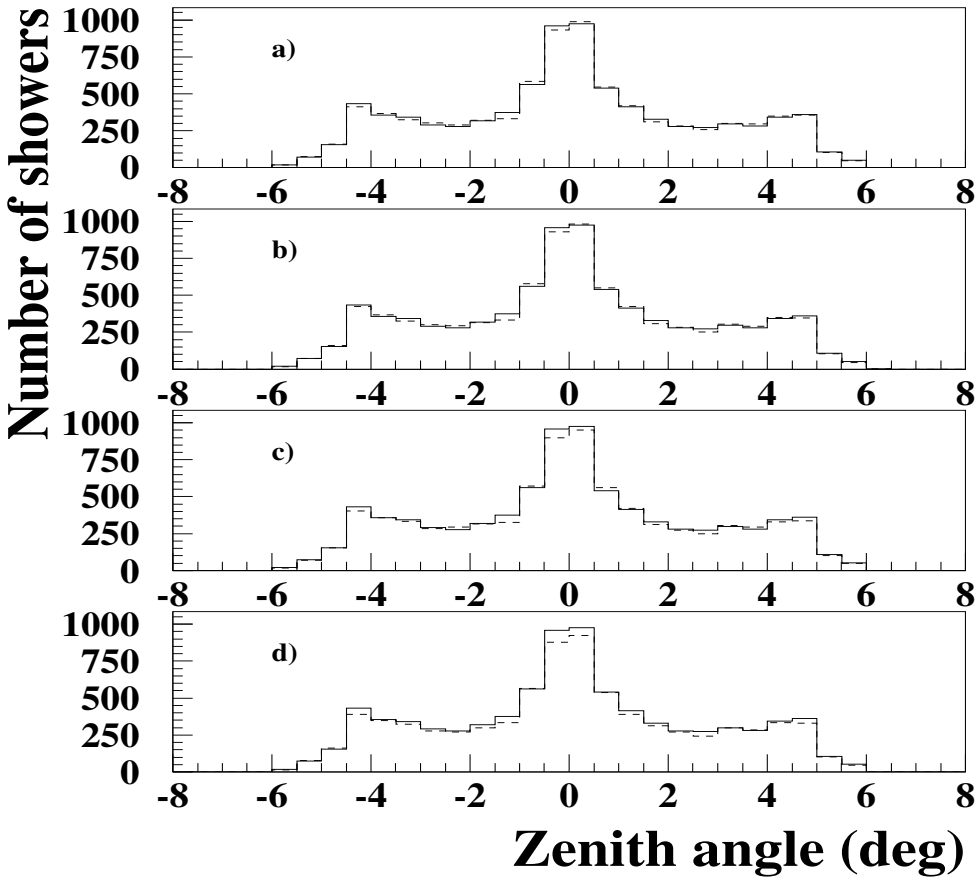

Figure 11.1: *The number of showers as a function of difference in angular distance to the source direction reconstructed with the experimental NSB (full line) and NSB increased on the software level (dashed line) by 0.5% (panel a.), 1% (panel b.), 5% (panel c.) and 10% (panel d.). In the lower plot a decrease of the fraction of events within the central region is obvious (notice that this is agreement with table 11.4). The variation of PT is the one shown in table 11.4 (notice that the reduction of events in the central region does not necessarily entails a reduction of the PT parameter).*

a	0	0.005	0.01	0.05	0.1
σ_{NSB}	0.974	0.978	0.983	1.018	1.064
Rec events	8412	8378	8355	8212	8016
Central events	2000	1990	1989	1934	1898
Ratio PT	0.460±0.012	0.460±0.012	0.462±0.012	0.456±0.012	0.458±0.013

Table 11.4: *Number of reconstructed (rec) and central events and ratio PT for different NSB levels. The σ_{NSB}, that indicates the increase of night-sky from column to column, is measured in the trace after having added the noise. The parameter a indicates the amount of noise that is added according to eq. 11.4.*

the lsq_t^2 software-cut (section 13.1.2), thus decreasing the number of reconstructed events in the second row of table 11.4.

In contrast, we expect a small variation in the ratio PT. An increased NSB will produce a migration of events reconstructed in the centre (well reconstructed) to the tails of the distribution shown in fig. 6.5. However it is also very likely that events in the tail of the distribution, which had a wrong identification heliostat-pulse but passed the lsq_t^2 cut due to their very low number of peaks (5-6), are rejected when the night-sky is increased (the noise peaks add to the number of existent peaks and the lsq_t^2 increases over the limit). In short, the ratio PT does not necessarily worsens with an increased night-sky. The change of PT will be determined by the balance between the number of events in the tails which are rejected with an increased NSB and the number of events which "abandon" the centre of the distribution of reconstructed directions (because they are rejected or because they migrate to the tails).

For the sources observed up to now the differences of the RMS NSB are a few tenths of a percent at maximum (see section 12.4) and therefore the effect over the reconstruction has been neglected.

11.4 Conclusions

Much work has been already done on the NSB effect by other experiments since the 1960s [55, 66].

In the wavefront samplers, the time correlations between different detectors discriminate the Cherenkov showers against the night-sky background. However, the night-sky has still a big influence in the recorded Cherenkov showers when the detectors work near the fluctuations of the night-sky as seen in this chapter. Working with a threshold very far above the NSB (like it is done for example in the HEGRA telescopes array) has the advantage of eliminating partially the night-sky effects but increases the energy threshold of the experiment. However, the heliostat arrays were conceived exactly to achieve a lower energy threshold than the existing Cherenkov telescopes.

In GRAAL, the effects of the NSB have been corrected successfully for the data analysed up to now (chapters 12 and 13). The random events have been subtracted from the raw data sample. For the analysis of data taken during the period September 1999-July 2000, affected by a large number of accidental events, the difference between ON and OFF source raw rates decreases strongly after subtraction of such events (see table 13.13). In contrast, for the other sources no significant variations are seen, indicating a low number of randoms, in agreement with the change of the detector setup.

The software padding is not necessary for our data sample due to the small ON-OFF differences of NSB involved (less than 1% for all the observed sources). However, this method would have to be applied if large (ca. 5%) differences of NSB are observed for some source.

The dynamical threshold decreases the difference in energy threshold induced by different values of NSB in ON and OFF positions up to a non-significant level for the sources discussed in this thesis. However, with an increase of statistics, a different correction procedure would be required.

Chapter 12

Selection and properties of the data

GRAAL has been taking data since September 1999. From that date to the end of March 2001 more than 250 hours of data on 18 different sources were recorded (see next section) and more than 80% of the data were analysed.

This chapter deals with the process of selection of "good nights" for analysis (as we will see later, the term "good" is very subjective). Section 12.2 describes the criteria used to select a sample of "good quality" data and section 12.3 explains the influence of the data acquisition conditions in the selection criteria. Once that a set of data has been chosen, it is important to know the characteristics of the sample, which change for each source, namely, the level of night-sky background, the PMTs current, the charge trigger rate and the energy threshold (given by the integrated charge parameter, section 8.2). Section 12.4 shows and discuss the properties of the selected set of data, especially focusing on the difference of the properties between ON and OFF positions.

12.1 Data sample

Table 12.1 shows the total data set taken with the fully completed detector from August of 1999 until March of 2001. The only significant change during this time was the introduction of the charge trigger in October 1999 in addition to the already existent sequence trigger.

12.2 Criteria for data selection

We are interested in selecting a "good" set of data for analysis. The requirements which must be fulfilled by the data are divided in two main parts: conditions related to the detector (section 12.2.1) and to the weather (section 12.2.2).

12.2.1 Detector condition

We must ensure that there were no malfunctions of the detector, neither of the heliostat field nor of the electronics, during data acquisition to consider valid a set of data.

A check of the good operation of the heliostat field, comprising the status of the heliostats and the communication between the heliostat control computer and the heliostat field, is done at the beginning of analysis (section 6.1.1). Mechanical disorders of more than 10 heliostats or a loss of communication during more than 30 s reveal a field malfunction. All periods of data

Source	Time (min)	Period	n_t	Time selected (min)
3C273	230	Jan-Feb 01	5	90
3C279	320	Apr-Jul 00	-	-
	390	Jan-Feb 01	5	90
3C454.3	470	Sep 99	9	280
	400	Sep 00	7	270
3EG J1835	860	Jul-Sep 00	9	490
BL Lac	1080	Aug-Sep 00	5	210
Crab nebula	2380	Sep 99-March 00	5	430
	1630	Sep 00- March01	5	230
GRB980703	500	Sep-Oct 99	-	-
GRB981220	50	Oct 99	5	0
GRB120899	80	Dec 99	5	0
GRB121699	20	Dec 99	5	0
GRB010222	1090	Feb-Mar 01	5	730
Kuehr0428+20.5	90	Dec 00	5	60
Mrk421	1690	Jan-May00	6	480
	1110	Feb-March 01	6	570
Mrk501	320	Mar-Apr 00	5	0
Pseudo source 1	500	Jul 00	7	250
Pseudo source 2	1250	Mar-Jun 00	-	-
PSRJ1939	310	Sept 99	-	-
Quasar 1204+281	220	March 00	-	-

Table 12.1: *Sources observed by GRAAL from September 1999 to March 2001,* **Time***: time of observation for each source,* **Period***: period of the year during which the source was observed,* $\mathbf{n}_t$*: threshold used in the analysis of the data (section 6.2.2),* **Time selected***: duration of the selected set of data for each source according to detector and meteorological conditions (see section 12.2). The sources for which n_t is not indicated ("-") have not been analysed yet.*

where the heliostat field was not working properly (for any of the previous reasons) are removed from analysis.

In addition, the high voltages and currents of the photomultipliers are constantly monitored together with the trigger rates (section 3.17) during data acquisition. A normal operation of all four detector channels is required to accept a set of data.

12.2.2 Meteorological selection

The choice of the criteria which decide the quality of a set of data is a very subtle task. The perception of the weather conditions by an observer is highly subjective and consequently data taken in nights which were reported as "good" by the night operator of the PSA were rejected after analysis (see below).

Besides a "general good quality" of the data, the stability of the weather conditions during a complete period ON-OFF of data acquisition must be ensured. The reason is that GRAAL tries to detect a source excess of gamma-rays by statistical comparison of data taken in the first part of the period (ON or pointing to the source) and the second part (OFF or pointing to a test position) (section 13.1.3) and weather instabilities during data acquisition can create a difference in the number of the recorded events.

12.2.2.1 Influence of the weather conditions on the quality of the data

In GRAAL, it was found that the quality of the data depends strongly on the atmospheric transmission. For example, in nights which were visibly hazy with a high relative humidity above 80% (a relatively frequent nightly weather condition at the PSA, section 3.1.1), the total trigger rate was low, the ratio of well reconstructed events to events with a misreconstructed angular direction (section 6.2.2)- called "PT" below - was reduced by up to a factor 2 and the lsq_t^2 of the fit to the timing front significantly increased. This is probably the result of selective absorption, i.e. Cherenkov light from the deeply penetrating part of the airshower, with increased temporal fluctuations, dominates the recorded signal. As gamma-induced showers develop mainly in the upper atmosphere a selection of data without selective absorption is important.

During the first winter of operation (October 1999-February 2000) it was found that a second effect of a high level of humidity (>80%) was the formation of dew on the heliostats (section 3.1.3.3), which caused a reduction on the total trigger rate of up to a factor 10.

The lsq_t^2 of the fit to the timing front increased not only with a low atmospheric transmission but also with high wind speeds (above 30 km/h) due to the "vibration" of the heliostats, that causes a fluctuation in the arrival times of the pulses.

Besides the above mentioned conditions, scattered clouds can alter the stability of a period ON-OFF by moving into the field of view of the Winston cones during a short period of time.

12.2.2.2 Parameters used for the selection of the data

The values of temperature, wind speed and humidity are recorded continously during data taking and every 20 min during the day. In addition, images of the Meteosat satellite and several web pages reporting the weather conditions in Almería were recorded every 3 hours. A weather report was also written by the night operator of the PSA three times during the night. All this information was checked for each of the nights before beginning data analysis.

The data reconstruction was found to be more sensitive to weather conditions than the human eye. The following parameters were chosen to "indicate" a low atmospheric transmission:

	Source			
	3C454.3	3EGJ1835	BL Lac	Crab nebula
PT	$\geq$0.8	$\geq$0.2[1]	$\geq$0.7	$\geq$0.8
Rate	$\geq$ 50	$\geq$ 40	$\geq$40	$\geq$50
RO	$>$ 0.95 and $<$ 1.05			
	Mrk421	Mrk501	Pseudo 1	
PT	$\geq$0.6	$\geq$0.5	$\geq$0.5	
Rate	$\geq$50	$\geq$50	$\geq$40	
RO	$>$ 0.95 and $<$ 1.05			

Table 12.2: *Limits imposed on the parameters for the selection of data taken from September 1999 to September 2000.*

- **PT** = (Number of events with reconstructed directions $< 1^\circ$ from pointing direction OFF source) / (Number of events with reconstructed directions $>3^\circ$ from pointing direction OFF source)
- Rate after all software cuts in OFF source direction

The previous parameters were calculated for the OFF source direction, since the ON source direction can be influenced by a gamma-ray excess. The reason to use the "rate after all software cuts" instead of the "total trigger rate" (or rate of hardware-triggered events) is that the total rate can be high due to e.g. accidental events or noisy events in "bright" nights and these events are rejected by the software cuts (section 13.1.2).

Three more parameters were used to exclude unstable weather conditions:

- Stability of the single peaks rate within a period ON-OFF
- Stability of the photomultipliers current within a period ON-OFF
- **RO** = (Number of events with reconstructed direction $> 3^\circ$ from pointing direction ON source) / (Number of events with reconstructed direction $> 3^\circ$ from pointing direction OFF source)

12.2.2.3 Parameter limits for data selection

The limits for the parameters of previous section were chosen such that a set of "good" nights -defined as showing fairly constant parameter values- was retained. Some of the parameters were shown to depend on the pointing position, e.g. PT. This is an expected behaviour since the quality of the reconstruction -indicated by the PT parameter- is influenced by the number of peaks used in the showerfront reconstruction and the number of peaks is clearly dependent on the pointing position (section 9.3.1). Therefore, the parameters depending on the pointing position have different limits for each source (see tables 12.2-12.3).

As a first quality "cut" general clear skies and humidities below 65% were required for all the data.

Tables 12.2-12.3 summarize the limits imposed on the parameters PT, RO and "rate after all software cuts in OFF source direction" (see previous section) for each of the sources.

[1]The reason for the small limit of PT is the bad quality of reconstruction for the source 3EG J1835+59 due to the overlap of the peaks (section 13.1.4.3).

	Source		
	3C273	3C279	Crab nebula
PT	$\geq$1.0	$\geq$1.0	$\geq$0.8
Rate	$\geq$50	$\geq$50	$\geq$50
RO	> 0.95 and < 1.05		
	Kuehr0428+20.5	Mrk421	GRB010222
PT	$\geq$1.1	$\geq$0.5	$\geq$0.5
Rate	$\geq$70	$\geq$60	$\geq$60
RO	> 0.95 and < 1.05		

Table 12.3: *Limits imposed on the parameters for the selection of data taken from October 2000 to March 2001.*

The ratio PT was found to be lower for sources near the zenith and in the north direction in comparison with southern sources with a large zenith angle ($> 30°$) due to the higher reconstruction efficiency of the latter.

The total trigger rate is higher for sources near the zenith than for those with a large zenith angle. However, the "rate after all software cuts" does not have to be necessarily higher for sources near the zenith, since a low reconstruction efficiency due to more overlapping peaks reduces in a larger percentage the initial number of events (total trigger rate) for these sources than for those far from the zenith. For sources which were observed during a long period of time (and therefore with different positions in the sky) the limits shown in tables 12.2-12.3 are a mean value of the limits imposed for each month.

The limits for RO were the same for all the observed sources, since RO is not affected by the position of the source.

12.3 Influence of the data acquisition conditions in the selection criteria

During the analysis of the data taken on the Crab nebula during the period 2000-2001 it was noticed that the quality of the reconstruction was inferior to the one of previous period. In particular, the ratio PT was smaller by 10% (from a mean PT of 1.0 in 1999-2000 to 0.9 in 2000-2001) and a larger percentage of data had to be rejected than in the previous period despite the better meteorological conditions and the absence of dew on the mirrors (this problem was solved during the 1999-2000 period, section 3.1.3.3).

It was found that the worsening of the reconstruction quality was due to a decrease of the number of peaks used in the reconstruction of the showerfront due to some inoperational heliostats in the period 2000-2001 with respect to the period 1999-2000. An increase of the time fluctuations, that would also produce a worse angular reconstruction, was not detected.

Fig. 12.1 shows the dependence of the ratio PT of section 12.2.2 with the number of peaks used in the reconstruction of the showerfront. It is observed that the ratio PT increases exponentially with the number of peaks. This is an expected behaviour which can be derived from the dependence of the angular resolution with the number of peaks shown in section 8.1. An improvement of the angular resolution of a sample due to a higher number of peaks produces a migration of events from the outer region ($>3°$) to the inner region ($<1°$), so that the ratio

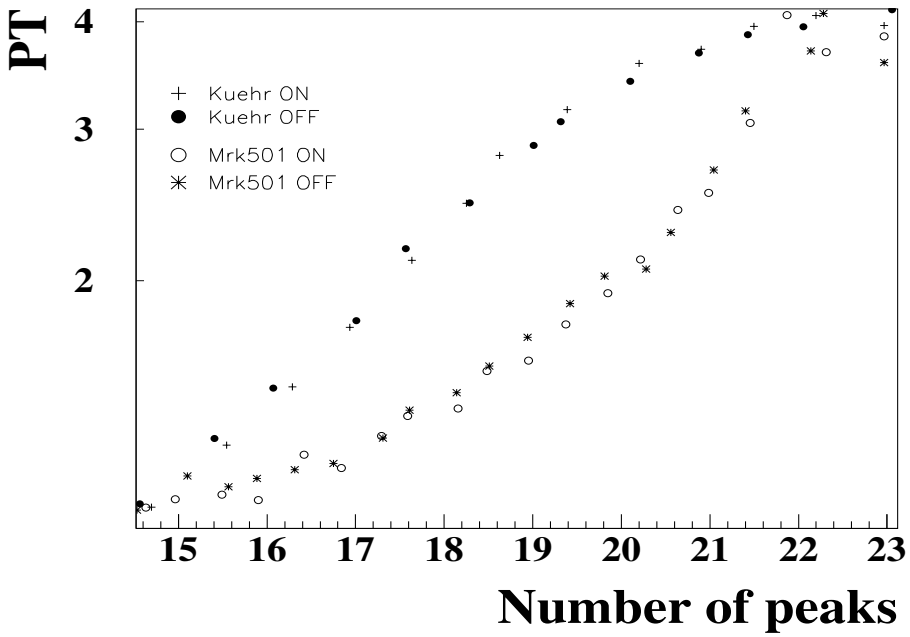

Figure 12.1: *Dependence of the ratio PT defined in section 12.2.2 with the number of peaks used for the reconstruction of the shower front for data taken on the source Mrk501 ON (open circles) and OFF (stars) and on the source Kuehr0428+20.5 ON (crosses) and OFF(filled circles). For the same number of peaks the ratio PT changes from source to source due to the different position of the peaks but it does not change from ON to OFF positions of a same source, since the same part of the sky is tracked.*

PT increases due to both effects (increase in the inner region and decrease in the outer region). Moreover, the relation between the ratio PT and the number of peaks changes from source to source (see fig. 12.1) -since the ratio PT is sensitive also to the position of the peaks- but *is the same for ON and OFF positions of the same source.* This is a crucial point for the search of a gamma-ray excess comparing the number of reconstructed events in the ON and OFF positions (section 13.1.3), since a different reconstruction efficiency in both positions can create a signal in the position with a higher efficiency.

12.4 Properties of the selected set of data

This section presents the properties of the set of data which has been selected for each source following the criteria of section 12.2.2. Each of the tables 12.4-12.5 contains the characteristics of the data taken on various sources while pointing to the source (ON) and pointing to a position on the sky (OFF) with a right ascension 2.625 degrees larger than in the ON direction.

The difference of NSB fluctuations between the ON and OFF positions (column 3 in tables 12.4-12.5) is especially important for all the reasons mentioned in chapter 11. For all the observed sources, the maximum difference between the value of σ_{NSB} for ON and OFF is 0.8% for Markarian 421. By measuring the random noise in complete darkness, we determined a

Source (time)	Current (μA)	Q-rate (kHz)	σ_{NSB} (ADC units)	log (mean IC)
3C454.3 (550 min)				
ON	17.7 ± 0.4	3.1	0.9505 (0.3922)	3.119 ± 0.003
OFF	20.3 ± 0.3	4.1	0.9540 (0.4006)	3.113 ± 0.003
EXCESS	-2.6	-1.0	-0.0035 (-0.0084)	0.006 ± 0.004
3EGJ1835+59 (490 min)				
ON	15.5 ± 0.6	1.7	0.9528 (0.3977)	3.122 ± 0.002
OFF	15.8 ± 0.6	1.8	0.9519 (0.3956)	3.116 ± 0.002
EXCESS	-0.3	-0.1	0.0009 (0.0021)	0.006 ± 0.003
BL Lac (210 min)				
ON	16.3±0.4	1.28	1.0419(0.5796)	2.959 ± 0.005
OFF	16.2±0.4	1.27	1.0387(0.5738)	2.957 ± 0.005
EXCESS	0.1	0.01	0.0032(0.0058)	0.002 ± 0.007
Crab 99-00 (430 min)				
ON	19.0±0.4	1.35	0.9493 (0.3893)	2.940 ± 0.004
OFF	19.3±0.3	1.49	0.9497 (0.3902)	2.937 ± 0.004
EXCESS	-0.3	-0.14	-0.0004 (-0.0009)	0.003 ± 0.006
Mrk 421 00 (480 min)				
ON	14.9 ± 0.3	6.88	0.9744(0.4471)	3.024 ± 0.003
OFF	13.7 ± 0.3	5.47	0.9666(0.4299)	3.031 ± 0.003
EXCESS	1.2	1.41	0.0078(0.0172)	-0.007 ± 0.004
Pseudo source (250 min)				
ON	16.6 ± 0.5	4.3	0.9564 (0.4063)	2.991 ± 0.003
OFF	17.3 ± 0.5	5.7	0.9588 (0.4119)	2.993 ± 0.003
EXCESS	-0.7	-1.4	-0.0024 (-0.0056)	-0.002 ± 0.005

Table 12.4: **Current** *(mean of 4 cones),* **Q-rate***: single trigger rate of charge integrating channel (mean of 4 cones),* σ_{NSB}*: RMS fluctuation of the measured NSB (in flash-ADC units) of all events in sample,* **log(mean IC)***: decadic logarithm of mean net-charge (in flash-ADC units) of all events in the sample. Rows are for the samples with pointing towards the indicated source ("ON") and on a sky position ("OFF") with a right ascension 2.625 degrees larger than in the ON direction. The data shown has been taken between September 1999 and September 2000.*

Source (time)	Current (μA)	Q-rate (kHz)	σ_{NSB} (ADC units)	log (mean IC)
3C273 (90 min)				
ON	15.9±0.2	1.38	0.9539(0.4005)	2.988 ± 0.007
OFF	16.5±0.2	1.53	0.9544(0.4015)	2.995 ± 0.007
EXCESS	-0.6	-0.15	-0.0005(-0.0010)	-0.007 ± 0.010
3C279 (90 min)				
ON	15.1±0.6	1.17	0.9447(0.3780)	2.988 ± 0.007
OFF	15.4±0.6	1.29	0.9484(0.3871)	2.979 ± 0.007
EXCESS	-0.3	-0.12	-0.0037(-0.0091)	0.009 ± 0.010
Crab 00-01 (230 min)				
ON	19.0 ± 0.5	3.1	0.9577 (0.4094)	2.977 ± 0.004
OFF	19.3 ± 0.5	3.1	0.9599 (0.4145)	2.983 ± 0.004
EXCESS	-0.3	0.0	-0.0022 (-0.0051)	-0.006 ± 0.006
GRB010222 (730 min)				
ON	14.4±0.3	1.0	0.9380(0.3609)	2.986 ± 0.002
OFF	14.7±0.3	1.1	0.9387(0.3628)	2.986 ± 0.002
EXCESS	-0.3	-0.1	-0.0007(-0.0019)	0.000 ± 0.003
Kuehr0428+20.5 (60 min)				
ON	18.3±0.0	0.63	0.9309(0.3419)	2.985 ± 0.009
OFF	18.3±0.0	0.79	0.9298(0.3390)	2.987 ± 0.008
EXCESS	0.0	-0.16	0.0011(0.0029)	-0.002 ± 0.012
Mrk 421 01 (570 min)				
ON	15.4 ± 0.2	1.97	0.9532(0.3987)	3.063 ± 0.003
OFF	14.3 ± 0.2	1.41	0.9465(0.3824)	3.061 ± 0.002
EXCESS	1.1	0.58	0.0067(0.0163)	0.002 ± 0.004

Table 12.5: *Entries as in table 12.5 but for data taken from October 2000 till March 2001.*

constant night-sky independent noise level with a RMS of 0.8658 (in ADC units). Subtracting this constant noise quadratically from the total noise we get the contribution from the NSB alone (number in brackets in third column of tables 12.4-12.5). For the source with the largest difference in noise level the NSB-induced component differs in ON- and OFF-source position by about 0.8%, so that the difference in brightness at the two positions can be estimated to be about 4%.

The NSB is related to the energy threshold (section 11.2.1.2). Therefore, it is logical to expect the largest difference in energy threshold between ON and OFF components for Mrk421. This source and 3EG J1835+59 show the most significant difference in integrated charge, which is proportional to the energy threshold (section 8.2), between ON and OFF positions (2σ and 1.75σ significance respectively) for the data presented in table 12.4. In table 12.5 all the sources have the same energy threshold within statistical fluctuations.

The effect of the difference in energy threshold for Mrk 421 will be further discussed in section 13.1.4 in connection with the observed excesses. It can be seen that the lowest energy threshold corresponds to the data taken on the Crab on period 1999-2000 and analysed with $n_t = 5$. In table 12.5 the highest energy threshold corresponds to the data taken on Mrk 421 due to the higher software threshold used for analysis ($n_t = 6$) in comparison with the other sources ($n_t = 5$). In table 12.4 we have to take into account that for the data taken on Crab and Mrk 421 the hardware threshold was effectively lower (the hardware settings were slightly modified in July 2000 to eliminate the random triggers, see section 11.2.1.1). Then, comparing the sources analysed with $n_t = 5$, Crab and BL Lac, we see that the former has lower threshold, since the BL Lac data was taken after the change of settings. The other sources in table 12.4 have been analysed with a higher software threshold (see n_t in table 12.1) and therefore the energy threshold is also higher.

The second column of the tables shows the current of the photomultipliers for the ON- and OFF-source positions. Although the current has been used traditionally to measure the differences in NSB between two regions of the sky, we found that the ratio between current and single rate (number of peaks above the hardware-threshold) depends on the weather conditions, i.e., in nights with a high level of humidity (>80%) the ratio single-rate to current was lower than in nights with low humidity (see also section 11.1).

Chapter 13

Search for a gamma source

The primary objective of GRAAL is the detection of gamma-ray sources which have not been observed yet by the ground-based telescopes at their lowest energy threshold.

To demonstrate the feasibility of the experiment for the detection of gamma rays, we have first observed the Crab nebula, a "standard candle" for VHE-gamma experiments. Then, preference has been given to the observation of possible "candidates" for VHE-gamma emitters with respect to known sources.

Section 13.1 explains the normalization technique which has been used throughout the last two years to search for gamma-ray sources. The results of the analysis of airshowers from the Crab pulsar, the blazar Markarian 421 and other potential sources are discussed. Section 13.2 explains a second method of analysis, which evaluates the total rate of the same data. Section 13.3 compares the two methods of analysis and gives a conclusion about the results.

13.1 Normalization technique

13.1.1 Time corrections

In GRAAL it can happen that the effective time of data acquisition is slightly different for the ON- and OFF-source periods. This difference in time must be corrected at the beginning of analysis, since a statistical comparison of the number of events taken in both periods can only be made for exactly the same data acquisition time.

During each period of 10 minutes of tracking a fraction of the total time (usually less than a 2%) is lost due to regular calibrations (section 4.3.5) and to the switch off of the photomultipliers if currents higher than 35 mA are detected (section 3.4). It might happen that the time lost in periods ON and OFF is different by a few seconds. During data analysis, the effective time is calculated for the ON and OFF positions and the number of events in the OFF position is corrected with a factor equal to "effective time in the ON position"/"effective time in the OFF position".

In addition, the dead time of the detector can be different for the ON and OFF periods due to the difference in trigger rate between both periods. Thus, the dead time is calculated for each period and the number of events in the OFF position is corrected with a factor equal to "fraction of accepted events in the ON position"/"fraction of accepted events in the OFF position", where the fraction of accepted events is given by the dead time of the setup (section 3.3.3.1).

The number of events in the OFF period was corrected with overall factors which were always smaller than 5% and usually of the order of 0-3%.

13.1.2 Software cuts

Two main software cuts have been imposed to the recorded events after the reconstruction of the showerfront with the method presented in chapter 6:

- Number of peaks used in the reconstruction of the shower front (called NREMAIN in section 9.2) ≥ 5.
- Value of lsq_t^2 obtained from the fit to the shower front (section 6.2.2) ≤ 100.

The value of the cuts has been chosen so that a fraction of misreconstructed events, with reconstructed directions more than 2° away from the pointing position, are accepted and can be used for normalization (see next section). The misreconstructed events are caused by a wrong assignment heliostat-pulse and are characterized by small NREMAIN (5-10) or large values of lsq_t^2 (2-100).

For events with only 5-10 reconstructed peaks, it is relatively easy to shift the time pattern in a way that fits some wrong direction with a low value of lsq_t^2. It has been shown that increasing the required number of reconstructed peaks to ≈ 10 the tails of fig. 6.5 become negligible (section 8.1).

For events with a large number of peaks (> 15), a wrong assignment heliostat-pulse is due to noise peaks which enter the fit and "confuse" the analysis program. These events have large values of lsq_t^2, between 2 and 100, due to the many peaks used in the fit. Less than 10% of the events that pass the first cut (in number of peaks) have values of lsq_t^2 larger than 2.

A third cut has been imposed on the value of the NSB fluctuation σ_{NSB} (see appendix A). This was done to reject a kind of events produced by electronic noise in the second photomultiplier (these events occur at a rate lower than 0.003 Hz).

13.1.3 Calculation of the excess

In the heliostat arrays, the detection of gamma-ray sources is made by means of statistical comparison of the events recorded in two positions of the sky: ON (pointing to the position of the "candidate" gamma source) and OFF (at a position with a right ascension 2.625° larger than in the ON position). Then, the significance of a signal is given by eq. 8.4 where

$$\mathrm{EXCESS} = \mathrm{ON} - \mathrm{OFF} \tag{13.1}$$

and

$$\mathrm{ERROR} = \sqrt{\mathrm{ON} + \mathrm{OFF}} \tag{13.2}$$

and ON and OFF are the number of events detected in the ON and OFF positions respectively.

In GRAAL, to avoid the influence of the NSB in the calculation of the excess, we chose a method that normalizes any excess to the ratio of ON- and OFF-source events for the results reported in the following sections.

The normalization technique is based on the angular reconstruction of the showers and has been used already by other wavefront samplers like ASGAT [96] and PACT [26, 231]. Traditionally, the number of events in the angular region where the gammas are expected, which is a region around the direction of pointing as big as the angular resolution of the experiment, is

normalized with a factor that accounts for the difference in time exposure and threshold of the ON and OFF samples. Thus, the normalized excess EXCESS_n is calculated according to the following equation:

$$\mathrm{EXCESS_n} = \mathrm{ON_{in}} - \mathrm{OFF_{in}} \left(\frac{\mathrm{ON}}{\mathrm{OFF}} \right)_{\mathrm{out}} \tag{13.3}$$

Here $(\mathrm{ON,OFF})_{in}$ stands for the number of events within "x degrees" from the source, resp. off source direction, where "x" is the angular resolution of the experiment. $(\mathrm{ON,OFF})_{out}$ stands for the number of events with directions deviating more than "y degrees" from the source direction, "y" being an angular distance where no more gamma rays are expected. The statistical error of EXCESS_n, ERR_n is calculated according to:

$$\mathrm{ERR_n} = \left(\mathrm{ON_{in}} + \mathrm{OFF_{in}} \times \left(\frac{\mathrm{ON}}{\mathrm{OFF}} \right)^2_{\mathrm{out}} + \left[\left(1 + \left(\frac{\mathrm{ON}}{\mathrm{OFF}} \right)_{\mathrm{out}} \right) \mathrm{ON_{out}} \times \frac{\mathrm{OFF^2_{in}}}{\mathrm{OFF^2_{out}}} \right] \right)^{0.5} \tag{13.4}$$

For GRAAL, the situation is somewhat different to ASGAT and PACT. As stated in section 10.2.1, the restricted field of view prevents a good reconstruction mainly of the hadronic showers, i.e., they are artificially reconstructed towards the pointing position (the array sees only a sub-shower within the field of view of the detector for showers far from the pointing direction). Therefore, the gammas and hadrons are contained mainly in the same angular region (0.7° for GRAAL) around the pointing position and the tails to angular distances larger than 2° are misreconstructed showers (section 6.2.2).

Nevertheless, we can profit of the misreconstructed showers and make the normalization considering the region where such showers are contained as the *out* region of eq. 13.3. We found (section 7.2.2) that a larger fraction of gamma-ray than proton events is reconstructed in the "central angular region", within 0.7° from the pointing direction (the ratio r_{io} of section 7.2.2 is a factor 1.5 larger for the former). Then, we expect a small hadron rejection factor when considering only the excess in the 0.7° region. Moreover, we assume that the number of misreconstructed showers must be the same in ON and OFF regions under equal conditions of NSB (the possible arguments against this hypothesis are discussed in section 13.1.5). Then, the normalization eliminates completely the influence of a different NSB in the ON and OFF positions.

We must take into account that some gammas are indeed put into the outer region due to misreconstruction. Therefore, a possible gamma signal will be decreased, both because the events in the outer region are not counted for the excess and because the fraction of the gammas in the outer region enters the normalization factor.

13.1.3.1 Excess in the lsq_t^2 distribution

The gamma-ray showers have a time showerfront narrower than the hadronic showers and consequently the lsq_t^2 of the fit of the showerfront to an spherical front must be smaller for the former (section 7.1.1). Therefore, we can search a gamma-ray excess by subtracting the distributions of lsq_t^2 in ON and OFF positions with a normalization to the outer region[1]. No significant excess was found for any of the analysed sources at low values of lsq_t^2, including those sources which showed a significant excess from the direction of the source with the comparison of trigger rates.

This is an expected result for our detector (section 7.2.1.1), since the lsq_t^2 distributions of MC gamma and hadron showers are equal within the errors due to the restricted field of view.

[1]This method, but without normalization to the outer region, has been previously applied by the CELESTE collaboration [67].

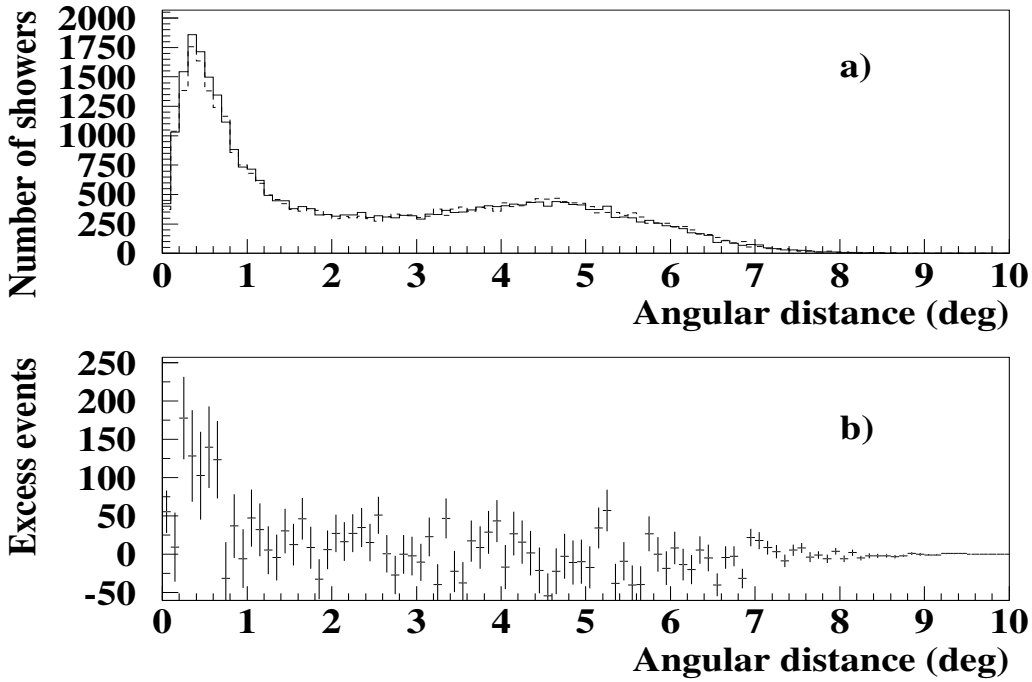

Figure 13.1: *The upper plot (a.) shows the number of events as a function of angular distance of reconstructed direction from source direction for ON-source events (full line) and OFF-source events (dashed line). No normalization of any kind was applied to this plot. The lower plot (b.) shows the difference ON-OFF, normalized to the number of events in the outer angular region, according to eq. 13.3. Data of the Crab pulsar taken under good meteorological conditions according to the cuts discussed in section 12.2.2 was used. The statistical errors of the individual bins are shown.*

13.1.4 Results

13.1.4.1 Observation of the Crab pulsar

Table 13.1 shows the results of the observation of the Crab pulsar during the period 1999/2000. We find $\mathrm{EXCESS}_n = 737 \pm 165$ calculated according to eqs. 13.3, 13.4. This corresponds to a 4.5 σ excess and a mean excess rate $\mathrm{EXCESS}_{nr} = 1.7/\mathrm{min}$. Fig. 13.1 shows the number of events as function of angular distance from the source direction, both for ON- and OFF-source direction and the normalized difference ON-OFF. The calculated excess is clearly seen in the angular region expected from the Monte-Carlo simulations (section 7.2.2). Fig. 13.2 displays the excess as a projection onto zenith and azimuth axis (panels a. and b. respectively).

An integral flux ϕ_{int} is calculated from this excess according to:

$$\phi_{\mathrm{int}} = (\mathrm{EXCESS_{nr}}/\mathrm{r}_\gamma)(\mathrm{r_p}/\mathrm{r_{obs}})\mathrm{t_c}\phi_{\mathrm{Whipple}} \tag{13.5}$$

Here $\phi_{Whipple} = \int_{E_{thresh}}^{\infty} 3.3 \times 10^{-7}\ \mathrm{E}^{-2.4}\ \mathrm{m}^{-2}\ \mathrm{sec}^{-1}\ \mathrm{TeV}^{-1}\ \mathrm{dE}$ is the integral gamma-ray flux from the Crab above a threshold energy E_{thresh} as observed by the Whipple collaboration [114]. r_γ is the gamma-ray rate expected in GRAAL from the MonteCarlo simulated effective area for gammas of fig. 8.6 based on this flux (0.011 Hz). Note that the absolute Whipple

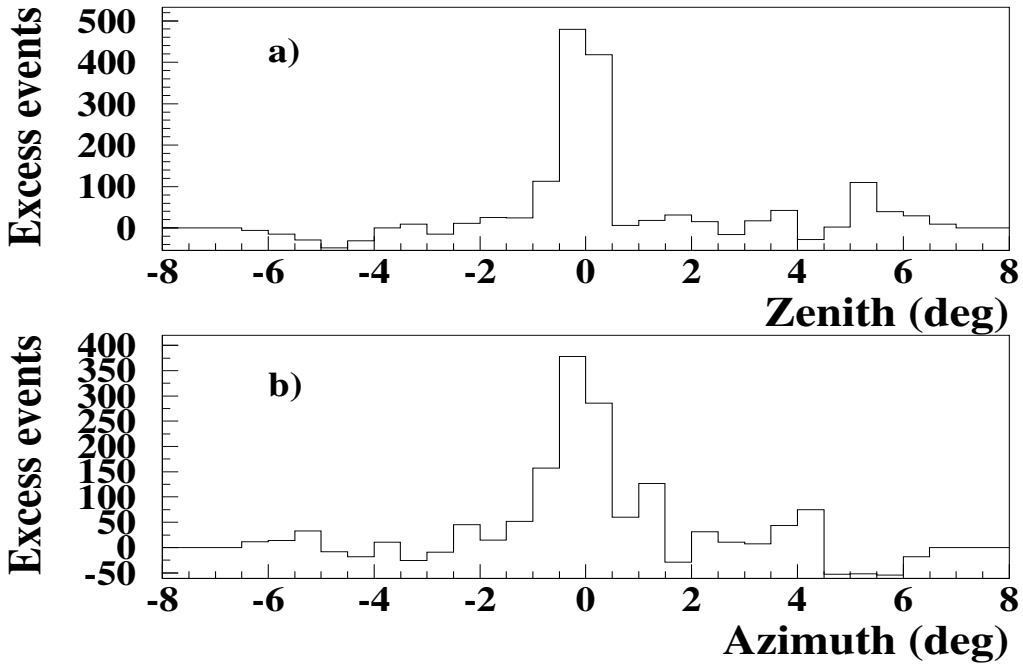

Figure 13.2: *Difference of the number of events in ON source direction and OFF source direction for the Crab data sample shown in fig. 13.1 as a function of deviation of the zenith (upper plot a.) resp. azimuth angle (lower plot b.) from the source direction.*

flux cancels in eq. 13.5 and we only adopt the spectral index from ref. [114]. r_p is the proton rate expected in GRAAL on the basis of the known proton flux ϕ_{ref} and the effective area for protons of fig. 8.6 (4.0 Hz). r_{obs} is the observed cosmic-ray rate in the final reconstructed sample, corrected for dead time (1.6 Hz). The factor (r_{obs}/r_p) is an empirical correction for the fact that our Monte Carlo calculated proton effective area predicts a somewhat higher proton rate than observed. t_c is a correction factor for the fact that some photons are expected in the "outer angular region" and was determined as 2.2(1.4) from weighted(unweighted) Monte Carlo data. The weighted value was chosen for the final result. The final integral flux above threshold assuming a differential spectral source index of -2.4 is:

$\phi_{int} = 2.2 \pm 0.4$ (stat) $^{+1.7}_{-1.3}$ (syst) $\times 10^{-9}$ cm^{-2} s^{-1} above threshold.

The systematic error of our flux determination is dominated by the uncertainty in absolute light-calibration (section 4.4). The relative difference: ((predicted ADC channel MC) - (predicted ADC channel LED))/(predicted ADC channel MC) was 21%, -31%, -13%, 29% for cones 1-4. From this, we estimate a systematic error of 30% for this conversion. We estimate a similar error due to uncertainties in the Monte Carlo simulations between the primary and the entrance of the cones which increase the error in the absolute light calibration to about 42%, corresponding to a flux error of about $^{+81}_{-60}$%. Another important source of overall systematic error is the systematic error of t_p (35%, section 9.3.2) in which uncertainties in the spectral weighting procedure and the detailed simulation of the trigger enter and which was added in quadrature. The final adopted systematic error is $^{+88}_{-69}$%.

Table 13.2 shows the results of the observation on the Crab pulsar during the period

	Raw events	Rec. events	Centr. events
ON	68702	33384	9415
OFF	75198	33056	8678
EXCESS	-6496 ± 379	328 ± 258	737 ± 165

Table 13.1: **Raw events**: *all hardware-triggered events which traces were recorded,* **Rec. events**: *number of events after angular reconstruction and software trigger,* **Centr. events**: *normalized number of events in central angular region (within 0.7 degrees of pointing direction), calculated as explained in section 13.1.3. Rows are for the samples with pointing towards the Crab pulsar ("ON") and on a sky position ("OFF") with a right ascension 2.625 degrees larger than in the ON direction. The total data-taking time ON was 430 minutes with an equal amount of OFF time.*

	Raw events	Rec. events	Centr. events
ON	29953	21472	7920
OFF	29817	21486	7850
EXCESS	136 ± 244	-14 ± 207	70 ± 125

Table 13.2: *Entries as in table 13.1 but for the data on the Crab pulsar taken in period 2000/2001. The total data-taking time ON was 230 minutes with an equal amount of OFF time.*

2000/2001. In spite of the absence of dew in the mirrors (which ruined most of the data of the period 1999/2000, section 3.1.3.3) during this period, a smaller fraction of the taken data was selected due to the worse angular reconstruction of the showers. This is probably due to the failure of some heliostats between both years (section 12.3). It is remarkable that the fraction of reconstructed events (which pass the software cuts) with respect to the total number of raw events is about 70%, much larger than the $\approx 50\%$ of the previous year. The reason for that is the number of random events, which was large in the period 1999/2000 and is negligible thereafter (section 11.2.1.1). No significant excess is found for the data of this period. This is due very likely to the bad angular reconstruction of period 2000/2001, that can produce a failure of the normalization process and therefore a decreasing of an already small (due to the short time of data taking) expected signal (see section 13.1.5).

13.1.4.2 Observation of Markarian 421

The blazar Markarian 421 has been observed by GRAAL during two flaring states, the first one occurred in February-March 2000 and the second one in February-March 2001. Tables 13.3 and 13.4 show the results of the observation for both periods. In both years an excess is observed both in the raw data and in the reconstructed events.

The excess in the reconstructed events, shown in the second column of tables 13.3-13.4 (1.9σ and 5.2σ respectively), is considerably reduced when the normalization process is applied. In principle, a reduction of the excess is expected after reconstruction, since the NSB is higher in the ON position (see tables 12.4-12.5). The observed reduction seems reasonable for year 2000, where a difference in integrated charge of 1.7 significance is observed in table 12.4 and the normalization factor of eq. 13.3 is >1 (increasing the number of events in the OFF region and therefore reducing the excess). However, it seems that the reduction is too high for year 2001.

	Raw events	Rec. events	Centr. events
ON	56751	33000	9775
OFF	55600	32513	9873
EXCESS	1151 ± 335	487 ± 256	-98 ± 180

Table 13.3: *Entries as in table 13.1 for the samples with pointing towards the blazar Mrk421 ("ON") and on a sky position ("OFF") with a right ascension 2.625 degrees larger than in the ON direction. The total data-taking time ON was 480 minutes with an equal amount of OFF time.*

	Raw events	Rec. events	Centr. events
ON	83321	43202	11161
OFF	80239	41675	10903
EXCESS	3082 ± 404	1527 ± 291	258 ± 183

Table 13.4: *Entries as in table 13.3 for the 2001 period of observation. The total data-taking time ON was 570 minutes with an equal amount of OFF time.*

Table 12.5 shows an integrated charge that is equal within statistical fluctuations for ON and OFF regions. In spite of that, the normalization factor is > 1 and reduces the excess.

Since a clear excess is seen in the ON-source position before the normalization is applied, we have made a daily comparison between the preliminary data of the HEGRA experiment and the GRAAL data for the samples taken during the flare of February-March 2001. The results are shown in section 13.2.1, included in the analysis of total rates.

13.1.4.3 Observation of 3EG J1835+59: the problems of a "northern" source

From July to September 2000 the unidentified EGRET source 3EG J1835+59 was observed. The data was taken during a total time of 860 min pointing towards the source and the same time pointing to the corresponding OFF position.

This source is situated at a right ascension of 278.87 deg and a declination of 59.32 deg. At the location of GRAAL, 3EG J1835+59 lies northwards from the heliostat field. This position is problematical for the reconstruction process and therefore no more northern sources were observed.

The number of peaks used in the reconstruction of the shower front determines the quality of the reconstruction (sections 8.1 and 9.3.1). The angular resolution increases with the number of peaks, e.g. an angular resolution of 0.6° is achieved with 30 reconstructed peaks (see fig. 8.2). On the other hand, showers with only 5 peaks are usually misreconstructed (sections 6.2.2, 8.1). GRAAL uses a total of 63 heliostats, therefore it seems reasonable to require 30 peaks for a good reconstruction (ca. 50% efficiency). However, during the analysis of 3EG J1835+59 we found that only 11.6 peaks (mean value) were reconstructed (see fig. 13.3, panel a.). The reason for the smaller number of reconstructed peaks in comparison with other directions (see e.g. 9.2) is the overlap of two or more peaks. The overlap is especially critical for northern directions, since the light path is short(long) from the source to the heliostats and long(short) from the heliostats to the tower for heliostats far(near) from the tower respectively. In short, the pathlengths of the light-rays are very similar for all the heliostats and therefore an overlap

occurs[2]. A rough estimate of the overlapping can be made by looking at the fraction of events that pass the sequence trigger (sect. 3.3.2.1). For example, only a 6% of the events pass the sequence trigger for 3EG J1835+59 in comparison with a 25% for the Crab nebula. The reason is that the sequence trigger requires well differentiated peaks.

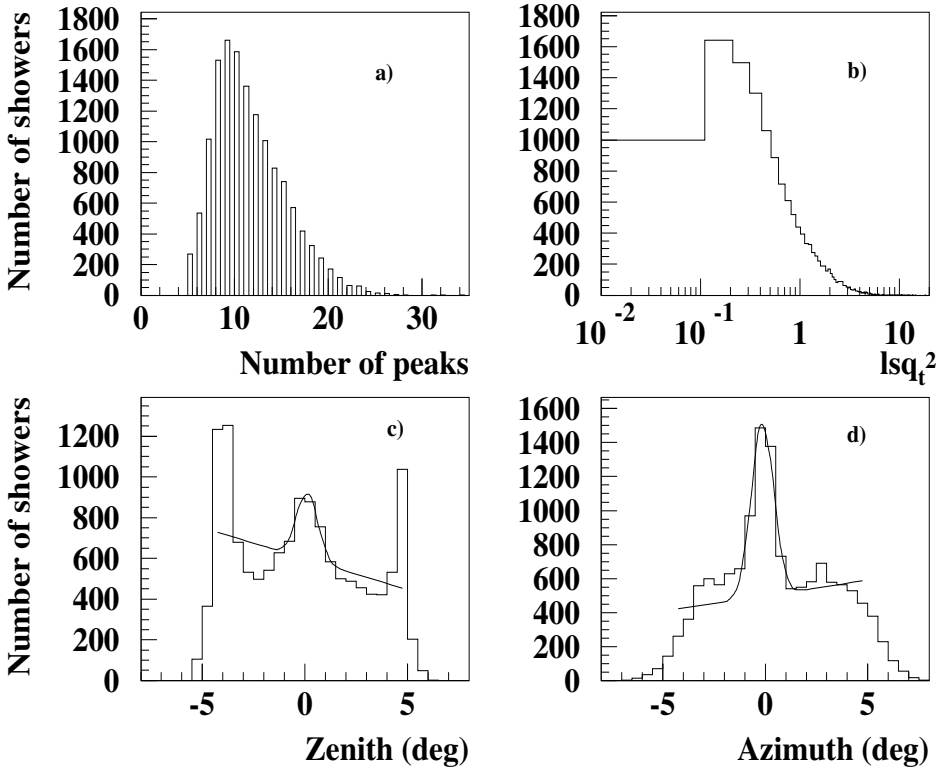

Figure 13.3: *Distribution of the number of identified peaks (panel a.), lsq_t^2 of the fit of the showerfront to an sphere (panel b.) and the projection of the deviation of the reconstructed directions from the pointing position for zenith (panel c.) and azimuth (panel d.) for a sample of data taken on the source 3EG J1835+59. The pointing position was zenith around 10 deg and azimuth around 180 deg (see appendix B for azimuth convention). The small number of reconstructed peaks (compare e.g. with fig. 9.3) is the reason for the bad angular reconstruction (compare with fig. 6.5).*

Several values for the parameters of the analysis program were tested in order to improve the angular reconstruction. For example, we tried different values for the number of rejected peaks during reconstruction (MAXIMUM REJECTED PEAKS, see appendix C). Allowing from 6 to 9 peaks to be rejected, the program tended to reject the maximum number of peaks to improve the lsq_t^2 of the fit, producing still a higher number of misreconstructed showers. On the other hand, allowing only 1 to 3 peaks to be rejected, some "fake" peaks (noise peaks, afterpulses) entered the fit and increased the lsq_t^2 value over the required limit (see table A.1 in appendix

[2]For southern sources the opposite happens. For heliostats near to the tower both paths (source-heliostat and heliostat-tower) are shorter than for heliostats far from the tower.

	Raw events	Rec. events	Centr. events
ON	45984	21639	-
OFF	46431	21772	-
EXCESS	-447 ± 304	-25 ± 212	-

Table 13.5: *Entries as in table 13.1 for the samples with pointing towards the unidentified gamma-ray source 3EG J1835+59 ("ON") and on a sky position ("OFF") with a right ascension 2.625 degrees larger than in the ON direction. The total data-taking time ON was 490 minutes with an equal amount of OFF time. The result for the central region is not given for this source because the quality of the angular reconstruction was strongly decreased for its direction pointing towards the north (see text).*

A). Then, the allowed time within peaks was reduced from 6 ns (section 6.1.2.2) to 3 ns, in order to increase the number of peaks. Only fake peaks were introduced with this method, thus worsening the angular reconstruction. Another trial consisted of considering only the N biggest peaks for the reconstruction (see BIG PEAKS in appendix C) where N took values from 8 to 15. The motivation was that big peaks are less influenced by NSB fluctuations and have a small chance of being noise peaks or afterpulses. The result was again disappointing. The conclusion was that no matter how good the peaks are, a sufficient number (around 15) of peaks is necessary to have a good reconstruction. On the other hand, if fake peaks enter the reconstruction, a wrong identification "heliostat-peak" can occur. Other parameters were tested to restrict the chance of the program to find a wrong solution. For example, the grid were the shower direction is searched (section 6.2.2) was reduced from the usual 5×5° to 3×3° without success.

The best results were obtained analysing the data with a software threshold level of $n_t = 9$, which is quite high in comparison with the analysis threshold of other sources (see table 12.1). In addition, the TIMEDIFF parameter (section 6.2.2) was increased from the usual 5 ns to 20 ns. The values of the other parameters were the standard ones (see appendix C).

Table 13.5 shows the results of the analysis. No significant excess is found in the direction of the source. Other results of the analysis of the showers taken on 3EG J1835+59 like the lsq_t^2 of the fit of the showerfront to an sphere and the angular reconstruction are shown in fig. 13.3.

Given the failure of the "normalization technique" (section 13.1.3) for this source, this is a good candidate for an analysis with the "total rate method" (section 13.2).

In general, sources near from the zenith will have more overlapping than southern sources at zenith angles of e.g. 30°. See for example the difference in the ratio PT (indicator of reconstruction quality) in tables 12.2-12.3 between the sources Mrk421 and GRB010222 (near the zenith) and 3C273 and 3C279 (southern sources at ca. 30° zenith angle).

13.1.4.4 Observation of 3C454.3: the problems of an analysis with a significant number of noise peaks

During September 1999 and September 2000 the radio source 3C454.3 was observed. The data was taken during a total time of 870 min pointing to the source (ON) and an equal amount of time pointing to a test region (OFF). The first set of data (September 1999) was taken only with the sequence trigger, whereas in September 2000 both the sequence and the charge trigger were already operational (see sect. 3.3.2.1 for a description of the trigger modes). This is the reason for the different threshold of analysis (see table 12.1).

	Raw events	Rec. events	Centr. events
ON	42516	30570	7525
OFF	44949	30889	7625
EXCESS	-2433 ± 296	-319 ± 248	54 ± 141

Table 13.6: *Entries as in table 13.1 for the samples with pointing towards the radio source 3C454.3 ("ON") and on a sky position ("OFF") with a right ascension 2.625 degrees larger than in the ON direction. The total data-taking time ON was 550 minutes with an equal amount of OFF time.*

When the data on this source was analysed for the first time, an excess in the ON position was found. While examining the reliability of the excess, we found out that the software threshold used at that time ($n_t = 5$, as for the Crab nebula) was too near the NSB fluctuations for the analysis of 3C454.3. A definitive analysis at a higher threshold $n_t = 9(7)$ for data taken on September 1999(2000) showed no significant excess (see table 13.6).

With an analysis software threshold too near to the NSB fluctuations many noise peaks are accepted for analysis.

A check was made on the data of 3C454.3 to prove that this sample had more noise peaks than the other sources if the analysis threshold used for most of such sources was applied (see table 12.1). The number of peaks that surpass the initial software threshold (n_t=5) was counted in the last 200 channels (100 ns) of the trace, where no more Cherenkov pulses are expected. Then, we extrapolated this value and found that ca. 3 "noise" peaks passed the software threshold for each event and that there were more peaks in the OFF than in the ON position ($\approx$ 3.6 (OFF) vs. 3 peaks (ON)). To prove that the detected peaks were really noise and not originated by some "external" source like muons, we checked the sample of data taken with the hut door closed and the tungsten lamp (sect. 11.3.1). For this set of data the currents and NSB fluctuations agreed within ca. 1% with the 3C454.3 data. We found a similar number of peaks for the tungsten lamp data, proving our hypothesis of noise peaks (with the door closed, an external source for the peaks can be ruled out).

The effects of a software threshold too close to the NSB fluctuations was first noticed for 3C454.3 due to the large difference of NSB between ON and OFF positions (for comparison see tables 12.4-12.5).

13.1.4.5 Other potential sources

Tables 13.7-13.12 present the results of the observation of potential gamma-ray sources for which no significant excess has been found. The data was taken under similar conditions to the data presented up to now.

The gamma-ray burst GRB010222 is a special case (see table 13.12). This gamma-ray burst was detected by BeppoSAX on February 22.3073484 UT. Among the GRBs detected on BeppoSAX, GRB010222 ranked second in fluence and third in flux [245]. A redshift of z = 1.477 was reported (see e.g. [120]). GRAAL began observations on this gamma-ray burst as soon as it was in the field of view of the detector, about 18 hours after its detection by BeppoSAX. The selected data sample is the largest of all observed sources with exception of Mrk 421. In the raw data a 1.6σ excess is found which enhances to a 2.2σ effect after reconstruction. Table 12.5 indicates the second lowest NSB for this source (after the Kuehr0428+20.5 object), a difference between the NSB of ON and OFF positions of 0.07% and a zero difference between the integrated

	Raw events	Rec. events	Centr. events
ON	24119	13136	2295
OFF	26911	13272	2299
EXCESS	-2792 ± 226	-136 ± 136	-7 ± 76

Table 13.7: *Entries as in table 13.1 for the samples with pointing towards a "pseudo source" at right ascension = 330.68 degrees and declination = 40.28 degrees ("ON") and on a sky position ("OFF") with a right ascension 2.625 degrees larger than in the ON direction. The total data-taking time ON was 250 minutes with an equal amount of OFF time.*

	Raw events	Rec. events	Centr. events
ON	7827	6394	2081
OFF	7792	6251	2017
EXCESS	35 ± 125	143 ± 112	64 ± 83

Table 13.8: *Entries as in table 13.1 for the samples with pointing towards the 3c273 at right ascension = 187.28 degrees and declination = 2.05 degrees ("ON") and on a sky position ("OFF") with a right ascension 2.625 degrees larger than in the ON direction. The total data-taking time ON was 90 minutes with an equal amount of OFF time.*

charge of ON and OFF positions. Although the excess is found in all the processes of analysis (raw data, reconstructed events and after normalization) in a consistent way, it is not significant enough to claim a detection.

13.1.5 Drawbacks of the normalization technique

The normalization technique can fail due to a "bad" angular reconstruction and/or to a "different" angular reconstruction in ON and OFF positions.

- If the angular reconstruction of events is bad (given by a large number of misreconstructed events and a small ratio PT) an existing gamma-ray signal can be eliminated with the normalization, even if the ratio PT is the same for ON and OFF positions. First, as the gamma-ray events are very similar to the hadrons, a poor hadronic angular resolution means also a poor resolution for the gammas. Consequently, only a small fraction of the gammas will remain in the "central region" where the excess is calculated. Second, since the most part of the gamma-ray events will be in this case in the "outer region" used

	Raw events	Rec. events	Centr. events
ON	7221	5820	1818
OFF	7250	5889	1920
EXCESS	-29 ± 120	-69 ± 108	-102 ± 80

Table 13.9: *Entries as in table 13.1 for the samples with pointing towards the 3c279 at right ascension = 194.046 degrees and declination = -5.789 degrees ("ON") and on a sky position ("OFF") with a right ascension 2.625 degrees larger than in the ON direction. The total data-taking time ON was 90 minutes with an equal amount of OFF time.*

	Raw events	Rec. events	Centr. events
ON	5616	4387	1309
OFF	5556	4365	1400
EXCESS	60 ± 106	22 ± 93	-91 ± 68

Table 13.10: *Entries as in table 13.1 for the samples with pointing towards the source Kuehr 0428+20.5 at right ascension = 67.77 degrees and declination = 20.63 degrees ("ON") and on a sky position ("OFF") with a right ascension 2.625 degrees larger than in the ON direction. The total data-taking time ON was 60 minutes with an equal amount of OFF time.*

	Raw events	Rec. events	Centr. events
ON	14784	11308	3636
OFF	14691	11173	3589
EXCESS	93 ± 172	135 ± 150	47 ± 83

Table 13.11: *Entries as in table 13.1 for the samples with pointing towards the BL Lac at right ascension = 330.68 degrees and declination = 42.28 degrees ("ON") and on a sky position ("OFF") with a right ascension 2.625 degrees larger than in the ON direction. The total data-taking time ON was 210 minutes with an equal amount of OFF time.*

	Raw events	Rec. events	Centr. events
ON	99938	65051	15966
OFF	99218	64287	15673
EXCESS	720 ± 446	764 ± 359	293 ± 178

Table 13.12: *Entries as in table 13.1 for the samples with pointing towards the gamma-ray burst GRB010222 at right ascension = 223.05 degrees and declination = 43.018 degrees ("ON") and on a sky position ("OFF") with a right ascension 2.625 degrees larger than in the ON direction. The total data-taking time ON was 790 minutes with an equal amount of OFF time.*

for normalization, the gamma-ray events will contribute to the normalization factor, thus eliminating any existing signal. Moreover, the normalization is expected to work if the considered difference in the ratio r_{io} between gammas and protons is true, but for some direction this difference is very small (see table 7.3) and in addition the error introduced by the weighting procedure must be taken into account (section 9.3.2).

- If the ratio PT of section 12.2.2 is different for the ON and OFF positions (even if it is large for both positions), an existent gamma-ray signal can be eliminated, but also a signal can be faked. In principle, and since exactly the same part of the sky is tracked during ON and OFF position, we expect the same reconstruction efficiency (section 9.3.1). However, if some heliostat fails only when observing one of the positions (ON or OFF) or if the NSB is very different between both positions, a slight difference in the ratio PT can appear (see sections 12.3 and 11.3.3 respectively). If this happens, the normalization factor can create a signal or eliminate an existent excess. To minimize the possible effect of different PT values, we have required normalization factors between 0.95 and 1.05 (parameter RO of section 12.2.2).

13.2 Technique of comparison of total rates

In order to check the consistency of the normalization method (previous section) the number of "total events" (hardware-triggered) before analysis has been compared for ON- and OFF-source periods.

Before the comparison two corrections must be made: first we must ensure that the effective time of data acquisition is exactly the same in both periods (section 13.1.1). Second, the number of accidental events has to be calculated and subtracted for each period (section 11.2.1.1). The subtraction of the accidental events is not applied in the analysis with reconstruction of the airshower direction since such events are rejected with the software cuts (section 11.3.1).

The factor which corrects for the different electronic dead time of the detector in periods ON and OFF (section 13.1.1) must not be taken into account for the analysis of the total counting rate since such a rate is not biased by the DAQ-dead time.

Then, there are two differences between the "total corrected rate" analysed in this section and the "raw" rate shown in tables 13.1-13.12, namely, the electronic dead time of the setup (which influences only the raw rate) and the rate of accidental events (which is subtracted only in the analysis of total rates).

Tables 13.13-13.14 show the total number of events as registered by the counters of GRAAL (first column) and after all the above mentioned corrections (second column) for each of the observed sources.

At this level of analysis it is expected that sources which have a significant difference in the level of NSB between ON- and OFF-source positions (see tables 12.4-12.5) show an excess of events in the noisier position. The significance of the excess depends on the difference of NSB and on the statistics accumulated for each source. It is difficult to decide what is a "significant difference" in the level of NSB. We have seen (section 11.2.1.2) that an increase in the NSB of a 5% produces an increase in the trigger rate of a 6%. This change in rate is high, but for the observed sources the maximum NSB difference between ON and OFF is 0.8% for Mrk421 and for the rest of the sources stays below 0.4% (see tables 12.4-12.5). This means that, assuming that the increase of NSB and rate is linear[3], we can expect a significant difference in the trigger

[3]This assumption is in fact very rough and we would need to make a detailed study at various NSB levels to

Source	Total events	Total corrected events
3C454.3		
ON	49141	46566
OFF	51982	46909
EXCESS	-2841 ± 318	-343 ± 306
3EG J1835+59		
ON	50264	49499
OFF	50914	50323
EXCESS	-650 ± 318	-824 ± 316
BL Lac		
ON	17337	17255
OFF	17222	17158
EXCESS	115 ± 186	97 ± 185
Crab 00		
ON	79194	58107
OFF	86428	58550
EXCESS	-7234 ± 407	-443 ± 341
Mrk421 00		
ON	64011	62907
OFF	63665	62365
EXCESS	346 ± 357	542 ± 354
Pseudo source		
ON	28808	26010
OFF	31993	26549
EXCESS	-3185 ± 246	-539 ± 229

Table 13.13: *Number of hardware-triggered events (labelled "total events") and number of events with subtraction of the expected number of accidental events and a correction for the different time of data acquisition in ON and OFF periods (labelled "total corrected events"). The data shown has been taken in the period September 1999-September 2000.*

Source	Total events	Total corrected events
3C273		
ON	8170	8170
OFF	8164	8144
EXCESS	-6 ± 128	-26 ± 128
3C279		
ON	7534	7534
OFF	7579	7584
EXCESS	-45 ± 122	-50 ± 123
Crab 01		
ON	30957	30259
OFF	30635	30136
EXCESS	322 ± 248	123 ± 246
GRB010222		
ON	109071	109071
OFF	108066	107926
EXCESS	1005 ± 466	1145 ± 466
Kuehr0428+20.5		
ON	5920	5920
OFF	5885	5939
EXCESS	35 ± 109	-19 ± 109
Mrk421 01		
ON	89529	89529
OFF	86411	86631
EXCESS	3118 ± 419	2898 ± 420

Table 13.14: *Entries as in table 13.14 but for data taken from October 2000 till March 2001.*

rate due to the different NSB only for Mrk 421. For the other sources, the difference will be within the statistical fluctuations unless the statistics are increased by more than a factor 10 with respect to the existent ones.

Looking at the tables 13.13-13.14 it can be observed that the difference in number of events between ON and OFF positions is non-significant for all the sources of the period October 2000-March 2001 (in which the number of random events was negligible) except for Mrk 421 and for GRB010222. These two sources present an excess also after reconstruction (see tables 13.4 and 13.12). This means that, if there exist only very small differences of NSB and if no accidental events are recorded, the analysis of total rates is a reliable method to detect a source, provided that the source flux is not very faint (see below).

In contrast, significant negative excesses in the total number of recorded events are observed for some sources of the period September 1999-September 2000 (see first column of table 13.13). For these sources (3C454.3, 3EGJ1835, Crab and Pseudo 1) the negative excess is completely dominated by the accidental events. Since the NSB level is higher in the OFF position with respect to the ON position, the number of accidental events will be also higher in OFF. In the second column of table 13.13 the accidental events have been subtracted and the only significant excess is observed for the sources 3EGJ1835+59 and the Pseudo source with 2.6σ and 2.3σ excess in the OFF position respectively. This excess is finally reduced to non-significant with the analysis presented in the previous section (see tables 13.5 and 13.7).

To evaluate the efficiency of the "total rate" analysis we have to take into account first, the possibility of inducing a fake signal with the analysis and second, the feasibility of the method to detect a source.

In the absence of accidental events and provided that the difference of NSB between ON and OFF positions is "very small", the analysis of total rates can indicate a gamma excess. The maximum difference of NSB levels required to consider this method valid is very difficult to determine, given the faintness of the gamma fluxes. For example, for the time of measurement on the Crab nebula during the 1999/2000 period and extrapolating the Whipple flux for such source [114], only 355 excess events are expected. A difference in the energy threshold of cosmic-ray protons between ON and OFF of only 5 GeV at an energy threshold of 2 TeV already produces a difference of 550 events for the same time of measurement and using the known cosmic-ray proton flux and a constant effective area of 8000 m^2.

The "total rate" analysis method turns out as completely useless when trying to detect a gamma ray flux from a faint "candidate source" (with faint it is meant already a 50% of the Crab flux), since the flux sensitivity of the experiment at the "total rate" level of analysis is very low. For example, about 460 hours of measurement in the ON-source position and the same time in the OFF-source position are needed to detect an excess of the Crab nebula at a 5σ level of significance (using the equation 8.4) without considering NSB effects and $\approx$ 1152 hours to increase the significance to 8σ under the same conditions.

13.2.1 Comparison of the excesses obtained by the GRAAL and HEGRA detectors for Mrk421

The problems of using the normalization technique for the analysis of the Mrk421 data were pointed out in section 13.1.4.2. In this section a daily comparison between the preliminary data of the HEGRA experiment and the GRAAL data (analysis of total rates) for the samples taken during the flare of February-March 2001 is made. The results are shown in table 13.15.

give conclusive results, but this is difficult taking into account the smallness of the considered effects.

Date	GRAAL (raw data)	HEGRA CT1	HEGRA CT System
	Flux [Crab units]		
22-23.02.01	2.1	1.1	1.4
18-19.03.01	0.9	0.6	0.7
22-23.03.01	2.4	1.8	2.9
23-24.03.01	2.6	5.1	5.3
24-25.03.01	3.2	1.5	2.3
27-28.03.01	8.0	(0.8)	no obs.
30-31.03.01	0.8	2.1	2.3

Table 13.15: *Comparison of the night excesses in the direction of Mrk 421 recorded by the HEGRA experiment, both by the CT1 single telescope and the by the CT System (taken from [109]), and GRAAL.*

The excesses reported by GRAAL are slightly larger than the ones given by the HEGRA collaboration in four of the nights. Considering the lower energy threshold of GRAAL in comparison with HEGRA and the magnitude of the differences between the HEGRA single telescope and system of telescopes, a good agreement is observed. For one of the nights, 23-24.03.01, the excess observed by GRAAL is smaller than for the HEGRA telescopes. For the night of 27-28.03.01 there is a complete disagreement between the excess reported by GRAAL and the one reported by the CT1 telescope. This can be due to bad weather conditions in the HEGRA site, since the system of telescopes did not make observations on that night and the single telescope CT1 reports the excess between brackets, indicating a non-completely normal operation. A factor which can influence the comparison is the large error involved in the flux calculations of GRAAL (section 13.1.4.1).

13.3 Conclusions

We have developed a dedicated analysis method for the GRAAL data. It compares the events recorded in two positions of the sky (ON and OFF) after the reconstruction of the shower direction and taking into account the difference of Night-Sky-Background between the two positions. This method is valid for analysis of sources with a good reconstruction efficiency (PT ≥ 0.8) and with a small difference of the NSB level between ON and OFF positions ($< 0.5\%$). With this method an excess of 4.5σ significance for the Crab pulsar has been obtained. In contrast, for sources with low reconstruction efficiencies (PT ≤ 0.6) the normalization technique reduces (or even destroys) a possible gamma excess by introducing a large fraction of the gamma events in the normalization factor. This is very likely the case of the source Mrk 421. Thus, the reliability of the normalization method is limited.

An alternative method consists of comparing the number of reconstructed events in ON and OFF positions without a normalization, as in column 2 of tables 13.1-13.12. With this kind of analysis we detect a significant excess signal from the direction of the Crab nebula and from Mrk 421. With this method it remains doubtful whether the difference of NSB between ON and OFF positions is affecting the results. However, it increases the sensitivity of the detector and it is therefore preferred.

A different method of analysis considers the number of hardware-triggered events after subtracting the accidental events and correcting for different acquisition times. This method is

good to check the consistency of the normalization method, but it can not be used as the unique analysis. The reason is the influence of the difference of NSB in the energy threshold of the ON and OFF positions, which is not corrected at this stage. A difference in the energy threshold of ON and OFF regions of ca. 5 GeV can produce a signal as significant as the one of the Crab nebula (sect. 13.2). Moreover, even if a detailed study of the influence of the NSB in the trigger rate is made to make a correction at this level, the sensitivity of the experiment remains low (section 13.2).

The lack of efficient methods of gamma-hadron discrimination (chapter 7) forces the election of analyses based on the comparison of rates between two positions of the sky to detect a gamma-ray excess. The problems derived from such analyses have shown up all throughout this chapter. The detection of strong (e.g. Mrk 421 or Crab) sources is possible with both a total rate analysis and after reconstruction of the events. However, for the detection of faint sources the reconstruction of the showers is mandatory. The influence of the NSB can not be neglected in this kind of analyses, although its effects can be corrected for samples with a very small difference in NSB levels and low statistics. The normalization method gives results independent of the NSB difference but is limited by the angular reconstruction efficiency.

A flux determination for the sources observed by GRAAL is difficult. The reason is that the total rate and the reconstruction efficiency in the direction of the source have to be considered for each source and compared with the Monte Carlo simulations (systematic errors are introduced by the limitations of the Monte Carlo itself like the conversion of p.e. to mV (section 4.4), but also by the weighting procedure (section 9.3.2) and by the fact that we have only Monte Carlo data in 6 incoming directions in comparison with the range of directions for the observed sources).

Conclusions and outlook

GRAAL finished operation in September 2001 and was dismantled in January 2002. During its two years of operation, GRAAL took reliably data following the planned technical specifications. It has been proven that the use of a heliostat array as a low cost Cherenkov telescope with a mirror area of a few thousand square metres is a feasible alternative to the use of dedicated Cherenkov telescopes.

The capital costs of the experiment in a facility used for solar-energy research during daytime represent only a few percent of the budget of dedicated telescopes like the projected MAGIC or HESS. Other solar-farm detectors, like CELESTE and STACEE, have costs ca. 10 times higher than GRAAL. This is due to the fact that GRAAL uses only 4 photomultipliers, vs. the 40 and 48 PMTs used by CELESTE [69] and STACEE [58] respectively, and a much simpler trigger electronics. In addition, the remote night-time operation implies a reduction of human resources and travelling costs with respect to all other experiments.

The Monte Carlo simulation has been an essential tool for the evaluation and correction of the systematic errors and for a complete understanding of this new technique of gamma-ray observation. The properties of experimentally detected showers -while showing statistically significant deviations from Monte-Carlo simulated proton showers- agree in some important parameters to within 10% typically.

The reconstruction of the incoming direction of the Cherenkov showers based on their time front was done for all the observed sources. Whereas the showers directions of all the southern sources were correctly reconstructed (within 0.7° from the real direction according to our Monte Carlo simulations), the reconstruction of northern sources like EG J1835+59 was inefficient for GRAAL due to the overlap of the signals from different parts of the showerfront. A decrease of the reconstruction efficiency is also partially seen for sources at the zenith due to a "moderate" pulse overlap, like Markarian 421. The average angular resolution of GRAAL is 0.7°. This relatively large value in comparison with the other heliostat arrays is very likely due to the higher compactness of our heliostat field; our heliostats are spread over an area (160×80 m^2) much smaller than the ones of CELESTE (240×200 m^2) or STACEE (300×150 m^2).

One of the main drawbacks of the heliostat approach has been the night-time weather conditions at the relatively low elevation of the heliostat field. The disadvantages of using a site initially chosen for solar-energy generation for the detection of gamma rays were already brought to attention at the early days of the solar-farms history. We found that the fraction of time (total duty cycle) with weather and moon-light conditions sufficient for the detection of gamma radiation was about 3-4% at the PSA, about a factor 5 lower than at astronomical sites. This is mainly due to the fact that the site-selection criteria for solar-facilities do not match the criteria of an astronomical site. For example, the latter require dark sites and preferentially at high altitudes, conditions which are irrelevant for a good operation of the solar power plants.

Regarding the sensitivity of the experiment, the lack of an efficient gamma-hadron separa-

tion technique has been the "major enemy" of all the heliostat arrays, including GRAAL. The rejection of hadron showers is achieved in other experiments by a comparison of the shower "shape" characteristics between gammas and hadrons together with the reconstruction of the shower arrival direction (isotropic distribution of hadrons vs. point direction of gammas). In GRAAL, the field of view restriction was shown to lead to a very similar time structure of the shower front in proton and gamma induced showers. Likewise, the light distribution of gamma and proton induced showers are hardly distinguishable. These two factors prevent a rejection of the hadronic background based on the shower characteristics. In addition, it was found that the restricted field of view biases the direction reconstruction of proton showers towards the pointing direction, so that a rejection of hadronic background based on its isotropic distribution against the point gamma signals fails to a great extent. Then, *the lack of hadron rejection methods forces (for all heliostat arrays) a consideration of absolute rates between two regions of the sky (ON- and OFF-source) to detect a gamma source.* This implies that the heliostat arrays need ca. a factor 5-10 more time to detect e.g. the Crab nebula with respect to the existing telescopes with gamma-hadron discrimination methods, i.e. the sensitivity is strongly decreased. *In addition, when absolute rates are considered, the NSB introduces systematic effects which can not be corrected at a high precision level.*

The large scatter in the energy reconstruction of the showers was also found to be a consequence of the small field of view, which prevents the detection of a fraction of the light for showers falling far from the centre of the array.

The heliostat arrays are detectors optimized to achieve low energy thresholds. There is only one experiment (CELESTE) with a clearly lower energy threshold (60 GeV) than the one of GRAAL (250 GeV). The GRAAL value is however higher than initially expected due to fake signals from afterpulsing of the PMTs and a small signal-to-noise ratio in comparison with Monte Carlo simulations. A low energy threshold requires first a large mirror area. GRAAL has the largest mirror area ($\sim$ 2500 m^2) of all existing or planned Cherenkov detectors. To take advantage of the large light collecting area, the heliostat arrays must be operated near the fluctuations of the NSB. In the absence of gamma-hadron separation techniques, the difference of night-sky-background between ON and OFF positions is crucial. The reason is that a difference of e.g. 10% in NSB can already produce a signal of the Crab intensity in the noisiest region. Consequently, an existent gamma-ray signal can be "eliminated" (if the OFF position is noisier) or, alternatively, a signal can be faked (if the ON position is noisier). The effect of different night-sky backgrounds in the ON- and OFF-source region is small after correction with software techniques for the relatively small event numbers discussed in this thesis and the observed maximal difference of NSB intensity of 4%. Nevertheless, this effect becomes a principal difficulty for the determination of absolute fluxes in somewhat larger samples.

In recent years, the field of the gamma-ray astronomy has experienced a big development. The ground-based detectors have increased their sensitivity more than a factor 10 (estimated as the time needed to detect the Crab nebula) during the last 10 years, opening the possibility of detections of faint gamma-ray sources. However, up to now only 4 point sources have been reliably proven ($\geq 5\sigma$ detection of at least two experiments) to emit gamma-rays at TeV energies and upper limits for the flux of many other candidate sources have been set, indicating small (less than $\sim$ 33 milliCrab for some sources) or perhaps inexistent gamma fluxes at the observation energies.

The conversion of existent solar farms to Cherenkov astronomy raised the hope of a rapid detection of more gamma-sources from the ground by lowering the energy threshold to the unexplored energy region between 30 and 300 GeV. However, the problems exposed above,

unfortunately inherent to all heliostat arrays, have reduced the sensitivity of the experiments much below the expectations (e.g. CELESTE needs ca. 6 hours to detect the Crab nebula at a level of 5 σ significance in comparison with the 20 min estimated in the proposal of the experiment). It seems that the detection of new gamma-ray sources with low fluxes will have to wait until the next generation of imaging Cherenkov telescopes is in operation. The other possibility is that the heliostat arrays solve the problems derived from the restricted field of view in order to increase their sensitivity. In this direction, CELESTE has tried a new pointing strategy, that consists in dividing the heliostats in two groups and focusing each group to a different part of the shower development (one of the parts being the maximum of the shower). This step towards imaging may help to increase the sensitivity of the solar detectors, but it will be at the expense of an increase in the energy threshold. Solar-2 might eventually profit from this idea given the hundreds of mirrors available in its heliostat field.

Appendix A

Software cuts

Table A.1 shows the software cuts applied to the MC and experimental data in order to obtain the different results of this thesis. The value of n_t used in the analysis of MC simulated and real data is also indicated. However, this is not a software cut, but a parameter of the analysis program (see appendix C). The main two software cuts are NREMAIN, defined as the number of reconstructed peaks, and lsq_t^2, which determines the goodness of the fit of the showerfront to an sphere. For all the standard analyses these two cuts have been applied. In addition, a third cut on the value of the NSB fluctuations (σ_{NSB}) has been imposed. This cut has been only included to reject a kind of events produced by electronic noise in the second photomultiplier. The rate of these events has been inferred from OF 2 observations to be less than 0.003 Hz.

We have used the logarithm of the integrated charge as an indicator of the energy threshold (see tables 12.4 and 12.5). Therefore, it has been mandatory to impose a limit on the integrated charge to accept only positive values. However, this cut is not really strict, since events with negative IC are most likely noise events, where the NSB negative fluctuations have more weight than the positive ones. Those events are rejected in the standard analysis already with the NREMAIN cut.

	MC simulated data			Real data
	Effective area Energy threshold Trigger rate	For comparison MC-real data: # of total/reconstructed peaks lsq_t^2, angular resolution	IC	
n_t (sect. 6.1.2.1)	9	6		5-9
NREMAIN (sect. 9.2)	≥ 5			
lsq_t^2 (sect. 6.2.2)	-	≤ 100	-	≤ 100
σ_{NSB} (sect. 6.1.2.1)	-	≤ 4	-	≤ 4
IC (sect. 6.1.3)	-	-	> 0	-

Table A.1: *Software cuts imposed on the data after analysis.*

Appendix B

Coordinate system

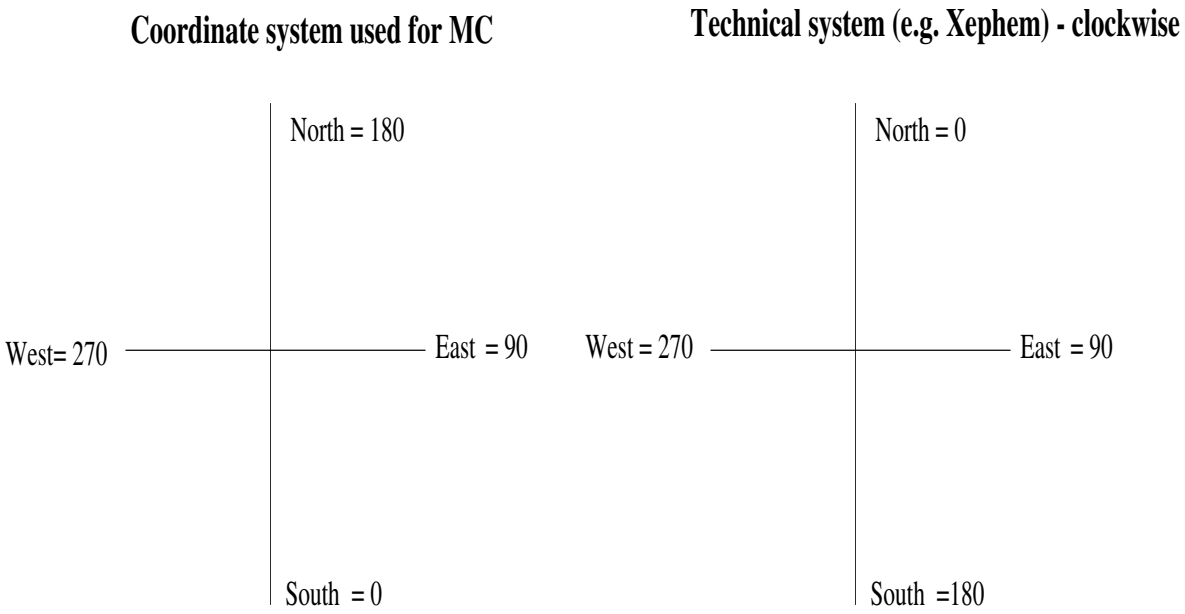

Figure B.1: *The convention for the azimuth coordinates used throughout this thesis is shown (left panel). The right panel indicates a standard technical system, like the used for example in Xephem [243].*

Appendix C

Parameters of the analysis program

The parameters used by the analysis program, with a short definition, are listed below. The standard values are indicated in brackets. The use of different values for the analysis of some source is indicated throughout the thesis.

- n_t (5): software threshold. n_t indicates the minimum amplitude (in NSB fluctuations units) of a peak to be considered for analysis (see section 6.1.2.1 for a detailed description).
- FIX THRESHOLD ("not-defined"): if defined, this parameter indicates an analysis with a fixed software threshold. Instead of imposing a variable threshold (dependent on the NSB fluctuations), an amplitude above a fixed number of ADC units (see below) is required to consider a peak for analysis (section 11.3.2).
- ADC THRESHOLD (ca. 5-7 ADC units): if a fix software threshold is considered (see above), this parameter gives the minimum amplitude (in ADC units) required to accept a peak. The limit depends on each source.
- WAITING TIME (6 ns): peaks arriving closer to each other than WAITING TIME are excluded to avoid a bias from overlapping pulses (section 6.1.2.2).
- MAXIMUM REJECTED PEAKS (5): number of peaks above software threshold that can be rejected by the program during analysis (section 6.2.2).
- FWHM (10 ns): maximum allowed pulse width (Full Width Half Maximum) to consider a pulse as a Cherenkov pulse. This limit is set to 10 ns to avoid the fit of many overlapped peaks as a single wide pulse. If overlapped pulses are to be considered this limit must have a large value.
- GRID SIZE (5×5 deg): size of the spatial grid where the position of a certain shower is searched for (section 6.2.2).
- GRID BIN (0.5 deg): initial binning of the grid where the position of a shower is searched for.
- GRID FINE BINNING (0.01 deg): final binning of the grid where the position of a shower is searched for. This binning is only used to obtain the final reconstructed position of a shower. The final position is searched with this binning in the adjacent bins to the one selected from previous binning (see above).

- SATURATED PEAKS (1): indicates if the program considers saturated peaks for the analysis. The parameter value 0(1) means acceptance(non-acceptance) of saturated peaks respectively.
- SHIFT (0-400 ns): difference in time between the arrival time of the first peak and the time at which the first peak is expected (section 6.2.2).
- SHIFT STEP (5 ns): initial bin width of the SHIFT parameter (see above).
- SHIFT FINE STEP (0.25 ns): final bin width of the SHIFT parameter (see above).
- TIMEDIFF (5 ns): maximum allowed time deviation between a measured peak and its expected position. Peaks with TIMEDIFF>5 ns are rejected by the program until the limit "MAXIMUM REJECTED PEAKS" (see above) is reached. Then, the peaks must be accepted even if TIMEDIFF $>$ 5ns (these peaks will increase the value of lsq_l^2) (section 6.2.2).
- BIG PEAKS (0): if set to 1 only the N (N is also a variable parameter) largest peaks are analysed.

List of Figures

List of Tables

Bibliography

[1] M. Aglietta et al., APh **3** (1995), 1

[2] F.A. Aharonian & A.M. Atoyan, Space Science Reviews **75** (1996) 357

[3] F.A. Aharonian et al., APh **6** (1997) 343

[4] F.A. Aharonian & A.M. Atoyan, Proceedings of the International Conference on Neutron Stars and Pulsars held on 1997 at Tokyo (Japan). Eds. Shibazaki [et al.] (Tokyo: Universal Academy Press) c1998. astro-ph/9803091

[5] F.A. Aharonian & A.M. Atoyan, A&A **351** (1999) 330

[6] F.A. Aharonian, A&A **342** (1999) 69

[7] F.A. Aharonian, New Astronomy **5** (2000) 377

[8] F.A. Aharonian et al., A&A **370** (2001) 112

[9] F.A. Aharonian et al., A&A **373** (2001) 292

[10] J. Arons, ApJ **266** (1983) 215

[11] F. Arqueros et al., A&A **359** (2000) 682

[12] R. Atkins et al. (The Milagro Coll.), ApJ **533** (2000) L119

[13] A.M. Atoyan & F.A. Aharonian, MNRAS **302** (1999) 253

[14] A.M. Atoyan et al., to be published in A&A. astro-ph/0112177

[15] A. Badul, B. Paczyński & D. Spergel, ApJ **316** (1987) L49

[16] P. Baillon et al., APh **1** (1993) 341

[17] M.G. Baring et al., ApJ **513** (1999) 311

[18] M.G. Baring, Proceedings of the GeV-TeV Gamma Ray Astrophysics Workshop "Towards a Major Atmospheric Cherenkov Detector VI", Snowbird, Utah 1999. Eds. Dingus et al. 2000. Vol. 515 p. 173

[19] J.A. Barrio et al., "The Magic Telescope", MPI-PhE/98-5 (1998)

[20] W. Bednarek, ApJ **402** (1993) L29

[21] W. Bednarek, A&A **336** (1998) 123

[22] T. Belloni et al., ApJ **479** (1997) L145

[23] E.G. Berezhko & H.J. Völk, APh **7** (1997) 183

[24] D.L. Bertsch et al., Nature **357** (1992) 306

[25] P.N. Bhat & V.R. Chitnis, Proceedings of the 27^{th} ICRC, Hamburg (2001) Vol. 7 p. 2961

[26] P.N. Bhat et al., Proceedings of the 27^{th} ICRC, Hamburg (2001) Vol. 7 p. 2589

[27] F. Blanco & F. Arqueros, Nucl. Instr. and Meth. in Phys. Res. A **414** (1998) 391

[28] R.D. Blanford & A. Levinson, ApJ **441** (1995) 79

[29] S.D. Bloom & A.P. Marscher, ApJ **461** (1996) 657

[30] D. Borque, "The Mini-GRAAL project", Diploma Thesis, Universidad Complutense de Madrid (1997)

[31] D. Borque (private communication in July 1999)

[32] D. Borque, PhD thesis, Universidad Complutense de Madrid (2001).

[33] M. Böttcher & C.D. Dermer, ApJ **501** (1998) L51

[34] M. Böttcher, Proceedings of the GeV-TeV Gamma Ray Astrophysics Workshop "Towards a Major Atmospheric Cherenkov Detector VI", Snowbird, Utah 1999. Eds. Dingus et al. 2000. Vol. 515 p. 31

[35] J.J. Brainerd, Nature **355** (1992) 522

[36] K.P. Braun, PSA Technical Report R24/94, 1994

[37] J.H. Buckley et al., A&A **329** (1998) 639

[38] H. Cabot et al., APh **9** (1998) 269

[39] J. N. Capdevielle et al. "The Karlsruhe Extensive Air Shower Simulation Code CORSIKA" Technical report KfK 4998, Kernforschungszentrum, Karlsruhe (1992).

[40] M. Catanese et al., ApJ **487** (1997) L143

[41] M. Catanese et al., ApJ **501** (1998) 616

[42] G. Cavallo & M.J. Rees, MNRAS **183** (1978) 359

[43] M.F. Cawley et al., Experimental Astronomy **1** (1990) 173

[44] M.F. Cawley, Proceedings of the GeV-TeV Astrophysics Workshop "Towards a Major Cherenkov Detector II", Calgary 1993. Eds. Lamb (1993) p. 176

[45] The CELESTE collaboration. "CELESTE experimental proposal: Cherenkov low energy sampling & timing experiment", 1996. http://wwwcenbg.in2p3.fr/extra/Astroparticule/celeste/e-index.html

[46] P.M. Chadwick et al., ApJ **513** (1999) 161

[47] P.M. Chadwick et al., Proceedings of the GeV-TeV Gamma Ray Astrophysics Workshop "Towards a Major Atmospheric Cherenkov Detector VI", Snowbird, Utah 1999. Eds. Dingus et al. 2000. Vol. 515 p. 276

[48] M. C. Chantell et al., Nucl. Instr. and Meth. in Phys. Res. A **408** (1998) 468

[49] K.S. Cheng, C. Ho & M. Ruderman, ApJ **300** (1986) 500

[50] K.S. Cheng, C. Ho & M. Ruderman, ApJ **300** (1986) 522

[51] J. Chiang & R.W. Romani, ApJ **400** (1992) 629

[52] V.R. Chitnis and P.N. Bhat, APh **12** (1999) 45

[53] V.R. Chitnis et al., Proceedings of the 27^{th} ICRC, Hamburg (2001) Vol. 7 p. 2793

[54] V.R. Chitnis & P.N. Bhat, Proceedings of the 27^{th} ICRC, Hamburg (2001) Vol. 7 p. 2914

[55] A.E. Chudakov et al., Proceedings of the 8^{th} ICRC, Jaipur, 1964, Vol. 4 p. 199

[56] D.P. Ciampa et al., Physical Review D **46** (1992) 3248

[57] E. Costa et al., Nature **387** (1997) 783

[58] C.E. Covault et al., Proceedings of the 27^{th} ICRC, Hamburg (2001) Vol. 7 p. 2810

[59] S. Danaher et al., Solar Energy **28** (1982) 33

[60] A. Dar, ApJ **500** (1998) L93

[61] J.K. Daugherty & A.K. Harding, ApJ **252** (1982) 337

[62] J.K. Daugherty & A.K. Harding, ApJ **458** (1996) 278

[63] B. Degrange et al., Proceedings of the GeV-TeV Gamma Ray Astrophysics Workshop "Towards a Major Atmospheric Cherenkov Detector III", Tokyo 1994. Eds. T. Kifune, p. 305

[64] O.C. de Jager & A.K. Harding, ApJ **396** (1992) 161

[65] O.C. de Jager et al., ApJ **457** (1996) 253

[66] O.C. de Jager (private communication)

[67] M. de Naurois, Proceedings of the 16^{th} ECRS Alcalá de Henares, 1998 p. 359

[68] M. de Naurois, PhD thesis, Université de Paris VI (2000)

[69] M. de Naurois et al., to be published in ApJ (2002), astro-ph/0107301

[70] C.D. Dermer, R. Schlickeiser & A. Mastichiadis, A&A **256** (1992) L27

[71] C.D. Dermer & R. Schlickeiser, ApJ **416** (1993) 458

[72] C.D. Dermer, S.J. Sturner & R. Schlickeiser, ApJS **109** (1997) 103

[73] M.E. Dieckmann et al., A&A **356** (2000) 377

[74] A. Djannati-Atai et al. (The THEMISTOCLE Collaboration), Proceedings of the 24^{th} ICRC, Rome, 1995, Vol. 2 p. 315

[75] S.G. Djorgovski et al., to appear in: Proceedings of the IX Marcel Grossmann Meeting, eds. V. Gurzadyan, R. Jantzen and R. Ruffini, (Singapore: World Scientific) 2001, astro-ph/0106574

[76] L.C. Drury, Space Science Reviews **36** (1983) 57

[77] L.C. Drury, W.J. Markiewicz & H.J. Völk, A&A **225** (1989) 179

[78] L.C. Drury, F.A. Aharonian & H.J. Völk, A&A **287** (1994) 959

[79] N.N. Efimov et al., Proceedings of the 13^{th} ICRC, Denver, Colorado 1973 Vol. 4 p. 2378

[80] D. Eichler et al., Nature **340** (1989) 126

[81] D.C. Ellison et al., Proceedings of the 26^{th} ICRC, Salt Lake City, Utah (1999) Vol. 3 p. 468

[82] D.J. Fegan, Journal of Physics G: Nuclear and Particle Physics **23** (1997) 1013

[83] J.M. Fierro et al., ApJ **413** (1993) L27

[84] G.J. Fishman & C.A.A. Meegan, ARA&A **33** (1995) 415

[85] Yu.A. Fomin & G.B. Khristiansen, Soviet Journal of Nuclear Physics, **14** (1971) 360

[86] D.A. Frail et al., Nature **389** (1997) 261

[87] C. Fryer, S. Woosley & D. Hartmann, ApJ **526** (1999) 152

[88] T.K. Gaisser, "Cosmic Rays and Particle Physics", Cambridge University Press (1990)

[89] W. Galbraith & J.V. Jelley, Nature **171** (1953) 349

[90] Y.A. Gallant et al., Proceedings of the 5^{th} Hunstville Symposium on Gamma-Ray Bursts, Hunstville, Alabama, 1999. Eds. R.M. Kippen, R.S. Mallozzi, G.J. Fishman. Vol. 526 p.524

[91] M. Georganopoulos, F.A. Aharonian & J.G. Kirk, submitted to A&A letters, astro-ph/0110379

[92] G. Ghisellini & P. Madau, MNRAS **280** (1996) 67

[93] G. Ghisellini, Invited talk at the 25th Johns Hopkins Workshop: "2001: A Relativistic Spacetime Odyssey. Experiments and Theoretical Viewpoints on General Relativity and Quantum Gravity", Florence, Sep. 2001, astro-ph/0111584

[94] B. Giebels et al., Nucl. Instr. and Meth. in Phys. Res. A **412** (1998) 329

[95] J. Goodman, ApJ **308** (1986) L47

[96] P. Goret et al., A& **270** (1993) 401

[97] R.J. Gould, Physical Review Letters **15** (1965) 577

[98] The GRAAL collaboration, to be published in APh 2002, astro-ph/0108270

[99] GRAAL website. http://hegra1.mppmu.mpg.de/GRAAL/

[100] I.A. Grenier, Proceedings of the GeV-TeV Gamma Ray Astrophysics Workshop "Towards a Major Atmospheric Cherenkov Detector VI", Snowbird, Utah 1999. Eds. Dingus et al. 2000. Vol. 515 p. 261

[101] J.P. Halpern & S.S. Holt, Nature **357** (1992) 222

[102] A.K. Harding, ApJ **245** (1981) 267

[103] A.K. Harding & T.K. Gaisser, ApJ **358** (1990) 561

[104] A.K. Harding & O.C. de Jager, Proceedings of the GeV-TeV Gamma Ray Astrophysics Workshop "Towards a Major Atmospheric Cherenkov Detector V", Kruger National Park, 1997. Eds. O.C. de Jager p. 64

[105] R.C. Hartman et al., ApJS **123** (1999) 79, http://cossc.gsfc.nasa.gov/cossc/egret/3rd_EGRET_Cat.html

[106] R.C. Hartman et al., ApJ **553** (2001) 683

[107] A. Haungs et al., APh **12** (1999) 145

[108] S. Hayakawa, Prog. Theor. Phys. **8** (1952) 571

[109] The HEGRA coll., http://www-hegra.desy.de/mrk-421/

[110] W. Hermsen, Space Science Reviews **36** (1983) 61

[111] M. Heß et al. (the HEGRA coll.), APh **11** (1999) 363

[112] HETE 2, http://space.mit.edu/HETE/

[113] A.M. Hillas, Proceedings of the 19^{th} ICRC, La Jolla, 1985 Vol. 3 p. 445

[114] A.M. Hillas et al., ApJ **503** (1998) 744

[115] W. Hofmann et al., Proceedings of the GeV-TeV Gamma Ray Astrophysics Workshop "Towards a Major Atmospheric Cherenkov Detector VI", Snowbird, Utah 1999. Eds. Dingus et al. 2000. Vol. 515 p. 500

[116] D. Horns (private communication)

[117] G.W. Hutchinson, Philos. Mag. **43** (1952) 847

[118] J.D. Jackson, Classical Electrodynamics, Wiley, N.Y. 1962

[119] J.V. Jelley & N.A. Porter, Quarterly Journal of the Royal Astronomical Society **4** (1963) 275

[120] S. Jha et al., ApJ **554** (2001) L155

[121] G.Kanbach et al., Space Science Reviews **49** (1988) 69

[122] G. Kanbach et al., A&A **289** (1994) 855

[123] A. Karle, PhD thesis, Ludwig-Maximilians-Universität München (1994)

[124] C.F. Kennel & F.V. Coroniti, ApJ **283** (1984) 694

[125] T. Kifune et al., ApJ, **438** (1995) L91

[126] J.G. Kirk & A. Mastichiadis, A&A **213** (1989) 75

[127] J.G. Kirk, Proceedings of the Cracow workshop on "Relativistic Jets in AGNs", p.145. astro-ph/9708040

[128] J.G. Kirk, F.M. Rieger & A. Mastichiadis, A&A **333** (1998) 452

[129] J.G. Kirk, L. Ball & O. Skjæraasen, APh **10** (1999) 31

[130] J.G. Kirk & R.O. Dendy, Journal of Physics G: Nuclear and Particle Physics **27** (2001) 1589

[131] D.A. Kniffen et al., ApJ **411** (1993) 133

[132] D.A. Kniffen et al., Proceedings of the GeV-TeV Gamma Ray Astrophysics Workshop "Towards a Major Atmospheric Cherenkov Detector VI", Snowbird, Utah 1999. Eds. Dingus et al. 2000. Vol. 515 p. 492

[133] K. Koyama et al., Nature **378** (1995) 255

[134] D. Kranich, PhD Thesis, Technische Universität München (2001)

[135] H. Krawczynski et al., ApJ **559** (2001) 187

[136] F. Krennrich et al., ApJ **560** (2001) L45

[137] L. Kuiper et al., A&A **351** (1999) 119

[138] S.R. Kulkarni, Nature **393** (1998) 35

[139] S.R. Kulkarni, Nature **398** (1999) 389

[140] P.O. Lagage & C.J. Cezarsky, A&A **125** (1983) 249

[141] D.Q. Lamb & D.E. Reichart, ApJ **536** (2000) 1

[142] C.D. Long et al., Proceedings of the 9^{th} ICRC, London, 1966 Vol. 1 p. 318

[143] M.S. Longair, "High Energy Astrophysics", Cambridge University Press, 1981 (reprinted with corrections 1997)

[144] S. Lucek & A.R. Bell, MNRAS **314** (2000) 65

[145] M.A. Malkov & H.J. Völk, A&A **300** (1995) 605

[146] K. Mannheim & P.L. Biermann, A&A **253** (1992) L21

[147] K. Mannheim, A&A **269** (1993) 67

[148] L. Maraschi, G. Ghisellini & A. Celotti, ApJ **397** (1992) L5

[149] L. Maraschi et al., ApJ **526** (1999) L81

[150] S. Markoff, H. Falcke & R. Fender, A&A **372** (2001) L25

[151] P. Massey & C.B. Foltz, PASP **112** (2000) 566

[152] A. Mastichiadis & O.C. de Jager, A&A **311** (1996) L5

[153] A. Mastichiadis & J.G. Kirk, A&A **320** (1997) 19

[154] A. Mastichiadis & J.G. Kirk, Proceedings of the Workshop in "Frontier objects in astrophysics", Vulcano, eds. F. Giovanelli, G.Mannocchi (1998)

[155] S.M. Matz et al., ApJ **434** (1994) 288

[156] H.A. Mayer-Hasselwander et al., ApJ **421** (1994) 276

[157] C.A. Meegan et al., Nature **355** (1992) 143

[158] P. Mészáros, Annual Review of Astronomy and Astrophysics **40** (2002) astro-ph/0111170

[159] R.A. Millikan & G.H. Cameron, Phys. Rev. **31** (1928) 921

[160] I.F. Mirabel & L.F. Rodríguez, Nature **392** (1998) 673

[161] I.F. Mirabel et al., A&A **330** (1998) L9

[162] I.F. Mirabel & L.F. Rodríguez, ARA&A **37** (1999) 409

[163] R. Mirzoyan & E. Lorenz, Measurement of the Night Sky Light background at La Palma, MPI-PhE/94-35 (1994)

[164] R. Mirzoyan et al., Proceedings of the GeV-TeV Gamma Ray Astrophysics Workshop "Towards a Major Atmospheric Cherenkov Detector IV", Padova 1995. Eds. M. Cresti, p. 230

[165] R. Mirzoyan et al., Nucl. Instr. and Meth. in Phys. Res. A **387** (1997) 74

[166] R. Monterreal, PSA Technical Report R12/95 RM (1995)

[167] P. Morrison, Nuovo Cimento **7** (1958) 858

[168] A. Mücke & R. Protheroe, APh **15** (2001) 121

[169] R. Mukherjee, Proceedings of the International Symposium on High-Energy Gamma-Ray astronomy, Heidelberg, 2000. Eds. F.H. Aharonian and H.J. Völk Vol. 558 p. 324

[170] H. Muraishi et al., A&A **354** (2000) L57

[171] H.I. Nel & O.C. de Jager, Ap&SS **230** (1995) 299

[172] Y.I. Neshpor et al., Astronomy Letters **24** (1998) 134

[173] T. Nishiyama et al., Proceedings of the 26^{th} ICRC, Salt Lake City, Utah (1999) Vol. 3 p. 370

[174] P.L. Nolan et al., ApJ **409** (1993) 697

[175] R.A. Ong, Physics Reports **305** (1998) 93

[176] S. Oser et al., ApJ **547** (2001) 949

[177] W.S. Paciesas et al., ApJS **122** (1999) 465

[178] B. Paczyński, ApJ **308** (1986) L43

[179] B. Paczyński, ApJ **348** (1990) 485

[180] B. Paczyński, ApJ **494** (1998) L45

[181] L. Padilla et al., Proceedings of the 26^{th} ICRC, Salt Lake City, Utah 1999, OG.2.3.17

[182] J.R. Patterson & A.M. Hillas, Nucl. Instr. and Meth. in Phys. Res. A **278** (1989) 553

[183] R. Petre, G.E. Allen & U. Hwang, Astronomische Nachrichten **320** (1999) 199

[184] F. Piron, PhD thesis, Université de Paris-Sud (U.F.R. Scientifique D'Orsay) (2000)

[185] F. Piron et al., A&A **374** (2001) 895

[186] R. Plaga et al., Proceedings of the 24^{th} ICRC, Rome, 1995 Vol. 1 p. 1005

[187] M. Pohl, A&A **307** (1996) L57

[188] M. Punch et al., Nature **358** (1992) 477

[189] J. Quinn et al., ApJ **456** (1996) L83

[190] J.P. Rachen, Proceedings of the GeV-TeV Gamma Ray Astrophysics Workshop "Towards a Major Atmospheric Cherenkov Detector VI", Snowbird, Utah 1999. Eds. Dingus et al. 2000. Vol. 515 p. 41

[191] P.V. Ramanamurthy & A.W. Wolfendale, "Gamma-ray astronomy", Cambridge University Press (1986)

[192] P.V. Ramanamurthy et al., ApJ **447** (1995) L109

[193] M.V.S. Rao & S. Sinha, Journal of Physics G: Nuclear and Particle Physics **14** (1988) 811

[194] B.C. Raubenheimer & H.J. Smit, APh **7** (1997) 63

[195] A. Razdan et al., to be published in APh, astro-ph/0109476

[196] E.M. Reynoso et al., AJ **117** (1999) 1827

[197] R.W. Romani & I.-A. Yadigaroglu, ApJ **438** (1995) 314

[198] R.W. Romani, ApJ **470** (1996) 469

[199] M.A. Ruderman & P.G. Shuterland, ApJ **196** (1975) 51

[200] T. Sako et al., Proceedings of the 25^{th} ICRC, Durban, 1997 Vol. 3 p. 193

[201] R.M. Sambruna et al., ApJ **538** (2000) 127

[202] M. Sánchez (Ed.), Solar Thermal Test Facilities, Solar PACES. Doc. CIEMAT (1996) 81

[203] B.M. Schäfer et al., Nucl. Instr. and Meth. in Phys. Res. A **465** (2001) 394

[204] N.J. Shaviv, PhD thesis (1996), Technion Report Ph-96-16

[205] E.J. Schneid et al., A&A **255** (1992) L13

[206] V. Schönfelder et al., "The Universe in Gamma Rays", Springer Verlag (2001)

[207] M. Sikora, M.C. Begelman & M.J. Rees, ApJ **421** (1994) 153

[208] M. Sommer et al., ApJ **442** (1994) L63

[209] R. Srinivasan et al., ApJ **489** (1997) 170

[210] The STACEE coll., The Solar Tower Atmospheric Cherenkov Effect Experiment (STACEE) Design Report, EFI preprint 97-17 (1997).

[211] F.W. Stecker, "Origin of cosmic rays", Eds. J.L. Osborne and A.W. Wolfendale, Reidel, Dordrecht (1975) p. 267

[212] S.J. Sturner & C.D. Dermer, ApJ **420** (1994) L79

[213] P.A. Sturrock, ApJ **164** (1971) 529

[214] Swift, http://swift.gsfc.nasa.gov/

[215] S.P. Swordy et al., ApJ **349** (1990) 625

[216] T. Tanimori et al., ApJ **492** (1998) L33

[217] T. Tanimori et al., ApJ **497** (1998) L25

[218] M. Tavani & J. Arons, ApJ **477** (1997) 439

[219] D.J. Thompson et al., Nature **359** (1992) 615

[220] D.J. Thompson et al., ApJ **516** (1999) 297

[221] D.J. Thompson, Proceedings of the International Symposium on High-Energy Gamma-Ray astronomy, Heidelberg, 2000. Eds. F.H. Aharonian and H.J. Völk Vol. 558 p. 103

[222] H.S. Tornabene & F.J. Cusimano, Canadian Journal of Physics **46** (1968) S81

[223] O.T. Tümer et al., Proceedings of the 21^{st} ICRC, Adelaide (1990) Vol. 4 p. 238

[224] O.T. Tümer, J.S. Hammond & A.D. Zych, Nuclear Physics B (Proc. Suppl.) **14A** (1990) 176

[225] O.T. Tümer et al., Proceedings of the 22^{nd} ICRC, Dublin (1991) Vol. 2 p. 634

[226] M. Ulrich et al., Journal of Physics G: Nuclear and Particle Physics **24** (1998) 883

[227] C.M. Urry & P. Padovani, PASP **107** (1995) 803

[228] H.C. van de Hulst, "Light Scattering by Small Particles", John Wiley & Sons, Inc. 1957

[229] J. van Paradijs et al., Nature **386** (1997) 686

[230] P.R. Vishwanath, Proceedings of the 27^{th} ICRC, Hamburg (2001) Vol. 7 p. 2954

[231] P.R. Vishwanath et al., Proceedings of the 27^{th} ICRC, Hamburg (2001) Vol. 6 p. 2415

[232] H.J. Völk, Proceedings of the GeV-TeV Gamma Ray Astrophysics Workshop "Towards a Major Atmospheric Cherenkov Detector V", Kruger National Park, 1997. Eds. O.C. de Jager p. 87

[233] T.C. Weekes, Physics Reports **160** (1988) 1

[234] T.C. Weekes et al., ApJ **342** (1989) 379

[235] T.C. Weekes, Space Science Reviews **9** (1992) 315

[236] T.C. Weekes, Proceedings of the GeV-TeV Gamma Ray Astrophysics Workshop "Towards a Major Atmospheric Cherenkov Detector VI", Snowbird, Utah 1999. Eds. Dingus et al. 2000. Vol. 515 p. 3

[237] T.C. Weekes et al., Proceedings of the GeV-TeV Gamma Ray Astrophysics Workshop "Towards a Major Atmospheric Cherenkov Detector VI", Snowbird, Utah 1999. Eds. Dingus et al. 2000. Vol. 515 p. 515

[238] T.C. Weekes, Proceedings of the International Symposium on High-Energy Gamma-Ray astronomy, Heidelberg, 2000. Eds. F.H. Aharonian and H.J. Völk Vol. 558 p. 15

[239] A.E. Wehrle et al., ApJ **497** (1998) 178

[240] W.T. Welford & R. Winston, "The Optics of Nonimaging Concentrators", Ed. Academic Press 1978

[241] G. Wettermark, "The solar power plants at Almería", Ed. by Energy research commission (Efn), Stockholm, 1986.

[242] B. Wiebel, Chemical composition in high energy cosmic rays, Report WUB 94-08 (1994), available on http://wpos6.physik.uni-wuppertal.de:8080/Public/papers-public.html

[243] Xephem, http://www.clearskyinstitute.com/xephem/xephem.html

[244] T. Yoshikoshi et al., ApJ **487** (1997) L65

[245] J.J.M. in 't Zand et al., ApJ **559** (2001) 710

[246] J.A. Zweerink et al., Proceedings of the 26^{th} ICRC, Salt Lake City, Utah 1999, Vol. 5 p. 223

Acknowledgements

A person without a project is still a person, but a project without certain people is not a project anymore. That is why I would like to thank and remember first of all two people who made the solar farm experiments to become a real project: E. Paré, father of the solar farm projects and P.N. Bhat, who contributed to the understanding of the wavefront samplers to a great extent. Without their dedication, the solar farm experiments, and this thesis, would not be a reality.

Behind a thesis there are not only a multiple number of doubts, but the same number of people who are always there to solve such doubts. I want to thank you all, and you know *who you are*, for having something to thank you. I am sure, there must have been a moment, at the beginning, where you could have said no. But somehow you missed it. My sincere gratitude goes to:

Dr. Habil. Rainer Plaga, head of the GRAAL collaboration, who gave me in April 1999 the opportunity of working for GRAAL and do this thesis. Thank you for having filled these three years with interesting discussions, fruitful work and "almost infinite" patient mails.

Jürgen Gebauer, for his advices and the morning talks.

All the rest of the members of the GRAAL collaboration, especially Prof. Fernando Arqueros and David, for sharing night shifts and listening to all my questions with stoicism.

Prof. Dr. John Kirk for the supervision of this thesis and Prof. Dr. Otto Nachtmann and Prof. Dr. Peter Ulmschneider for accepting to be part of the examiners.

David Smith, head of the CELESTE collaboration, for explanations about the heliostat approach both at the CELESTE site and in numerous e-mails.

All the PSA staff, J. Ballestrín and A. Valverde for excellent working conditions and all the PSA operators and guards for their worries about me in the long nights of shift in the experiment. Pepe y Carmela por hacer el mejor café de la costa mediterránea.

All the members of the astroparticle physics group in the Max Planck Institut für Physik in Munich: Dr. Eckart Lorenzt for his support, Toni for giving an end to my problems with the computers, Juan for his answers to my dayly questions, Wolfang, Razmic, Sven, David, Martin, Markus, Franz, Robert, Daniel, Vincenzo, Sybille, Michaela and those who already left the group, Manolito, Alvin, Katya, Harald and José Carlos.

Mis padres, Teresa y José Luis por creer en los rayos gamma y en mí y por "estar llenos de cielo" y compartirlo. Lucía, por haberme dado más de lo que doy, por ser un lujo que puedo disfrutar a diario y por seguir siendo mi hermana después de las inclemencias de estos últimos 3 meses. Toda mi familia, por los veranos de Cabañas y las charlas dominicales en A Rúa. Paula, por sus bailes.

Ana Bermúdez, Belén, Marilí, Elena, Sandra, Majo, Isa, Lucía, Alba, Ángela, Ana Villot, Paula, Carmen y Santu por las tertulias del Fontecada y todo lo que sigue. Piwi, Gundi, Alejandro, Nacho, Dani, Quico, Oscar, Carba y Fran por las tardes del Franco.

Pedro, por apoyarme en mi decisión de escribir esta tesis.

Jes, Sam, Mari Luz, Jorge, Sito, Vero, Silvana, Patricia, Nacho, Max, Fidel por las partidas de mus en la cafetería de la Facultad y por el futbolín.

Lourdes por presentarme a Carmiña y a mi ahijado Javi, y a ellos por las tardes en el parque.

My friends in Heidelberg, Mabel, Claudia, Christoph, Juanma, Jeroen, Justyna, Idoia and Montse, for making my first year in Germany unforgettable.

All of you in Munich, Fefa for being always near me (although it is easy living a floor above...) and for her imagination, David for showing me Süd Tirol, the Edelweiss and for his photos, Patrick for the trip to Bretagne (because we learnt that one can live with "very few" things) and for his inspiring crêpes, Simon for his philosophical reflections, Ossie for his personal string theory (I would say red, Ossie), Paul for his organization skills, Dave for sharing his quietness, Kae for the Japanese lessons and her energy, Kazu for his delicious sushi, Rob for his corrections and for his tips for concerts, Otto and Martin for organizing the ski weekends, Axel for his sister's wine, Neeta for her smile, Paddy for his singing and for the snowboard lessons, Verena and Johanna for their laugh, Marcus for his mother's Stollen.

Dimitri, bei Meri, for his gyros and good mood.

Todos aquéllos que me habéis visitado en Munich durante estos tres años, además de los ya mencionados, Marcos, Andrés, Paco, Nacho y Rosa.

Si me he olvidado de alguien que merecía ser recordado, espero que comprenda que el olvido a veces se equivoca. Muchas gracias por todo.